Viscous contact problems in glaciology

Gonzalo Gonzalez de Diego
Oriel College
University of Oxford

A thesis submitted for the degree of
Doctor of Philosophy

Trinity Term 2023

Acknowledgements

I am deeply grateful for the supervision I have received from Ian and Patrick. They have happily shared their knowledge and experience in applied mathematics throughout these four years. Their commitment to producing outstanding and earnest research has been a constant source of inspiration.

Most of the research contained in this thesis was produced in the Andrew Wiles Building. I am indepted to the community I have encountered there. Not just for the intelectual stimulation resulting from seminars and casual conversations over coffee, but for the friendships I have developed in this time.

A major discovery in these years of doctoral studies has been the glaciological community. The icy maths reading group we held in Oxford, the Karthaus summer school in 2022, the IGS conference in Bilbao in 2022, and two visits to Northumbria University have been opportunities to meet the scientists and mathematicians that are fascinated by glaciers. Meeting these people, who are driven by love and awe of nature, has crystallised my wish to continue dedicating myself to the cryospheric sciences.

Abstract

Viscous contact problems describe the time evolution of fluid flows in contact with a surface from which they can detach and reattach. They can be modelled by coupling the Stokes equations with contact boundary conditions and a free boundary equation that evolves the geometry of the domain occupied by the fluid. These problems are of particular importance in glaciology, where they arise in the study of grounding lines and subglacial cavities. This work investigates the numerical approximation of viscous contact problems with applications to these two examples in glaciology.

We commence by formulating the viscous contact problems that model subglacial cavitation and marine ice sheets in Chapter 1. We state the different variational inequalities that arise in these problems and are equivalent to the Stokes equations with contact boundary conditions.

We then propose a novel framework for building numerical schemes for these problems in Chapter 2. This framework considers a family of discrete variational inequalities and establishes certain conditions that should be satisfied when approximating the free boundary equations. We then describe the numerical scheme that is used for the remainder of this work and compare it with different schemes that fit the framework introduced beforehand.

Chapter 3 is dedicated to the numerical analysis of one of the Stokes variational inequalities formulated in this work. We give rigorous proofs on the conditions under which it is well-posed and its finite element approximation converges. By developing theoretical tools based on existing work in the numerical analysis of variational inequalities and p-Stokes systems, our analysis deals with three substantial difficulties arising in this system: the presence of rigid modes in the space of admissible velocity fields, the nonlinear rheology used in glaciology, and the friction boundary condition enforced at the base of glaciers.

Chapter 4 presents a numerical investigation of subglacial cavitation and its application to glacial sliding under steady and unsteady conditions. We reconstruct steady friction laws by calculating several steady cavity shapes. These steady

results are validated by comparing them to a linearised analytical method. We then perturb some of these steady states with oscillating water pressures that reveal an interplay between the frequency of the perturbations and the resulting sliding speed and cavity volume. Moreover, we find that if the steady state is located on the downsloping or rate-weakening part of the friction law, the cavity evolves towards the upsloping section, indicating that the downsloping part is unstable.

Finally, we explore steady marine ice sheet configurations in Chapter 5. We do so by computing steady states to the parallel slab marine ice sheet problem, which we propose in this chapter. In this problem, a slab of ice of uniform thickness flows down an inclined bedrock into the ocean. We enforce influx conditions that allow us to explore a spectrum of flow regimes, ranging from sliding to shear-dominated flow. We find that the flux-thickness relationship at the grounding line takes the form of power laws with exponents $n + 1$ and $n + 2$ in these two limits, respectively, where n is a non-dimensional parameter in Glen's law, the power law rheology used commonly used in glaciology. We derive analytical approximations in these limits which resemble our numerical findings closely, with visible deviations in some cases. Our numerical results allow us to understand the shortcomings of these commonly used analytical methods. Moreover, in the context of the parallel slab problem, we find that the flux-thickness relationships are strictly monotonically increasing and that the bedrock plays a prominent role in the sliding dominated regime.

Contents

Chapter 1

Introduction

Viscous contact problems are time-dependent fluid flow problems in which the fluid is in contact with a solid surface from which it can detach and reattach. Contact problems of this type arise when modelling glacial ice flow, which is typically treated as a viscous fluid flow [42, 58, 44, 93]. On a large scale, they are relevant to marine ice sheets with a grounding line [89, 24, 91] and, on a smaller scale, to the formation of subglacial cavities when the ice slides over bedrock undulations [31, 87, 36]. These problems share a very similar mathematical structure and are of great importance for understanding ice sheet dynamics and predicting future sea level rise [85, 25].

This work is an analytical, computational, and glaciological study of viscous contact problems. Although several computations of viscous contact problems exist in the literature [36, 24, 28, 49, 97], these studies have rarely explored the mathematical structure of these problems. Given the importance that they have in glaciology, we believe that a more detailed analysis of viscous contact problems could reveal many properties of their rich mathematical structure and could be beneficial for building improved numerical schemes. Therefore, one of the main goals of this work is to propose a framework for discretising these problems based on a rigorous understanding of a Stokes variational inequality that arises in the mathematical model. In particular, we build a numerical solver for viscous contact problems based on this framework, and provide an extensive validation via comparisons with different methods and analytical results.

With this solver we then explore the two paradigmatic examples of viscous contact problems in glaciology: subglacial cavitation and marine ice sheet dynamics. Our investigation of these two problems broadly consists in the computation of steady states and, in the case of subglacial cavitation, their unsteady perturbations. For subglacial cavitation, this essentially amounts to constructing steady friction laws for glacial sliding with cavitation and studying the effects of unsteady water pressures. For marine ice sheets, our steady computations allow us to explore flux-thickness relationships at the grounding line. These

computations offer novel insights into the physics of these two fundamental problems in glaciology. Moreover, our steady computations for both problems are backed with analytical results which not only validate our numerical solver but provide knowledge of the range of validity of these analytical models.

This chapter, the introduction of the thesis, is mostly concerned with the mathematical formulation of a viscous contact problem. It also includes an outline of the thesis and some clarifications on the mathematical notation we use. It contains a detailed explanation of the equations of flow and the boundary conditions for a general two-dimensional viscous contact problem. We also specify the form that these equations take when considering the more particular problems of subglacial cavitation and marine ice sheets.

1.1 Outline of the thesis

This thesis can be seen as structured into two separate bodies: one concerned with the numerical approximation of viscous contact problems (Chapters 2 and 3) and another with the computational exploration of the two viscous contact problems arising in glaciology (Chapters 4 and 5).

In Chapter 2, we propose a class of numerical schemes for solving viscous contact problems and then, in Section 2.3, we introduce the main numerical scheme used in the subsequent chapters of this thesis. Although the description of the general class of schemes employs an abstract framework that requires a cumbersome notation, Section 2.3 avoids these technicalities and is written in a self-contained manner. This facilitates the understanding of our numerical scheme for viscous contact problems for a reader who, for example, might only be interested in the glaciological applications in Chapters 4 and 5.

A fundamental aspect of the mathematical formulation of viscous contact problems is that the Stokes equations with contact boundary conditions are essentially a variational inequality when written as a variational statement. Chapter 3 is dedicated to the mathematical analysis of this variational inequality and its numerical approximation via finite element methods. The goal of this chapter is to give a rigorous justification for the finite element method used in the numerical scheme presented in Section 2.3. In this analysis, we develop new techniques, based on the finite element analysis of variational inequalities and of the p-Stokes equations, for dealing with the lack of coercivity of the variational inequality and with the nonlinearities due to the flow rheology and basal friction.

The first glaciological application is on subglacial cavitation and is found in Chapter 4. In this chapter, we investigate the formation of subglacial cavities and its effects on glacial sliding. This investigation involves the computation of steady friction laws and a rigorous

comparison with a linearised model for subglacial cavitation. Then, motivated by an extensive body of fieldwork, we provide a new study on the effects of unsteady water pressures on glacial sliding by perturbing several steady cavity states.

Our second glaciological application, in Chapter 5, focuses on marine ice sheets and the numerical computation of flux-thickness relationships at the grounding line. We propose a novel test problem for studying an ice sheet's grounding zone and provide a series of numerical results that expose a spectrum of steady state regimes, ranging from sliding to shear-dominated flow. Furthermore, two analytically-derived approximate flux-thickness laws for sliding and shear-dominated flows are presented that offer an insight into the dominating force balance underlying steady marine ice sheet configurations.

1.2 Notation

We include a brief description of the mathematical notation used mostly in this chapter and Chapters 2 and 3. In particular, here we focus on notational aspects related to function spaces and inequalities. Further notational clarifications on the discrete problem are postponed to Section 2.1 in Chapter 2.

Given a normed vector space X, the dual of X is denoted by X' and the pairing between elements in the primal and dual spaces by $\langle f, x\rangle_X$ for $f \in X'$ and $x \in X$. We will work with the Lebesgue and Sobolev spaces $W^{m,r}(\Omega)$, where $m \geq 0$ and $r \geq 1$, defined as the set of functions with weak derivatives up to order m which are r-integrable. When $m = 0$ we write $L^r(\Omega)$. The space of polynomials of degree k over a simplex E (interval, triangle, tetrahedron) is denoted by $\mathcal{P}_k(E)$. The space of functions over a domain Ω that have up to k continuous derivatives is written as $\mathcal{C}^k(\Omega)$, and whenever $k = 0$ (continuous functions on Ω) we simply write $\mathcal{C}(\Omega)$. Vector-valued functions and vector-valued function spaces will be denoted with bold symbols, e.g. $\boldsymbol{u}$ and $\boldsymbol{W}^{m,r}(\Omega)$.

Throughout this work, we repeatedly refer to the normal and tangential components of vector fields along the boundaries of a domain. Given a domain Ω, the vector $\boldsymbol{n}$ denotes the unit outwards-pointing vector normal to the boundary of Ω, which we denote by $\partial\Omega$. The tangential component of a vector field $\boldsymbol{v} : \Omega \to \mathbb{R}^2$ on $\partial\Omega$ is given by $\mathbf{T}\boldsymbol{v} = \boldsymbol{v} - (\boldsymbol{v} \cdot \boldsymbol{n})\boldsymbol{n}$. Here, $\mathbf{T} = \mathbf{I} - \boldsymbol{n}\boldsymbol{n}^\top$ is the orthogonal projection onto the tangential component.

In Chapter 3, for a domain Ω and two functions $f : \Omega \to \mathbb{R}$ and $g : \Omega \to \mathbb{R}$, we write $f \sim g$, $f \lesssim g$, and $f \gtrsim g$ if there exist generic constants $c, C > 0$ such that $cf(\boldsymbol{x}) \leq g(\boldsymbol{x}) \leq Cf(\boldsymbol{x})$, $cf(\boldsymbol{x}) \leq g(\boldsymbol{x})$, and $cf(\boldsymbol{x}) \geq g(\boldsymbol{x})$ for all $\boldsymbol{x} \in \Omega$, respectively. We assume that these generic constants do not depend on the mesh size or on the continuous and discrete solutions of the problem.

1.3 Modelling ice as a viscous fluid

Ice flow is generally modelled as a viscous fluid which evolves according to the Stokes equations with a simple non-linear rheology that relates deviatoric stress and strain rate [93, 33]. In general, for a given flow velocity $\boldsymbol{u}$, the deviatoric stress τ and strain rate $\mathbf{D}\boldsymbol{u}$ are related by an effective viscosity η:

$$\tau = 2\eta(|\mathbf{D}\boldsymbol{u}|)\mathbf{D}\boldsymbol{u}, \tag{1.1}$$

where $\mathbf{D}\boldsymbol{u}$ is the symmetric part of the velocity gradient, that is

$$\mathbf{D}\boldsymbol{u} = \frac{1}{2}\left(\nabla\boldsymbol{u} + \nabla\boldsymbol{u}^\top\right), \tag{1.2}$$

and $|\cdot|$ represents the Frobenius norm of a matrix: for $B \in \mathbb{R}^{m\times m}$ with components B_{ij} we have $|B|^2 = \sum_{ij} B_{ij}^2$.

Glen's law [42] is the most common choice of rheological law for ice and it establishes the following formula for the effective viscosity:

$$\eta(|\mathbf{D}\boldsymbol{u}|) = \frac{1}{2}\mathcal{A}^{-1/n}\left(\frac{1}{2}|\mathbf{D}\boldsymbol{u}|^2\right)^{\frac{1-n}{2n}}. \tag{1.3}$$

Here, the parameter $\mathcal{A} > 0$ is a temperature dependent parameter which we shall consider constant in this work (that is, we consider the isothermal case). The parameter n is also constant and is usually set to $n = 3$; for $n = 1$ we recover the standard linear Stokes flow.

When analysing the variational inequality that arises in the weak formation of the Stokes equations, the rheological law (1.3) is written as

$$\eta(|\mathbf{D}\boldsymbol{u}|) = \frac{1}{2}\alpha(r)|\mathbf{D}\boldsymbol{u}|^{r-2}, \tag{1.4}$$

where $\alpha(r) = (1/2)^{(r-2)/2}\mathcal{A}^{1-r}$ is constant and $r = 1 + 1/n$ is in $(1, 2]$ for $n \geq 1$. Note that such an expression for $\eta(|\mathbf{D}\boldsymbol{u}|)$ reveals the r-Stokes nature of the problem when considered as a variational problem in the setting of Sobolev spaces.

At a computational level, numerical problems may arise when implementing Glen's law due to the singular behaviour of $\eta(|\mathbf{D}\boldsymbol{u}|)$ around $|\mathbf{D}\boldsymbol{u}| = 0$. One common way of dealing with this issue is to use a regularised effective viscosity, defined by

$$\eta_\epsilon(|\mathbf{D}\boldsymbol{u}|) = \frac{1}{2}\alpha(r)(|\mathbf{D}\boldsymbol{u}|^2 + \epsilon)^{\frac{r-2}{2}}, \tag{1.5}$$

where $\epsilon > 0$ is a small parameter. Such a regularisation is not required when $r = 2$ (that is, $n = 1$).

1.4 Formulation of a viscous contact problem

A viscous contact problem is a time dependent flow problem modelled with the Stokes equations with contact boundary conditions and free boundary equations. We use the Stokes equations instead of the Navier-Stokes equations because we only focus on ice, which flows under very low Reynolds numbers. In this work we consider two-dimensional domains Ω of fixed horizontal length L whose upper and lower boundaries are curves given by the functions $\theta(x,t)$ and $s(x,t)$ respectively; that is,

$$\Omega(t) = \left\{(x,z) \in \mathbb{R}^2 : 0 < x < L, \quad \theta(x,t) < z < s(x,t)\right\}. \tag{1.6}$$

The domain Ω is assumed to be in contact with a solid surface, the bedrock, described by the function $b(x)$. We denote the boundary of Ω by $\partial\Omega$, the lower boundary by Γ_b, and the top boundary by Γ_t. Additionally, we write Γ_b as the disjoint union of an attached region Γ_a and a detached region Γ_d; these subsets are defined as

$$\Gamma_a(t) = \{(x,z) \in \partial\Omega : z = \theta(x,t), \quad b(x) = \theta(x,t)\}, \tag{1.7a}$$

$$\Gamma_d(t) = \{(x,z) \in \partial\Omega : z = \theta(x,t), \quad b(x) < \theta(x,t)\}. \tag{1.7b}$$

At each instant in time, the fluid occupying the domain $\Omega = \Omega(t)$ flows with a velocity $\boldsymbol{u}$ and a pressure p which satisfy the Stokes equations:

$$-\nabla \cdot (2\eta(|\mathbf{D}\boldsymbol{u}|)\mathbf{D}\boldsymbol{u}) + \nabla p = \boldsymbol{f} \quad \text{in } \Omega, \tag{1.8a}$$

$$\nabla \cdot \boldsymbol{u} = 0 \quad \text{in } \Omega. \tag{1.8b}$$

Here, the vector field $\boldsymbol{f}$ is a body force to be specified in each problem. We restrict our attention to the case where the viscous flow is ice and the effective viscosity $\eta(|\mathbf{D}\boldsymbol{u}|)$ is given by Glen's law (1.3). For a given velocity and pressure field, we define the stress tensor $\boldsymbol{\sigma} = \boldsymbol{\sigma}(\boldsymbol{u}, p)$ by

$$\boldsymbol{\sigma} = 2\eta(|\mathbf{D}\boldsymbol{u}|)\mathbf{D}\boldsymbol{u} - p\mathbf{I}, \tag{1.9}$$

where $\mathbf{I}$ is the identity tensor field. We then define the normal and tangential stresses on $\partial\Omega$ as

$$\sigma_{nn} = (\boldsymbol{\sigma}\boldsymbol{n}) \cdot \boldsymbol{n} \quad \text{and} \quad \boldsymbol{\sigma}_{nt} = \mathbf{T}(\boldsymbol{\sigma}\boldsymbol{n}). \tag{1.10}$$

A fundamental property of viscous contact problems is that the fluid can detach from the bedrock at any moment in time. Mathematically, this possibility is realised by enforcing contact boundary conditions along the attached region Γ_a:

$$\boldsymbol{u} \cdot \boldsymbol{n} \leq 0, \quad \sigma_{nn} \leq -p_w \quad \text{and,} \quad (\boldsymbol{u} \cdot \boldsymbol{n})(\sigma_{nn} + p_w) = 0 \quad \text{on } \Gamma_a. \tag{1.11}$$

We write these contact boundary conditions in terms of a water pressure p_w because, in all of the problems considered in this work, we assume a thin later of water, which we treat as inviscid, exists in between the ice and the bedrock. This water pressure is a non-negative function which is either assumed to be spatially constant, as in the subglacial cavity problem, or linearly varying with depth, as in the marine ice sheet case. By introducing p_w, we incorporate the effects of subglacial hydrological systems into our model [30]. We note that, in all cases considered in this work, p_w is known beforehand when solving the viscous contact problems.

Notice that in (1.11) we are enforcing the ice to either remain attached (i.e. $\boldsymbol{u} \cdot \boldsymbol{n} = 0$) whenever the normal stress exerted by the ice on the bedrock is larger than the water pressure, or to have the possibility of detaching ($\boldsymbol{u} \cdot \boldsymbol{n} < 0$) if the stress equals the water pressure.

Given the velocity field $\boldsymbol{u} = (u, w)$, the free boundaries $\theta(x,t)$ and $s(x,t)$ evolve from $t = 0$ to $t = T$ according to the free boundary equations

$$\frac{\partial s}{\partial t} + u\frac{\partial s}{\partial x} - w = a_t \qquad \text{on } (0,L)\times(0,T), \tag{1.12a}$$

$$\frac{\partial \theta}{\partial t} + u\frac{\partial \theta}{\partial x} - w = a_b \qquad \text{on } (0,L)\times(0,T). \tag{1.12b}$$

Equations (1.12) are derived from a surface mass balance statement that equates the ice flux through the free surface with the terms a_b and a_t, known as accumulation functions, see [44, Section 5.1.2]. The accumulation functions a_t and a_b represent sources of mass along the boundary regions Γ_t and Γ_b of the ice sheet, respectively. A positive accumulation means that ice is added to the flow by the densification of snow or the freezing of water. On the other hand, a negative accumulation represents a mass loss due to melting, for example. In the problems considered in this document, we set $a_t = a_b = 0$.

Remark 1.1. Along the top and lower boundaries, we have that

$$\boldsymbol{u}\cdot\boldsymbol{n} = \frac{-1}{\sqrt{1+\left(\frac{\partial s}{\partial x}\right)^2}}\left(u\frac{\partial s}{\partial x} - w\right) \qquad \text{on } \Gamma_t, \tag{1.13a}$$

$$\boldsymbol{u}\cdot\boldsymbol{n} = \frac{1}{\sqrt{1+\left(\frac{\partial \theta}{\partial x}\right)^2}}\left(u\frac{\partial \theta}{\partial x} - w\right) \qquad \text{on } \Gamma_b. \tag{1.13b}$$

These equalities are used in the construction of numerical schemes for viscous contact problems in Chapter 2 when discretising the free boundary equations (1.12).

Additionally, the functions $\theta(x,t)$ and $s(x,t)$ must also comply with the constraints

$$\theta(x,t) \geq b(x) \qquad x \in (0,L) \text{ and } t \in [0,T], \tag{1.14a}$$

$$s(x,t) > \theta(x,t) \qquad x \in (0,L) \text{ and } t \in [0,T]. \tag{1.14b}$$

The problems considered in this document have a clear dominating direction of flow which is from left to right. Since the free boundary equations (1.12) have an advective nature, we enforce boundary conditions for s and θ at $x = 0$. Finally, we also note that initial conditions for θ and s must also be provided to have a well-posed problem.

Remark 1.2. The boundary conditions (1.11) are also called the Signorini boundary conditions and are well-known in the context of elastic contact problems [68, 48], where the vector field $\boldsymbol{u}$ represents the displacement vector. In fact, as we explain in Chapter 3, the Stokes and elasticity equations equipped with contact boundary conditions share many similarities. Therefore, many ideas and results from the numerical analysis of elastic contact problems can be transferred to the viscous case. One of the main goals of this work is to explore this connection further, since we believe that it hasn't been done sufficiently. An important remark is that the main difference between the elastic and viscous contact problem is the need to evolve the domain in time through the free boundary equations (1.12). As we describe in Chapter 2, the presence of the free boundary equations introduces numerical difficulties that do not arise in the elastic case.

Additional boundary conditions are required to close the Stokes equations and have a well-posed system. Different boundary conditions are used for the viscous contact problems that arise in subglacial cavitation and in marine ice sheets. Once the required boundary conditions are prescribed, we can then introduce the weak formulations of the Stokes equations for each of the problems considered. Since not all readers may be familiar with the weak formulation of a partial differential equation, in Section 1.5 below we explain what a weak formulation is and why it is important. Then, we introduce the problems of subglacial cavitation in Section 1.6 and of marine ice sheets in Section 1.7, together with the corresponding sets of boundary conditions and weak formulations.

1.5 The weak formulation of the Stokes equations as a variational inequality

A weak formulation of a partial differential equation (PDE) is an integral statement of the equation written in terms of weak derivatives. A weak formulation expresses the action of a functional on test functions belonging to a given space; in this sense, it is a variational statement (we study the variations of a functional along different directions specified by the test functions), and thus weak formulations naturally arise in the calculus of variations [62]. In the engineering literature, the term virtual work is used to refer to these variations [84]. The function spaces in which solutions and test functions exist are generally Sobolev spaces;

an introduction to the theory of Sobolev spaces, weak derivatives, and their application to PDEs can be found in [27].

It is desirable to work with weak formulations of PDEs for analytical and computational reasons. From an analytical point of view, the weak formulation of the Stokes equations reveals its equivalence to a minimisation problem whose well-posedness can be investigated with techniques from the calculus of variations. This is carried out in Section 3.1.4, where we prove a theorem for one of the Stokes problems considered in this document which specifies under what conditions a unique solution exists. On the other hand, from a computational point of view, the design and implementation of a finite element method for the Stokes equations is based on its weak formulation. Moreover, in the particular case where the Stokes equations are complemented with the contact boundary conditions (1.11), its weak formulation is given by a variational inequality. As explained in Section 3.3, the finite element method is arguably the most natural way to solve a variational inequality numerically.

In this work, three weak formulations of the Stokes equations as variational inequalities are introduced: Variational inequalities A and B arise when modelling subglacial cavities and Variational inequality C in the context of marine ice sheets. The sense in which these variational inequalities are equivalent to the strong form of the Stokes equations (1.8) is made precise in Section 3.1. In particular, Variational inequality C, which is taken as a representative example in Chapter 3, is derived in Lemma 3.1 from the Stokes equations in the setting of a marine ice sheet.

The first step in defining a weak formulation is choosing suitable function spaces in which to seek the unknowns. Given a domain Ω, we seek the velocity in the subspace

$$V \subset \boldsymbol{W}^{1,r}(\Omega) \tag{1.15}$$

and the pressure in the space

$$Q = L^{r'}(\Omega). \tag{1.16}$$

The definition of the subspace V depends on the velocity boundary conditions, which are specific to the different problems considered below; therefore, we postpone its precise definition to the next two sections. The scalar $r' = (1 - r^{-1})^{-1}$ is the Hölder conjugate of r. As mentioned in the previous paragraph, the weak formulation of the Stokes equations with contact conditions can be written as a variational inequality, and it is expressed in terms of a convex subset of V which we denote by K and is defined by

$$K = \{\boldsymbol{v} \in V : \boldsymbol{v} \cdot \boldsymbol{n} \leq 0 \,\text{on}\, \Gamma_a\}\,. \tag{1.17}$$

The variational inequalities A-C below are expressed in terms of operators defined on function spaces. The operators $A : V \to V'$ and $B : Q \to V'$ are common to all three and are defined by

$$\langle A\boldsymbol{u}, \boldsymbol{v}\rangle_V = \int_\Omega \alpha |\mathbf{D}\boldsymbol{u}|^{r-2} (\mathbf{D}\boldsymbol{u} : \mathbf{D}\boldsymbol{v}) \, \mathrm{d}x, \tag{1.18a}$$

$$\langle Bq, \boldsymbol{v}\rangle_V = \int_\Omega (\nabla \cdot \boldsymbol{v}) \, q \, \mathrm{d}x. \tag{1.18b}$$

These operators incorporate the action of the r-Laplacian and divergence operators in the weak form of the Stokes equations (1.8) and are widely used throughout this document.

Remark 1.3. It is important to note that the spaces V and Q, the set K, and the operators A and B introduced above depend on a domain Ω. In the problems considered here, the domains occupied by the ice on which we solve the variational inequalities evolve over time, and therefore the definitions of these mathematical objects also depend on time. However, for the reader's sake, we do not indicate this dependence in the notation.

When solving the variational inequality numerically, instead of working with $A : V \to V'$, it is preferable to use an operator defined in terms of the regularised viscosity (1.6) to avoid issues around points where the strain rate of the velocity is zero or close to zero. We therefore introduce the operator $A_\epsilon : V \to V'$, defined by

$$\langle A_\epsilon \boldsymbol{u}, \boldsymbol{v}\rangle_V = \int_\Omega \alpha \left(|\mathbf{D}\boldsymbol{u}|^2 + \epsilon\right)^{\frac{r-2}{2}} (\mathbf{D}\boldsymbol{u} : \mathbf{D}\boldsymbol{v}) \, \mathrm{d}x, \tag{1.19}$$

where $\epsilon > 0$. We note that this regularisation is only necessary when $r \in (1, 2)$. In the linear problem the effective viscosity is constant and this singularity disappears.

1.6 Subglacial cavitation

Subglacial cavitation is a phenomenon that occurs at the base of a glacier or an ice sheet and consists of the detachment of the ice sheet from the bed along the lee side of an obstacle due to high basal water pressures [70, 31, 87]. It is considered a fundamental mechanism in glacial sliding over hard beds. In Chapter 4, which is fully dedicated to subglacial cavitation and glacial sliding, one can find an in-depth account of the relationship between subglacial cavitation and glacial sliding, together with a literature review in Section 4.1.

Subglacial cavities form at the ice-bedrock interface, over length scales corresponding to the size of the bedrock obstacles. These length scales are generally several orders of magnitude smaller than those of the glacier. For this reason, and following [36], the computational domain Ω in which we model the formation of cavities is a thin layer of ice of finite height located under a larger mass of ice, see Figure 1.1. We assume the bedrock, and therefore

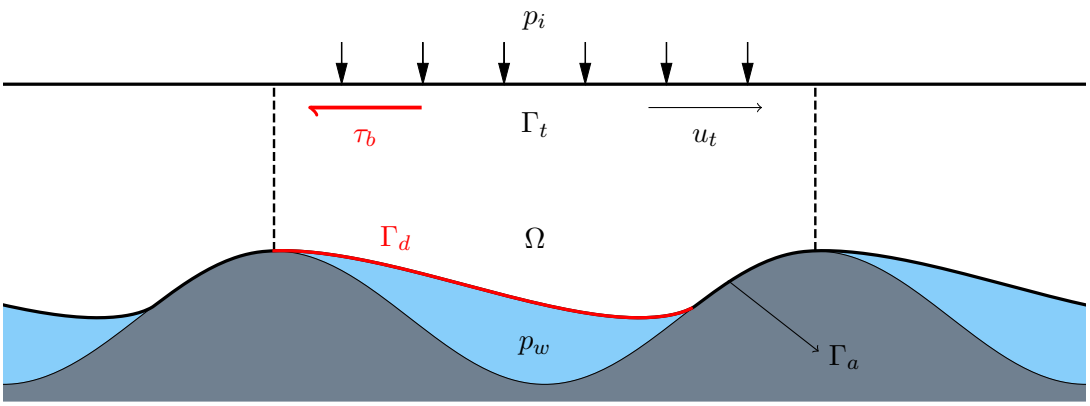

Figure 1.1: The periodic domain Ω on which we model the evolution of a subglacial cavity. The top boundary Γ_t represents a fictional boundary between the domain and the remaining mass of ice above it. The lower boundary is the union of Γ_a and Γ_d, the attached and detached regions, respectively. The subset Γ_d, in red, represents the cavity roof created by the detachment of ice from the bedrock. The domain Ω is assumed to be periodic, but for computational purposes we consider the bounded subset of $\mathbb{R}^2$ enclosed by the dashed vertical lines.

also Ω, to be periodic in the horizontal direction. The upper boundary Γ_t represents a fictional boundary separating Ω from the ice above and therefore remains unchanged in time, i.e. $s(x,t) = H$, where H is the height of the domain. Although we can consider beds of arbitrary shape, in this document, when studying subglacial cavitation, we restrict our attention to sinusoidal beds of amplitude r_b given by

$$b(x) = r_b \left(\cos\left(2\pi \frac{x}{L}\right) - 1 \right). \tag{1.20}$$

Along the cavitated region Γ_d of the lower boundary, the ice is in contact with water at a pressure p_w on which it slides freely, so we prescribe

$$\sigma_{nn} = -p_w \quad \text{and} \quad \boldsymbol{\sigma}_{nt} = 0 \quad \text{on } \Gamma_d. \tag{1.21}$$

For the subglacial cavity problem, we assume this water pressure to be uniform along the length of the bedrock because gravity is unimportant on the spatial scales under consideration. For this reason, we also set the body force $\boldsymbol{f} = 0$ in the subglacial cavity problem. The effect of gravity is captured by the normal boundary condition on the top boundary Γ_t; here, we enforce

$$\sigma_{nn} = -p_i \quad \text{on } \Gamma_t, \tag{1.22}$$

where p_i is the overburden ice pressure due to the weight of the ice lying above the domain.

On the attached region Γ_a, the contact boundary conditions (1.11) hold, and since we assume the ice to be lubricated by a thin layer of water connected to the subglacial drainage system, we allow the ice to slide freely and therefore set $\boldsymbol{\sigma}_{nt} = 0$, which in fact holds on the whole lower boundary $\Gamma_b = \Gamma_a \cup \Gamma_d$ due to (1.21). Finally, we close the system with either the Dirichlet boundary condition

$$u = u_t \quad \text{on } \Gamma_t, \tag{1.23}$$

or the Neumann boundary condition

$$\boldsymbol{\sigma}_{nt} = \tau_b \, (1, 0)^\top \quad \text{on } \Gamma_t, \tag{1.24}$$

where τ_b is the basal shear stress and u_t is a horizontal velocity related to the basal sliding speed u_b in a manner specified in Chapter 4 ("basal" in this context refers to the larger-scale ice flow problem, which views the whole domain Ω as being at the base of the ice sheet). These two different horizontal boundary conditions on Γ_t allow us to consider two different ways of thinking about modelling a subglacial cavity. On the one hand, the portion of ice above the cavity may be kinematically connected to the remainder of the ice sheet, and therefore slides at a given speed determined by the surrounding ice. Mathematically, this is modelled by enforcing the Dirichlet boundary condition (1.23), and the corresponding basal shear stress can be calculated via the integral

$$\tau_b = -\frac{1}{L} \int_{\Gamma_b} (\sigma_{nn} + p_w) \, \mathrm{d}s, \tag{1.25}$$

as in [87, 36]. On the other hand, the basal shear stress must balance the horizontal force in the ice above (this results from an overall force balance on the domain Ω). So we could instead prescribe the basal stress τ_b as a boundary condition, and compute the sliding speed. In this scenario, we enforce (1.24) and compute the basal sliding speed by averaging the horizontal velocity along the lower boundary, that is,

$$u_b = \frac{1}{L} \int_{\Gamma_b} u \, \mathrm{d}s, \tag{1.26}$$

as in [36]. Enforcing the Dirichlet or the Neumann boundary conditions lead to different variational inequalities, which we present below.

Variational inequality A. When we enforce the Dirichlet boundary condition (1.23) in the subglacial cavity problem over a given domain Ω, the Stokes equations are equivalent to a variational inequality written in terms of the space

$$V = \left\{ \boldsymbol{v} \in \boldsymbol{W}^{1,r}(\Omega) : \mathbf{T}\boldsymbol{v} = 0 \text{ on } \Gamma_t, \, \boldsymbol{v} \text{ is periodic in the } x \text{ direction} \right\}. \tag{1.27}$$

In order to enforce (1.23), we need to introduce a divergence-free velocity field $\hat{\boldsymbol{u}} \in \boldsymbol{W}^{1,r}(\Omega)$ which is periodic in the x direction and satisfies $\mathbf{T}\hat{\boldsymbol{u}} = u_t\,(1,0)^\top$ on Γ_t and $\hat{\boldsymbol{u}} \cdot \boldsymbol{n} = 0$ on Γ_a. Then, the variational inequality can be written as: find $(\boldsymbol{u}^*, p) \in K \times Q$ such that

$$\langle A(\boldsymbol{u}^* + \hat{\boldsymbol{u}}) - Bp - f, \boldsymbol{v} - \boldsymbol{u}^* \rangle_V + \langle Bq, \boldsymbol{u}^* \rangle_V \geq 0 \quad \forall (\boldsymbol{v}, q) \in K \times Q, \tag{1.28}$$

where the forcing term $f \in V'$ is given by

$$\langle f, \boldsymbol{v} \rangle_V = -\int_{\Gamma_t} p_i(\boldsymbol{v} \cdot \boldsymbol{n})\,\mathrm{d}s - \int_{\Gamma_b} p_w(\boldsymbol{v} \cdot \boldsymbol{n})\,\mathrm{d}s. \tag{1.29}$$

The solution to the Stokes equations with Dirichlet boundary conditions (1.23) is then given by $(\boldsymbol{u}, p)$, where $\boldsymbol{u} = \boldsymbol{u}^* + \hat{\boldsymbol{u}}$.

Variational inequality B. The Stokes equations with Neumann boundary conditions (1.24) on a domain Ω are formulated in terms of the space

$$V = \left\{ \boldsymbol{v} \in \boldsymbol{W}^{1,r}(\Omega) : \boldsymbol{v} \text{ is periodic in the } x \text{ direction} \right\}, \tag{1.30}$$

and the forcing term $f \in V'$ is given by

$$\langle f, \boldsymbol{v} \rangle_V = \int_{\Gamma_t} \tau_b(\boldsymbol{v} \cdot (0,1)^\top)\,\mathrm{d}s - \int_{\Gamma_t} p_i(\boldsymbol{v} \cdot \boldsymbol{n})\,\mathrm{d}s - \int_{\Gamma_b} p_w(\boldsymbol{v} \cdot \boldsymbol{n})\,\mathrm{d}s. \tag{1.31}$$

The Stokes equations are then equivalent to the variational inequality given by: find $(\boldsymbol{u}, p) \in K \times Q$ such that

$$\langle A\boldsymbol{u} - Bp - f, \boldsymbol{v} - \boldsymbol{u} \rangle_V + \langle Bq, \boldsymbol{u} \rangle_V \geq 0 \quad \forall (\boldsymbol{v}, q) \in K \times Q. \tag{1.32}$$

In Chapter 4, we solve a viscous contact problem defined in terms of Variational inequality A when constructing steady friction laws for glacial sliding with cavitation. In this case, for a fixed horizontal speed u_t and a set of effective pressures $p_i - p_w$, we find steady cavity shapes by evolving the viscous contact problem in time, and then we compute the basal shear stress τ_b with (1.25). When investigating the effects of oscillating water pressures on glacier sliding, we solve a viscous contact problem with Variational inequality B. Therefore, we set the basal shear stress τ_b as a Neumann boundary condition and compute the sliding speed u_b with (1.26).

1.7 Marine ice sheets

A marine ice sheet is an ice sheet that slides from the continent into the ocean, where it goes afloat, creating a floating ice shelf. The point where the ice detaches from the bedrock is known as the grounding line. Much of the Antarctic ice sheet's margin is a floating ice shelf

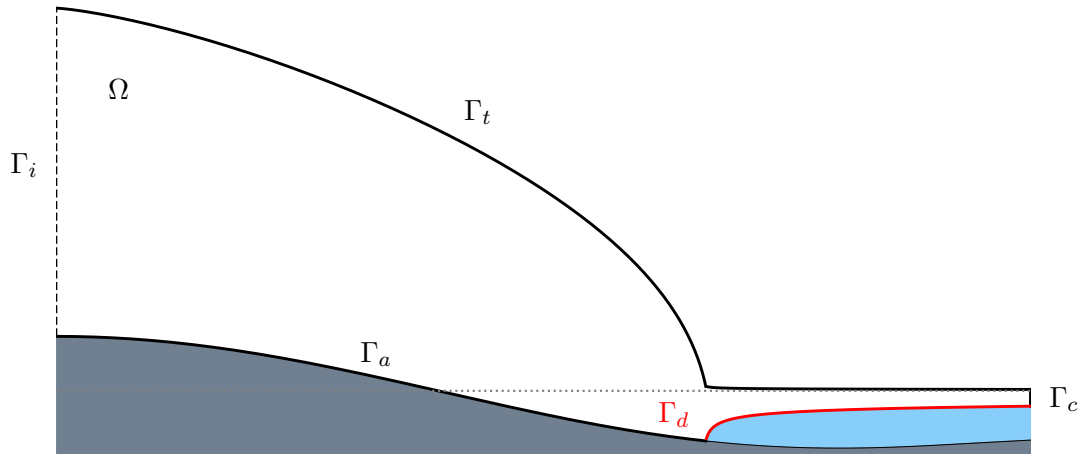

Figure 1.2: The domain Ω on which we model the evolution of a marine ice sheet. The boundary Γ_i to the left represents a fictional boundary between the grounded portion of the sheet and the remaining ice upstream. The boundary Γ_c to the right is the calving front from which ice flows out into the sea. The boundaries Γ_t, Γ_d and Γ_a are the ice-atmosphere, ice-ocean and ice-bedrock interfaces, respectively. The grey dotted line marks the sea level.

[9] and the study of possible marine ice sheet instabilities has led to a considerable body of research on grounding line dynamics [105, 89, 88, 91]. In order to study the dynamics of the grounding line, we consider a domain Ω which contains the transition region from grounded to floating ice, as depicted in Figure 1.2. Given a Cartesian coordinate system with coordinates (x, z), we set the sea level at a (possibly time dependent) height $z = z_{sl}(t)$. We assume the water is in hydrostatic equilibrium and therefore at a pressure p_w which depends on the vertical coordinate z via the expression

$$p_w(z) = \rho_w g \max\{0, z_{sl} - z\}, \tag{1.33}$$

where ρ_w is the density of the water and g is the acceleration due to gravity. The body forces acting on the ice are due to gravity. As a result, when solving the Stokes equations (1.8), the vector field $\boldsymbol{f}$ represents the effect of Earth's gravitational field:

$$\boldsymbol{f} = -\rho g \begin{pmatrix} 0 \\ 1 \end{pmatrix}. \tag{1.34}$$

Throughout this document, whenever applicable, we set the ice and water densities to $\rho = 917\,\mathrm{kg/m^3}$ and $\rho_w = 1000\,\mathrm{kg/m^3}$, respectively, and the gravitational acceleration to $g = 9.81\,\mathrm{m/s^2}$.

The top boundary Γ_t represents the interface between the ice and the atmosphere; we

neglect the stresses exerted by the atmosphere on the ice sheet and set

$$\boldsymbol{\sigma n} = 0 \quad \text{on } \Gamma_t. \tag{1.35}$$

On the attached region Γ_a we enforce the contact boundary conditions (1.11), with p_w given by (1.33), and a sliding condition, the friction law, which relates the tangential stress $\boldsymbol{\sigma}_{nt}$ with the tangential velocity $\mathbf{T}\boldsymbol{u}$. We remark that this friction law is essentially what we calculate with the subglacial cavity problem, described above in Section 1.6. As we show in Chapter 4, we can build a friction law by finding steady cavity shapes and establishing a relationship between τ_b (the tangential basal stress) and u_b (the tangential basal velocity). For the marine ice sheet problem, we assume this function takes the form of a power law for simplicity, as originally proposed by Weertman [104], and we enforce the condition

$$\boldsymbol{\sigma}_{nt} = -C|\mathbf{T}\boldsymbol{u}|^{r-2}\mathbf{T}\boldsymbol{u} \quad \text{on } \Gamma_a, \tag{1.36}$$

where $C > 0$ is a sliding coefficient. This coefficient generally depends on the water pressure in the subglacial hydrology system and on the small-scale roughness of the bedrock [32, 73]; however, for the work on marine ice sheets, we simply assume it to be constant (Chapter 4 contains an in depth investigation of glacial sliding, with a historical overview on research into glacial sliding in Section 4.1).

The ice sheet is floating on the detached region Γ_d and we neglect any tangential stresses caused by ice-ocean interactions. Therefore, we prescribe

$$\boldsymbol{\sigma n} = -p_w \boldsymbol{n} \quad \text{on } \Gamma_d. \tag{1.37}$$

The left boundary at $x = 0$, which we denote by Γ_i, represents a fictional boundary between Ω and the remainder of the ice sheet, located upstream of the grounding line. On Γ_i, we enforce influx conditions for the normal velocity $\boldsymbol{u} \cdot \boldsymbol{n}$ and the tangential stress $\boldsymbol{\sigma}_{nt}$:

$$\boldsymbol{u} \cdot \boldsymbol{n} = u_i \quad \text{and} \quad \boldsymbol{\sigma}_{nt} = \sigma_{nt,i} \begin{pmatrix} 0 \\ 1 \end{pmatrix} \quad \text{on } \Gamma_i, \tag{1.38}$$

where u_i and $\sigma_{nt,i}$ are functions to be specified. The right boundary Γ_c at $x = L$ represents a calving front, which we assume to be in contact with the water, and we set

$$\boldsymbol{\sigma n} = -p_w \boldsymbol{n} \quad \text{on } \Gamma_c. \tag{1.39}$$

Finally, we need to enforce boundary conditions for θ and s at $x = 0$. In all problems of interest, detachment should not occur at $x = 0$ and we therefore enforce $\theta(0, t) = b(0)$. Different conditions can be considered for the upper surface s. For example, a standard setup found in computational glaciology is that of a marine ice sheet sliding from an ice

divide (that is, a symmetry axis) at $x = 0$ and into the ocean, where it goes afloat and ends at a calving front [88, 24, 79]. In this case, we set $u_i = 0$ and $\sigma_{nt,i} = 0$ on Γ_i, and enforce

$$\frac{\partial s}{\partial x} = 0 \quad \text{at } x = 0. \tag{1.40}$$

This setup with homogeneous boundary conditions on Γ_i is considered in Chapter 3, where we analyse the finite element approximation of the resulting variational inequality for marine ice sheets. In Chapter 5, we introduce a different setup for the marine ice sheet problem in which we consider an ice sheet on a tilted bedrock that slides into the ocean such that, far upstream of the grounding line, its geometry is that of a parallel slab of constant thickness. The functions u_i and $\sigma_{nt,i}$ are defined accordingly (see Chapter 5), and a constant thickness boundary condition is prescribed for the upper surface s.

Variational inequality C. The Stokes equations in the marine ice sheet problem presented above can be formulated as a variational inequality in terms of the space

$$V = \left\{ \boldsymbol{v} \in \boldsymbol{W}^{1,r}(\Omega) : \boldsymbol{v} \cdot \boldsymbol{n} = 0 \text{ on } \Gamma_i \right\}. \tag{1.41}$$

If $u_i \neq 0$ on Γ_i, we need a divergence-free velocity field $\hat{\boldsymbol{u}} \in W^{1,r}(\Omega)$ such that $\hat{\boldsymbol{u}} \cdot \boldsymbol{n} = u_i$ on Γ_i and $\hat{\boldsymbol{u}} \cdot \boldsymbol{n} = 0$ on Γ_a. The nonlinear sliding boundary condition (1.36) is introduced via the nonlinear operator $G : V \to V'$ defined by

$$\langle G\boldsymbol{u}, \boldsymbol{v} \rangle_V = \int_{\Gamma_a} C|\mathbf{T}\boldsymbol{u}|^{r-2} \left(\mathbf{T}\boldsymbol{u} \cdot \mathbf{T}\boldsymbol{v}\right) \mathrm{d}s. \tag{1.42}$$

Then, the weak formulation of the instantaneous Stokes problem is given by: find $(\boldsymbol{u}^*, p) \in K \times Q$ such that

$$\langle A(\boldsymbol{u}^* + \hat{\boldsymbol{u}}) + G(\boldsymbol{u}^* + \hat{\boldsymbol{u}}) - Bp - f, \boldsymbol{v} - \boldsymbol{u}^* \rangle_V + \langle Bq, \boldsymbol{u}^* \rangle_V \geq 0 \quad \forall (\boldsymbol{v}, q) \in K \times Q, \tag{1.43}$$

where the forcing term $f \in V'$ is given by

$$\langle f, \boldsymbol{v} \rangle_V = \int_\Omega \boldsymbol{f} \cdot \boldsymbol{v} \, \mathrm{d}x - \int_{\Gamma_b \cup \Gamma_c} p_w(\boldsymbol{v} \cdot \boldsymbol{n}) \, \mathrm{d}s + \int_{\Gamma_i} \sigma_{nt,i} \left(\boldsymbol{v} \cdot (0,1)^\top \right) \mathrm{d}s. \tag{1.44}$$

As in Variational inequality A, the solution to the Stokes problem is given by $(\boldsymbol{u}, p)$ with $\boldsymbol{u} = \boldsymbol{u}^* + \hat{\boldsymbol{u}}$.

Remark 1.4. If $r \in (1, 2)$, the operator $G : V \to V'$ given by (1.42) has a singularity at $\mathbf{T}\boldsymbol{u} = 0$. Therefore, at a numerical level, a regularised form of this operator is required, as in (1.19) with the operator A. We introduce

$$\langle G_\epsilon \boldsymbol{u}, \boldsymbol{v} \rangle_V = \int_{\Gamma_a} C \left(|\mathbf{T}\boldsymbol{u}|^2 + \epsilon \right)^{\frac{r-2}{2}} \left(\mathbf{T}\boldsymbol{u} \cdot \mathbf{T}\boldsymbol{v}\right) \mathrm{d}s \tag{1.45}$$

for a regularisation parameter $\epsilon > 0$.

1.8 Concluding remarks

In this chapter, we have introduced a general formulation for a two-dimensional viscous contact problem. In this formulation, the fluid occupies a domain Ω, enclosed between two surfaces that evolve in time. The velocity and pressure of the fluid are determined by the Stokes equations at each instant in time, and the surfaces evolve according to two free boundary equations. Under the fluid we assume a solid surface to exist (the bedrock, in the case where the fluid is ice). The Stokes equations are equipped with contact boundary conditions along the region of the lower boundary that is in touch with this solid surface. These contact boundary conditions allow the fluid to detach from the bedrock and render the weak formulation of the Stokes equations into a variational inequality.

After presenting the general formulation of a viscous contact problem we will work with, we describe two viscous contact problems that arise in glaciology. The first problem is that of subglacial cavitation, which occurs along the ice-bedrock interface of an ice sheet and is fundamental for understanding glacial sliding. The second problem, of a much larger scale, is that of a marine ice sheet, which flows from the continent into the ocean, where it goes afloat at the grounding line. For these two problems, we specify the variational inequalities that arise when formulating the Stokes equations. We introduce these two problems early on because we will return to them for the remainder of the thesis, either as numerical tests to investigate the performance of numerical schemes, or as applications with a glaciological interest.

Chapter 2

Numerical methods for viscous contact problems

A viscous contact problem is a viscous flow problem with contact conditions that allow the fluid to detach from a solid surface. In Chapter 1 we presented a mathematical model for these problems built in terms of the Stokes equations with contact boundary conditions and free boundary equations. This chapter concentrates on the design of numerical methods for this coupled problem. More specifically, we propose a class of numerical methods for solving this system which decouples these two sets of equations in time, resulting in explicit time-stepping schemes for the discrete free boundary equations. In these methods, the contact boundary conditions are enforced by rewriting the Stokes system as a discrete variational inequality. Moreover, we identify certain properties of the discrete system which establish an interdependence between the discrete Stokes and free boundary equations that turns out to be fundamental when constructing accurate and robust schemes. Finally, we propose a concrete numerical scheme which belongs to this general class with which we simulate the glaciological applications in Chapters 4 and 5. Our choice of scheme is justified by a series of numerical results included at the end of this chapter that compare it to other methods.

Practically all numerical computations of viscous contact problems which solve the full Stokes equations have been carried out with the solver in Elmer/Ice [38]. These include computations of subglacial cavity problems [36, 50, 49] and of marine ice sheets [24, 28]. These works, which have pioneered the numerical resolution of viscous contact problems, do not appear to recognize the variational structure of the Stokes equations with contact boundary conditions. Additionally, some of these results appear to be under-resolved, see for example Figures 2 and 3 in [36]. These points have been one of the main motivations for developing the novel framework presented here, which attempts to exploit the structure of the Stokes variational inequality. To the knowledge of the author, the only numerical

results for viscous contact solvers that have not been computed with Elmer/Ice are those of [97], in which a penalty method for solving the Stokes variational inequality is proposed.

After introducing the notation required for describing our numerical setup in Section 2.1, we present the general class of numerical schemes in Section 2.2 that decouple the Stokes and free boundary equations in time. Then, in Section 2.3, we present the main numerical scheme that we work with in the remaining chapters of this document. In Section 2.3, we write a self-contained description of the main numerical scheme that avoids the abstract framework and notation from Section 2.2, for the convenience of readers who might be unfamiliar with a functional analytic approach to partial differential equations and the finite element method. In Section 2.4, we conclude this chapter with a comparison of numerical schemes that fall within the general class presented in Section 2.2. These comparisons demonstrate the importance of discretising the Stokes and free boundary equations in the interdependent way which we describe in Section 2.2.2 and justify the use of the main numerical scheme from Section 2.3 throughout the document.

2.1 Notation for the discrete problem and assumptions

In viscous contact problems, we consider a time dependent free boundary equation coupled to a variational inequality posed on an evolving domain. Its discretisation requires a partition of a given time interval $[0, T]$ into N_T subintervals. In this work, we consider uniform partitions with subintervals of duration $\Delta t = T/N_T$, resulting in a finite number of time steps $t_k = k\Delta t$ for $k = 0, 1, ..., N_T$. For simplicity, we assume that the domain Ω^k at a time step t^k is polygonal. We denote the upper and lower boundaries by θ_h^k and s_h^k, such that

$$\Omega^k = \left\{(x, y) \in \mathbb{R}^2 : 0 < x < L,\, \theta_h^k(x) < y < s_h^k(x)\right\}. \tag{2.1}$$

The spatial discretisation of the Stokes equations is built in terms of a triangulation $\mathcal{T}_h^k$ of Ω^k (a definition of a triangulation of a domain can be found in [11, Definition 3.3.11]). Since the domain is evolving from one time step to the next, a new mesh must be generated at each time step. We do this by deforming the mesh with an algorithm that we describe in the next section. With this algorithm, the mesh connectivity remains unchanged and we only displace the vertices in the vertical direction. We note that under large deformations, remeshing is necessary in order to avoid an excessive deterioration of the mesh; however, in the problems considered in this document, such issues have not arisen.

As a result of the invariance in mesh connectivity, the numbers of vertices $M^\theta + 1$ and $M^s + 1$ along the lower and upper boundaries, respectively, remain unchanged. Moreover, since we only displace the mesh vertices in the vertical direction, the x coordinates of these points are also constant in time. We denote these points by (x_i^θ, θ_i^k) for $i = 0, 1, ..., M^\theta$ and

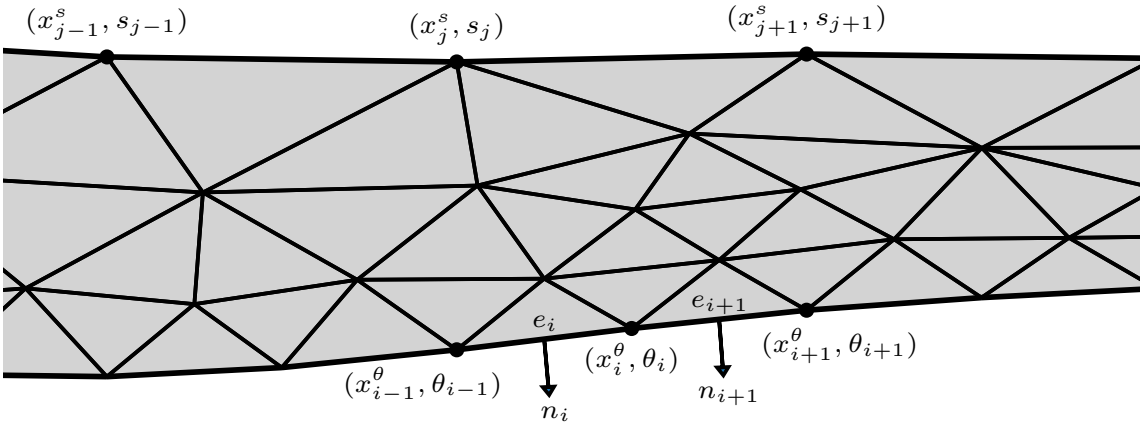

Figure 2.1: Notation and ordering for the nodes, edges, and the normal unit vectors along the top and lower boundaries of the domain.

(x^s_i, s^k_i) for $i = 0, 1, ..., M^s$, ordered from left to right as in Figure 2.1. Since we assume the domain Ω^k to be polygonal, the functions θ^k_h and s^k_h belong to the following spaces of continuous piecewise linear functions:

$$U^\theta_h = \left\{ \chi_h \in C([0, L]) : \chi_h|_{[x^\theta_i, x^\theta_{i+1}]} \in \mathcal{P}_1([x^\theta_i, x^\theta_{i+1}]) \text{ for } i = 0, 1, ..., M^\theta - 1 \right\}, \tag{2.2a}$$

$$U^s_h = \left\{ \chi_h \in C([0, L]) : \chi_h|_{[x^s_i, x^s_{i+1}]} \in \mathcal{P}_1([x^s_i, x^s_{i+1}]) \text{ for } i = 0, 1, ..., M^s - 1 \right\}. \tag{2.2b}$$

For simplicity, we also assume that the bedrock b is a continuous piecewise linear function in U^θ_h.

At each time step t_k, the top and lower boundaries are denoted by Γ^k_t and Γ^k_b, respectively. At the discrete level, the attached and detached regions of the lower boundaries, denoted by Γ^k_a and Γ^k_d respectively, are determined by a contact criterion which is specific to the numerical scheme and therefore will not coincide with the definitions given in (1.7) in general. We denote the set of vertices and edges of a mesh $\mathcal{T}_h$ by $\mathcal{V}(\mathcal{T}_h)$ and $\mathcal{E}(\mathcal{T}_h)$, respectively. We assume that every edge $e \in \mathcal{E}(\mathcal{T}^k_h)$ along the lower boundary Γ^k_b is either contained in Γ^k_a or in Γ^k_d; we write $\mathcal{E}(\mathcal{T}^k_h, \Gamma^k_a)$ for the edges in Γ^k_a and $\mathcal{E}(\mathcal{T}^k_h, \Gamma^k_d)$ for those in Γ^k_d. We denote the edge on Γ^k_b that connects the point (x^θ_i, θ^k_i) with $(x^\theta_{i+1}, \theta^k_{i+1})$ by e_i for $i = 0, 1, ..., M^\theta - 1$.

The superscript used in the notation above to indicate the time step is removed whenever references to a particular time step are not necessary for the definition of a mathematical object such as a space or an operator. For example, in Section 2.2.1, we introduce the discrete variational inequality for an arbitrary domain Ω and triangulation $\mathcal{T}_h$. Although in practice these will coincide with a domain Ω^k and triangulation $\mathcal{T}^k_h$ at time t^k, the definition of the discrete variational inequality does not require this information.

Table 2.1: Discrete normal trace operators used in this section. For each operator, we indicate the subregion of the boundary $\partial\Omega$ onto which a vector field is mapped and the system in which this operator is used.

Symbol	Region	Use
γ_h	Γ_b	Discrete variational inequality (2.8)
γ_h^a	Γ_a	Discrete variational inequality (2.8)
ζ_h^s	Γ_t	Discrete upper free boundary equation (2.12b)
ζ_h^θ	Γ_b	Discrete lower free boundary equation(2.12a)

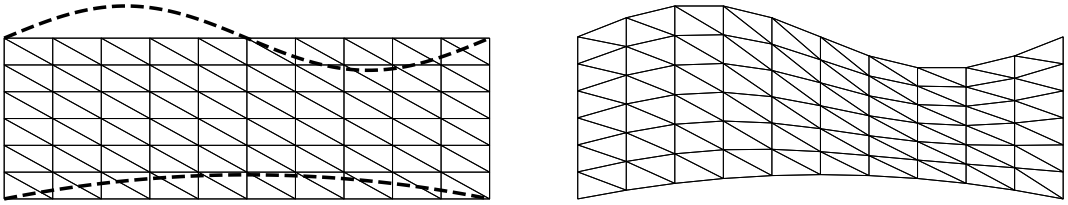

Figure 2.2: Example of an application of the mesh deformation algorithm (2.3). The initial configuration, shown on the left, corresponds with a uniform rectangular mesh. We then deform it by perturbing the nodes of the upper and lower surfaces with the sinusoidal and parabolic functions which we plot with a dashed line. The deformed mesh that results from the application of the algorithm is then plotted to the right.

2.2 A general class of numerical schemes for viscous contact problems

In this section we present a class of schemes for solving viscous contact problems numerically. The general form that these schemes take is summarised in Algorithm 1. We restrict our attention to schemes that decouple the Stokes and free boundary equations in time. The Stokes equations are solved with the finite element method and the free boundary equations with an explicit finite difference scheme. Below, we introduce the discrete systems, which are built in terms of the finite element pair $V_h \times Q_h$ for the velocity and pressure solutions and the operators γ_h, ζ_h^θ and ζ_h^s, which represent discrete analogues of the normal trace operator. The discrete trace operators used throughout this section are listed in Table 2.1 for the convenience of the reader. These spaces and operators are defined for a given domain Ω with a triangulation $\mathcal{T}_h$. However, this dependence is not specified in the notation in order to keep it simple and readable.

The final ingredients of the numerical scheme are a contact criterion $\mathfrak{C}$ and a mesh deformation algorithm $\mathfrak{D}$. The contact criterion $\mathfrak{C}$ takes as input a lower boundary θ_h and bedrock b in U_h^θ, together with a contact tolerance $\text{tol} > 0$, and returns the attached region $\Gamma_a \subset \Gamma_b$ of the lower boundary. Finally, for a domain Ω^k defined in terms of θ_h^k and s_h^k at

Algorithm 1: A general algorithm for viscous contact problems

Set the bedrock function b ;
Set an initial domain Ω^0 with upper and lower surfaces (s_h^0, θ_h^0) ;
Triangulate the domain with $\mathcal{T}_h^0$;
Set contact tolerance tol > 0;
for $k = 0, 1, 2, \ldots$ **do**
  Set Γ_a^k and Γ_d^k according to the contact criterion $\mathfrak{C}$;
  Compute a velocity solution $\boldsymbol{u}_h^k \in V_h$ to the discrete variational inequality (2.8) posed on Ω^k with attached region Γ_a^k;
  Compute θ_h^{k+1} and s_h^{k+1} with the discrete free boundary equation (2.12) ;
  If $\theta_i^{k+1} - b(x_i) <$ tol, set $\theta_i^{k+1} = b(x_i)$;
  If $\theta_i^{k+1} \geq s_i^{k+1}$, raise error;
  Compute $\mathcal{T}_h^{k+1}$ with the mesh deformation algorithm $\mathfrak{D}$;

a time step t^k, a triangulation of this domain $\mathcal{T}_h^k$ is generated according to an operator $\mathfrak{D}$. In this document, the operator $\mathfrak{D}$ we use builds $\mathcal{T}_h^k$ by performing a linear displacement in the vertical direction of the vertices of an initial mesh $\mathcal{T}_h^0$, which triangulates the domain Ω^0 with surfaces θ_h^0 and s_h^0. In particular, given the points $(x^0, y^0) \in \mathcal{V}(\mathcal{T}_h^0)$, we compute the point $(x^k, y^k) \in \mathbb{R}^2$ with

$$x^k = x^0, \tag{2.3a}$$

$$y^k = \theta_h^k(x^k) + \frac{s_h^k(x^k) - \theta_h^k(x^k)}{s_h^0(x^k) - \theta_h^0(x^k)} \left(y^0 - \theta_h^0(x^k) \right). \tag{2.3b}$$

The mesh $\mathcal{T}_h^k$ is then constructed by preserving the topology of $\mathcal{T}_h^0$ and defining $\mathcal{V}(\mathcal{T}_h^k)$ in terms of the points $\{(x^k, y^k)\}$ computed with the equations above. To illustrate the mesh deformation algorithm, we present an example in Figure 2.2. Here, we take a uniform rectangular mesh as the initial mesh and we deform it by perturbing the upper and lower surfaces with a sinusoidal and parabolic functions, respectively. We can observe that the mesh topology remains unchanged, as do the horizontal coordinates of the mesh nodes.

2.2.1 The discrete variational inequality

The weak formulation of the Stokes equations with contact boundary conditions (1.11) is equivalent to a variational inequality, as explained in Section 1.4. The variational inequalities A-C introduced in Chapter 1 are three particular instances that arise in the viscous contact problems we consider. The solver for these variational inequalities is built in terms of a finite element pair $V_h \times Q_h$ in which the discrete velocity and pressure are sought. Additionally, we introduce a discrete counterpart of the normal trace operator that maps a velocity field $\boldsymbol{v}_h$ to its discrete normal component along the lower boundary Γ_b of a domain

Ω. We denote this discrete normal trace operator by $\gamma_h : V_h \to \Sigma_h$, where $\Sigma_h \subset L^2(\Gamma_b)$ is the range of γ_h and is a space of discrete functions defined along Γ_b. The pair $V_h \times Q_h$ and the operator γ_h are therefore the components from which we build a discrete variational inequality.

The finite element space $V_h \times Q_h$ for the velocity and pressure must be chosen such that the pair is "inf-sup" stable with respect to the divergence operator, as specified in Chapter 3. Several stable pairs with different properties are known to exist, see [10, 61]. In this work, we take $V_h \times Q_h$ to be the so-called Taylor-Hood pair, which was first introduced in [99]. In this case, the velocity space is set equal to continuous piecewise quadratic vector fields and the pressure space to continuous piecewise linear scalar fields:

$$V_h = \{\boldsymbol{v}_h \in V : \boldsymbol{v}_h|_c \in \boldsymbol{\mathcal{P}}_2(c) \quad \forall c \in \mathcal{T}_h\}\,, \tag{2.4a}$$

$$Q_h = \{q_h \in Q : q_h|_c \in \mathcal{P}_1(c) \quad \forall c \in \mathcal{T}_h\}\,. \tag{2.4b}$$

The space V in the definition of V_h above is a subset of $\boldsymbol{W}^{1,r}(\Omega)$ to be specified for each viscous contact problem. We choose this pair because it does not require an excessive amount of degrees of freedom per cell to guarantee stability, the velocity space is conforming in the sense that it is a subset of $\boldsymbol{W}^{1,r}(\Omega)$, and it is easily implementable in Firedrake [83]. It should be noted that this pair is not exactly divergence-free; that is, at the discrete level we do not enforce $\nabla \cdot \boldsymbol{u}_h = 0$ in Ω when solving the discrete Stokes variational inequality, but a weak version of this statement implicit in the variational inequality. This can have negative consequences for the accuracy of the scheme [61].

Remark 2.1. A different finite element pair is considered Section 3.3 that is also stable, conforming, and easily implementable. It is known as the P2P0 pair because the velocity is a continuous piecewise quadratic function and the pressure is piecewise constant. Section 3.3 focuses on that scheme because having a piecewise constant pressure simplifies the analysis of the finite element approximation of solutions to the discrete Stokes variational inequality.

The next step in the discretisation of the variational inequality is the definition of a convex subset K_h of V_h in which the discrete velocity field is contained. This is carried out by choosing the discrete normal trace operator $\gamma_h : V_h \to \Sigma_h$. Different choices of γ_h lead to different numerical schemes with very different properties, as shown in Section 2.4. On the attached region Γ_a, we define the space Σ_h^a on Γ_a by restricting functions in Σ_h to Γ_a; that is,

$$\Sigma_h^a = \{\xi_h|_{\Gamma_a} : \xi_h \in \Sigma_h\}\,. \tag{2.5}$$

We then introduce the discrete normal trace operator onto Γ_a, defined by

$$\gamma_h^a : V_h \to \Sigma_h^a, \quad \boldsymbol{v}_h \mapsto (\gamma_h \boldsymbol{v}_h)|_{\Gamma_a}, \tag{2.6}$$

and the discrete convex subset $K_h \subset V_h$ given by

$$K_h = \{\boldsymbol{v}_h \in V_h : \gamma_h^a \boldsymbol{v}_h \leq 0\}. \tag{2.7}$$

This definition of the discrete convex set K_h indicates that a choice of discrete trace operator γ_h essentially equates to a choice of discrete non-penetration condition. At the continuous level, the non-penetration condition is given by $\boldsymbol{u} \cdot \boldsymbol{n} \leq 0$ on Γ_a and is one of the contact conditions in (1.11). However, at the discrete level, it is not necessary to enforce this same condition, although this can also be done, as in Scheme 5 below.

With the above definitions, we can now introduce the discrete variational inequality. The specification of this variational equality requires a choice of viscous contact problem. Since the subglacial cavity problem with Variational inequality B is taken as a reference problem in Section 2.4 below, we present the discrete counterpart to this variational inequality: find $(\boldsymbol{u}_h, p_h) \in K_h \times Q_h$ such that

$$\langle A_\epsilon \boldsymbol{u}_h - B p_h - f, \boldsymbol{v}_h - \boldsymbol{u}_h \rangle_V + \langle B q_h, \boldsymbol{u}_h \rangle_V \geq 0 \quad \forall (\boldsymbol{v}_h, q_h) \in K_h \times Q_h, \tag{2.8}$$

where the operator $A_\epsilon : V \to V'$ is defined in (1.19) and $\epsilon > 0$ is the regularisation parameter that should be introduced whenever $r \neq 2$.

From a computational point of view, the variational inequality (2.8) can be solved by transforming it into a variational equality with a nonsmooth residual. One can then apply the semi-smooth Newton method to solve the resulting nonlinear system. In this chapter, we consider two methods for writing the variational inequality as an equality; a more complete overview can be found in [48, 100].

One approach consists in approximating solutions to the discrete variational inequality (2.8) with a penalty method by solving the following nonlinear variational equation: find $(\boldsymbol{u}_h^\delta, p_h^\delta) \in V_h \times Q_h$ such that

$$\langle A \boldsymbol{u}_h^\delta - B p_h^\delta + \frac{1}{\delta} \Pi \boldsymbol{u}_h^\delta - f, \boldsymbol{v}_h \rangle_V + \langle B q_h, \boldsymbol{u}_h \rangle_V = 0 \quad \forall (\boldsymbol{v}_h, q_h) \in V_h \times Q_h, \tag{2.9}$$

where the penalty operator $\Pi : V_h \to V_h'$ is given by

$$\langle \Pi \boldsymbol{u}_h, \boldsymbol{v}_h \rangle_V = \int_{\Gamma_a} (\gamma_h \boldsymbol{u}_h + |\gamma_h \boldsymbol{u}_h|) \, \gamma_h \boldsymbol{v}_h \, \mathrm{d}s, \tag{2.10}$$

and $\delta > 0$ is the penalty parameter. As $\delta \to 0$, we can expect $(\boldsymbol{u}_h^\delta, p_h^\delta) \to (\boldsymbol{u}_h, p_h)$ in $V \times Q$, where $(\boldsymbol{u}_h, p_h) \in K_h \times Q_h$ is the solution to the discrete variational inequality (2.8).

A second way of solving the discrete variational inequality is by rewriting it as a mixed problem with a Lagrange multiplier which represents the effective normal stresses $\sigma_{nn} + p_w$ on Γ_a. The mixed formulation requires a cone $\Lambda_h \subset (\Sigma_h^a)'$, which contains our choice of negative elements in the dual of Σ_h^a. The problem then takes the following form: find $(\boldsymbol{u}_h, p_h, \lambda_h) \in V_h \times Q_h \times \Lambda_h$ such that

$$\langle A\boldsymbol{u}_h - Bp_h - f, \boldsymbol{v}_h\rangle_V - \langle \lambda_h, \gamma_n^a \boldsymbol{v}_h\rangle_{\Sigma_h^a} = 0 \qquad \forall \boldsymbol{v}_h \in V_h, \tag{2.11a}$$

$$\langle Bq_h, \boldsymbol{u}_h\rangle_V = 0 \qquad \forall q_h \in Q_h, \tag{2.11b}$$

$$\langle \mu_h - \lambda_h, \gamma_n^a \boldsymbol{u}_h\rangle_{\Sigma_h^a} \geq 0 \qquad \forall \mu_h \in \Lambda_h. \tag{2.11c}$$

In the next chapter, in Section 3.2, we consider a class of numerical methods for solving the discrete variational inequality where Λ_h consists of the point-wise negative functions in Σ_h^a and the duality pairing in Σ_h^a is given by the $L^2(\Gamma_a)$ inner product.

We still need to rewrite (2.11c) as an equality, and this partly depends on the form that Λ_h and the duality pairing $\langle\cdot,\cdot\rangle_{\Sigma_h^a}$ take. In general this involves rewriting (2.11c) as a nonlinear equation, as explained in [54]. In Section 3.3.2, we describe how this can be done when Σ_h is given by piecewise constant functions.

2.2.2 The discrete free boundary equation

The numerical solution of the free boundary equations (1.12) is carried out with a class of explicit finite difference schemes built in terms of two additional normal trace operators $\zeta_h^\theta : V_h \to U_h^\theta$ and $\zeta_h^s : V_h \to U_h^s$ for the lower and upper surfaces of the ice sheet, see (2.2) for the definition of the spaces U_h^θ and U_h^s. Normal trace operators are used because the free boundary equations (1.12) can be written in terms of the normal velocity at the continuous level, as explained in Remark 1.1.

Given a velocity field $\boldsymbol{u}_h \in V_h$, the lower and upper surfaces $(\theta_h^k, s_h^k) \in U_h^\theta \times U_h^s$ at time t^k, and a time step $\Delta t > 0$, the discrete free boundary equations for $(\theta_h^{k+1}, s_h^{k+1}) \in U_h^\theta \times U_h^s$ are given by

$$\theta_i^{k+1} = \theta_i^k - \Delta t \sqrt{1 + \left(\frac{\theta_i^k - \theta_{i-1}^k}{x_i^\theta - x_{i-1}^\theta}\right)^2} \left(\zeta_h^\theta \boldsymbol{u}_h\right)_i \quad \text{for } i = 1, 2, ..., M^\theta, \tag{2.12a}$$

$$s_i^{k+1} = s_i^k + \Delta t \sqrt{1 + \left(\frac{s_i^k - s_{i-1}^k}{x_i^s - x_{i-1}^s}\right)^2} \left(\zeta_h^s \boldsymbol{u}_h\right)_i \quad \text{for } i = 1, 2, ..., M^s. \tag{2.12b}$$

In the equations above, the subscript i refers to the values of functions in U_h^θ or U_h^s at the nodes x_i^θ or x_i^s. The derivative inside the square root is approximated by a backward

difference approximation to keep the general scheme (2.12) coherent with the upwinding schemes presented in Sections 2.3 and 2.4 below.

It is important to note that the free boundary equations (1.12) are advection equations. In the viscous contact problems considered in this work, there is always a dominating direction of flow from left to right. As a result, its discrete counterparts are susceptible to instabilities characteristic of advection equations, as described in standard textbooks [69]. This should be taken into account when designing the normal trace operators ζ_h^θ and ζ_h^s. In the schemes we present below, we achieve this stabilisation by taking values of the normal velocity upstream of a node. As a result, the discrete free boundary equations considered are essentially upwinding methods for advection equations [69, Section 10.4]. In Scheme 3 below, we demonstrate that this stabilisation is necessary by showing how a numerical result deteriorates without it. In [37], this stabilisation is achieved by adding an additional term to the discrete free boundary equations that acts as a stabiliser.

It must also be taken into account that, since the free boundary equations are solved in conjunction with the discrete Stokes variational inequality, the trace operators γ_h and ζ_h^θ should be designed in a coherent manner to avoid the detachment of the lower boundary from the bedrock due to numerical errors. This coherence is referred to as a contact consistency condition between γ_h and ζ_h^θ and can be defined more precisely as follows: consider a situation at a given time step t^k in which the ice is attached to the bedrock at two adjacent edges $\{e_i, e_{i+1}\} \subset \mathcal{E}(\mathcal{T}_h^k, \Gamma_a^k)$; that is, $\theta_h^k = b$ on $e_i \cup e_{i+1}$. Moreover, assume that at that instant in time, once the discrete Stokes variational inequality is solved on Ω^k, the normal trace of the resulting velocity field $\boldsymbol{u}_h^k$ is zero along these edges; i.e. we have that $\gamma_h \boldsymbol{u}_h^k = 0$ on $e_i \cup e_{i+1}$. Then, we say that the operators γ_h and ζ_h^θ are contact-consistent if

$$\gamma_h \boldsymbol{u}_h^k = 0 \quad e_i \cup e_{i+1} \qquad \Longrightarrow \qquad \zeta_h^\theta \boldsymbol{u}_h^k = 0 \quad \text{on } x_i^\theta. \tag{2.13}$$

In other words, if $\gamma_h \boldsymbol{u}_h$ is zero in the neighborhood of an attached vertex, we have that $\zeta_h^\theta \boldsymbol{u}_h^k$ is zero on that vertex, since (x_i^θ, θ_i^k) is the vertex in between e_i and e_{i+1}.

The numerical schemes presented below in Section 2.4 give examples of different ways in which this condition can be satisfied. Moreover, in that section we demonstrate the importance of contact consistency with numerical examples which expose the inaccuracy of Scheme 4, a non contact-consistent scheme.

2.3 A numerical scheme for solving viscous contact problems

The numerical scheme for viscous contact problems used throughout this document is presented here. In order to make this section self-contained, we first describe the scheme with

a simple notation that avoids the technicalities introduced in Section 2.2 for the generalised framework.

Since this scheme falls into the class of methods for solving viscous contact problems introduced in Section 2.2, Algorithm 1 is a sketch of the main elements of the numerical scheme. Of the steps to be carried out at each time step t^k, the first three (involving the contact criterion, the discrete variational inequality, and the discrete free boundary equation) need to be specified in detail.

- **The contact criterion**. This criterion establishes what subset of the lower surface of the domain Ω^k is attached to the bedrock and which is detached. Given a bedrock b, a cavity roof θ_h^k, and a tolerance tol > 0, we define the attached and detached regions Γ_a^k and Γ_d^k as follows: for each edge e_i, where $i = 0, 1, ..., M^\theta - 1$,

$$e_i \text{ is contained in } \Gamma_a^k \text{ if and only if } \theta_i^k - b(x_i) < \text{tol}. \tag{2.14}$$

  That is, an edge is considered to be attached to the bedrock if and only if the node immediately downstream is close enough to the bed, in accordance with the upwinding scheme we present below for the discrete free boundary equation. The ordering of the edges e_i and nodes (x_i, θ_i^k) follows the convention shown in Figure 2.1.

- **Discrete variational inequality.** For concreteness, we focus on Variational inequality B here, although the extension to Variational inequalities A and C is straightforward. Given a subset Γ_a^k of the boundary attached to the bedrock and a triangulation $\mathcal{T}_h^k$ of Ω^k, in terms of which we define the velocity-pressure finite element pair $V_h \times Q_h$, we define the discrete convex subset $K_h \subset V_h$ by

$$K_h = \left\{ \boldsymbol{v}_h \in V_h : \int_e \boldsymbol{v}_h \cdot \boldsymbol{n} \, \mathrm{d}s \leq 0 \quad \forall e \in \mathcal{E}(\mathcal{T}_h^k, \Gamma_a^k) \right\}. \tag{2.15}$$

  We then solve the following variational inequality: find $(\boldsymbol{u}_h^k, p_h^k) \in K_h \times Q_h$ such that

$$\langle A_\epsilon \boldsymbol{u}_h^k - B p_h^k - f, \boldsymbol{v}_h - \boldsymbol{u}_h^k \rangle_V + \langle B q_h, \boldsymbol{u}_h^k \rangle_V \geq 0 \quad \forall (\boldsymbol{v}_h, q_h) \in K_h \times Q_h, \tag{2.16}$$

  where $\epsilon > 0$ is a regularisation parameter to be set whenever $n > 1$ in Glen's law (1.3). We solve this variational inequality with the Lagrange multiplier method, as explained in Chapter 3.

- **Discrete free boundary equation.** Once we have the velocity field $\boldsymbol{u}_h^k$, we solve the discrete free boundary equation

$$\theta_i^{k+1} = \theta_i^k - \Delta t \sqrt{1 + \left(\frac{\theta_i^k - \theta_{i-1}^k}{x_i^\theta - x_{i-1}^\theta} \right)^2} \left[\frac{1}{|e_i|} \int_{e_i} \boldsymbol{u}_h^k \cdot \boldsymbol{n} \, \mathrm{d}s \right] \quad \text{for } i = 1, 2, ..., M^\theta. \tag{2.17}$$

Therefore, the surface at the node on x_i^θ is evolved with the average value of $\boldsymbol{u}_h^n \cdot \boldsymbol{n}$ along the edge located immediately upstream, see Figure 2.1. This results in an upwinding scheme that is clearly contact-consistent in the sense of (2.13). If necessary, the discrete free boundary equation for the upper surface s_h^{k+1} is solved in the same way.

Remark 2.2. Given the definitions in (1.7), perhaps a more natural contact criterion would mark an edge e_i along the lower boundary as attached if and only if the edge was approximately on the bedrock b. In other words, for $e_i \in \mathcal{E}(\mathcal{T}_h, \Gamma_b)$, we would write $e_i \in \mathcal{E}(\mathcal{T}_h, \Gamma_a)$ if and only if $\theta_i - b(x_i) < \text{tol}$ and $\theta_{i+1} - b(x_{i+1}) < \text{tol}$. However, we discarded this choice of contact criterion because, when computing steady states for the subglacial cavities in Chapter 4 with it, we found that the numerical approximation would not reach a steady state. Instead, it would settle into a periodic mode in which a node along the upstream-facing side of the obstacle was detaching itself from the bedrock and then reattaching itself to it. This situation does not occur with (2.14) for the subglacial cavitation problem.

Remark 2.3. In terms of the abstract notation used in Section 2.2 for the general algorithm, in this scheme the normal trace operator γ_h maps vector fields $\boldsymbol{v}_h \in V_h$ onto piecewise constant functions on Γ_b, that is,

$$\gamma_h \boldsymbol{v}_h|_e = \frac{1}{|e|} \int_e \boldsymbol{v} \cdot \boldsymbol{n} \, \mathrm{d}s \quad \forall e \in \mathcal{E}(\mathcal{T}_h, \Gamma_b). \tag{2.18}$$

Hence, we set Σ_h equal to the space of piecewise constant functions on Γ_b,

$$\Sigma_h = \left\{ \mu_h \in L^2(\Gamma_b) : \mu_h|_e \in \mathcal{P}_0(e) \quad \forall e \in \mathcal{E}(\mathcal{T}_h, \Gamma_b) \right\}. \tag{2.19}$$

The normal trace operator ζ_h^θ along the lower boundary is defined by setting

$$(\zeta_h^\theta \boldsymbol{v}_h)_i = \gamma_h \boldsymbol{v}_h|_{e_i}, \tag{2.20}$$

i.e. the velocity at each node on x_i^θ is taken from the edge located immediately upstream, see Figure 2.1. The trace operator ζ_h^s on the upper surface is defined in the same way: the normal velocity at each node on x_i^s is taken as the edge-wise averaged normal velocity along the edge immediately upstream.

As a result of the free boundary equations (1.12), the total flux of mass through the free surfaces is regulated by the time derivative of those free surfaces; for example, for the lower boundary Γ_b we find that

$$\int_0^L \frac{\partial \theta}{\partial t} \, \mathrm{d}x = \int_{\Gamma_b} \boldsymbol{u} \cdot \boldsymbol{n} \, \mathrm{d}s. \tag{2.21}$$

An important consideration is whether an equality analogous to (2.21) holds at the discrete level. By (2.17), we find that

$$\int_{\Gamma_b} \boldsymbol{u}_h^k \cdot \boldsymbol{n} \, \mathrm{d}s = \sum_{i=1}^{M^\theta} \int_{e_i} \boldsymbol{u}_h^k \cdot \boldsymbol{n} \, \mathrm{d}s = \frac{1}{\Delta t} \sum_{i=1}^{M^\theta} \left(\theta_i^{k+1} - \theta_i^k\right) \left(x_i^\theta - x_{i-1}^\theta\right). \tag{2.22}$$

On the other hand, since $\theta_h^{k+1} - \theta_h^k \in U_h^\theta$ is a piecewise linear function, we can compute its integral from $x = 0$ to $x = L$. For concreteness, we will assume the domain is periodic in the horizontal direction, as in the subglacial cavity problem, and therefore $\theta_0^k = \theta_{M^\theta}^k$. As a result, we find that

$$\begin{aligned} \int_0^L \frac{\theta_h^{k+1} - \theta_h^k}{\Delta t} \, \mathrm{d}x &= \frac{1}{2\Delta t} \sum_{i=1}^{M^\theta} \left[\theta_i^{k+1} + \theta_{i-1}^{k+1} - \left(\theta_i^k + \theta_{i-1}^k\right)\right] \left(x_i^\theta - x_{i-1}^\theta\right) \\ &= \frac{1}{2\Delta t} \left[\sum_{i=1}^{M^\theta - 1} \left(\theta_i^{k+1} - \theta_i^k\right) \left(\Delta x_i^\theta + \Delta x_{i+1}^\theta\right) + \left(\theta_{M^\theta}^{k+1} - \theta_{M^\theta}^k\right) \left(\Delta x_1^\theta + \Delta x_{M^\theta}^\theta\right) \right], \end{aligned} \tag{2.23}$$

where we have introduced the grid spacing $\Delta x_i^\theta = x_i^\theta - x_{i-1}^\theta$. If the grid spacing is constant and $\Delta x_i^\theta = \Delta x$ for all $i = 1, ..., M^\theta$, we find that

$$\int_0^L \frac{\theta_h^{k+1} - \theta_h^k}{\Delta t} \, \mathrm{d}x = \int_{\Gamma_b} \boldsymbol{u}_h^k \cdot \boldsymbol{n} \, \mathrm{d}s, \tag{2.24}$$

indicating that mass is not added or removed when the discrete free boundaries are evolved.

However, mass is artificially lost whenever a free boundary node penetrates into the bedrock (since the discrete contact boundary conditions hold up to machine precision, this can only happen whenever the lower free boundary reattaches to the bedrock). This occurs because, as indicated in Algorithm 1, nodes that penetrate into the bedrock are moved upwards and set to the surface of the bedrock. For sufficiently small time steps, we expect this loss to be negligible.

2.4 Examples of other schemes and numerical results

We conclude this chapter with a series of numerical results computed with seven different schemes that fall within the class of methods presented in Section 2.2. With these results we wish to convince the reader of the utility of the abstract framework introduced in Section 2.2 and of the accuracy and robustness of the particular scheme presented in Section 2.3. Moreover, these tests will allow us to justify the importance of the two notions of contact consistency and stabilisation introduced in Section 2.2.1 when discussing the discretisation of the free boundary equation.

Two numerical tests, which we present below, are performed for each of the schemes. These tests are representative of the kind of computations which are carried out in the following chapters of this document when finding steady configurations.

Numerical test 1 (Subglacial cavity problem)**.** The first test simulates the formation of a subglacial cavity and therefore corresponds with the configuration presented in Section 1.6. Following the setup presented in Chapter 4, we work with non-dimensional variables. This effectively corresponds to setting the length and height of the domain to $L = 1$ and height $H = 1$, and the fluidity factor in Glen's law to $\mathcal{A} = 0.5$. The bed is given by a sinusoidal function of amplitude $r_b = 0.08$. We build a uniform triangular mesh over a square with 16 elements along the horizontal direction and 3 along the vertical, with each of the resulting grid squares crossed by a diagonal from bottom right to top left. Then, we deform the square into the initial configuration with the mesh deformation algorithm $\mathfrak{D}$. For the boundary conditions, we prescribe the shear stress $\tau_b = 0.4$ and the effective pressure $p_i - p_w = 1$ on the top boundary (note that the problem only depends on the effective pressure, not on the individual values for the overburden and water pressures, see Section 4.2.2). We then evolve the cavity over 100 time steps of duration $\Delta t = 0.01$ from an initial state in which the cavity is fully attached state ($\theta^0(x) = b(x)$ for all $x \in [0, L]$). We consider a Newtonian flow here and set $n = 1$ in Glen's law.

Numerical test 2 (Marine ice sheet problem)**.** For the second numerical test, we solve the marine ice sheet problem presented in Section 1.7. More concretely, we follow the setup presented in Chapter 5, where a uniform thickness slab of ice flows down an inclined bedrock and into the sea, where it goes afloat. We consider an initial geometry given by a uniform thickness marine ice sheet whose shelf floats according to Archimedes' principle. We set the bedrock angle to 1° and the length of the domain to 40 km, such that the bed height to the far left of the domain is 200 m. As in the previous test, we set $n = 1$ and $A = 10^{-13}\,\mathrm{Pa}^{-1}\,\mathrm{s}^{-1}$. The friction coefficient is $C = 10^{11}\,\mathrm{Pa\,m}^{-1}\,\mathrm{s}^{-1}$. The thickness of the incoming slab of ice is $H = 200\,\mathrm{m}$. We triangulate the domain by building a uniform triangular mesh over a rectangle of length L and height H with 400 elements along the horizontal direction and 4 along the vertical, which we then deform into the initial configuration with the algorithm $\mathfrak{D}$. Just as before, the triangulation is built by crossing each grid square with a diagonal traversing it from bottom right to top left. We set the time steps to 10^6 s and we evolve the ice over 500 steps.

We now describe the seven numerical schemes used to compute these tests. In order to facilitate the distinction of the different schemes, we denote these by chaining abbreviations of the method used to solve the discrete variational inequality numerically and the forms of

the discrete trace operators γ_h and ζ_h^θ. For example, the scheme presented in Section 2.3 is referred to by "LMAvgUp" because we solve the variational inequality with the Lagrange multiplier method, the operator γ_h takes the average edge-wise value of $\boldsymbol{u}_h \cdot \boldsymbol{n}$ and the operator ζ_h^θ effectively introduces upwinding into the discrete free boundary equation. When describing a scheme, we only give the definition of the discrete trace operator ζ_h^θ on the lower boundary, omitting that of ζ_h^s to shorten the characterisation of the schemes; where necessary, the operator ζ_h^s is defined analogously to ζ_h^θ. We note that the tolerance used in the contact criterion is set to $\text{tol} = 10^{-9}$ in all but schemes 4 and 5.

Scheme 1 (LMAvgUp)**.** This is the main scheme used in this document for solving viscous contact problems, which we present in Section 2.3 above in more detail. The discrete normal trace operator γ_h returns the edge-wise average value of $\boldsymbol{v}_h \cdot \boldsymbol{n}$, that is,

$$\gamma_h \boldsymbol{v}_h|_e = \frac{1}{|e|} \int_e \boldsymbol{v} \cdot \boldsymbol{n} \, \mathrm{d}s \quad \forall e \in \mathcal{E}(\mathcal{T}_h, \Gamma_b), \tag{2.25}$$

and therefore Σ_h is given by the set of piecewise constant functions on Γ_b. The normal trace operator ζ_h^θ at each node is given by the edge-wise averaged normal velocity along the edge immediately upstream. For the lower boundary,

$$(\zeta_h^\theta \boldsymbol{v}_h)_i = \gamma_h \boldsymbol{v}_h|_{e_i}. \tag{2.26}$$

As a result, the scheme for the free boundary equation is stabilised and is contact-consistent. The discrete variational inequality is solved with a Lagrange multiplier method.

The next three schemes are small variations of the main scheme, Scheme 1. We present these schemes to give an understanding of the effects of penalisation of the discrete variational inequality and stabilisation and contact consistency of the discrete free boundary equation.

Scheme 2 (PenAvgUp)**.** As explained in Section 2.2.1, the discrete variational inequality can be rewritten as a variational equality either by introducing a penalisation term or a Lagrange multiplier. In contrast to Scheme 1, which uses a Lagrange multiplier, in this scheme we solve the variational inequality with a penalisation term. Therefore, the variational inequality takes the form of equation (2.9), and a penalty parameter $\delta > 0$ must be chosen. For Numerical test 1, we set $\delta = 10^{-6}$, and for 2 we have $\delta = 10^{-14}$.

Scheme 3 (LMAvgAvg)**.** In order to illustrate the importance of upwinding, this numerical scheme is identical to Scheme 1 with the only difference that the normal trace operator ζ_h^θ at each node takes the average value of the velocities on adjacent edges, as opposed to taking

the velocity from the edge immediately upstream. For the lower boundary, at each node (x_i^θ, θ_i), the operator ζ_h^θ takes the value

$$(\zeta_h^\theta \boldsymbol{v}_h)_i = \frac{1}{2}\left(\gamma_h \boldsymbol{v}_h|_{e_i} + \gamma_h \boldsymbol{v}_h|_{e_{i+1}}\right). \tag{2.27}$$

As a result, the discrete free boundary equation does not contain any upwinding.

Scheme 4 (LMAvgMP)**.** We now build a scheme that is not contact-consistent in the sense of (2.13). To do this, we take Scheme 1 and only modify the normal trace operator ζ_h^θ. For a vector field $\boldsymbol{v}_h \in V_h$ and for a node (x_i^θ, θ_i) along Γ_b, instead of taking the edge-wise average values of $\boldsymbol{v} \cdot \boldsymbol{n}$ along $e_i \in \mathcal{E}(\mathcal{T}_h, \Gamma_b)$, we now take the values of $\boldsymbol{v} \cdot \boldsymbol{n}$ at the midpoint $\boldsymbol{x}_i^m \in \mathbb{R}^2$ of e_i; that is,

$$(\zeta_h^\theta \boldsymbol{v}_h)_i = (\boldsymbol{v}_h \cdot \boldsymbol{n})(\boldsymbol{x}_i^m). \tag{2.28}$$

Note that this scheme is not contact-consistent because $\int_{e_i \cup e_{i+1}} \boldsymbol{v} \cdot \boldsymbol{n} \, \mathrm{d}s = 0$ does not imply that $(\boldsymbol{v}_h \cdot \boldsymbol{n})(\boldsymbol{x}_i^m) = 0$. However, the scheme does implement a form of upwinding because for each node we take the values of the normal velocity at the midpoint located immediately upstream. A consequence of this lack of contact consistency is that, due to numerical errors, the whole of the lower boundary quickly detaches from the bedrock. In order to avoid total detachment and the subsequent breakdown of the computations, we have to increase the contact criterion tolerance tol. For Numerical test 1, we set tol $= 10^{-3}$, and tol $= 10^{-1}$ for 2.

We conclude the list of schemes with an example of a scheme which contains what is arguably the most natural choice for formulating the discrete variational inequality (Scheme 5), together with two variations on a scheme with a more exotic choice of discrete normal trace operator γ_h.

Scheme 5 (PenPWMP)**.** A natural way of solving the discrete variational inequality (2.8) is by defining $K_h = K \cap V_h$. In this case, we have that

$$\gamma_h : \boldsymbol{v}_h \mapsto (\boldsymbol{v}_h \cdot \boldsymbol{n})|_{\Gamma_b} \tag{2.29}$$

and

$$\Sigma_h = \{(\boldsymbol{v}_h \cdot \boldsymbol{n})|_{\Gamma_b} : \boldsymbol{v}_h \in V_h\}. \tag{2.30}$$

Therefore, the discrete normal trace operator coincides with the standard normal trace operator $\boldsymbol{v}_h \mapsto \boldsymbol{v}_h \cdot \boldsymbol{n}$ that assigns a vector field with its the normal component along the boundary. This corresponds with the approach taken in [97]. The discrete variational

inequality can be approximately solved with the penalty method, as explained in Section 2.3. In this case, for a penalty parameter $\delta > 0$, we solve the nonlinear variational equation (2.9) with the penalty operator $\Pi : V_h \to V_h'$ given by (2.10), with γ_h defined by (2.29). The free boundary equation is discretised in a stable and contact-consistent way as follows: let $\boldsymbol{x}_i^m \in \mathbb{R}^2$ denote the midpoint along the edge $e_i \in \mathcal{E}(\mathcal{T}_h, \Gamma_b)$ and, as in Scheme 4, define the trace operator ζ_h^θ by

$$(\zeta_h^\theta \boldsymbol{v}_h)_i = (\boldsymbol{v}_h \cdot \boldsymbol{n})(\boldsymbol{x}_i^m). \tag{2.31}$$

In this way, the velocity at each node (x_i^θ, θ_h^k) is taken from the midpoint immediately upstream. For a given tolerance $\mathrm{tol} > 0$, we use the contact criterion (2.14). As indicated below, when solving Numerical test 1 (the subglacial cavity problem), we find that the normal velocity ζ_h^θ is not as accurate as expected. A consequence of this is that, unless the tolerance for the contact criterion is increased, total detachment will occur within a few time steps and the computation will collapse. For this reason, and only when solving Numerical test 1, we set $\mathrm{tol} = 10^{-3}$. The penalty parameter δ is set to $\delta = 10^{-6}$ for Numerical test 1 and $\delta = 10^{-14}$ for Numerical test 2.

Scheme 6 (PenUpUp)**.** In the previous numerical schemes, stabilisation of the free boundary equations is achieved by taking the values of the normal velocity located upstream of a node. We can also build a stable scheme by working from the standard upwinding scheme for the free boundary equation (1.12b), given by

$$\theta_i^{k+1} = \theta_i^k - \Delta t \left(u_i \frac{\theta_i^k - \theta_{i-1}^k}{x_i^\theta - x_{i-1}^\theta} - w_i \right) \quad \text{for } i = 1, 2, ..., M^\theta, \tag{2.32}$$

where we use the notation $\boldsymbol{u}_h(x_i^\theta, \theta_i^k) = (u_i, w_i)$. In terms of the framework presented in Section 2.2, a contact-consistent scheme can be built by setting Σ_h equal to the set of piecewise constant functions on Γ_b as in (2.19). Then, if we set

$$\gamma_h \boldsymbol{u}_h|_{e_i} = \frac{1}{\sqrt{1 + \left(\dfrac{\theta_i^k - \theta_{i-1}^k}{x_i^\theta - x_{i-1}^\theta} \right)^2}} \left(u_i \frac{\theta_i^k - \theta_{i-1}^k}{x_i^\theta - x_{i-1}^\theta} - w_i \right) \tag{2.33}$$

and

$$(\zeta_h^\theta \boldsymbol{u}_h)_i = \gamma_h \boldsymbol{u}_h|_{e_i} \tag{2.34}$$

for $i = 1, 2, ..., M^\theta$, we see that we obtain a contact-consistent algorithm and we recover (2.32). The discrete variational inequality can be solved with the penalty method by formulating (2.9) with the penalty operator given by (2.10), with γ_h defined as in (2.33). We

complete the numerical scheme by using the contact criterion from Section 2.3, given by (2.14). We solve the Numerical test 1 with $\delta = 10^{-6}$ and 2 with $\delta = 10^{-14}$.

Scheme 7 (PenUpUp2)**.** The numerical results below suggest that while Scheme 6 performs excellently on the subglacial cavity problem (Numerical test 1), it is unable to solve the marine ice sheet problem (Numerical test 2). Interestingly, a small modification to Scheme 6 improves the method substantially for computing the evolution of the marine ice sheet, but deteriorates its effectiveness for the subglacial cavity problem. This modification is exclusive to the definition of γ_h, and leaves the form of ζ_h^θ introduced in Scheme 6 untouched. What we do is enrich the space Σ_h with respect to Scheme 6, setting

$$\Sigma_h = \{\mu_h \in \mathcal{C}(\Gamma_b) : \mu_h|_e \in \mathcal{P}_2(e) \quad \forall e \in \mathcal{E}(\mathcal{T}_h, \Gamma_b)\}, \tag{2.35}$$

and, for the nodes (x_i, θ_i) and the midpoints $\boldsymbol{x}_i^m$ of the edge e_i,

$$(\gamma_h \boldsymbol{v}_h)(x_i, \theta_i) = \frac{1}{\sqrt{1 + \left(\dfrac{\theta_i^k - \theta_{i-1}^k}{x_i^\theta - x_{i-1}^\theta}\right)^2}} \left(u_i \frac{\theta_i^k - \theta_{i-1}^k}{x_i^\theta - x_{i-1}^\theta} - w_i\right) \tag{2.36a}$$

$$(\gamma_h \boldsymbol{v}_h)(\boldsymbol{x}_i^m) = (\boldsymbol{v}_h \cdot \boldsymbol{n})(\boldsymbol{x}_i^m). \tag{2.36b}$$

In short, this scheme corresponds with Scheme 6 with the difference that instead of only penalising the terms (2.36a) of $\gamma_h \boldsymbol{v}_h$, we also penalise the midpoint terms (2.36b). Regarding the penalisation parameter δ, we set $\delta = 10^{-6}$ for Numerical test 1 and $\delta = 10^{-16}$ for 2.

Figures 2.3 and 2.4 illustrate the numerical computations for Numerical tests 1 and 2, respectively, performed with Schemes 1 to 7. For each test case and scheme, we present the ice geometry (in blue) and the discrete normal trace operator $\zeta_h^\theta \boldsymbol{u}_h$ (in red) at three instants in time. Of all the computations presented in Figures 2.3 and 2.4, those obtained with Scheme 1 (LMAvgUp) can be assumed to be "correct". In Chapters 4 and 5, we offer several comparisons with analytical models that allow us to validate our computations with Scheme 1. In fact, Schemes 1 and 2, its equivalent counterpart with the penalty method, are the only schemes capable of solving both numerical tests accurately. For this reason, we use it throughout the rest of this document to compute the viscous contact problems we consider.

Scheme 5 (PenPWMP), which is arguably the most straightforward way of solving the viscous contact problem, is unable to solve the subglacial cavity problem (Figure 2.3), but performs excellently on the marine ice sheet problem (Figure 2.4). As already mentioned, a very similar scheme to Scheme 5, based on the discrete variational inequality formulated with $\gamma_h \boldsymbol{u}_h = \boldsymbol{u}_h \cdot \boldsymbol{n}$ and solved with the penalty method, is used in [97] to simulate the

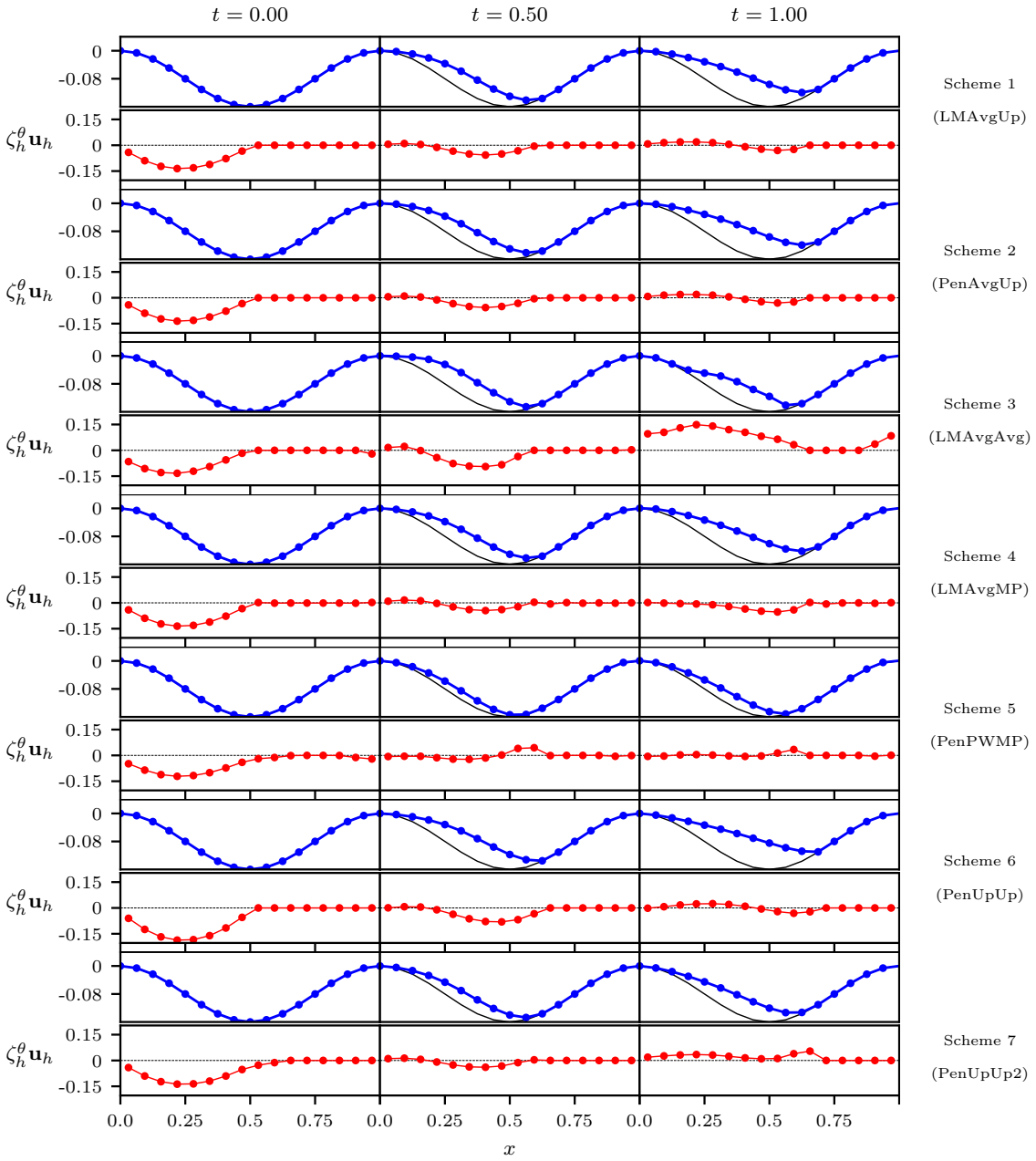

Figure 2.3: Numerical results for the subglacial cavitation problem (Numerical test 1) computed with Schemes 1 to 7. For this test case, we initially set the ice to be fully attached to the bedrock and we compute its detachment and the formation of a subglacial cavity. In these plots, we show the lower ice surface in blue and the discrete normal trace operator $\zeta_h^\theta \boldsymbol{u}_h$ in red at three time steps for each scheme.

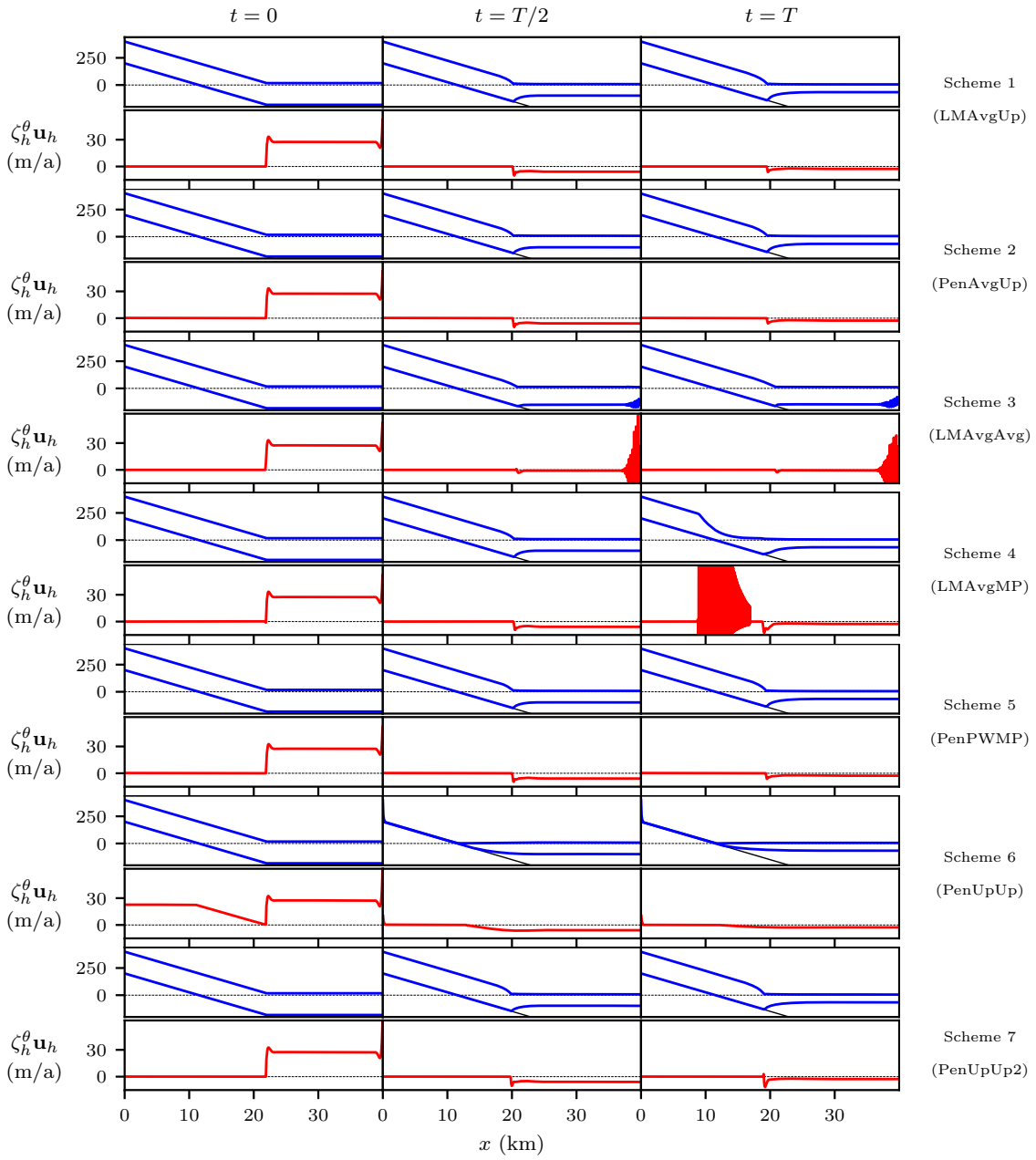

Figure 2.4: Numerical results for the marine ice sheet problem (Numerical test 2) computed with Schemes 1 to 7. Starting from an initial condition where the ice has a constant thickness, in this numerical test we let the ice sheet advance towards a steady state. As a result, the ice shelf thins and the grounding line retreats. In these panels, we show the upper and lower ice surfaces in blue and the discrete normal trace operator $\zeta_h^\theta \boldsymbol{u}_h$ at the base in red at three time steps for each scheme, with $T = 5 \times 10^8$ s being the total simulation time.

response of a marine ice sheet to tidal cycles. Interestingly, when solving the subglacial cavity problem with this scheme, the discrete normal velocity $\boldsymbol{u}_h \cdot \boldsymbol{n}$ along the cavity roof is inaccurate. This can already be seen in Figure 2.3 at $t = 0$, where only four nodes of $\zeta_h^\theta \boldsymbol{u}_h$ for Scheme 5 are visibly zero, as opposed to the seven or eight nodes one sees for the other schemes.

Schemes 6 (PenUpUp) and 7 (PenUpUp2) are two other examples of schemes that perform well with one of the numerical tests, but not with the other. As we see in Figure 2.3, the computations with Scheme 6 for the subglacial cavity problem are very similar to those of Scheme 1. However, Scheme 6 fails to solve the marine ice sheet problem; Figure 2.4 shows that it is unable to enforce the contact conditions effectively. The results in Figure 2.4 for scheme 6 indicate that, due to the lack of enforcement of the non-penetration condition $\zeta_h^\theta \boldsymbol{u}_h \leq 0$ on Γ_a, the ice velocity along the upper surface $\zeta_h^s \boldsymbol{u}_h$ is directed towards the bed due to the conservation of mass, leading to an almost complete disappearance of the grounded ice component. For the marine ice sheet problem, this issue disappears with Scheme 7, which is a slight variation of Scheme 6 where the normal velocity $\gamma_h \boldsymbol{u}_h$ contains more degrees of freedom. However, Scheme 7 is not capable of achieving the accuracy we find with Scheme 6 for the subglacial cavity problem. We remark that adding more degrees of freedom to $\gamma_h \boldsymbol{u}_h$ translates into penalising more degrees of freedom associated to $\boldsymbol{u}_h \cdot \boldsymbol{n}$. This point, together with the previous one on Scheme 5 (PenPWMP), can be taken as an indication that weaker penalisations (in the sense of including fewer degrees of freedom associated to $\boldsymbol{u}_h \cdot \boldsymbol{n}$) work better for the subglacial cavity problem, while stronger penalisations are more effective for the marine ice sheet problem.

The numerical results with Schemes 3 (LMAvgAvg) and 4 (LMAvgMP) demonstrate the importance of contact consistency between γ_h and ζ_h^θ, as defined in Section 2.2.2, and of stabilising the free boundary equations. It is clear from Figures 2.3 and 2.4 that a centred finite difference scheme for the free boundary equation, as effectively implemented in Scheme 3 and as opposed to a backwards finite difference scheme that introduces upwinding, leads to highly deteriorated solutions. The same can be said of an non contact-consistent scheme such as Scheme 4, especially for the marine ice sheet computations in Figure 2.4, where detachment of the ice sheet along the grounded area eventually occurs. For the subglacial cavity computations in Figure 2.3, the lack of contact consistency leads to less dramatic results, although one can observe differences with respect to Scheme 1 when comparing the values of $\zeta_h^\theta \boldsymbol{u}_h$ at $t = 1$. We remind the reader that the computations with Scheme 4 required an increase in the tolerance of the contact criterion with respect to Scheme 1 to avoid a total detachment of the ice from the bedrock. This indicates that another consequence

of dismissing the notion of contact consistency is a loss in robustness with respect to the tolerance of the contact criterion.

Schemes 1 (LMAvgUp) and 2 (PenAvgUp) yield almost identical results. As explained in Section 2.2.1, in the limit where $\delta \to 0$, the solutions computed with a penalty term and with a Lagrange multiplier coincide. It remains to investigate whether the performance of other schemes built in terms of the penalty method, such as Schemes 5 and 6, perform differently when the discrete Stokes variational inequality is solved with a Lagrange multiplier.

2.5 Discussion

In the preceding sections of this chapter, we consider the numerical approximation of solutions to viscous contact problems in the two-dimensional configuration set out in Chapter 1. We present a general framework for solving viscous contact problems in Section 2.2 which decouples the Stokes problem from the free boundary equations. In Section 2.2.1, the Stokes problem is then reformulated as a discrete variational inequality that enforces a discrete version of the contact boundary conditions. When discretising the free boundary equation in Section 2.2.2, we identify two properties of the scheme (contact consistency of the normal trace operator and stabilisation) that turn out to be very important for the robustness and accuracy of numerical calculations. Satisfying these two properties poses numerical challenges for solving viscous contact problems that set them apart from their elastic counterparts.

With this general framework, we propose a numerical scheme in Section 2.3 that is used throughout this document for solving viscous contact problems in a glaciological context. We also propose six other schemes in Section 2.4 and compare them by computing two numerical tests. These computations reveal the importance of the two properties of contact consistency and stability of the discretisation mentioned in the previous paragraph. They also justify our choice of main numerical scheme by comparing it to other candidates.

Two obvious extensions of this work that should be investigated in the future are the construction of implicit schemes that couple the Stokes and free boundary problems and the approximation of solutions to three dimensional viscous contact problems. Implicit methods would probably remain stable under much higher time steps Δt, reducing the computational time for many tests. It would also pave the way for the computation of steady states by solving the steady system directly with a nonlinear solver, such as a semi-smooth Newton method [54], instead of advancing an initial state until a steady state is reached as we do in Chapters 4 and 5. This has the potential of achieving dramatic reductions in computational times, since advancing towards a steady state often involves the computation of oscillating regimes that only dampen slowly, as we show in Section 4.3.1. Regarding three-dimensional

viscous contact problems, we note that our stabilisation of the free boundary equations relies heavily on the domain being two-dimensional. Therefore, an extension to three dimensions would require an exploration of analogous stabilisations in the three dimensional case. We note that three dimensional viscous contact problems have been performed in Elmer/Ice [50, 49], so this implementation could be a starting point for future research.

Given the importance of Elmer/Ice in viscous contact problems, an appropriate understanding of this solver is an outstanding task left for future work. We note that a clear understanding of how this solver enforces contact conditions is not clear from the references. It would be of great interest to see how Elmer/Ice's solver for viscous contact problems fits into the general framework of Section 2.2 and how it compares to our solver from Section 2.3.

A final point that could be addressed in future work is the implementation of Lagrange multiplier methods for schemes such as Schemes 5 to 7. The main difficulty here is that either the space of Lagrange multipliers or the duality pairing in Σ_h^a become non-trivial. For example, in Scheme 5, the space of Lagrange multipliers belongs to a space of piecewise quadratic polynomials whose continuity from element to element depends on whether two adjacent edges are co-linear or not. This creates difficulties when using Firedrake for the implementation which should be considered carefully. Although they do not perform exceptionally well in the tests carried out above, it remains to investigate whether enforcing the contact conditions with a Lagrange multiplier improves their performance. Perhaps the issues we find when, for example, computing Numerical test 1 with Scheme 5 or Numerical test 2 with Scheme 6, no longer arise when the variational inequalities are solved with Lagrange multipliers.

Chapter 3

Analysis and approximation of the Stokes variational inequality

The variational inequalities presented in Chapter 1 are amenable to a mathematical analysis that establishes rigorous statements on the existence, uniqueness, and stability of solutions and their finite element approximation. This chapter is dedicated to that analysis, and we focus on Variational inequality C from Chapter 1 for the sake of concreteness and simplicity, although most of the results we present here are extendable to Variational inequalities A and B. With these analyses, we partially give a rigorous foundation to the numerical methods from Chapter 2. Much of the content of this chapter has been published in [20].

The first part of this chapter, Section 3.1, is concerned with the continuous formulation of the variational inequality. We start by determining the sense in which different formulations of Variational inequality C are equivalent, including its formulation as a system of partial differential equations with contact conditions (the strong formulation), as a minimisation problem, and as a mixed problem with a Lagrange multiplier. This section concludes with a proof on the conditions under which the variational inequality is well-posed. An important property of the variational inequalities considered in this document is that, under certain conditions, rigid body modes are present in the space of admissible velocities. As a consequence, a property of differential operators called coercivity, which essentially states that the operators grow rapidly towards the extremes of a space (see [27, Section 8.2]), is lost. Thus, the variational inequalities become semicoercive. For this reason, a modification of a classical result in the analysis of variational inequalities from [29] is required for establishing the existence and uniqueness of solutions.

The second part of the chapter, constituted by Sections 3.2 and 3.3, is a theoretical investigation of the approximation of solutions to the variational inequality when posed as a mixed problem with a Lagrange multiplier. Section 3.2 considers an abstract discretisation in terms of a class of finite-dimensional subspaces. These discretisations fit into the

framework presented in the previous chapter, in Section 2.2.1, for the discrete variational inequality, although they are less general, as explained in Remark 3.3. Then, in Section 3.3, we use the abstract framework from Section 3.2 to establish the convergence of a concrete finite element approximation. Ideally, this concrete finite element scheme would have coincided with the main numerical scheme for the variational inequality from Section 2.3, which uses Taylor-Hood elements for the velocity-pressure pair. However, as explained in Remark 3.7, certain complications arise when analysing this scheme which need to be studied carefully in future work. Alternatively, we consider a scheme based on the P2P0 elements for the velocity and pressure.

The theoretical tools used in this chapter are drawn from many different sources. The Stokes variational inequalities we consider in this document are superficially similar to the elastic contact problem with Signorini or unilateral boundary conditions, whose analysis and discretisation is studied in [68, 48]. However, the variational inequality we study in this chapter includes three substantial difficulties that must be addressed carefully: the presence of rigid body modes in the space of admissible velocities, the nonlinear rheological law used to model ice as a viscous fluid, and the nonlinearity of the friction boundary condition (1.36). Two analytical studies in glaciology [90, 17] carry out a similar analysis to the one we present in Section 3.1. One major difference is that the variational inequalities encountered in these references arise due to Coulomb friction boundary conditions, as opposed to contact boundary conditions. A consequence of this is that our minimisation problem is posed over a convex set that is not a vector space in general. Therefore, a different approach based on a proof from [29] must be taken to establish the existence and uniqueness of minimisers in the presence of rigid modes, which we present in Section 3.1.4.

For the analysis of the discretised problem, we appeal to the literature on the finite element approximation of elastic contact problems [13, 48, 23], in particular when these are written as mixed problems with Lagrange multipliers [14, 18, 52, 8]. However, due to the three difficulties stated in the previous paragraph, we require additional techniques from other numerical studies. The nonlinearities introduced via the rheological power law and the friction law can be handled with tools developed for analysing the finite element approximation of p-Laplacian and p-Stokes problems [5, 6, 22, 7, 55], as seen in Section 3.2.2. Rigid modes in the space of admissible velocities render the variational inequality semicoercive. Although the finite element approximation of semicoercive variational inequalities has been studied in the past [47, 96, 2], existing analyses use purely indirect arguments which give very limited information on how different meshes and finite elements affect the discretisation. Here, we present a novel constructive approach based on the use of a specially designed projection operator onto the subspace of rigid modes that satisfies a Korn

type inequality, see (3.21). Error estimates are then obtained in Lemma 3.5 for the rigid component of the velocity error by exploiting the fact that the dimension of the subspace of rigid modes is at most one for Variational inequality C.

3.1 Analysis of the variational inequality

This section contains an analysis of Variational inequality C, presented in Chapter 1. In this analysis, we first give rigorous statements which clarify the sense in which this variational inequality is equivalent to the Stokes equations with contact boundary conditions (the strong formulation). Moreover, we also show that it can be rewritten in terms of a Lagrange multiplier (the mixed formulation) and as a minimisation problem. The mixed formulation is used further on in this chapter to build a numerical scheme for solving the variational inequality. On the other hand, reformulating the variational inequality as a minimisation problem allows us to use techniques from the calculus of variations to establish under what conditions we have a unique solution.

3.1.1 Strong formulation of the Stokes problem

The marine ice sheet problem under consideration in this chapter consists of a symmetric ice dome resting on the continent and sliding into the ocean. This is the most common configuration considered when studying marine ice sheets [89, 88, 24] and is generally used as a benchmark test case [79]. We exploit the symmetry of the problem and only solve the flow equations on the domain $\Omega \subset \mathbb{R}^2$ which represents one half of the ice sheet, as seen in Figure 1.2. We assume Ω to be connected and polygonal. The latter assumption is made to simplify the analysis of the discrete problem considered in Section 3.3, but we expect the essential results presented here to extend to domains with smooth enough boundaries.

As in Figure 1.2, the boundary of Ω is the closure of the disjoint union of the open sets Γ_i, Γ_a, Γ_d, Γ_c, and Γ_t. The set Γ_i is the ice divide of the ice sheet, which is essentially its symmetry axis. As such, it is a vertical surface on which we enforce the symmetry conditions (1.38) with $u_i = 0$ and $\sigma_{nt,i} = 0$. The sets Γ_a and Γ_i are the attached and detached regions of the lower boundary, respectively. We assume each set to be the union of a finite number of subsets, each open and connected with positive measure. On Γ_a we enforce the contact conditions (1.11) and the nonlinear friction law (1.36). The regions Γ_t and Γ_c represent the top surface of the ice sheet and its calving front, respectively. As such, they are both assumed to be connected and of positive measure.

The regions Γ_i, Γ_t, and Γ_c have stress boundary conditions, see (1.35), (1.37), and (1.39). From an analytical point of view, it is helpful to define the surface

$$\Gamma_s = \Gamma_d \cup \Gamma_t \cup \Gamma_c \tag{3.1}$$

and enforce the general condition $\boldsymbol{\sigma n} = p_s \boldsymbol{n}$ for some scalar field p_s defined on Γ_s. Then, the system of equations we analyse and discretise is given by

$$-\nabla \cdot \left(\alpha |\mathbf{D}\boldsymbol{u}|^{r-2}\mathbf{D}\boldsymbol{u}\right) + \nabla p = \boldsymbol{f} \qquad \text{in } \Omega, \tag{3.2a}$$

$$\nabla \cdot \boldsymbol{u} = 0 \qquad \text{in } \Omega, \tag{3.2b}$$

$$\boldsymbol{\sigma n} = p_s \boldsymbol{n} \qquad \text{on } \Gamma_s, \tag{3.2c}$$

$$\boldsymbol{\sigma}_{nt} = 0 \qquad \text{on } \Gamma_i, \tag{3.2d}$$

$$\boldsymbol{u} \cdot \boldsymbol{n} = 0 \qquad \text{on } \Gamma_i, \tag{3.2e}$$

$$\boldsymbol{\sigma}_{nt} = -C|\mathbf{T}\boldsymbol{u}|^{r-2}\mathbf{T}\boldsymbol{u} \qquad \text{on } \Gamma_a, \tag{3.2f}$$

$$\boldsymbol{u} \cdot \boldsymbol{n} \leq 0, \quad \sigma_{nn} \leq -p_w \quad \text{and} \quad (\boldsymbol{u} \cdot \boldsymbol{n})(\sigma_{nn} + p_w) = 0 \qquad \text{on } \Gamma_a. \tag{3.2g}$$

Here, α is the non-negative constant defined in Section 1.3 and $r \in (1, 2]$. The system (3.2) can be interpreted as the strong form of the Variational inequality C. In this case, the differential operators in (3.2a) and (3.2b) can be defined in terms of classical derivatives.

3.1.2 The weak formulation as a variational inequality

As explained in Section 1.5, the system of equations given by (3.2) can be written in terms of weak derivatives as a variational statement. This results in Variational inequality C, which we write down once more in this section with a slightly different notation. The spaces V and Q are given by

$$V = \left\{\boldsymbol{v} \in \boldsymbol{W}^{1,r}(\Omega) : \boldsymbol{v} \cdot \boldsymbol{n} = 0 \text{ on } \Gamma_i\right\} \quad \text{and} \quad Q = L^{r'}(\Omega),$$

as in Chapter 1. The convex set K, which we already defined in Section 1.5, can be rewritten in terms of the operator $\gamma_n : V \to L^r(\Gamma_a)$, the normal trace operator onto Γ_a. This operator is built by extending to V the operator $\boldsymbol{v} \mapsto \boldsymbol{v} \cdot \boldsymbol{n}$ on Γ_a, defined on smooth functions. We note that γ_n is the continuous analogue of the discrete operator γ_h^a introduced in Chapter 2. Then, we may write

$$K = \left\{\boldsymbol{v} \in V : \gamma_n \boldsymbol{v} \leq 0 \quad \text{a.e. on } \Gamma_a\right\}.$$

The weak formulation of (3.2) can then be stated as the following variational inequality: find $(\boldsymbol{u}, p) \in K \times Q$ such that

$$\langle A\boldsymbol{u} + G\boldsymbol{u} - Bp - f, \boldsymbol{v} - \boldsymbol{u}\rangle_V + \langle Bq, \boldsymbol{u}\rangle_V \geq 0 \quad \forall (\boldsymbol{v}, q) \in K \times Q. \tag{3.3}$$

Here, for the reader's convenience, we recall the definition of the operators $A : V \to V'$ and $G : V \to V'$ from (1.18a) and (1.42) :

$$\langle A\boldsymbol{u}, \boldsymbol{v}\rangle_V = \int_\Omega \alpha|\mathbf{D}\boldsymbol{u}|^{r-2}\left(\mathbf{D}\boldsymbol{u} : \mathbf{D}\boldsymbol{v}\right) \mathrm{d}x, \tag{3.4a}$$

$$\langle G\boldsymbol{u}, \boldsymbol{v}\rangle_V = \int_{\Gamma_a} C|\mathbf{T}\boldsymbol{u}|^{r-2}\left(\mathbf{T}\boldsymbol{u} \cdot \mathbf{T}\boldsymbol{v}\right) \mathrm{d}s, \tag{3.4b}$$

for all $(\boldsymbol{u}, \boldsymbol{v}) \in V \times V$. We also recall the definition of B, which represents the negative of the weak gradient, from (1.18b):

$$\langle Bq, \boldsymbol{v}\rangle_V = \int_\Omega q\left(\nabla \cdot \boldsymbol{v}\right) \mathrm{d}x \tag{3.5}$$

for $(\boldsymbol{v}, q) \in V \times Q$. Finally, the dual element $f \in V'$ encodes the action of the body and boundary forces acting on the system:

$$\langle f, \boldsymbol{v}\rangle_V = \int_\Omega \boldsymbol{f} \cdot \boldsymbol{v}\, \mathrm{d}x + \int_{\Gamma_s} p_s\left(\boldsymbol{v} \cdot \boldsymbol{n}\right) \mathrm{d}s - \int_{\Gamma_a} p_w\left(\boldsymbol{v} \cdot \boldsymbol{n}\right) \mathrm{d}s \tag{3.6}$$

for any $\boldsymbol{v} \in V$. In order for (3.6) to make sense, we require $\boldsymbol{f} \in L^{r'}(\Omega)$, $p_s \in L^{r'}(\Gamma_s)$ and $p_w \in L^{r'}(\Gamma_a)$.

The sense in which the variational inequality (3.3) and the partial differential equation (3.2) are equivalent is made specific in Lemma 3.1 below.

Lemma 3.1. *If $(\boldsymbol{u}, p) \in \boldsymbol{\mathcal{C}}^2(\Omega) \times \mathcal{C}^1(\Omega)$, then the strong formulation given by equations (3.2) holds if and only if the variational inequality (3.3) is satisfied.*

Proof. Let $(\boldsymbol{u}, p) \in \boldsymbol{\mathcal{C}}^2(\Omega) \times \mathcal{C}^1(\Omega)$ solve (3.2). It is clear that if (3.2b) holds, then $\langle Bq, \boldsymbol{u}\rangle_V = 0$ for all $q \in Q$. Let $\boldsymbol{v} \in K$ and multiply (3.2a) by $\boldsymbol{v} - \boldsymbol{u}$ and integrate over Ω. The equality

$$\begin{aligned} -\int_\Omega \left[\nabla \cdot \left(\alpha|\mathbf{D}\boldsymbol{u}|^{r-2}\mathbf{D}\boldsymbol{u}\right) - \nabla p\right] \cdot (\boldsymbol{v} - \boldsymbol{u})\, \mathrm{d}x = \\ \langle A\boldsymbol{u} - Bp, \boldsymbol{v} - \boldsymbol{u}\rangle_V - \int_{\partial\Omega} \boldsymbol{\sigma}(\boldsymbol{v} - \boldsymbol{u}) \cdot \boldsymbol{n}\, \mathrm{d}s \end{aligned} \tag{3.7}$$

follows from the divergence theorem. We also have that

$$\int_{\partial\Omega} \boldsymbol{\sigma}(\boldsymbol{v} - \boldsymbol{u}) \cdot \boldsymbol{n}\, \mathrm{d}s = \int_{\partial\Omega} \left(\sigma_{nn}(\boldsymbol{v} - \boldsymbol{u}) \cdot \boldsymbol{n} + \boldsymbol{\sigma}_{nt} \cdot (\boldsymbol{v} - \boldsymbol{u})\right) \mathrm{d}s.$$

Moreover, as a result of the contact conditions (3.2g),

$$\int_{\Gamma_a} \sigma_{nn}(\boldsymbol{v} - \boldsymbol{u}) \cdot \boldsymbol{n}\, \mathrm{d}s \geq -\int_{\Gamma_a} p_w\left(\boldsymbol{v} - \boldsymbol{u}\right) \cdot \boldsymbol{n}\, \mathrm{d}s,$$

from which the variational inequality (3.3) follows.

The converse statement is deduced by means of the integration by parts formula (3.7) and the use of the fundamental lemma of calculus of variations with suitable test functions. The examples in [43, 48] contain similar derivations. □

The variational inequality (3.3) can also be understood as a minimisation problem. This property is fundamental for proving that the Stokes variational inequality is well-posed because it allows us to use tools from the calculus of variations. Given the convex set of divergence-free functions $\mathring{K}$, defined as

$$\mathring{K} = \{\boldsymbol{v} \in K : \nabla \cdot \boldsymbol{v} = 0 \quad \text{a.e. on } \Omega\},$$

the variational inequality (3.3) is equivalent to the minimisation of the functional

$$\mathcal{J}(\boldsymbol{v}) = \frac{1}{r}\int_\Omega \alpha|\mathbf{D}\boldsymbol{v}|^r \,\mathrm{d}x + \frac{1}{r}\int_{\Gamma_a} C|\mathbf{T}\boldsymbol{v}|^r \,\mathrm{d}s - \langle f, \boldsymbol{v}\rangle_V \tag{3.8}$$

over $\mathring{K}$. Lemmas 9 and 12 of [17] show that $\mathcal{J}$ is convex and Gâteaux differentiable, with derivative

$$\langle D\mathcal{J}(\boldsymbol{u}), \boldsymbol{v}\rangle_V = \langle A\boldsymbol{u} + G\boldsymbol{u} - f, \boldsymbol{v}\rangle_V. \tag{3.9}$$

The equivalence between the minimisation of $\mathcal{J}$ and (3.3) hinges on the so-called inf-sup condition of the operator B over the space V_a, which is the kernel of γ_n:

$$V_a = \{\boldsymbol{v} \in V : \gamma_n \boldsymbol{v} = 0 \quad \text{on } \Gamma_a\}. \tag{3.10}$$

This inf-sup condition of B is

$$\sup_{\boldsymbol{v}\in V_a} \frac{\langle Bq, \boldsymbol{v}\rangle_V}{\|\boldsymbol{v}\|_V} \gtrsim \|q\|_Q \quad \forall q \in Q, \tag{3.11}$$

and it essentially states that the operator B restricted to V_a is injective and has a bounded inverse from its range. This property allows us to recover a unique pressure once we have a velocity that minimises $\mathcal{J}$. Condition (3.11) is proved in [64, Lemma 3.2.7].

Lemma 3.2. *Given a solution $(\boldsymbol{u}, p) \in K \times Q$ of the variational inequality (3.3), the velocity field is then divergence free, i.e. $\boldsymbol{u} \in \mathring{K}$, and is a minimiser of the functional $\mathcal{J} : \mathring{K} \to \mathbb{R}$ defined in (3.8). Conversely, if $\boldsymbol{u} \in \mathring{K}$ minimises $\mathcal{J} : \mathring{K} \to \mathbb{R}$, then there is a unique $p \in Q$ such that $(\boldsymbol{u}, p) \in K \times Q$ solves (3.3).*

Proof. For the first part of the lemma, for a test function $\boldsymbol{v} \in \mathring{K}$, the variational inequality (3.3) can be written as

$$\langle A\boldsymbol{u} + G\boldsymbol{u} - f, \boldsymbol{v} - \boldsymbol{u}\rangle_V \geq 0 \quad \forall \boldsymbol{v} \in \mathring{K}. \tag{3.12}$$

We can then use the convexity and differentiability of $\mathcal{J}$ to show that $\mathcal{J}(\boldsymbol{u}) \leq \mathcal{J}(\boldsymbol{v})$ for all $\boldsymbol{v} \in \mathring{K}$. Indeed, by the definition of Gâteaux differentiability, we have that

$$\langle D\mathcal{J}(\boldsymbol{u}), \boldsymbol{v} - \boldsymbol{u}\rangle_V = \lim_{t\to 0} \frac{\mathcal{J}(\boldsymbol{u} + t(\boldsymbol{v} - \boldsymbol{u})) - \mathcal{J}(\boldsymbol{u})}{t}. \tag{3.13}$$

Moreover, by the convexity of $\mathcal{J}$,

$$\mathcal{J}(\boldsymbol{u}+t(\boldsymbol{v}-\boldsymbol{u}))-\mathcal{J}(\boldsymbol{u})\leq t(\mathcal{J}(\boldsymbol{v})-\mathcal{J}(\boldsymbol{u}))\quad\forall t>0. \tag{3.14}$$

Then, $\mathcal{J}(\boldsymbol{v})-\mathcal{J}(\boldsymbol{u})\geq 0$ can be deduced from (3.12), (3.13), and (3.14).

Conversely, if we assume $\boldsymbol{u}\in\mathring{K}$ to minimise $\mathcal{J}$ over $\mathring{K}$, then $\boldsymbol{u}$ solves (3.12). Now, using [3, Lemma 3.3], we can decompose $\boldsymbol{v}\in K$ into the sum $\boldsymbol{v}=\boldsymbol{v}_0+\boldsymbol{w}$ of a divergence-free velocity field $\boldsymbol{v}_0\in\mathring{K}$ and the field $\boldsymbol{w}\in V_a$. Then, the variational inequality (3.3) will hold if there is a $p\in Q$ such that

$$\langle A\boldsymbol{u}+G\boldsymbol{u}-f,\boldsymbol{w}\rangle_V=\langle Bp,\boldsymbol{w}\rangle_V\quad\forall\boldsymbol{w}\in V_a. \tag{3.15}$$

By (3.11), there is a $p\in Q$ for which (3.15) holds and it is unique. □

3.1.3 The mixed formulation with a Lagrange multiplier

The numerical scheme we use to compute solutions to viscous contact problems is based on a formulation of the variational inequality with a Lagrange multiplier that enforces the contact boundary condition. This formulation, which we call mixed in the sense of mixed methods from the finite element literature, see [10], is the continuous counterpart to (2.11).

In order to define the space where we seek the Lagrange multiplier, we denote the range of γ_n by Σ, that is,

$$\Sigma=\operatorname{Ran}\gamma_n.$$

We remark that Σ is the continuous counterpart to Σ_h^a introduced in Chapter 2. We equip this space with the $W^{1-1/r,r}(\Gamma_a)$ norm. We assume the geometry of Ω and Γ_a to be sufficiently regular for this space to be a Banach space, see [68, Section 5], [48, Chapter III], and [1, Chapter 7] for discussions on normal traces and trace spaces. The Lagrange multiplier is sought in the convex cone of multipliers

$$\Lambda=\left\{\mu\in\Sigma':\langle\mu,\zeta\rangle_\Sigma\geq 0\quad\forall\zeta\in\Sigma\text{ s.t. }\zeta\leq 0\text{ a.e. on }\Gamma_a\right\}.$$

The mixed formulation of (3.3) is: find $(\boldsymbol{u},p,\lambda)\in V\times Q\times\Lambda$ such that

$$\langle A\boldsymbol{u}+G\boldsymbol{u}-Bp-f,\boldsymbol{v}\rangle_V-\langle\lambda,\gamma_n\boldsymbol{v}\rangle_\Sigma=0\qquad\forall\boldsymbol{v}\in V, \tag{3.16a}$$

$$\langle Bq,\boldsymbol{u}\rangle_V=0\qquad\forall q\in Q, \tag{3.16b}$$

$$\langle\mu-\lambda,\gamma_n\boldsymbol{u}\rangle_\Sigma\geq 0\qquad\forall\mu\in\Lambda. \tag{3.16c}$$

The Lagrange multiplier λ essentially coincides with $\sigma_{nn} + p_w$ on Γ_a. Indeed, if the solution to (3.16) is sufficiently smooth for integration by parts to hold, we arrive at $\lambda = \sigma_{nn} + p_w$ on Γ_a. Moreover, the conditions $\lambda \in \Lambda$ and (3.16c) are equivalent to

$$\langle \mu, \gamma_n \boldsymbol{u} \rangle_\Sigma \geq 0 \quad \forall \mu \in \Lambda, \quad \lambda \in \Lambda, \quad \text{and} \quad \langle \lambda, \gamma_n \boldsymbol{u} \rangle_\Sigma = 0, \tag{3.17}$$

which is a weak representation of the contact boundary conditions (3.2g).

Once again, the proof of the equivalence between (3.3) and (3.16) requires an inf-sup condition on γ_n in order to recover a unique Lagrange multiplier for a pair $(\boldsymbol{u}, p)$ which solve the variational inequality (3.3). This condition takes the following form:

$$\sup_{\boldsymbol{v} \in V} \frac{\langle \mu, \gamma_n \boldsymbol{v} \rangle_\Sigma}{\|\boldsymbol{v}\|_V} \gtrsim \|\mu\|_{\Sigma'} \quad \forall \mu \in \Sigma'. \tag{3.18}$$

The inf-sup condition (3.18) is a direct consequence of the inverse mapping theorem, since γ_n is surjective onto the Banach space Σ.

Lemma 3.3. *If $(\boldsymbol{u}, p) \in K \times Q$ solves the variational inequality (3.3), then there is a unique $\lambda \in \Lambda$ such that $(\boldsymbol{u}, p, \lambda)$ is a solution of the mixed problem (3.16). Conversely, if $(\boldsymbol{u}, p, \lambda) \in V \times Q \times \Lambda$ solves (3.16), then $(\boldsymbol{u}, p)$ is a solution of (3.3).*

Proof. Equation (3.16a) can be rewritten as

$$\gamma_n' \lambda = A\boldsymbol{u} + G\boldsymbol{u} - Bp - f \quad \text{in } V'. \tag{3.19}$$

Here, $\gamma_n' : \Sigma' \to V'$ refers to the dual operator of γ_n, defined by

$$\langle \gamma_n' \mu, \boldsymbol{v} \rangle_V = \langle \mu, \gamma_n \boldsymbol{v} \rangle_\Sigma \quad \forall (\mu, \boldsymbol{v}) \in \Sigma' \times V. \tag{3.20}$$

Since $\gamma_n : V \to \Sigma$ has a closed range, we have that $\operatorname{Ran} \gamma_n' = (\operatorname{Ker} \gamma_n)^\circ$, where

$$(\operatorname{Ker} \gamma_n)^\circ = \left\{ \mu \in \Sigma' : \langle \mu, \phi \rangle_\Sigma = 0 \quad \forall \phi \in \operatorname{Ker} \gamma_n \right\}.$$

Therefore, if $(\boldsymbol{u}, p) \in K \times Q$ is a solution to (3.3), then there is unique $\lambda \in \Sigma'$ if $A\boldsymbol{u} + G\boldsymbol{u} - Bp - f \in (\operatorname{Ker} \gamma_n)^\circ$. For a $\boldsymbol{w} \in \operatorname{Ker} \gamma_n$, we clearly have that $\boldsymbol{u} + \boldsymbol{w} \in K$. Using the variational inequality (3.3), we can write

$$\langle A\boldsymbol{u} + G\boldsymbol{u} - Bp - f, \boldsymbol{w} \rangle_V = 0,$$

which means that $A\boldsymbol{u} + G\boldsymbol{u} - Bp - f \in (\operatorname{Ker} \gamma_n)^\circ$. Next, we must show that $\lambda \in \Lambda$ and that (3.16c) holds. By setting $\boldsymbol{v} = 0$ and $\boldsymbol{v} = 2\boldsymbol{u}$ in (3.3) we see that $\langle \lambda, \gamma_n \boldsymbol{u} \rangle_\Sigma = 0$. Since $\gamma_n \boldsymbol{u} \leq 0$ in Σ, it follows that (3.16c) must hold. Finally, $\lambda \in \Lambda$ follows from (3.3), (3.19), and the fact that $\boldsymbol{v} + \boldsymbol{u} \in K$ for any $\boldsymbol{v} \in K$.

For the second part of the lemma, if $(\boldsymbol{u}, p, \lambda) \in V \times Q \times \Lambda$ solves (3.16), then $\nabla \cdot \boldsymbol{u} = 0$ a.e. in Ω, $\langle \lambda, \gamma_n \boldsymbol{v} \rangle_\Sigma \geq 0$ for all $\boldsymbol{v} \in K$, and $\langle \lambda, \gamma_n \boldsymbol{u} \rangle_\Sigma = 0$. This implies that $\langle \mu, \gamma_n \boldsymbol{u} \rangle_\Sigma \geq 0$ for all $\mu \in \Lambda$, hence $\boldsymbol{u} \in \mathring{K}$. The variational inequality then follows directly from (3.16) by testing with $(\boldsymbol{v} - \boldsymbol{u}, q)$, where $(\boldsymbol{v}, q) \in K \times Q$. □

3.1.4 Existence, uniqueness and stability of solutions

Lemmas 3.2 and 3.3 allow us to establish results concerning existence and uniqueness of solutions for the variational inequality (3.3) and its mixed formulation (3.16) by studying the functional $\mathcal{J}$ on $\mathring{K}$. The existence of minimisers to $\mathcal{J}$ depends on whether the set

$$R_V = \left\{ \boldsymbol{v}_R \in V : \int_\Omega |\mathbf{D}\boldsymbol{v}_R|^r \,\mathrm{d}x + \int_{\Gamma_a} |\mathbf{T}\boldsymbol{v}_R|^r \,\mathrm{d}s = 0 \right\}$$

is equal to or larger than the trivial set $\{0\}$. As shown in [68, Lemma 6.1], the kernel of $\mathbf{D}$ coincides with the set of rigid modes in Ω, defined by

$$R = \left\{ \boldsymbol{v}_R \in \boldsymbol{H}^1(\Omega) : \boldsymbol{v}_R(x,y) = \begin{pmatrix} a \\ b \end{pmatrix} + \omega \begin{pmatrix} -y \\ x \end{pmatrix}, \quad (a,b,\omega) \in \mathbb{R}^3 \right\}.$$

Hence, R_V is the set of rigid modes $\boldsymbol{v}_R \in R$ satisfying $\mathbf{T}\boldsymbol{v}_R = 0$ on Γ_a and $\boldsymbol{v}_R \cdot \boldsymbol{n} = 0$ on Γ_i. For this reason, the dimension of R_V can be at most 1 whenever Γ_a is a flat surface perpendicular to Γ_i. In this case, R_V is given by purely vertical translations.

Remark 3.1. Although a flat bedrock may appear to be unrealistic, these are considered in many theoretical studies of marine ice sheets [89, 79, 97]. One-dimensional subspaces of rigid modes in V also arise in marine ice sheets which can slide freely ($C = 0$). More importantly, the theoretical framework we introduce here for dealing with the case when $\dim R_V = 1$ can be applied to the study of existence and uniqueness of solutions for Variational inequalities A and B in Section 1.6, arising when modelling subglacial cavitation, as explained in Remark 3.2 below.

We define the projection operator $\mathbb{P} : V \to R_V$ by

$$\mathbb{P}(\boldsymbol{v}) = \begin{cases} \dfrac{\int_{\Gamma_a} \boldsymbol{v} \cdot \boldsymbol{n} \,\mathrm{d}s}{\int_{\Gamma_a} \boldsymbol{e}_R \cdot \boldsymbol{n} \,\mathrm{d}s} \boldsymbol{e}_R & \text{if } \dim R_V = 1, \\ 0 & \text{if } \dim R_V = 0, \end{cases}$$

where $\boldsymbol{e}_R \in R_V$ is a basis function that spans R_V when $\dim R_V = 1$. We choose this projection operator because it satisfies $\mathbb{P}(K) \subset K$. The operator $\mathbb{Q} = \mathbb{I} - \mathbb{P}$ then maps elements in V onto a closed subspace whose intersection with R_V is $\{0\}$. As a result, we have the following variation of Korn's inequality:

Lemma 3.4. *The inequality*

$$\|\mathbb{Q}\boldsymbol{v}\|_V \lesssim \|\mathbf{D}\boldsymbol{v}\|_{L^r(\Omega)} + \|\mathbf{T}\boldsymbol{v}\|_{L^r(\Gamma_a)} \tag{3.21}$$

holds uniformly for all $\boldsymbol{v} \in V$.

Proof. Following the proof of [17, Lemma 3], we first notice that (3.21) follows from

$$\int_\Omega |\boldsymbol{v}|^r \,\mathrm{d}x \lesssim \int_\Omega |\mathbf{D}\boldsymbol{v}|^r \,\mathrm{d}x + \int_{\Gamma_a} |\mathbf{T}\boldsymbol{v}|^r \,\mathrm{d}s \quad \forall \boldsymbol{v} \in \operatorname{Ran} \mathbb{Q} \tag{3.22}$$

due to the generalised Korn inequality [17, Lemma 2]. Since $\operatorname{Ran} \mathbb{Q} \cap R_V = \{0\}$, the proof of (3.21) is completed by assuming (3.22) to be false and mimicking the steps in the proof of [17, Lemma 3]. □

Whenever $R_V \neq \{0\}$, the system (3.16) is semicoercive in the sense that the operator $A + G$ has a nontrivial kernel. In Theorem 3.1 below, we show that a consequence of semicoercivity is that (3.16) will have a solution only when the following compatibility condition holds:

$$\langle f, \boldsymbol{v}_R \rangle_V < 0 \quad \forall \boldsymbol{v}_R \in (R_V \cap K) \setminus \{0\}. \tag{3.23}$$

Condition (3.23) allows us to establish the well-posedness of (3.16) and error estimates, because the restriction of the map $\boldsymbol{v}_R \mapsto \langle f, \boldsymbol{v}_R \rangle_V$ to the boundary of the unit ball in $K \cap R_V$ is a continuous map defined over a compact set. Therefore, whenever (3.23) holds, we have the inequality

$$\delta \|\boldsymbol{v}_R\|_V \leq -\langle f, \boldsymbol{v}_R \rangle_V \quad \forall \boldsymbol{v}_R \in R_V \cap K, \tag{3.24}$$

where

$$\delta = \min_{\substack{\boldsymbol{v}_R \in R_V \cap K, \\ \|\boldsymbol{v}_R\|_V = 1}} -\langle f, \boldsymbol{v}_R \rangle_V.$$

Inequality (3.24) is used to prove that the solutions to the continuous and discrete problems are bounded from above in Theorems 3.1 and 3.2 below, respectively. It is also used in the proof of Lemma 3.5 to obtain error estimates for the rigid component of the velocity error.

The importance of the compatibility condition (3.23) is well-known in the study of semicoercive variational inequalities, see [56, 96, 68] in the context of general variational inequalities and [90, 17] in a glaciological setting. The compatibility condition has the geometrical interpretation that the applied force f should have an obtuse angle with the directions of escape of the body given by $R_V \cap K$, which in this case correspond with vertical upward movements whenever Γ_a is flat.

Theorem 3.1. *If $R_V = \{0\}$, then a solution to (3.16) exists and is unique. If $R_V \neq \{0\}$, then there is a unique solution to (3.16) provided the compatibility condition (3.23) holds. Conversely, if $R_V \neq \{0\}$ and a solution exists, we have that*

$$\langle f, \boldsymbol{v}_R \rangle_V \leq 0 \quad \forall \boldsymbol{v}_R \in R_V \cap K. \tag{3.25}$$

Moreover, a solution $(\boldsymbol{u}, p, \lambda) \in V \times Q \times \Lambda$ *of* (3.16) *is bounded from above, i.e.*

$$\|\boldsymbol{u}\|_V + \|p\|_Q + \|\lambda\|_{\Sigma'} \lesssim 1, \tag{3.26}$$

if (3.23) *holds when* $R_V \neq \{0\}$.

Proof. All of the statements of this theorem but (3.26) follow from Theorem A.1 in Appendix A. With Lemma 3.4, we have that all of the assumptions stated in Appendix A hold for our case. Based on our definition of R_V above, it is straightforward to see that $R_V^* = 0$, and therefore if inequality (3.23) holds, so does (A.5). As a result, a minimiser to $\mathcal{J}$ exists, and therefore a solution to the mixed problem (3.16). As stated in Theorem A.1, if $\boldsymbol{u}$ minimises $\mathcal{J}$, any other solution will be of the form $\boldsymbol{u} + \boldsymbol{v}_R$, with $\boldsymbol{v}_R \in R_V$ and $\langle f, \boldsymbol{v}_R \rangle_V = 0$. However, if (3.23) holds, it is clear that $\langle f, \boldsymbol{v}_R \rangle_V = 0$ implies $\boldsymbol{v}_R = 0$ because $\dim R_V \leq 1$.

To prove (3.26), we first note that (3.16a) and (3.21) lead to

$$\|\mathbb{Q}\boldsymbol{u}\|_V^r \lesssim \langle A\boldsymbol{u} + G\boldsymbol{u}, \boldsymbol{u} \rangle_V = \langle f, \boldsymbol{u} \rangle_V. \tag{3.27}$$

If $R_V = \{0\}$, we have that $\|\boldsymbol{u}\|_V^{r-1} \lesssim \|f\|_{V'}$. If $R_V \neq \{0\}$ and (3.23) holds, then $\langle f, \mathbb{P}\boldsymbol{u} \rangle_V \leq 0$ and we find that $\|\mathbb{Q}\boldsymbol{u}\|_V^{r-1} \lesssim \|f\|_{V'}$. By using the inf-sup conditions (3.11) and (3.18) and Hölder's inequality, we can establish the bound

$$\|\lambda\|_{\Sigma'} + \|p\|_Q \lesssim \|\mathbb{Q}\boldsymbol{u}\|_V^{r-1} + \|f\|_{V'}. \tag{3.28}$$

The above inequality and (3.27) allow us to bound the norms of λ and p from above:

$$\|\lambda\|_{\Sigma'} + \|p\|_Q \lesssim \|f\|_{V'}. \tag{3.29}$$

We then use (3.24) to show that

$$\|\mathbb{P}\boldsymbol{u}\|_V \lesssim -\langle f, \mathbb{P}\boldsymbol{u} \rangle_V = \langle \lambda, \gamma_n(\mathbb{Q}\boldsymbol{u}) \rangle_\Sigma \lesssim \|f\|_{V'}^{r'}. \tag{3.30}$$

We finally establish the bound (3.26) by putting together (3.27), (3.29), and (3.30), and noting that $\|\boldsymbol{u}\|_V \leq \|\mathbb{P}\boldsymbol{u}\|_V + \|\mathbb{Q}\boldsymbol{u}\|_V$. □

Remark 3.2. Although a rigorous proof for the existence and uniqueness of solutions to Variational inequalities A and B would require a careful investigation on the equivalence of formulations and a derivation of a Korn-type inequality as in Lemma 3.4, we can nevertheless explore the validity of the conditions of Theorem A.1 by examining the space of rigid modes for these variational inequalities. For Variational inequality A, the space of rigid modes in V is given by vertical motions, i.e.

$$R_{V,A} = \left\{ \boldsymbol{v}_R = \begin{pmatrix} 0 \\ a \end{pmatrix} : a \in \mathbb{R} \right\}. \tag{3.31}$$

Horizontal motions are not contained in V due to the Dirichlet boundary condition (1.23). As a result, $\dim R_{V,A} = 1$ and, as in Theorem 3.1, we have a unique solution if and only if $\langle f, \boldsymbol{v}_R \rangle_V < 0$ for all $\boldsymbol{v}_R \in (R_{V,A} \cap K) \setminus \{0\}$, which implies that $p_i - p_w > 0$ is a necessary and sufficient condition for the existence and uniqueness of solutions.

The situation is more complicated for Variational inequality B, because in this case horizontal motions are contained in V and we have that

$$R_{V,B} = \left\{ \boldsymbol{v}_R = \begin{pmatrix} a \\ b \end{pmatrix} : (a, b) \in \mathbb{R}^2 \right\}. \tag{3.32}$$

By noting that $\boldsymbol{n}$ is proportional to $(\partial\theta/\partial x, -1)^\top$ along the lower boundary, we can see how the well-posedness of Variational inequality B depends on the geometry of the attached region Γ_a. If Γ_a is flat and $\partial\theta/\partial x = 0$ on it, then $R^*_{V,B}$ contains the horizontal vector fields and conditions (A.5) cannot be verified unless $\tau_b = 0$; as a result, the problem has no solution if we enforce $\tau_b > 0$. For the more realistic case when Γ_a is not flat, one has that $R^*_{V,B} = \{0\}$. In this case, a careful investigation on when conditions (A.5) hold depends strongly on the geometry of Γ_a. For all cases, we still need $p_i - p_w > 0$ to hold, since vertical modes are present in $R_{V,B}$.

3.2 Abstract discretisation of the variational inequality

In this section we propose an abstract discretisation of the mixed system (3.16) built in terms of a collection of finite dimensional spaces satisfying certain key properties. We can then introduce a discrete system analogous to (3.16) and investigate the conditions under which we have a unique solution. Then, we prove Lemmas 3.5, 3.6, and 3.7, which establish upper bounds for the errors of the discrete solutions.

3.2.1 The discrete mixed formulation

For each parameter $h > 0$, let $V_h \subset V$, $Q_h \subset Q$, and $\Sigma^a_h \subset L^2(\Gamma_a)$ be finite dimensional subspaces. We also assume that $R_V \subset V_h$ to avoid the need of introducing discrete compatibility conditions. We define the discrete convex sets

$$\Lambda_h = \{\mu_h \in \Sigma^a_h : \mu_h \leq 0 \text{ on } \Gamma_a\},$$

and

$$K_h = \{\boldsymbol{v}_h \in V_h : \langle \mu_h, \gamma_n \boldsymbol{v}_h \rangle_\Sigma \geq 0 \quad \forall \mu_h \in \Lambda_h\}.$$

An immediate consequence of the definitions of Λ_h and K_h is that $\Lambda_h \subset \Lambda$ but $K_h \not\subset K$ unless $\gamma_n(V_h) \subset \Sigma^a_h$. By the assumption $R_V \subset V_h$ and the fact that R_V is given by purely vertical translations whenever $R_V \neq \{0\}$, we have that $K \cap R_V = K_h \cap R_V$.

Remark 3.3. In Section 2.2 of the previous chapter, we introduced a general discretisation of the Stokes variational inequality based on the discrete normal trace operator γ_h^a and the discrete space Σ_h^a. In this section, we also consider a general discrete space Σ_h^a in which the Lagrange multiplier is sought; however, instead of working with the operator γ_h^a, we hold on to the continuous normal trace operator γ_n and work with its projection onto Σ_h^a, as is clear from the definition of K_h above. Hence, one could also write that the associated operator γ_h^a, in the notation of Section 2.2, is given by the projection

$$\langle \mu_h, \gamma_h^a \boldsymbol{v}_h \rangle_\Sigma = \langle \mu_h, \gamma_n \boldsymbol{v}_h \rangle_\Sigma$$

for all $\mu_h \in \Sigma_h^a$ and all $\boldsymbol{v}_h \in V_h$. In this sense, the abstract discretisation considered in this section is less general than the one presented in Section 2.2; however, the class of discretisations considered here makes the analysis simple while maintaining a relatively high level of generality.

The discrete analogue of the variational inequality (3.3) is: find $(\boldsymbol{u}_h, p_h) \in K_h \times Q_h$ such that

$$\langle A\boldsymbol{u}_h + G\boldsymbol{u}_h - Bp_h - f, \boldsymbol{v}_h - \boldsymbol{u}_h \rangle_V + \langle Bq_h, \boldsymbol{u}_h \rangle_V \geq 0 \quad \forall (\boldsymbol{v}_h, q_h) \in K_h \times Q_h. \tag{3.33}$$

This discrete variational inequality can be written as a mixed problem by introducing a Lagrange multiplier. This results in the discrete mixed formulation that is the counterpart of (3.16): find $(\boldsymbol{u}_h, p_h, \lambda_h) \in V_h \times Q_h \times \Lambda_h$ such that

$$\langle A\boldsymbol{u}_h + G\boldsymbol{u}_h - Bp_h - f, \boldsymbol{v}_h \rangle_V - \langle \lambda_h, \gamma_n \boldsymbol{v}_h \rangle_\Sigma = 0 \qquad \forall \boldsymbol{v}_h \in V_h, \tag{3.34a}$$

$$\langle Bq_h, \boldsymbol{u}_h \rangle_V = 0 \qquad \forall q_h \in Q_h, \tag{3.34b}$$

$$\langle \mu_h - \lambda_h, \gamma_n \boldsymbol{u}_h \rangle_\Sigma \geq 0 \qquad \forall \mu_h \in \Lambda_h. \tag{3.34c}$$

An advantage of using a mixed formulation at the discrete level is that we explicitly enforce a discrete version of the contact conditions (3.2g). Just as in (3.17), it is possible to show that the conditions $\lambda_h \in \Lambda_h$ and (3.34c) are equivalent to

$$\langle \mu_h, \gamma_n \boldsymbol{u}_h \rangle_\Sigma \geq 0 \quad \forall \mu_h \in \Lambda_h, \quad \lambda_h \in \Lambda_h, \quad \text{and} \quad \langle \lambda_h, \gamma_n \boldsymbol{u}_h \rangle_\Sigma = 0. \tag{3.35}$$

In order to state a minimisation problem equivalent to (3.34), we must introduce the subspace of V_h of discretely divergence-free functions and the discrete convex set $\mathring{K}_h$:

$$\mathring{V}_h = \{\boldsymbol{v}_h \in V_h : \langle Bq_h, \boldsymbol{v}_h \rangle_V = 0 \quad \forall q_h \in Q_h\} \quad \text{and} \quad \mathring{K}_h = \mathring{V}_h \cap K_h.$$

Then, the discrete mixed problem (3.34) is equivalent to the minimisation over $\mathring{K}_h$ of the functional $\mathcal{J} : V \to \mathbb{R}$ defined in (3.8), provided that two discrete inf-sup conditions hold. For $V_{a,h} = V_h \cap V_a$, these discrete conditions can be stated as

$$\sup_{\boldsymbol{v}_h \in V_{a,h}} \frac{\langle Bq_h, \boldsymbol{v}_h \rangle_V}{\|\boldsymbol{v}_h\|_V} \gtrsim \|q_h\|_Q \quad \forall q_h \in Q_h, \tag{3.36}$$

$$\sup_{\boldsymbol{v}_h \in V_h} \frac{\langle \mu_h, \gamma_n \boldsymbol{v}_h \rangle_\Sigma}{\|\boldsymbol{v}_h\|_V} \gtrsim \|\mu_h\|_\Sigma \quad \forall \mu_h \in \Sigma_h^a. \tag{3.37}$$

When the conditions (3.36) and (3.37) hold, then (3.33), (3.34), and the minimisation of $\mathcal{J}$ over $\mathring{K}$ are equivalent problems. The proofs for such equivalences require the same arguments as the proofs presented in Section 3.1. If $\mathcal{J}$ admits a unique minimiser over $\mathring{K}_h$, the discrete inf-sup conditions guarantee a unique solution for (3.34) and set constraints on the choice of spaces V_h, Q_h, and Σ_h^a used when approximating solutions of (3.16). As in the continuous case, the well-posedness of (3.34) requires the compatibility condition (3.23) to hold. The theorem below can be proved in the same way as Theorem 3.1.

Theorem 3.2. *Assume that the discrete inf-sup conditions* (3.36) *and* (3.37) *hold. If* $R_V = \{0\}$*, then a solution to* (3.34) *exists and is unique. If* $R_V \neq \{0\}$*, then there is a unique solution to* (3.34) *if the compatibility condition* (3.23) *holds. Conversely, if* $R_V \neq \{0\}$ *and a solution exists,* (3.25) *must hold. The solution of* (3.16) *is bounded from above independently of* h*, provided* (3.23) *holds when* $R_V \neq \{0\}$*.*

3.2.2 Upper bounds for the velocity error

An important tool presented in [7, 55] for establishing error estimates for non-Newtonian flows is the use of the function $\mathbf{F}$. Here, for ease of notation, we denote by $\mathbf{F}$ an operator that acts on both $\mathbb{R}^{2\times 2}$ and $\mathbb{R}^2$ by

$$\mathbf{F}(\mathrm{A}) = |\mathrm{A}|^{\frac{r-2}{2}}\mathrm{A} \quad \text{for } \mathrm{A} \in \mathbb{R}^{2\times 2} \text{ or } \mathrm{A} \in \mathbb{R}^2. \tag{3.38}$$

This operator is closely related to the operators A and G. Let the operator $\mathrm{E} : V \times V \to \mathbb{R}$ be given by

$$\mathrm{E}(\boldsymbol{u}, \boldsymbol{v}) = \|\mathbf{F}(\mathbf{D}\boldsymbol{u}) - \mathbf{F}(\mathbf{D}\boldsymbol{v})\|^2_{L^2(\Omega)} + \|\mathbf{F}(\mathbf{T}\boldsymbol{u}) - \mathbf{F}(\mathbf{T}\boldsymbol{v})\|^2_{L^2(\Gamma_a)}.$$

We then have that

$$\mathrm{E}(\boldsymbol{u}, \boldsymbol{v}) \sim \langle A\boldsymbol{u} - A\boldsymbol{v}, \boldsymbol{u} - \boldsymbol{v} \rangle_V + \langle G\boldsymbol{u} - G\boldsymbol{v}, \boldsymbol{u} - \boldsymbol{v} \rangle_V \tag{3.39}$$

for all $\boldsymbol{u}, \boldsymbol{v} \in V$. The following variation of Young's inequality,

$$\langle A\boldsymbol{u} - A\boldsymbol{v}, \boldsymbol{u} - \boldsymbol{w} \rangle_V + \langle G\boldsymbol{u} - G\boldsymbol{v}, \boldsymbol{u} - \boldsymbol{w} \rangle_V \leq \varepsilon \mathrm{E}(\boldsymbol{u}, \boldsymbol{v}) + c_\varepsilon \mathrm{E}(\boldsymbol{u}, \boldsymbol{w}), \tag{3.40}$$

is valid for any $\boldsymbol{u}, \boldsymbol{v}, \boldsymbol{w} \in V$ and $\varepsilon > 0$, with the constant $c_\varepsilon > 0$ depending on ε. Additionally, the inequalities

$$\|\mathbf{D}\boldsymbol{v} - \mathbf{D}\boldsymbol{w}\|^2_{L^r(\Omega)} \lesssim \|\mathbf{F}(\mathbf{D}\boldsymbol{v}) - \mathbf{F}(\mathbf{D}\boldsymbol{w})\|^2_{L^2(\Omega)} \, \||\mathbf{D}\boldsymbol{v}| + |\mathbf{D}\boldsymbol{w}|\|^{2-r}_{L^r(\Omega)}, \tag{3.41}$$

$$\|\mathbf{T}\boldsymbol{v} - \mathbf{T}\boldsymbol{w}\|^2_{L^r(\Gamma_a)} \lesssim \|\mathbf{F}(\mathbf{T}\boldsymbol{v}) - \mathbf{F}(\mathbf{T}\boldsymbol{w})\|^2_{L^2(\Gamma_a)} \, \||\mathbf{T}\boldsymbol{v}| + |\mathbf{T}\boldsymbol{w}|\|^{2-r}_{L^r(\Gamma_a)}, \tag{3.42}$$

hold for any $\boldsymbol{v}, \boldsymbol{w} \in \boldsymbol{W}^{1,r}(\Omega)$. A proof for inequalities (3.39) and (3.41) can be found in [55, Lemmas 2.3, 2.4], and [7, Lemma 2.7] for (3.40), for the case without friction. The presence of the operator G requires a version of [55, Lemmas 2.3, 2.4] and [7, Lemma 2.7] stated in terms of vectors in $\mathbb{R}^d$. Since these results are based on algebraic inequalities for matrices, the extension to vectors in $\mathbb{R}^d$ can be proved by considering diagonal matrices.

By applying the triangle inequality, (3.21), and (3.41)-(3.42), the velocity error can be decomposed into two components as

$$\|\boldsymbol{u} - \boldsymbol{u}_h\|_V \lesssim \|\mathbb{P}(\boldsymbol{u} - \boldsymbol{u}_h)\|_V + \mathrm{E}(\boldsymbol{u}, \boldsymbol{u}_h). \tag{3.43}$$

For the first term on the right of (3.43), which represents the rigid component of the error, we present the following result:

Lemma 3.5. *Assume that $R_V \neq \{0\}$ and that the compatibility condition (3.23) holds. Let $(\boldsymbol{u}, p, \lambda) \in V \times Q \times \Lambda$ be the solution to (3.16) and $(\boldsymbol{u}_h, p_h, \lambda_h) \in V_h \times Q_h \times \Lambda_h$ to (3.34). Then,*

$$\|\mathbb{P}(\boldsymbol{u} - \boldsymbol{u}_h)\|_V \lesssim \mathrm{E}(\boldsymbol{u}, \boldsymbol{u}_h) + \|\lambda - \mu_h\|_{\Sigma'} \quad \forall\, \mu_h \in \Lambda_h. \tag{3.44}$$

Proof. Under the assumption that $R_V \neq \{0\}$, we either have that $\mathbb{P}(\boldsymbol{u} - \boldsymbol{u}_h) \in R_V \cap K$ or $-\mathbb{P}(\boldsymbol{u} - \boldsymbol{u}_h) \in R_V \cap K$. If $\mathbb{P}(\boldsymbol{u} - \boldsymbol{u}_h) \in R_V \cap K$, then inequality (3.24) and the continuous mixed system (3.16) allow us to write

$$\|\mathbb{P}(\boldsymbol{u} - \boldsymbol{u}_h)\|_V \lesssim -\langle f, \mathbb{P}(\boldsymbol{u} - \boldsymbol{u}_h)\rangle_V = \langle \lambda, \gamma_n(\mathbb{P}(\boldsymbol{u} - \boldsymbol{u}_h))\rangle_\Sigma,$$

where the equality follows from $\langle A\boldsymbol{u} + G\boldsymbol{u} - Bp, \mathbb{P}(\boldsymbol{u} - \boldsymbol{u}_h)\rangle_V = 0$. Then, by noting that $\mathbb{P}(\boldsymbol{u} - \boldsymbol{u}_h) = -\mathbb{Q}(\boldsymbol{u} - \boldsymbol{u}_h) + \boldsymbol{u} - \boldsymbol{u}_h$ and $\langle \lambda, \gamma_n \boldsymbol{u}\rangle_\Sigma = 0$, using inequalities (3.21) and (3.41)-(3.42), and using the uniform in h boundedness of solutions to (3.34) (see Theorem 3.2), we arrive at

$$\|\mathbb{P}(\boldsymbol{u} - \boldsymbol{u}_h)\|_V \lesssim \mathrm{E}(\boldsymbol{u}, \boldsymbol{u}_h) - \langle \lambda, \gamma_n \boldsymbol{u}_h\rangle_\Sigma. \tag{3.45}$$

On the other hand, if $-\mathbb{P}(\boldsymbol{u} - \boldsymbol{u}_h) \in R_V \cap K$, then, by appealing to (3.23) and the discrete mixed system (3.34),

$$\|\mathbb{P}(\boldsymbol{u} - \boldsymbol{u}_h)\|_V \lesssim \langle f, \mathbb{P}(\boldsymbol{u} - \boldsymbol{u}_h)\rangle_V = -\langle \lambda_h, \gamma_n(\mathbb{P}(\boldsymbol{u} - \boldsymbol{u}_h))\rangle_\Sigma.$$

Following the same steps as before, we deduce that

$$\|\mathbb{P}(\boldsymbol{u}-\boldsymbol{u}_h)\|_V \lesssim \mathrm{E}(\boldsymbol{u},\boldsymbol{u}_h) - \langle \lambda_h, \gamma_n \boldsymbol{u}\rangle_\Sigma \leq \mathrm{E}(\boldsymbol{u},\boldsymbol{u}_h), \tag{3.46}$$

where the final inequality follows from the fact that $\lambda_h \leq 0$ on Γ_a by the definition of Λ_h. As a result of (3.45) and (3.46), we have that

$$\|\mathbb{P}(\boldsymbol{u}-\boldsymbol{u}_h)\|_V \lesssim \mathrm{E}(\boldsymbol{u},\boldsymbol{u}_h) + \max\{0, -\langle \lambda, \gamma_n \boldsymbol{u}_h\rangle_\Sigma\}$$

in all cases. Finally, given a $\mu_h \in \Lambda_h$, we have

$$-\langle \lambda, \gamma_n \boldsymbol{u}_h\rangle_\Sigma \leq \langle \mu_h - \lambda, \gamma_n \boldsymbol{u}_h\rangle \lesssim \|\lambda - \mu_h\|_{\Sigma'}$$

because $\langle \mu_h, \gamma_n \boldsymbol{u}_h\rangle_\Sigma \geq 0$. □

Remark 3.4. As mentioned at the start of this chapter, previous analyses of finite element approximations of semicoercive variational inequalities either only consider the error in a seminorm [56] or use indirect arguments to prove the convergence of the approximate solution in the complete norm [103, 47, 96, 2, 16]. In these cases, arguments by contradiction involving a sequence of triangulations are used. In Lemma 3.5, on the other hand, we provide a fully constructive proof for bounding the rigid component of the velocity error from above. This result is a key ingredient in obtaining the error estimates for the finite element scheme presented in the next section. The proof of Lemma 3.5 relies on $\dim R_V \leq 1$, which holds for almost all Stokes variational inequalities considered in glaciology [24, 79, 28, 97, 19], except for Variational inequality B under certain conditions.

The second term on the right of (3.43) can be bounded from above by using the properties of the operator E.

Lemma 3.6. *Let the triples* $(\boldsymbol{u}, p, \lambda) \in V \times Q \times \Lambda$ *and* $(\boldsymbol{u}_h, p_h, \lambda_h) \in V_h \times Q_h \times \Lambda_h$ *be solutions to* (3.16) *and* (3.34)*, respectively. Then*

$$\mathrm{E}(\boldsymbol{u},\boldsymbol{u}_h) \lesssim \mathrm{E}(\boldsymbol{u},\boldsymbol{v}_h) + \|p-q_h\|_Q^2 + \langle \lambda - \lambda_h, \gamma_n(\boldsymbol{v}_h - \boldsymbol{u}_h)\rangle_\Sigma \tag{3.47}$$

holds for all $(\boldsymbol{v}_h, q_h) \in \mathring{V}_h \times Q_h$.

Proof. From (3.16a) and (3.34a), we see that, for any $(\boldsymbol{v}_h, q_h) \in \mathring{V}_h \times Q_h$, we have

$$\begin{aligned}
\langle A\boldsymbol{u} - A\boldsymbol{u}_h, \boldsymbol{u}-\boldsymbol{u}_h\rangle_V + \langle G\boldsymbol{u} - G\boldsymbol{u}_h, \boldsymbol{u}-\boldsymbol{u}_h\rangle_V = \\
\langle A\boldsymbol{u} - A\boldsymbol{u}_h, \boldsymbol{u}-\boldsymbol{v}_h\rangle_V + \langle G\boldsymbol{u} - G\boldsymbol{u}_h, \boldsymbol{u}-\boldsymbol{v}_h\rangle_V \\
+\langle B(p-q_h), \boldsymbol{v}_h - \boldsymbol{u}_h\rangle_V + \langle \lambda - \lambda_h, \gamma_n(\boldsymbol{v}_h - \boldsymbol{u}_h)\rangle_\Sigma
\end{aligned}$$

Using (3.39) and (3.40)

$$\begin{aligned}\mathrm{E}(\boldsymbol{u},\boldsymbol{u}_h) \lesssim\ & \varepsilon_1 \mathrm{E}(\boldsymbol{u},\boldsymbol{u}_h) + c_{\varepsilon_1}\mathrm{E}(\boldsymbol{v},\boldsymbol{v}_h) \\ & + \langle B(p-q_h), \boldsymbol{v}_h - \boldsymbol{u}_h\rangle_V + \langle \lambda - \lambda_h, \gamma_n(\boldsymbol{v}_h - \boldsymbol{u}_h)\rangle_\Sigma\end{aligned}$$

for an arbitrary $\varepsilon_1 > 0$. Additionally, by using Young's inequality,

$$\langle B(p-q_h), \boldsymbol{v}_h - \boldsymbol{u}_h\rangle_V \lesssim c_{\varepsilon_2} \|p-q_h\|_Q^2 + \varepsilon_2 \|\mathbf{D}(\boldsymbol{u}_h - \boldsymbol{v}_h)\|_{L^r(\Omega)}^2$$

for any $\varepsilon_2 > 0$. Then, via (3.41), and by setting ε_1 and ε_2 sufficiently small, inequality (3.47) is established. □

Remark 3.5. If the pair $V_h \times Q_h$ is divergence free in the sense that $\langle Bq_h, \boldsymbol{w}_h\rangle_V = 0$ for all $q_h \in Q_h$ implies that $\nabla \cdot \boldsymbol{w}_h = 0$, then the term $\|p-q_h\|_Q^2$ in inequality (3.47) can be removed.

3.2.3 Upper bounds for the pressure and Lagrange multiplier errors

We finalise the analysis of the abstract discretisation by bounding the errors for the pressure and the Lagrange multiplier from above.

Lemma 3.7. *Assume that the discrete inf-sup conditions* (3.36) *and* (3.37) *hold. Let* $(\boldsymbol{u}, p, \lambda) \in V \times Q \times \Lambda$ *be the solution of* (3.16) *and* $(\boldsymbol{u}_h, p_h, \lambda_h) \in V_h \times Q_h \times \Lambda_h$ *of* (3.34). *Then*

$$\|p - p_h\|_Q \lesssim \mathrm{E}(\boldsymbol{u},\boldsymbol{u}_h)^{1/r'} + \|p - q_h\|_Q\,, \tag{3.48}$$

$$\|\lambda - \lambda_h\|_{\Sigma'} \lesssim \mathrm{E}(\boldsymbol{u},\boldsymbol{u}_h)^{1/r'} + \|p - q_h\|_Q + \|\lambda - \mu_h\|_{\Sigma'}\,, \tag{3.49}$$

for all $q_h \in Q_h$ *and* $\mu_h \in \Sigma_h^a$.

Proof. Since Q_h and Σ_h^a are subsets of Q and Σ respectively, we can obtain the following equality from (3.16a) and (3.34a):

$$\begin{aligned}\langle A\boldsymbol{u} - A\boldsymbol{u}_h, \boldsymbol{v}_h\rangle_V + \langle G\boldsymbol{u} - G\boldsymbol{u}_h, \boldsymbol{v}_h\rangle_V = \\ \langle B(p-p_h), \boldsymbol{v}_h\rangle_V + \langle \lambda - \lambda_h, \gamma_n \boldsymbol{v}_h\rangle_\Sigma \quad \forall \boldsymbol{v}_h \in V_h.\end{aligned} \tag{3.50}$$

The inf-sup condition (3.36) for the pressure space holds over the space $V_{a,h} \subset V_h$ of vector fields with a normal component vanishing on Γ_a. For $\boldsymbol{v}_h \in V_{a,h}$, from equation (3.50) we derive

$$\langle B(p_h - q_h), \boldsymbol{v}_h\rangle_V = \langle A\boldsymbol{u} - A\boldsymbol{u}_h, \boldsymbol{v}_h\rangle_V + \langle G\boldsymbol{u} - G\boldsymbol{u}_h, \boldsymbol{v}_h\rangle_V + \langle B(p-q_h), \boldsymbol{v}_h\rangle_V.$$

From the inf-sup condition (3.36) it follows that

$$\|p_h - q_h\|_Q \lesssim \sup_{\boldsymbol{v}_h \in V_{a,h}} \left(\frac{\langle A\boldsymbol{u} - A\boldsymbol{u}_h, \boldsymbol{v}_h\rangle_V + \langle G\boldsymbol{u} - G\boldsymbol{u}_h, \boldsymbol{v}_h\rangle_V}{\|\boldsymbol{v}_h\|_V} \right) + \|p - q_h\|_Q\,. \tag{3.51}$$

By Hölder's inequality and [55, Lemma 2.4], we have that

$$\sup_{\boldsymbol{v}_h \in V_{a,h}} \left(\frac{\langle A\boldsymbol{u} - A\boldsymbol{u}_h, \boldsymbol{v}_h \rangle_V}{\|\boldsymbol{v}_h\|_V} \right) \lesssim \|\mathbf{F}(\mathbf{D}\boldsymbol{u}) - \mathbf{F}(\mathbf{D}\boldsymbol{u}_h)\|_{L^2(\Omega)}^{2/r'} . \tag{3.52}$$

For the friction term, following the argument used in [55, Lemma 2.4], we can show that

$$\big\| |\mathbf{T}\boldsymbol{u}|^{r-2}\mathbf{T}\boldsymbol{u} - |\mathbf{T}\boldsymbol{u}_h|^{r-2}\mathbf{T}\boldsymbol{u}_h \big\|_{L^2(\Gamma_a)} \lesssim \|\mathbf{F}(\mathbf{T}\boldsymbol{u}) - \mathbf{F}(\mathbf{T}\boldsymbol{u}_h)\|_{L^2(\Gamma_a)}^{2/r'}$$

and therefore

$$\sup_{\boldsymbol{v}_h \in V_h} \left(\frac{\langle G\boldsymbol{u} - G\boldsymbol{u}_h, \boldsymbol{v}_h \rangle_V}{\|\boldsymbol{v}_h\|_V} \right) \lesssim \|\mathbf{F}(\mathbf{T}\boldsymbol{u}) - \mathbf{F}(\mathbf{T}\boldsymbol{u}_h)\|_{L^2(\Gamma_a)}^{2/r'} .$$

Finally, (3.48) follows by applying the triangle inequality to $\|p - p_h\|_Q$ and using (3.51) and (3.52). The bound (3.49) follows in the same way. □

Lemmas 3.5, 3.6, and 3.7 give discretisation error estimates in terms of best approximation results. To derive a convergence result, we require bounds on these best approximations. We discuss this in the context of a finite element discretisation in the next section.

3.3 Analysis of a finite element scheme with P2P0 elements

We conclude this chapter with an application of the results from Section 3.2 for the analysis of a concrete finite element discretisation of the mixed problem (3.16). We built the discrete system in terms of a non-degenerate sequence of triangulations of the domain (non-degenerate in the sense of [11, Definition 4.4.13]). We use the notation introduced in Section 1.2: for an $h > 0$, the triangulation of Ω is denoted by $\mathcal{T}_h$ and its set of edges by $\mathcal{E}(\mathcal{T}_h)$, with $\mathcal{E}(\mathcal{T}_h, \Gamma_s)$ and $\mathcal{E}(\mathcal{T}_h, \Gamma_a)$ denoting the edges contained in $\overline{\Gamma}_s$ and $\overline{\Gamma}_a$, respectively. Here, $h > 0$ denotes the maximum cell diameter in $\mathcal{T}_h$, and we assume that every edge $e \in \mathcal{E}(\mathcal{T}_h)$ in $\partial\Omega$ is either in $\overline{\Gamma}_s$, $\overline{\Gamma}_a$ or $\overline{\Gamma}_i$. Associated to each $\mathcal{T}_h$ are the finite element spaces V_h, Q_h, and Σ_h^a, defined by

$$V_h = \{\boldsymbol{v}_h \in \boldsymbol{\mathcal{C}}(\Omega) : \boldsymbol{v}_h|_c \in \boldsymbol{\mathcal{P}}_2(c) \quad \forall c \in \mathcal{T}_h, \quad \boldsymbol{v}_h \cdot \boldsymbol{n} = 0 \quad \text{on } \Gamma_i\} , \tag{3.53a}$$

$$Q_h = \{q_h \in L^2(\Omega) : q_h|_c \in \mathcal{P}_0(c) \quad \forall c \in \mathcal{T}_h\} , \tag{3.53b}$$

$$\Sigma_h^a = \{\mu_h \in L^2(\Gamma_a) : \mu_h|_e \in \mathcal{P}_0(e) \quad \forall e \in \mathcal{E}(\mathcal{T}_h, \Gamma_a)\} . \tag{3.53c}$$

This discretisation of the variational inequality uses the P2P0 element for the velocity-pressure pair. As a result, it no longer falls within the class of methods from Section 2.2 because the pressure space Q_h consists of piecewise constant functions, as opposed to the piecewise linear continuous functions used in the Taylor-Hood pair. As we explain in Remark 3.7 below, using a piecewise constant pressure simplifies the analysis greatly, and its extension to piecewise linear continuous functions remains an open question.

3.3.1 Convergence of the finite element approximation

In this section, we use the abstract framework presented in Section 3.2 to prove the convergence of a finite element approximation computed with the spaces (3.53) as the size of the mesh tends to zero. The proofs we present make use of the technical constructions relegated to Appendix B.

The first step in establishing the convergence of this discretisation is to investigate whether the discrete mixed problem (3.34) is well-posed for this choice of $V_h \times Q_h \times \Sigma_h^a$, subject to the compatibility condition (3.23). Specifically, we must verify the discrete inf-sup conditions (3.36) and (3.37). The pair $V_h \times Q_h$ is well-known to satisfy (3.36), see [10, Proposition 8.4.3] for the case of $r = 2$; the general case $r \in [1, \infty]$ follows from the same arguments by using the interpolation operator π_V discussed in Appendix B.2. A proof for (3.37) is presented below using a similar argument to the one presented in [18, Proposition 3.3].

Lemma 3.8. *The finite element pair V_h and Σ_h^a defined in (3.53) is inf-sup stable in the sense of (3.37).*

Proof. Let $\mu_h \in \Sigma_h^a$. By the Hahn-Banach theorem, there is a $\psi \in \Sigma$ such that $\langle \mu_h, \psi \rangle_\Sigma = \|\mu_h\|_{\Sigma'}$ and $\|\psi\|_\Sigma = 1$. The extension operator $\Phi : \Sigma \to V_h$ from Appendix B.3 is bounded uniformly with respect to h and satisfies

$$\langle \mu_h, \gamma_n(\Phi\psi) \rangle_\Sigma = \langle \mu_h, \psi \rangle_\Sigma \quad \forall \mu_h \in \Sigma_h^a,$$

for all $\psi \in \Sigma$. Then

$$\|\mu_h\|_{\Sigma'} = \frac{\langle \mu_h, \psi \rangle_\Sigma}{\|\psi\|_\Sigma} \lesssim \frac{\langle \mu_h, \gamma_n(\Phi\psi) \rangle_\Sigma}{\|\Phi\psi\|_V} \leq \sup_{\boldsymbol{v}_h \in V_h} \frac{\langle \mu_h, \gamma_n \boldsymbol{v}_h \rangle_\Sigma}{\|\boldsymbol{v}_h\|_V}$$

and the result follows. □

We end this section with a discussion on the approximability of the mixed system (3.16). We show that the approximate solutions $(\boldsymbol{u}_h, p_h, \lambda_h)$ converge to the exact solutions of (3.16) as $h \to 0$ under a regularity condition, and we establish a rate of convergence for these approximations.

Theorem 3.3. *Assume that the compatibility condition (3.23) holds whenever $R_V \neq \{0\}$. Let the triple $(\boldsymbol{u}, p, \lambda) \in V \times Q \times \Lambda$ be the solution to (3.16) and $(\boldsymbol{u}_h, p_h, \lambda_h) \in V_h \times Q_h \times \Lambda_h$ to (3.34). Additionally, assume that $(\boldsymbol{u}, p, \lambda) \in W^{2,r}(\Omega) \times W^{1,r'}(\Omega) \times W^{1-1/r',r'}(\Gamma_a)$ and $\mathbf{F}(\mathbf{D}\boldsymbol{u}) \in \boldsymbol{W}^{1,2}(\Omega)$ and $\mathbf{F}(\mathbf{T}\boldsymbol{u}) \in \boldsymbol{W}^{1,2}(\Gamma_a)$. Then*

$$\|\boldsymbol{u} - \boldsymbol{u}_h\|_V \lesssim h, \tag{3.54a}$$

$$\|p - p_h\|_Q + \|\lambda - \lambda_h\|_{\Sigma'} \lesssim h^{2/r'} + h. \tag{3.54b}$$

Proof. We proceed by first finding a suitable upper bound for the term involving the Lagrange multiplier in (3.47). Since $\langle \lambda_h, \gamma_n \boldsymbol{u}_h \rangle_\Sigma = 0$ and $\langle \mu_h, \gamma_n \boldsymbol{v}_h \rangle_\Sigma \geq 0$ for all $(\boldsymbol{v}_h, \mu_h) \in K_h \times \Lambda_h$, one can show that

$$\begin{aligned} \langle \lambda - \lambda_h, \gamma_n(\boldsymbol{v}_h - \boldsymbol{u}_h) \rangle_\Sigma \leq \langle \lambda - \mu_h, \gamma_n(\boldsymbol{v}_h - \boldsymbol{u}) \rangle_\Sigma \\ + \langle \lambda - \mu_h, \gamma_n(\boldsymbol{u} - \boldsymbol{u}_h) \rangle_\Sigma + \langle \mu_h, \gamma_n \boldsymbol{v}_h \rangle_\Sigma \end{aligned} \tag{3.55}$$

for all $(\boldsymbol{v}_h, \mu_h) \in K_h \times \Lambda_h$. By applying Young's inequality in (3.55) and using inequalities (3.43), (3.44), and (3.47), we arrive at

$$\|\boldsymbol{u} - \boldsymbol{u}_h\|_V \lesssim \mathrm{E}(\boldsymbol{u}, \boldsymbol{v}_h)^{1/2} + \|p - q_h\|_Q + \|\lambda - \mu_h\|_{\Sigma'} + \langle \mu_h, \gamma_n \boldsymbol{v}_h \rangle_\Sigma \tag{3.56}$$

for all $(\boldsymbol{v}_h, q_h, \mu_h) \in \mathring{K}_h \times Q_h \times \Lambda_h$.

Let $\pi_V : V \to V_h$ be the interpolation operator introduced in Appendix B.2. Additionally, let $\pi_Q : Q \to Q_h$ and $\pi_\Sigma : L^2(\Gamma_a) \to \Sigma_h^a$ be standard interpolation operators onto the space of piecewise constant functions. We refer to [26] and the results in Appendix B.1 for proofs of optimal interpolation error estimates in the Q and Σ' norms. From the properties of these interpolation operators it follows that $\pi_V \boldsymbol{u} \in \mathring{K}_h$ and $\pi_\Sigma \lambda \in \Lambda_h$. Additionally, we have that $\int_e \boldsymbol{u} \cdot \boldsymbol{n} \, \mathrm{d}s = \int_e (\pi_V \boldsymbol{u}) \cdot \boldsymbol{n} \, \mathrm{d}s$ for all $e \in \mathcal{E}(\mathcal{T}_h)$, so

$$\langle \pi_\Sigma \lambda, \gamma_n \pi_V \boldsymbol{u} \rangle_\Sigma = \langle \lambda, \pi_\Sigma(\gamma_n \boldsymbol{u}) \rangle_\Sigma = \langle \lambda, \pi_\Sigma(\gamma_n \boldsymbol{u}) - \gamma_n \boldsymbol{u} \rangle_\Sigma.$$

Since $\langle \pi_\Sigma \lambda, \pi_\Sigma(\gamma_n \boldsymbol{u}) - \gamma_n \boldsymbol{u} \rangle_\Sigma = 0$, we have that

$$\langle \pi_\Sigma \lambda, \gamma_n \pi_V \boldsymbol{u} \rangle_\Sigma = \langle \lambda - \pi_\Sigma \lambda, \pi_\Sigma(\gamma_n \boldsymbol{u}) - \gamma_n \boldsymbol{u} \rangle_\Sigma. \tag{3.57}$$

Therefore, by setting $\boldsymbol{v}_h = \pi_V \boldsymbol{u}$, $q_h = \pi_Q p$, and $\mu_h = \pi_\Sigma \lambda$ in (3.56) and using (3.57), we can show that

$$\|\boldsymbol{u} - \boldsymbol{u}_h\|_V \lesssim \mathrm{E}(\boldsymbol{u}, \pi_V \boldsymbol{u})^{1/2} + \|p - \pi_Q p\|_Q + \|\lambda - \pi_\Sigma \lambda\|_{\Sigma'} + \|\gamma_n \boldsymbol{u} - \pi_\Sigma(\gamma_n \boldsymbol{u})\|_\Sigma . \tag{3.58}$$

We then establish (3.54a) with the approximation properties of the interpolation operators presented in the Appendices B.1 and B.2 for π_Σ and π_V respectively, and [26] for π_Q. The estimate (3.54b) then follows from Lemma 3.7. □

Remark 3.6. The velocity and pressure error estimates coincide with those obtained in [7, Theorem 2.14] and in [55, Theorem 3.1] for the r-Stokes system without contact or friction boundary conditions. This indicates that these boundary conditions and the Lagrange multiplier do not reduce the order of convergence. This may be due to the use of piecewise constant elements for Σ_h^a. In [18], a proof with non-optimal convergence rates is presented for the case when continuous piecewise quadratic polynomials are used for the Lagrange multiplier.

Remark 3.7. A convergence result analogous to Theorem 3.3 for the velocity-pressure pair given by Taylor-Hood elements would require a different approach because the projection operator $\pi_V : V \to V_h$ does not guarantee the preservation of the discrete divergence, stated in Appendix B.2 in (B.5), when Q_h is the set of continuous piecewise linear functions. Therefore, $\pi_V \boldsymbol{u}_h$ no longer belongs to $\mathring{K}_h$ and we cannot follow the steps taken in the proof of Theorem 3.3.

3.3.2 Discrete algebraic formulation

We now present an algebraic counterpart of (3.34) using the finite element spaces specified in (3.53) in terms of matrices and vectors. Let $V_h = \operatorname{span}\{\boldsymbol{v}_i\}_{i=1}^{N_v}$, $Q_h = \operatorname{span}\{q_j\}_{j=1}^{N_q}$, and $\Sigma_h^a = \operatorname{span}\{\mu_k\}_{k=1}^{N_\mu}$, where $N_v = \dim V_h$, $N_q = \dim Q_h$, and $N_\mu = \dim \Sigma_h^a$. For the functions $(\boldsymbol{u}_h, p_h, \lambda_h) \in V_h \times Q_h \times \Sigma_h^a$, we write $\mathbf{u}$, $\mathbf{p}$ and $\boldsymbol{\lambda}$ for the vectors containing the respective degrees of freedom (DoFs) in $\mathbb{R}^{N_v}$, $\mathbb{R}^{N_q}$ and $\mathbb{R}^{N_\mu}$. In order to write an algebraic counterpart of (3.34c), we need to introduce the discrete normal trace operator

$$\boldsymbol{\gamma_n} : \mathbb{R}^{N_v} \to \mathbb{R}^{N_\mu}$$

that returns the average normal components of a vector $\boldsymbol{v}_h \in V_h$ along the edges on Γ_a. That is, for each $i \in \{1, 2, ..., N_\mu\}$

$$(\boldsymbol{\gamma_n} \mathbf{v})_i = \frac{1}{|e_i|} \int_{e_i} \boldsymbol{v}_h \cdot \boldsymbol{n} \, \mathrm{d}s,$$

where $e_i \in \mathcal{E}(\mathcal{T}_h, \Gamma_a)$ is the unique edge along Γ_a associated to the degree of freedom in Σ_h^a with index i. Then, the algebraic counterpart of (3.34) can be written in terms of matrices and vectors as

$$\mathbf{A}_\varepsilon(\mathbf{u}) + \mathbf{G}_\varepsilon(\mathbf{u}) - \mathbf{B}\mathbf{p} - \mathbf{D}\boldsymbol{\lambda} = \mathbf{f}, \tag{3.59a}$$

$$\mathbf{B}^\top \mathbf{u} = 0, \tag{3.59b}$$

$$\boldsymbol{\lambda} + \mathbf{C}(\boldsymbol{\lambda}, \mathbf{u}) = 0. \tag{3.59c}$$

Here, we have introduced the matrices $\mathbf{B} \in \mathbb{R}^{N_v \times N_q}$ and $\mathbf{D} \in \mathbb{R}^{N_v \times N_\mu}$, the vector $\mathbf{f} \in \mathbb{R}^{N_v}$, and the nonlinear operators $\mathbf{A}_\varepsilon : \mathbb{R}^{N_v} \to \mathbb{R}^{N_v}$, $\mathbf{G}_\varepsilon : \mathbb{R}^{N_v} \to \mathbb{R}^{N_v}$, and $\mathbf{C} : \mathbb{R}^{N_\mu} \times \mathbb{R}^{N_v} \to \mathbb{R}^{N_\mu}$. The matrices are given by the elements $\mathbf{B}_{ij} = \langle B q_j, \boldsymbol{v}_i \rangle_V$ and $\mathbf{D}_{ij} = \langle \mu_j, \gamma_n \boldsymbol{v}_i \rangle_\Sigma$ and the vector by $\mathbf{f}_i = \langle f, \boldsymbol{v}_i \rangle_V$. The nonlinear operators are defined as

$$[\mathbf{A}_\varepsilon(\mathbf{u})]_i = \int_\Omega \alpha \left(\varepsilon + |\mathbf{D}\boldsymbol{u}_h|^2\right)^{\frac{r-2}{2}} (\mathbf{D}\boldsymbol{u}_h : \mathbf{D}\boldsymbol{v}_i) \, \mathrm{d}x, \tag{3.60}$$

$$[\mathbf{G}_\varepsilon(\mathbf{u})]_i = \int_\Omega C \left(\varepsilon + |\mathbf{T}\boldsymbol{u}_h|^2\right)^{\frac{r-2}{2}} (\mathbf{T}\boldsymbol{u}_h \cdot \mathbf{T}\boldsymbol{v}_i) \, \mathrm{d}x, \tag{3.61}$$

$$\mathbf{C}(\boldsymbol{\lambda}, \mathbf{u}) = \max\{0, -\boldsymbol{\lambda} + c(\boldsymbol{\gamma_n} \mathbf{u})\}. \tag{3.62}$$

Here, $\varepsilon > 0$ is the regularisation term in (1.19) and (1.45). In (3.62), the max operation is understood to be carried out componentwise on each of the elements in the vector $-\boldsymbol{\lambda} + c(\boldsymbol{\gamma_n}\mathbf{u}) \in \mathbb{R}^{N_\mu}$. The non-negative constant $c > 0$ is a numerical parameter that can help us avoid numerical issues whenever the magnitudes of the terms in $\boldsymbol{\lambda}$ differ from those in $\boldsymbol{\gamma_n}\mathbf{u}$ by several orders of magnitude. The value of c can be chosen arbitrarily in the sense that, in the ideal case where no rounding errors are present, it does not affect the outcome of $\mathbf{C}$.

The use of the operator $\mathbf{C}$ in (3.62) is a common way of expressing contact conditions. A particular advantage is that the nonlinear system (3.59) can be solved with a semi-smooth Newton method that enjoys superlinear convergence in a neighbourhood of the solution [54]. Equation (3.59c) is equivalent to (3.34c) whenever Σ_h^a is defined as in (3.53c). By solving (3.59c) we enforce

$$\boldsymbol{\gamma_n}\mathbf{u} \leq 0, \quad \boldsymbol{\lambda} \leq 0, \quad \text{and} \quad (\boldsymbol{\gamma_n}\mathbf{u}) \cdot \boldsymbol{\lambda} = 0, \tag{3.63}$$

exactly, which is the algebraic equivalent of the discrete contact conditions (3.35).

3.3.3 A numerical test

We present numerical results computed for a Stokes variational inequality with a manufactured solution on the domain $\Omega = (0,1)^2$ to have an empirical demonstration of the validity of the convergence rates estimated in Theorem 3.3. The manufactured solution considered here is taken from [7] and is given by

$$\hat{\boldsymbol{u}}(\boldsymbol{x}) = |\boldsymbol{x}|^{\alpha_p - 1}(x_2, -x_1)^\top, \quad \hat{p}(\boldsymbol{x}) = |\boldsymbol{x}|^\gamma, \tag{3.64}$$

where the parameters α_p and γ are chosen such that $\boldsymbol{u} \in \boldsymbol{W}^{2,r}(\Omega)$, $p \in W^{1,r'}(\Omega)$, $\mathbf{F}(\mathbf{D}\boldsymbol{u}) \in \boldsymbol{W}^{1,2}(\Omega)$ and $\mathbf{F}(\mathbf{T}\boldsymbol{u}) \in \boldsymbol{W}^{1,2}(\Gamma_a)$ hold. This is ensured whenever $\alpha_p > 1$ and $\gamma > -1 + \frac{2}{r}$, so we set $\alpha_p = 1.01$ and $\gamma = -1 + \frac{2}{r} + 0.01$ in order to be critically close to the regularity assumed in Theorem 3.3.

Contact boundary conditions are enforced on the lower boundary $\{y = 0\}$. Given the velocity and pressure fields defined in (3.64), we have that

$$(\hat{\boldsymbol{u}} \cdot \boldsymbol{n})(x_1) = -x_1^{\alpha_p}, \quad \hat{\lambda}(x_1) = -x_1^\gamma,$$

on $\{y = 0\}$. In order to define the contact boundary conditions in such a way that both the kinematic and dynamic conditions are active, we define the "obstacles"

$$\chi(x_1) = \begin{cases} (\hat{\boldsymbol{u}} \cdot \boldsymbol{n})(x_1) & \text{if } x_1 \leq 0.5 \\ -2^{-\alpha_p} & \text{if } x_1 > 0.5 \end{cases}, \quad \rho(x_1) = \begin{cases} 0 & \text{if } x_1 \leq 0.5 \\ \hat{\lambda}(x_1) & \text{if } x_1 > 0.5 \end{cases}.$$

Then, for this numerical test we solve the Stokes system (3.2a)-(3.2b) together with the boundary conditions

$$\boldsymbol{u}\cdot\boldsymbol{n}\leq\chi,\quad \lambda\leq\rho,\quad \text{and}\quad (\boldsymbol{u}\cdot\boldsymbol{n}-\chi)(\lambda-\rho)=0\quad \text{on } \{y=0\}, \tag{3.65a}$$

$$\boldsymbol{u}\cdot\boldsymbol{n}=\hat{\boldsymbol{u}}\cdot\boldsymbol{n}\quad \text{on } \{x=0\}, \tag{3.65b}$$

$$\sigma_{nn}=\hat{\sigma}_{nn}\quad \text{on } \partial\Omega\setminus(\{y=0\}\cup\{x=0\}), \tag{3.65c}$$

$$\boldsymbol{\sigma}_{nt}=\hat{\boldsymbol{\sigma}}_{nt}\quad \text{on } \partial\Omega, \tag{3.65d}$$

where $\hat{\boldsymbol{\sigma}}=\boldsymbol{\sigma}(\hat{\boldsymbol{u}},\hat{p})$. Boundary conditions are set for the normal velocity along $\{x=0\}$ in (3.65b) to mimic the boundary conditions enforced at Γ_i and make $\dim R_V=1$. In this case, R_V is a one-dimensional vector space containing vertical motions. Therefore,

$$R_V\cap K=\{(0,\theta):\theta\leq\min\chi\},$$

and, since $f=A_\varepsilon\hat{\boldsymbol{u}}+G_\varepsilon\hat{\boldsymbol{u}}-B\hat{p}-\gamma_n'\hat{\lambda}$, we have that

$$\langle f,\boldsymbol{v}_R\rangle_V=\theta\int_0^1 x^\gamma\,\mathrm{d}x<0$$

for all $\boldsymbol{v}_R=(0,\theta)$ with $\theta<0$ (note that $\min\chi<0$). This proves that the compatibility condition (3.23) holds and the system is well-posed. Although the functional setting of this numerical test differs slightly from the setting studied in this chapter, the numerical test contains the fundamental elements of the setting analysed.

We compute solutions to the r-Stokes system on $\Omega=(0,1)^2$ with boundary conditions (3.65) on a sequence of uniformly refined meshes using the finite element spaces in (3.53). The regularisation parameter in (3.60) is set to $\varepsilon=10^{-4}$. In Glen's law (1.3) we fix $\mathcal{A}=0.5$ and for the friction boundary condition we set $C=1$. We consider the values $n=1$, 2, 3, and 4, which correspond with $r=2$, 1.5, 1.33, and 1.25. The resulting orders of convergence for the velocity are shown in Tables 3.1 and 3.2, and for the pressure and Lagrange multiplier in Table 3.3. For the Lagrange multiplier error, we use the discrete norm

$$\|\mu_h\|_{\Sigma',h}=h^{1/r'}\|\mu_h\|_{L^{r'}(\Gamma_a)},$$

which should yield the same order of convergence as the one that would be obtained with the Σ' norm by a standard inverse inequality.

Table 3.1 indicates that the orders of convergence for the velocity in the seminorm $\|\mathbf{D}(\cdot)\|_{L^r(\Omega)}$ and in the V-norm coincide. This demonstrates that the presence of rigid modes in the velocity space does not affect the accuracy of the velocity computation in the V-norm. The computed orders of convergence for the velocity in the V-norm coincide with those estimated in (3.54a). In Table 3.2 we see that the orders of convergence for

Table 3.1: Calculated orders of convergence for the velocity computed with a manufactured solution together with estimated orders according to Theorem 3.3.

	$\|\mathbf{D}(\boldsymbol{u}) - \mathbf{D}(\boldsymbol{u}_h)\|_{L^r(\Omega)}$				$\|\boldsymbol{u} - \boldsymbol{u}_h\|_V$			
$h\backslash r$	2.00	1.50	1.33	1.25	2.00	1.50	1.33	1.25
3.54×10^{-1}	-	-	-	-	-	-	-	-
1.77×10^{-1}	0.96	1.05	1.08	1.11	0.97	1.10	1.14	1.18
8.84×10^{-2}	0.97	1.03	1.05	1.07	0.98	1.06	1.09	1.12
4.42×10^{-2}	0.97	1.02	1.04	1.06	0.98	1.04	1.06	1.08
2.21×10^{-2}	0.97	1.02	1.03	1.04	0.98	1.03	1.04	1.06
1.10×10^{-2}	0.97	1.01	1.02	1.03	0.98	1.02	1.03	1.04
1	1.00	1.00	1.00	1.00	1.00	1.00	1.00	1.00

Table 3.2: Calculated orders of convergence for the velocity in the $L^r(\Omega)$-norm computed with a manufactured solution.

	$\|\boldsymbol{u} - \boldsymbol{u}_h\|_{L^r(\Omega)}$			
$h\backslash r$	2.00	1.50	1.33	1.25
3.54×10^{-1}	-	-	-	-
1.77×10^{-1}	1.97	2.07	1.99	1.85
8.84×10^{-2}	1.95	1.95	1.87	1.72
4.42×10^{-2}	1.96	1.96	1.86	1.71
2.21×10^{-2}	1.96	1.97	1.87	1.72
1.10×10^{-2}	1.96	1.98	1.87	1.74

Table 3.3: Calculated orders of convergence for the pressure and the Lagrange multiplier computed with a manufactured solution together with estimated orders according to Theorem 3.3.

	$\|p - p_h\|_Q$				$\|\lambda - \lambda_h\|_{\Sigma',h}$			
$h\backslash r$	2.00	1.50	1.33	1.25	2.00	1.50	1.33	1.25
3.54×10^{-1}	-	-	-	-	-	-	-	-
1.77×10^{-1}	0.88	0.93	0.96	0.98	1.00	1.00	1.00	0.98
8.84×10^{-2}	0.90	0.94	0.97	0.98	1.00	1.00	0.98	0.93
4.42×10^{-2}	0.91	0.95	0.97	0.95	1.01	1.00	0.96	0.87
2.21×10^{-2}	0.92	0.95	0.97	0.90	1.01	1.00	0.93	0.80
1.10×10^{-2}	0.93	0.96	0.96	0.84	1.01	1.00	0.88	0.73
$2/r'$	1.00	0.67	0.5	0.4	1.00	0.67	0.5	0.4

the velocity in the $L^r(\Omega)$-norm appear to increase by one when compared to the orders computed with the V-norm. On the other hand, the orders of convergence obtained for the pressure appear to be independent of r. A closely related problem (without contact boundary conditions) is solved in the work of Belenki et al. [7]. In the work of Belenki et al., the problem is formulated as an r-Stokes problem with Dirichlet boundary conditions and the MINI element is used for the velocity and pressure. Interestingly, their numerical results deliver the predicted orders of convergence for the pressure error. Hence, the apparent suboptimality of (3.54b) for the pressure could be due to the finite elements used here or to the presence of contact boundary conditions and a Lagrange multiplier. Regarding the Lagrange multiplier, the estimated orders of convergence are exceeded, but a dependence on r is observed.

3.4 Discussion

This chapter provides a theoretical analysis of Variational inequality C and its discretisation with the finite element method. We focus on this variational inequality for the sake of concreteness and simplicity, and indicate in Remark 3.2 how some of the analytical results would extend to Variational inequalities A and B. We prove in Theorem 3.1 the well-posedness of Variational inequality C whenever the subspace of rigid modes in the velocity space is of dimension at most one under the condition that a compatibility condition holds. In Section 2.2.1, we present a family of finite element discretisations of this variational inequality, closely related to those considered in Section 2.2.1. We then prove an analogous well-posedness result for the discrete system in Theorem 3.2 and, using techniques from [7, 55], establish upper bounds for the approximation errors. Then, in Section 3.3, we choose a concrete finite element approximation based on the P2P0 elements for the velocity-pressure pair. The analysis is completed by showing that this approximation converges to the continuous solution under some regularity requirements in Theorem 3.3. We conclude the section by presenting the discrete algebraic set of nonlinear equations that this finite element scheme results in and showing some numerical results that validate our convergence estimates.

This study intends to establish a theoretical justification for the discrete variational inequality we consider in the main numerical scheme for viscous contact problems used in this work and introduced in Section 2.3. An obvious issue is that, although our discrete variational inequality in its mixed form belongs to the class of approximations from Section 3.2, it does not coincide with the discrete problem in Section 3.3. Therefore, future work should establish a complete analysis as in Section 3.3 for a discretisation that uses the Taylor-Hood pair for the velocity and pressure as in Section 2.3. As we explain in

Remark 3.7, the analysis with the Taylor-Hood pair is complicated because, to the best of our knowledge, no projection operator $\pi_V : V \to V_h$ that satisfies $\pi_V(\mathring{K}) \subset \mathring{K}_h$ has been proposed in the literature. Therefore, the construction of such an operator should be considered to complete the analysis.

A major assumption of this paper is that the domain is two-dimensional. An extension of the analysis presented here to three dimensions would require a careful consideration of the rigid modes present in the velocity space, since the space of rigid modes in three dimensions is larger than in two dimensions. In most problems of interest, three dimensional marine ice sheets are considered to be enclosed within two lateral walls, see for example [28]. In this case, if the lateral walls and the bedrock are flat, the space of rigid modes in V is once again reduced to vertical movements and is therefore one-dimensional. As a consequence, much of the analysis from this paper would still be valid in three dimensions. However, the extension operator presented in Appendix B.3, used to prove Lemma 3.8, relies heavily on the fact that the domain is two-dimensional. Therefore, the choice of finite elements used to solve the variational inequality would have to be chosen and studied carefully.

Chapter 4

Subglacial cavitation and glacial sliding

Subglacial cavitation is the first of the two viscous contact problems described in Chapter 1. It occurs along a thin boundary layer in between the ice and the bedrock and involves the detachment of ice in the lee side of obstacles due to high water pressures. Subglacial cavities are important for large-scale glacial dynamics because they play an important role in how ice sheets slide over a bedrock. This chapter contains a numerical exploration on subglacial cavitation and its effect on glacial sliding using the numerical tools developed in Chapter 2. The content in Sections 4.3 and 4.4 has been published in [19].

We start this chapter with a literature review on glacial sliding, with an emphasis on sliding with cavitation. This content makes clear in what way subglacial cavitation is a fundamental mechanism in glacial sliding. Then, in Section 4.2, we formulate our mathematical model for subglacial cavitation and explore some basic properties of this system. This section includes much of the content from Section 1.6, but we reformulate the system in a non-dimensional manner in this chapter. In Section 4.3, we compute the steady friction law for ice flowing over a sinusoidal bed for linear and nonlinear rheologies, expanding on the results in [36]. Furthermore, in this section we compare our results with those obtained from the linearised theory to validate the algorithm. Finally, in Section 4.4, we explore the effects of unsteady water pressures on glacial sliding by calculating the basal sliding velocities and cavity shapes under oscillating water pressures.

4.1 Past research on glacial sliding with cavitation

When modelling the large scale evolution of an ice sheet or a glacier over a bedrock, the Stokes equations must be solved together with an adequate set of boundary conditions, as we explain in Chapter 1. At the ice-bedrock interface, a nonlinear relationship known as a friction law is usually used that relates the basal shear stress τ_b to the basal sliding speed u_b.

Field measurements provide evidence that basal sliding can account for a large proportion of a glacier's motion [66]. In addition, sliding is a fundamental mechanism in determining the stability of marine ice sheets [101, 15]. Consequently, the accuracy of any computation of ice motion largely depends on the accuracy of the friction law used and on its capability to capture the fundamental mechanisms that regulate basal sliding. The difficulty in observing such phenomena has prompted a large amount of theoretical, computational, and empirical research.

Historically, a first attempt at constructing a realistic friction law over hard beds was carried out by Weertman [104], who considered relegation and viscous deformation along obstacles in the bed as the major contributions to sliding. Relegation refers to the phenomenon of ice melting at high pressure in the upstream faces of obstacles and the subsequent transportation downstream and re-freezing. The resulting friction law is a power law of the form

$$\tau_b = C u_b^m, \quad C, m > 0. \tag{4.1}$$

A friction law of this form allows for an unbounded increase in basal stress with the sliding velocity. We remark that this is the friction law we use when modelling marine ice sheets in this work, with $m = 1/n$, see Section 1.7 and Chapter 5.

A decade after Weertman's proposal, Lliboutry identified subglacial cavitation, where the ice sheet detaches from the bedrock in the lee of an obstacle, as a fundamental mechanism involved in sliding [70]. When cavitation occurs, Lliboutry predicted that the basal stress would decrease with the sliding velocity. Under cavitation, the water pressure of subglacial water p_w and the overburden ice pressure p_i become important; in particular, Lliboutry's friction law took the effective pressure $N = p_i - p_w$ into account.

A theory for sliding in the presence of cavitation was developed by Fowler [31], using ideas from Nye [77] and Kamb [65]. This theory presents a solution to a simplified local boundary layer problem of ice flowing over a periodic bed. By allowing the formation of one cavity per period, a complex Hilbert problem is formulated which allows the determination of the basal shear stress. Below, in Section 4.3, we include calculations carried out with this method to validate our numerical results; moreover, Appendix C provides a short description of this analytical method.

Such a theory was revised and extended by Schoof [87], whose method allows for an arbitrary number of cavities to occur over a bedrock with a more general shape. Schoof confirmed the existence of a maximum for the basal stress τ_b when ice slides over smooth obstacles of small amplitude. This bound on the basal stress depends on the slope of the obstacle and on the effective pressure N; it was predicted by Iken [59] and Schoof calls it

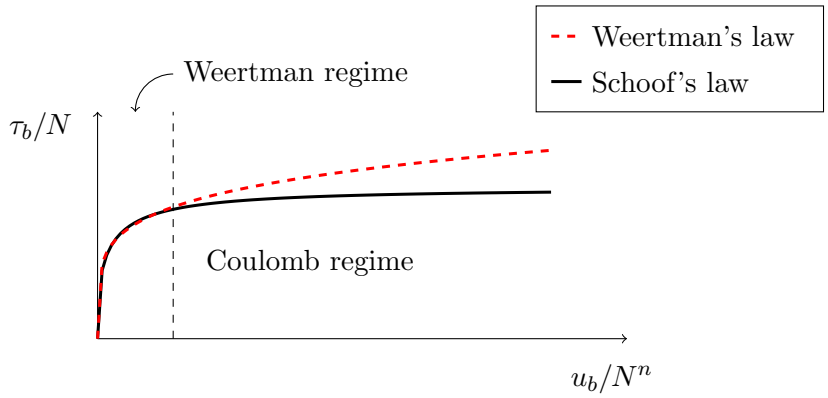

Figure 4.1: The friction laws proposed by Weertman [104] and by Schoof [87], see equations (4.1) and (4.3) respectively. The two different regimes (Weertman and Coulomb) in Schoof's law are indicated.

Iken's bound. In Lemma 4.2, we include a proof of this bound which essentially follows Schoof's approach in [87]. Both Fowler and Schoof built their theories on the assumption of a linear rheology.

In reality, the bedrock of a glacier is unknown and we can expect it to contain obstacles of multiple sizes and amplitudes. Therefore, it is unclear how a realistic friction law can be constructed based on the theories of Fowler and Schoof. In particular, a major source of uncertainty is whether Iken's bound holds for arbitrary beds. According to Fowler [32], such a maximum should not be reached in reality because larger obstacles will always exist that are capable of providing drag. This reasoning is used to justify an unbounded increase in basal stress with velocity, suggesting that the friction law takes the form of a Weertman style law which incorporates the effects of N:

$$\tau_b = C u_b^m N^n, \quad C, m > 0, \tag{4.2}$$

where n is the parameter in Glen's law, see (1.3). However, according to Schoof, Iken's bound is dependent on the slope of obstacles, not on their size. Hence, a law of type (4.2) would only be valid if the larger obstacles also have increasingly pronounced slopes. In [87], Schoof proposes

$$\frac{\tau_b}{N} = C \left(\frac{u_b}{u_b + N^n \Lambda_0} \right)^{1/n}, \quad C, \Lambda_0 > 0 \tag{4.3}$$

as a friction law. A law as in (4.3) is essentially a regularised Coulomb law. This point motivates the idea of two existing sliding regimes: a Weertman regime for high values of N and a Coulomb regime for lower N [101, 73], see Figure 4.1. Coulomb style laws have also been shown to be appropriate for sliding over soft deformable beds composed of sediments,

see [102]. This implies that a friction law as in (4.3) would unify the treatment of hard and soft beds.

Introducing the effective pressure as an additional variable in the friction law inherently leads to a coupling between glacial dynamics and the subglacial hydrology system. In fact, under certain circumstances, the hydrology system is treated as a spatially distributed network of connected subglacial cavities [51, 94, 30, 40]. A relationship between subglacial hydrology and glacial dynamics has also been suggested by field measurements on mountain glaciers and the Greenland ice sheet, where a clear correlation between water pressure and surface velocity has been observed [60, 98, 4, 57]. These studies are the main motivation behind our investigation of unsteady glacial sliding in Section 4.4.

Regarding empirical results on glacial sliding, one can consider two different approaches to verifying glacial friction laws. The first approach consists in carrying out small scale experiments that reproduce the boundary layer problem in the ice-bedrock interface. In this manner, Zoet and Iverson have confirmed many aspects of Schoof and Iken's results in sinusoidal [107] and stepped beds [108]. The second approach measures the ability of a friction law to enable large-scale models to fit large scale measurements of surface ice speed. For example, in [63], different friction laws are used to predict the evolution of Pine Island Glacier. According to the authors, a regularised Coulomb law yields the most precise results.

The theories considered above use many simplifying assumptions in order to obtain models that can be solved analytically or with simple numerical solvers. One must assume that the problem is stationary, the bedrock is smooth with small obstacles, the rheology is given by a linear law, and the effective pressure is constant. This leaves many unanswered questions; for example, the effect that periodic variations in time in the subglacial hydrology can have on the friction law have not been studied, even though there is evidence of diurnal changes in the water pressure in the base of glaciars [60]. Problems such as this one could be approached with numerical methods. As mentioned in the Chapter 1, very few numerical tests involving the full Stokes equations with cavitation have been carried out. The existing results essentially amount to those in [36, 50, 49]. The numerical results in this chapter are therefore a further contribution to the numerical investigation of glacial sliding with cavitation.

4.2 Non-dimensional formulation of the problem

We now proceed to write down the equations for the subglacial cavity problem. These are presented in Chapter 1, and they consist of the Stokes equations (1.8) formulated on the time-dependent periodic domain $\Omega(t)$, which is defined in terms of a cavity roof θ, together

with the contact boundary conditions (1.11). The domain Ω represents a thin boundary layer in between the ice and the bedrock, see Figure 1.1. The lower boundary Γ_b is the cavity roof and the upper boundary Γ_t is a fictitious boundary, required for computational purposes, between the boundary layer and the remainder of the ice sheet.

We repeat the set of equations for modelling the formation of subglacial cavities here for the reader's convenience, although in a non-dimensional form. Given a length scale $[x]$ and a velocity scale $[u]$, we define the additional scales

$$[\sigma] = \left(\frac{[u]}{2\mathcal{A}[x]}\right)^{1/n} \quad \text{and} \quad [t] = \frac{[x]}{[u]}, \tag{4.4}$$

which represent the characteristic scales for stress and time. The length scale is set equal to the length of the cavity, $[x] = L$. In this chapter, when computing steady cavity states, we enforce a horizontal velocity boundary condition $u = u_t$ at the top boundary Γ_t; therefore, we take this to be the characteristic velocity, such that $[u] = u_t$. For the unsteady computations in Section 4.4, where we do not prescribe this boundary condition, this scaling is inherited from the steady state which we perturb.

From this point until the end of the chapter, all variables considered are non-dimensional. To avoid an excessively tedious notation, we refer to these non-dimensional variables with the same notation as their dimensional counterparts. For a non-dimensional time $T > 0$, the solution of our problem is given by a velocity $u : \Omega \times [0, T] \to \mathbb{R}^2$, a pressure $p : \Omega \times [0, T] \to \mathbb{R}$ and a cavity roof $\theta : [0, 1] \times [0, T] \to \mathbb{R}$. Here, the domain Ω depends on time and is defined in terms of θ as

$$\Omega(t) = \left\{(x, z) \in \mathbb{R}^2 : 0 < x < 1, \quad \text{and} \quad \theta(x, t) < z < 1\right\}. \tag{4.5}$$

We denote the lower boundary of $\Omega(t)$ by $\Gamma_b(t)$ and we introduce $\Gamma_a(t)$ and $\Gamma_d(t)$, the subsets of Γ_b where the cavity roof $\theta(x, t)$ is attached or detached from the bedrock b, that is,

$$\Gamma_a(t) = \left\{(x, z) \in \mathbb{R}^2 : 0 < x < 1, \quad z = \theta(x, t) \quad \text{and} \quad b = \theta(x, t)\right\}, \tag{4.6a}$$

$$\Gamma_d(t) = \left\{(x, z) \in \mathbb{R}^2 : 0 < x < 1, \quad z = \theta(x, t) \quad \text{and} \quad b < \theta(x, t)\right\}. \tag{4.6b}$$

As explained in Section 1.6, in this work we only consider sinusoidal beds of nondimensional amplitude r_b given by

$$b(x) = r_b \left(\cos\left(2\pi x\right) - 1\right) \quad \text{for } x \in [0, 1].$$

At each time step $t \in [0, T]$ and for a given domain $\Omega = \Omega(t)$, the velocity and pressure are the solutions of the Stokes equations equipped with the following set of boundary

conditions:

$$-\nabla \cdot \left(\alpha |\mathbf{D}\boldsymbol{u}|^{\frac{1-n}{n}} \mathbf{D}\boldsymbol{u}\right) + \nabla p = 0 \qquad \text{in } \Omega, \tag{4.7a}$$

$$\nabla \cdot \boldsymbol{u} = 0 \qquad \text{in } \Omega. \tag{4.7b}$$

$$\sigma_{nn} = -p_i \qquad \text{on } \Gamma_t, \tag{4.7c}$$

$$\boldsymbol{\sigma}_{nt} = 0 \qquad \text{on } \Gamma_b, \tag{4.7d}$$

$$\sigma_{nn} = -p_w \qquad \text{on } \Gamma_d, \tag{4.7e}$$

$$\boldsymbol{u} \cdot \boldsymbol{n} \leq 0, \quad \sigma_{nn} \leq -p_w \quad \text{and} \quad (\boldsymbol{u} \cdot \boldsymbol{n})(\sigma_{nn} + p_w) = 0 \qquad \text{on } \Gamma_a. \tag{4.7f}$$

Since the domain Ω is assumed to be periodic in the horizontal direction, we apply periodic boundary conditions at $x = 0$ and $x = 1$. In (4.7), the term $\alpha = 2^{(1+n)/(2n)}$ arises due to our choice of scaling. In (4.7a), we neglect gravity, whose effect we encode in the overburden ice pressure p_i in (4.7c); we assume $p_i > 0$ to be spatially uniform along the upper boundary. We also assume the water pressure $p_w \geq 0$ to be spatially uniform along the length of the bedrock because gravity is unimportant on the spatial scales under consideration. The contact boundary conditions are given by (4.7e), and these realise the possibility of ice detaching from the bedrock. The system of equations (4.7) requires one final boundary condition in the tangential direction along Γ_t. In this section, we consider either the Dirichlet boundary condition

$$u = 1 \quad \text{on } \Gamma_t, \tag{4.8}$$

or the Neumann boundary condition

$$\boldsymbol{\sigma}_{nt} = \tau_b \, (1, 0)^\top \quad \text{on } \Gamma_t, \tag{4.9}$$

where τ_b is the basal shear stress. These boundary conditions lead to a different variational inequality which the Stokes system is equivalent to, see Variational inequalities A and B in Section 1.6.

Finally, by writing the components of the velocity field as $\boldsymbol{u} = (u, w)$, we close the system with the free boundary equation

$$\frac{\partial \theta}{\partial t} + u \frac{\partial \theta}{\partial x} - w = 0 \quad \text{on } [0, 1] \times [0, T] \tag{4.10}$$

together with the inequalities

$$b \leq \theta \quad \text{and} \quad \theta < 1 \quad \text{on } [0, 1] \times [0, T], \tag{4.11}$$

and an initial condition

$$\theta(x, 0) = \theta_0(x) \quad x \in [0, L]. \tag{4.12}$$

From the non-dimensional system formulated above, it is easily deduced that a stationary solution given by the triple $(\boldsymbol{u}, p, \theta)$ depends only on the rheological parameter n, the amplitude of the bedrock r_b, the overburden p_i and the water pressure p_w. However, as we mention below in Section 4.2.2, the pair $(\boldsymbol{u}, \theta)$ in fact only depends on n, r_b, and the effective pressure $p_i - p_w$. If we enforce (4.9) instead of (4.8), one could point out that τ_b is then another parameter; however, we can remove this dependence by choosing a velocity scale in terms of τ_b.

4.2.1 Computation of the basal shear stress and the sliding speed

As made clear in the literature review in Section 4.1, subglacial cavitation is considered a fundamental mechanism in glacial sliding, which is concerned with the relationship between basal shear stress τ_b and sliding speed u_b. In the context of the subglacial configuration we presented above, we define these two values by

$$\tau_b = -\int_{\Gamma_b} (\sigma_{nn} + p_w)\, n_x \, \mathrm{d}s \quad \text{and} \quad u_b = \int_{\Gamma_b} u \, \mathrm{d}s, \tag{4.13}$$

where n_x is the horizontal components of the outwards-pointing normal vector $\boldsymbol{n} = (n_x, n_y)$. The basal shear stress can also be written in terms of the Lagrange multiplier λ, which we introduce in Sections 2.2.1 and 3.1.3, as

$$\tau_b = -\int_{\Gamma_b} \lambda n_x \, \mathrm{d}s, \tag{4.14}$$

since we have $\lambda = \sigma_{nn} + p_w$ at the continuous level. The numerical algorithm we use to carry out the computations in this chapter also solves for the Lagrange multiplier λ, as specified in Section 2.3. Therefore, in our numerical computations, we compute τ_b with (4.14).

The formula for u_b presented in (4.13) might seem strange if the subglacial cavity domain is interpreted as a boundary layer between an ice sheet and the bedrock. This would suggest we take the sliding speed to be the average value of the horizontal velocity along the top boundary Γ_t. However, our computations indicate that, if the height of the domain H is sufficiently large, we can expect the shear stress to approach a constant value and the horizontal velocity u to vary with z^n as z approaches H. That is, we observe that u/z^n is equal to a positive constant far away from the lower boundary. Therefore, the horizontal velocity along the top boundary depends strongly on the height of the domain. For this reason, and following [36], we use (4.13) to calculate u_b. In this case, we find that u_b is independent of H for sufficiently large values of H. In particular, throughout this paper we set $H = 1$, which is equal to the non-dimensional length of the cavity. In agreement with [36], we find this value of H to be sufficiently large.

4.2.2 Some properties of the solution

We now present some important properties of the solution $(\boldsymbol{u}, p, \theta)$ to the subglacial cavity system that can be deduced from the model. We first introduce a new variable, the effective pressure N, which we define as

$$N = p_i - p_w. \tag{4.15}$$

Since p_w is assumed to be spatially uniform, the velocity solution $\boldsymbol{u}$ to the Stokes equations (4.7) depends only on the effective pressure N, rather than on the separate values we choose for p_i and p_w. We can see this by substituting the pressure p in (4.7) by $p - p_w$. An important consequence of this is that the cavity geometry θ, the basal shear stress τ_b, and the sliding velocity u_b depend only on N. For this reason, our study of glacial sliding included in the next sections only considers the effective pressure N, with no reference to the values of p_i and p_w.

The results we present below rely on an integral statement of force balance. If we integrate (4.7a) and apply the divergence theorem, we find that

$$\int_{\Gamma_t} (\sigma_{nn}\boldsymbol{n} + \boldsymbol{\sigma}_{nt})\, \mathrm{d}s = -\int_{\Gamma_b} (\sigma_{nn}\boldsymbol{n} + \boldsymbol{\sigma}_{nt})\, \mathrm{d}s. \tag{4.16}$$

Now, by noting that

$$\boldsymbol{n} = (0,1)^\top \quad \text{on } \Gamma_t \quad \text{and} \quad \boldsymbol{n} = \frac{1}{\sqrt{1 + \left(\frac{\partial \theta}{\partial x}\right)^2}} \left(\frac{\partial \theta}{\partial x}, -1\right)^\top \quad \text{on } \Gamma_b, \tag{4.17}$$

and applying boundary conditions (4.7c) and (4.7d), we may deduce that

$$\int_{\Gamma_t} \left(\boldsymbol{\sigma}_{nt} \cdot (1,0)^\top\right) \mathrm{d}s = -\int_0^1 \sigma_{nn}|_{\Gamma_b} \frac{\partial \theta}{\partial x}\, \mathrm{d}x, \tag{4.18a}$$

$$p_i = -\int_0^1 \sigma_{nn}|_{\Gamma_b}\, \mathrm{d}x. \tag{4.18b}$$

Lemma 4.1. *If a solution to the Stokes problem (4.7) exists, then the effective pressure must be non-negative, such that $N \geq 0$.*

Proof. We can see that $p_i - p_w \geq 0$ by taking (4.18b) and using inequality $\sigma_{nn} \leq -p_w$ from the contact boundary conditions (4.7f). □

The necessity of the condition $N \geq 0$ for solutions to exist can also be seen to follow from Theorem A.1. Moreover, it can also be deduced from Variational inequalities A and B by testing with vertical rigid modes. It is also interesting to note that the condition $N > 0$ is sufficient for the existence of solutions, as we explain in Remark 3.2.

Lemma 4.2. *The basal shear stress τ_b can be written as*

$$\tau_b = \int_{\Gamma_t} \left(\boldsymbol{\sigma}_{nt} \cdot (1,0)^\top \right) \, \mathrm{d}s. \tag{4.19}$$

Moreover, it satisfies the following bound,

$$\tau_b \leq N \sup_{x \in [0,1]} \left| \frac{\partial \theta}{\partial x} \right|. \tag{4.20}$$

Inequality (4.20) is normally referred to as Iken's bound.

Proof. Equation (4.19) follows from (4.18a), by writing

$$\int_{\Gamma_t} \left(\boldsymbol{\sigma}_{nt} \cdot (1,0)^\top \right) \, \mathrm{d}s = \tau_b + p_w \int_0^1 \frac{\partial \theta}{\partial x} \, \mathrm{d}x \tag{4.21}$$

and noting that the second term to the right is zero due to the periodicity of θ. To prove inequality (4.20), we first note that $-\sigma_{nn} - p_w \geq 0$ by the contact conditions (4.7f), and therefore we find that

$$\tau_b \leq \sup_{x \in [0,1]} \left| \frac{\partial \theta}{\partial x} \right| \int_0^1 \left(-\sigma_{nn}|_{\Gamma_b} - p_w \right) \, \mathrm{d}x. \tag{4.22}$$

By (4.18b), we know that $-\int_0^1 \sigma_{nn}|_{\Gamma_b} \, \mathrm{d}x = p_i$, and with this equality we can complete the proof. □

The alternative expression for the basal shear stress (4.19) justifies the use of τ_b as a boundary condition in (4.9). Iken's bound (4.20) was first proposed in [59] and indicates that, whenever subglacial cavitation is accounted for, one can expect a friction law to have an upper bound. A similar proof to ours can also be found in [87].

4.3 Steady sliding with cavitation

The sliding of a glacier over its bedrock has been widely studied since Weertman's seminal work in 1957 [104]. In general, these studies attempt to build a function known as the friction law that captures the steady relationship between the basal sliding speed u_b, the basal shear stress τ_b, and other variables such as the effective pressure N. This friction law can then be used to prescribe a boundary condition at the ice-bedrock interface in large-scale glacier models which do not resolve the smaller-scale shape of that interface.

In this section, we compute steady solutions to the subglacial cavity system presented in Section 4.2 with the Dirichlet boundary condition (4.8). These computations are carried out with the numerical solver for viscous contact problems introduced in Section 2.3. We first present detailed results for a single steady state in Section 4.3.1 to evaluate the accuracy

Table 4.1: Information about the different meshes and the time step used to compute the steady cavity states together with calculations of the basal shear stress τ_b, the basal sliding speed u_b, and the detachment and reattachment points of the cavity.

n_e	mesh cells	Δt	τ_b	u_b	reattachment	detachment
16	96	0.04	0.014546	0.98678	0.7500	1.0000
32	192	0.02	0.015734	0.98565	0.7188	1.0000
64	768	0.01	0.015477	0.98596	0.7188	1.0000
128	3072	0.005	0.015712	0.98574	0.7109	1.0000
256	12800	0.0025	0.015740	0.98571	0.7109	0.9961

of the solver and the effect of mesh refinement. Then, in Section 4.3.2 we compute friction laws for different values of the parameter n in Glen's law (1.3). Throughout this section, we compare our numerical results with those obtained with the semi-analytical method proposed in [31, 87] and summarised in Appendix C.

4.3.1 Steady subglacial cavities

We find solutions to the steady state of the subglacial cavity system with the Dirichlet boundary condition (4.8) by evolving the cavity from an initial state until the $L^2([0,1])$ norm of the discrete derivative in time of θ, given by

$$D_t\theta_h^k = \sqrt{\int_0^1 \left[\frac{\theta_h^{k+1} - \theta_h^k}{\Delta t}\right]^2 \mathrm{d}x}, \tag{4.23}$$

is below a prescribed threshold of 10^{-4}. In this section, we find steady cavities for a Newtonian flow ($n = 1$ in Glen's law (1.3)) over a bed of small amplitude $r_b = 0.01$. We set the non-dimensional effective pressure to $N = 0.3$. The choice of a linear rheology and a bedrock of small amplitude allows us to compare our results with the analytical solution of the linearised cavitation problem considered in [31, 87]. A brief description of this method is included in Appendix C.

We use five different meshes with n_e cells uniformly distributed along the lower boundary. In Table 4.1 we present the non-dimensional basal shear stress τ_b and sliding speed u_b along the cavities for the five computations. These values suggest that, as we refine the mesh, our computations of the basal shear stress, sliding speed, and cavity endpoints converge.

In Figure 4.2 we present the steady cavity shape and normal stresses σ_{nn} along the attached region Γ_a for the different meshes. We can see from these figures that the cavity shape is accurately computed even with the coarsest mesh. Additionally, we also present the stress distribution obtained from the linearised theory, which is uniquely determined for

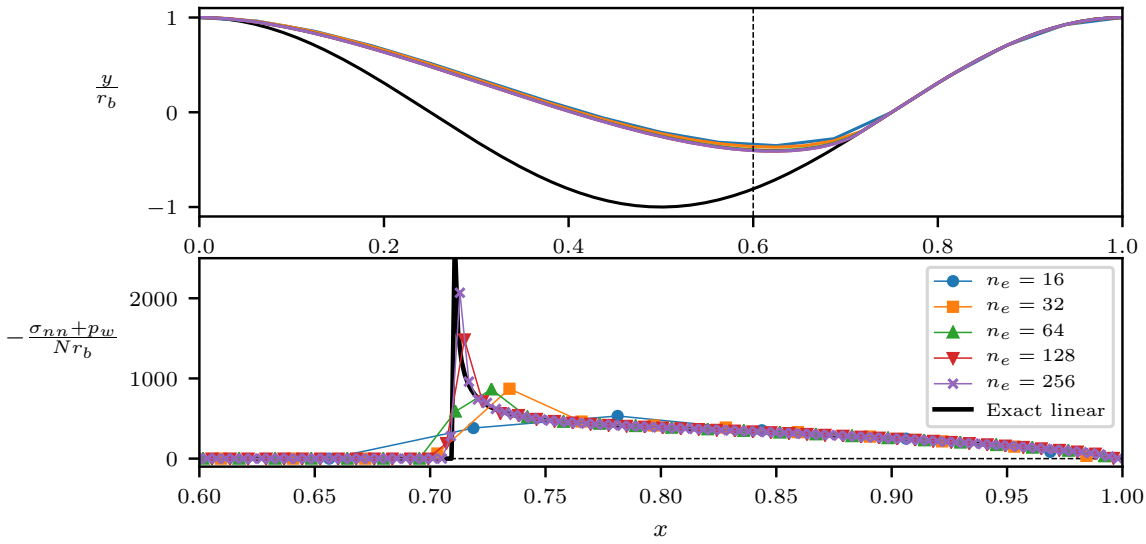

Figure 4.2: (top) Steady cavity shapes and (bottom) normal stresses along the attached region computed with different mesh sizes. In black, the stress distribution obtained from the linearised theory. Here, the amplitude of the obstacle is set to $r_b = 0.01$, the rheological parameter to $n = 1$, the scaled effective pressure to $N = 0.3$, and n_e represents the number of elements along the lower boundary.

an effective pressure N and a sliding speed u_b. The result from the linearised theory plotted in Figure 4.2 is computed with the value of u_b calculated with the most refined mesh.

The plot for the normal stress distribution demonstrates that the contact conditions (4.7f) are satisfied exactly at the discrete level for all of the meshes, because $\sigma_{nn} + p_w \leq 0$. This plot also exhibits the singularity of the normal stresses at the reattachment point, which also appears in the linearised solution. This singularity complicates the approximation of the normal stresses along the attached region and can lead to very inaccurate computations of the friction law in largely cavitated states. However, Figure 4.2 also indicates that, with increasing mesh refinement, the solver appears to converge towards the linearised solution.

We remark that it may appear confusing that there are non-zero values of $\sigma_{nn} + p_w$ left of the position of the reattachment node given in Table 4.1 (this is particularly visible for the coarsest mesh with $n_e = 16$). However, this is due to the contact criterion, which treats the edge immediately upstream of the first reattached node as part of Γ_a, see Section 2.3 in Chapter 2. Moreover, at the discrete level, the Lagrange multiplier λ, which we use to calculate τ_b, is piecewise constant on each edge along the lower boundary. In Figure 4.2, these values, the degrees of freedom of λ, are plotted at the midpoints of each edge.

As the cavities evolve towards a steady state, waves of decreasing amplitude travel along the roof of the cavity. As a result, convergence towards the steady state becomes rather slow. This can be seen in Figure 4.3, where we have plotted the variation in time of the

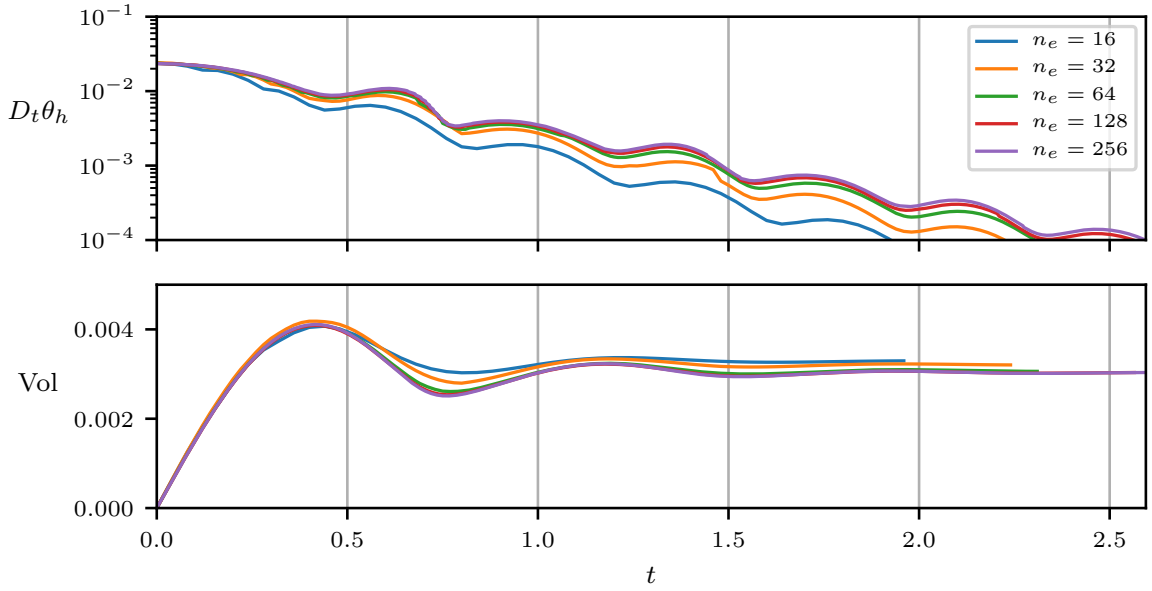

Figure 4.3: Variation in time of (top) $D_t\theta_h$, the $L^2(\Omega)$-norm of the discrete time derivative of θ_h, and (bottom) the cavity volume Vol for the evolution of the cavity towards a steady state. Here, the amplitude of the obstacle is set to $r_b = 0.01$, the rheological parameter to $n = 1$, the scaled effective pressure to $N = 0.3$, and n_e represents the number of elements along the lower boundary.

norm of the discrete time derivative of θ, which sets our criterion for when a steady state is reached, and the cavity volume. We note that for the most refined computation, with $n_e = 256$ elements along the lower boundary, we set $\Delta t = 0.0025$, implying that over 1000 time steps are required to converge to the steady state. This figure also reveals a clear convergence of the transient, time-dependent solution of the numerical computations, suggesting that these oscillations are not of a numerical nature.

4.3.2 Computation of the linear and nonlinear steady friction law

We next perform similar calculations to those of Section 4.3.1 but for varying effective pressure N, power-law exponent n, and bed amplitude r_b. This allows us to map out a steady friction law for ice sliding over a hard bed with cavitation as in [36]. Our non-dimensional formulation from Section 4.2 reveals that τ_b depends only on N, r_b, and n; therefore, we can expect that

$$\tau_b = \tau_b(u_b, N, r_b, n). \tag{4.24}$$

On the other hand, dimensional analyses of the steady problem show that the scaled basal shear stress τ_b/N depends only on the ratio u_b/N^n, and not independently on u_b or N [31] (the same will not be true of the unsteady problem in Section 4.4). Several previous studies

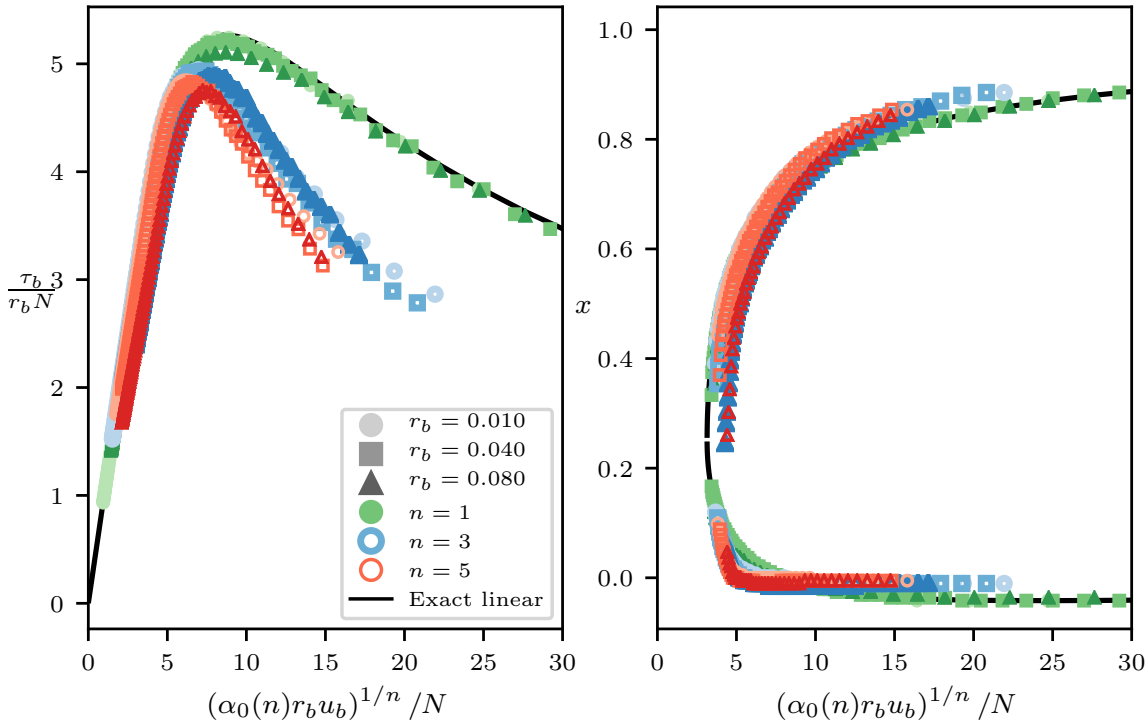

Figure 4.4: (left) Computed friction law for steady glacial sliding with cavitation. (right) Cavity endpoints. The parameter n in Glen's law (1.3) is set to $n = 1$ (green), 3 (blue), and 5 (red); for each n, we compute the friction law for beds of amplitude $r_b = 0.01$ (circles, light), 0.04 (squares), and 0.08 (triangles, dark). For these computations, we use a mesh with 192 cells along the lower boundary. The parameter $\alpha_0(n)$ is computed from the slope of the curve near the origin for the lowest r_b.

have suggested what form the friction law should take, both with and without cavitation [65, 34, 31, 45, 87, 36]. The law proposed in [45] for the uncavitated case can be written as

$$\left(\frac{\tau_b}{r_b N}\right)^n = \alpha_0(n) \frac{r u_b}{N^n}, \tag{4.25}$$

where $\alpha_0(n)$ is a function depending on n. The function $\alpha_0(n)$ is related to the parameter c_0 (which also depends on n) considered in [45] via

$$\alpha_0(n) = \frac{(2\pi)^{n+2}}{2c_0}. \tag{4.26}$$

For a Newtonian flow, the complex analysis method presented in [31, 87] yields an exact solution to the linearised problem. In particular, for high effective pressures, no cavitation occurs and a linear friction law as in (4.25) with $c_0 = 1$ is found. For (nondimensional) effective pressures lower than a critical value $8\pi^2 r_b u_b$, cavitation occurs and the friction law becomes non-linear, varying with N as well as u_b.

We compute the friction law over a sinusoidal bed of different amplitudes r_b and for $n = 1$, 3, and 5, and we plot the results in Figure 4.4 using the scaling suggested by

(4.25). The mesh has 192 cells along the lower boundary and 7296 cells in total. The location of the cavity endpoints is also plotted in Figure 4.4, along with the solution to the linearised problem calculated with the method from [31, 87]. For each n, the parameter $\alpha_0(n)$ is computed by calculating the slope of the curve near the origin (where there is no cavitation) for the lowest value of r_b. The corresponding values of the parameter c_0 can then be calculated from (4.26); these values can be found in Table 4.2 together with those obtained in [45] and [36]. We see that the results obtained in these works are broadly similar to ours and that the value $c_0 = 1$ obtained in the linearised theory is approached in all cases when $n = 1$.

The computed friction laws with cavitation in Figure 4.4 are multivalued for $\tau_b/(rN)$ as expected [31, 87]. This aspect of the law justifies the use of the Dirichlet boundary condition $u = 1$ on Γ_t instead of the alternative Neumann boundary condition, given by (4.9). We find that if we use the Neumann boundary condition $\boldsymbol{\sigma}_{nt} = \tau_b(1, 0)^\top$ and initiate the cavity from a fully attached state, the solver always evolves to the steady state associated to the upsloping region of the curve (see also Section 4.4).

For fixed values of r_b and n, the friction laws in Figure 4.4 present an initial segment near the origin where τ_b/N increases linearly with $u_b^{1/n}/N$. In this linear segment little or no cavitation has occurred, and along it we find that the validity of the friction law (4.25) decreases with increasing values of r_b and n. For example, when $n = 5$, one can observe that the linear segment of the friction law for $r_b = 0.08$ clearly does not collapse onto the corresponding linear segment for $r_b = 0.01$ (we would expect them to be indistinguishable along this linear segment if (4.25) was valid for all values of n and r_b). As soon as the cavity size increases and this linear behaviour is lost, the aspect of these curves largely differ for different values of n. In fact, Figure 4.4 suggests that a limit curve exists for each value of n as $r_b \to 0$.

In Figure 4.4, we use a different scaling to the one used in [36]. In [36], the computed maximum value reached by τ_b/N is included in the scaling for the friction law. In this way, the maximum value reached by the scaled friction law equals 1 by design. However, we preferred the scaling based on (4.25) because it contains fewer terms that are unknown a priori. It is also worth mentioning that, for different values of n, the curves in Figure 4.4 do not collapse into a single curve when plotted with the scaling from [36].

For the linear case with $n = 1$, the numerical results computed with the finite element solver highly resemble those obtained with the linearised solution. For $r_b = 0.08$ a slight difference with the linearised solution can be seen near the peak of the friction law. This difference is probably a consequence of nonlinear effects that are accentuated with increasing amplitudes of bedrock roughness.

Table 4.2: Value of the parameter c_0 associated to the friction laws. This parameter is computed with the slope of these curves near the origin.

	$r_b = 0.01$	[45]	[36]
$n = 1$	1.0006	0.9936	0.9771
$n = 3$	0.3433	0.3294	0.2769
$n = 5$	0.1252	0.1153	-

4.4 Unsteady sliding with cavitation

In the previous section, the sliding law was constructed by computing steady cavity states. However, field measurements from alpine glaciers and from the Greenland Ice Sheet have found short term variations in the water pressure, on timescales down to hours [59, 60, 98, 4, 57]. In these studies, variations of water pressure have been correlated with variations in surface speeds, vertical strain, and uplift. Subglacial cavitation has been considered a possible mechanism causing these correlations [60, 72, 98]. These observations motivate an investigation of glacier sliding under unsteady conditions. In this section, we therefore compute the evolution in time of subglacial cavities under oscillating water pressures and calculate the corresponding unsteady basal sliding speed and shear stresses. The study published by Iken of the transient stages between steady cavity shapes [59] is the only numerical investigation of unsteady cavitation solving the Stokes problem known to the author.

We initialise the computations from a steady state corresponding to a point in the sliding law determined by an effective pressure N_0, a basal sliding speed $u_{b,0}$, and a basal shear stress $\tau_{b,0}$. Instead of prescribing the Dirichlet boundary condition $u = 1$ on Γ_t, we enforce the Neumann boundary condition $\boldsymbol{\sigma}_{nt} = \tau_{b,0}(1, 0)^\top$ on Γ_t. We consider it more physically realistic to have the basal shear stress fixed rather than the sliding speed because we can expect the basal stresses to balance the gravitational driving stresses, which are essentially fixed on these timescales. In practice, if water pressure variations are spatially localised, the driving stress can be transferred to neighbouring regions of the bed, but it is not easy to account for this within the current boundary-layer treatment of the problem. We set $n = 3$ in Glen's law to model the nonlinear rheology of ice. The numerical scheme from Section 2.3 is used with a mesh with 192 elements along the lower boundary over a sinusoidal bed of amplitude $r_b = 0.08$.

The effects of unsteady water pressures differ depending on the initial steady state from which we evolve the cavity. To illustrate this, we first evolve two different points along the upsloping component of the steady sliding law by oscillating the effective pressure with

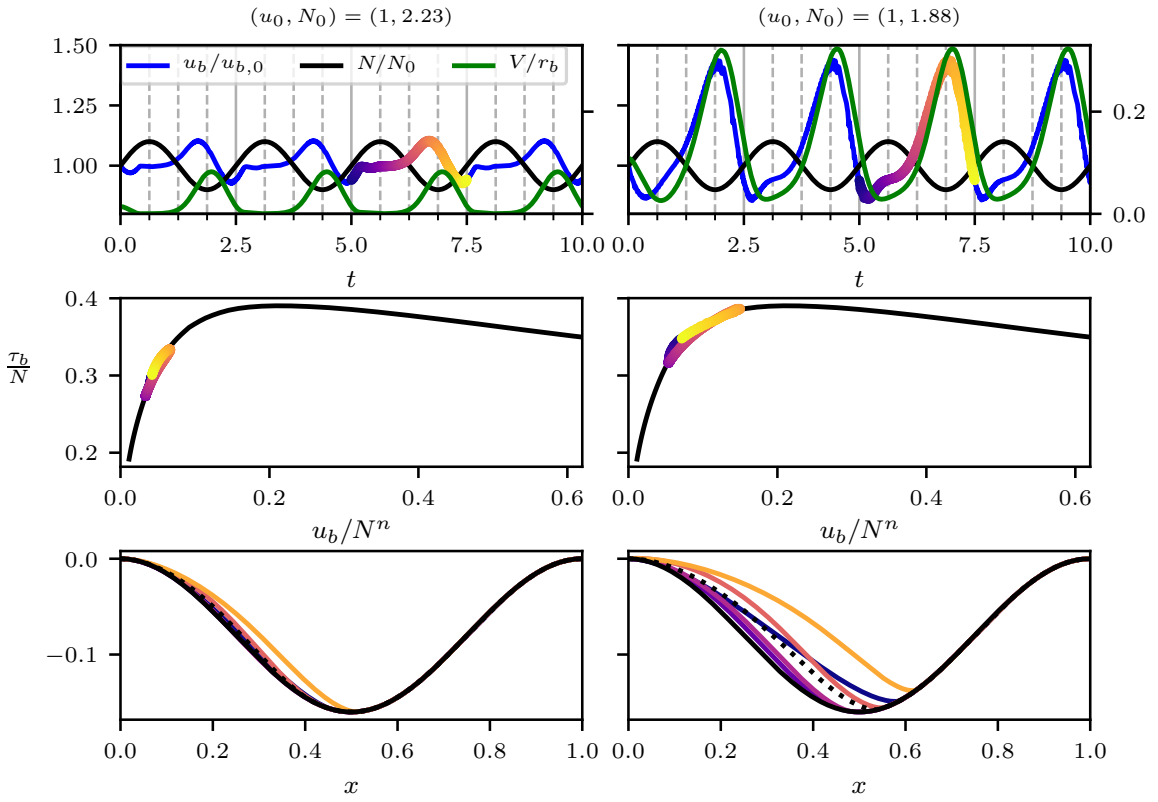

Figure 4.5: Unsteady cavitation for imposed oscillating effective pressures N and fixed basal shear stress τ_b around the states with $(u_{b,0}, N_0) = (1, 2.2281)$ (left) and $(1, 1.8843)$ (right). (top) Evolution of the cavity volume V (right axis) and basal sliding speed u_b (left axis, also for N). (middle) One period of each solution is superimposed on the steady sliding law, as indicated by the coloured dots. (bottom) Cavity shapes at different time instants with coloured lines; the dotted lines represent the steady cavity shapes for $(u_{b,0}, N_0)$.

an amplitude of $0.1N_0$ and a fixed non-dimensional frequency of 0.4. As a reference, note that one non-dimensional time unit is approximately the time taken for ice at the top of the domain to traverse one wavelength of the bed. The results are plotted in Figure 4.5. These results indicate that, with increasing cavitation, the amplitude of the sliding speed increases. For the case of small cavitation (top-left panel of Figure 4.5), the sliding speed is slightly out of phase with the effective pressure. However, this phase difference disappears with larger cavitation, as observed in the top-right panel of Figure 4.5 and also in Figures 4.6 and 4.7 below. This implies that the maximum sliding speed is most often reached when the effective pressure is lowest. Field measurements have also found maximum surface speeds to take place at moments of maximum water pressures [60, 98]. On the other hand, the phase difference between the sliding speeds and the cavity volume appears to change in each numerical test: in the top-left panel of Figure 4.5, one can observe that the maximum sliding speed is reached when the cavity is still growing, while in the top-right panel of

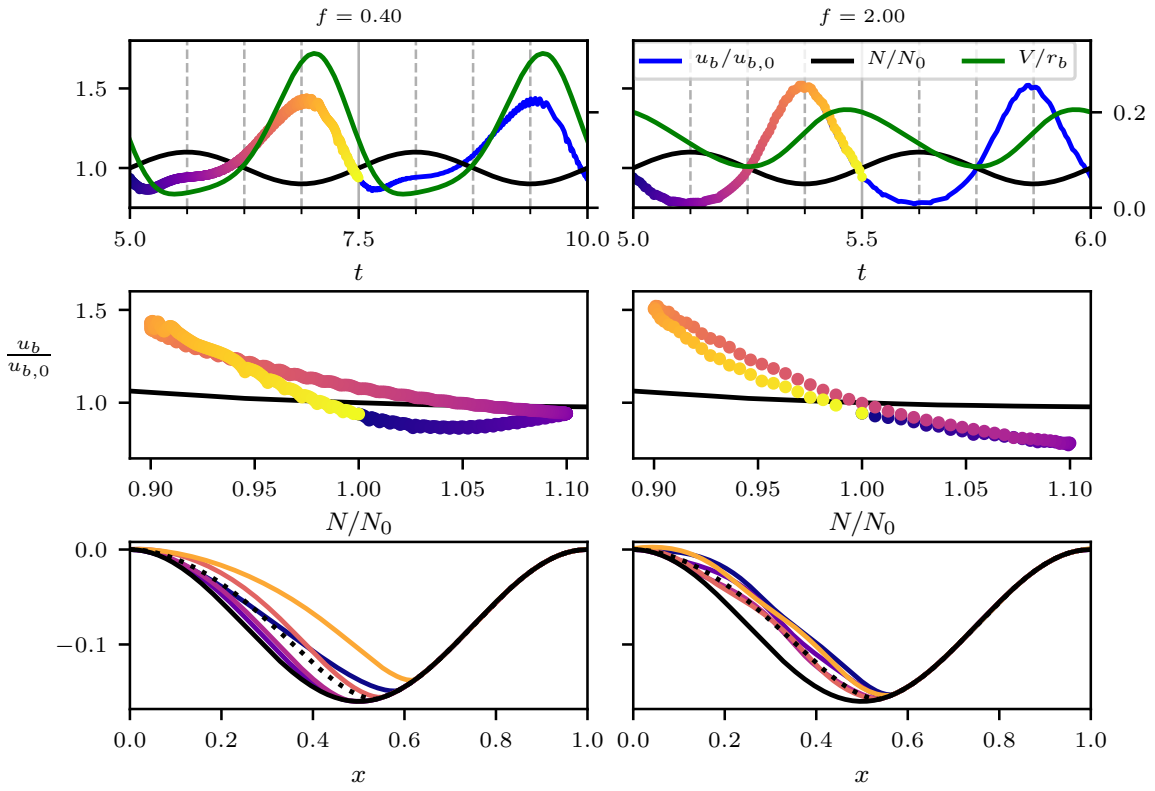

Figure 4.6: Unsteady cavitation around the state with $(u_{b,0}, N_0) = (1, 1.8843)$ for imposed oscillating effective pressures N, with non-dimensional frequencies of 0.4 (left) and 2 (right), and fixed basal shear stress τ_b . (top) Evolution of the cavity volume V (right axis) and basal sliding speed u_b (left axis, also for N). (middle) Sliding speed is plotted against effective pressure in coloured dots, together with the steady solution in black. (bottom) Cavity shapes at different time instants with coloured lines; the dotted lines represent the steady cavity shapes for $(u_{b,0}, N_0)$.

Figure 4.5 it is reached at the time of maximum cavitation. There are slight oscillations in the computed sliding speed when the cavity volume is at its largest. These are numerical artefacts due to the stress singularity at the reattachment point of the cavity having an increasing effect on the overall solution of the problem as the cavity volume grows. In these situations, a small displacement of the reattachment point has a large effect on the stress distribution along the bed and therefore also on the computed sliding speed.

As mentioned above, the non-dimensional time it takes a fluid particle to traverse the domain is of order $t \approx 1$. Therefore, the scaled frequency $f = 0.4$ can be considered a relatively slow frequency that allows the cavity to approximately follow the steady shapes associated to the effective pressure at each instant in time as calculated in Section 4.3. In Figure 4.6, we compare results obtained with frequencies $f = 0.4$ and $f = 2$ to examine the effect of faster oscillations in the water pressure. With a higher frequency, the magnitude of the change of cavity volume is significantly lower. In contrast, the amplitude of the sliding

speed increases slightly with a higher frequency. The phase difference between the velocity and the cavity volume also changes when the frequency is increased. For a high frequency, the maximum velocity is no longer attained when the cavity reaches its largest extent, but before, when the cavity is still growing. More specifically, the top-right panel of Figure 4.6 indicates that the maximum of the sliding speed and of the rate of change of the cavity volume occur simultaneously.

We can therefore expect a phase difference between the sliding speed and the cavity volume to arise for large frequencies. For very low frequencies, at each time instant t, the cavity shape is approximately that of the corresponding steady state for the values of $N(t)$, $u_b(t)$, and $\tau_b(t)$. Therefore, since u_b increases with the cavity volume under steady conditions, this phase difference will disappear. When comparing the top-left and right panels of Figure 4.5, we see that this phase difference is larger when the cavity is smallest.

Following [98], in Figure 4.6 we also plot the sliding speed against the effective pressure throughout one cycle. For the lower frequency $f = 0.4$, a clear loop arises in which the sliding speed is greater during cavity growth. For the higher frequency $f = 2$, the loop nearly collapses into a single line. These plots can be compared with those obtained from field measurements in [98, Figure 5]; a qualitative similarity between both is that higher speeds are reached when N decreases. Additionally, similar plots are presented in [4, Extended Data Figure 4]. These plots also show the extent to which unsteady sliding can differ from its steady counterpart.

The downsloping section of the friction curve produces a so-called rate-weakening sliding regime in which, for a supposed fixed effective pressure, an increase in the sliding speed is accompanied by a decrease in the basal drag. Rate-weakening sliding has been observed in a laboratory setting for ice sliding over a sinusoidal bed [107], although several authors have questioned whether such a sliding regime can arise for more realistic bed geometries [32, 87, 49]. An implication of rate-weakening sliding is that the sliding law becomes double-valued, as seen in Figure 4.4. This invalidates the commonly used shallow ice approximation of the Stokes equations which requires the friction law to be invertible [93].

In Figure 4.7 we perturb a steady state along the downsloping section of the curve with an oscillating effective pressure of nondimensional frequency $f = 0.4$ with the amplitude set to $0.1N_0$ (left panels) and $0.01N_0$ (right panels). As shown in the middle-left and right panels of Figure 4.7, we observe that, for perturbations with both large and small amplitudes, the cavity quickly evolves towards the steady state along the upsloping section for a similar value $\tau_{b,0}/N_0$. In fact, we find that this phenomenon continues to occur for different frequencies in the oscillations of the effective pressure and different steady states along the downsloping section of the sliding law. This finding could offer an additional reason to not use a sliding

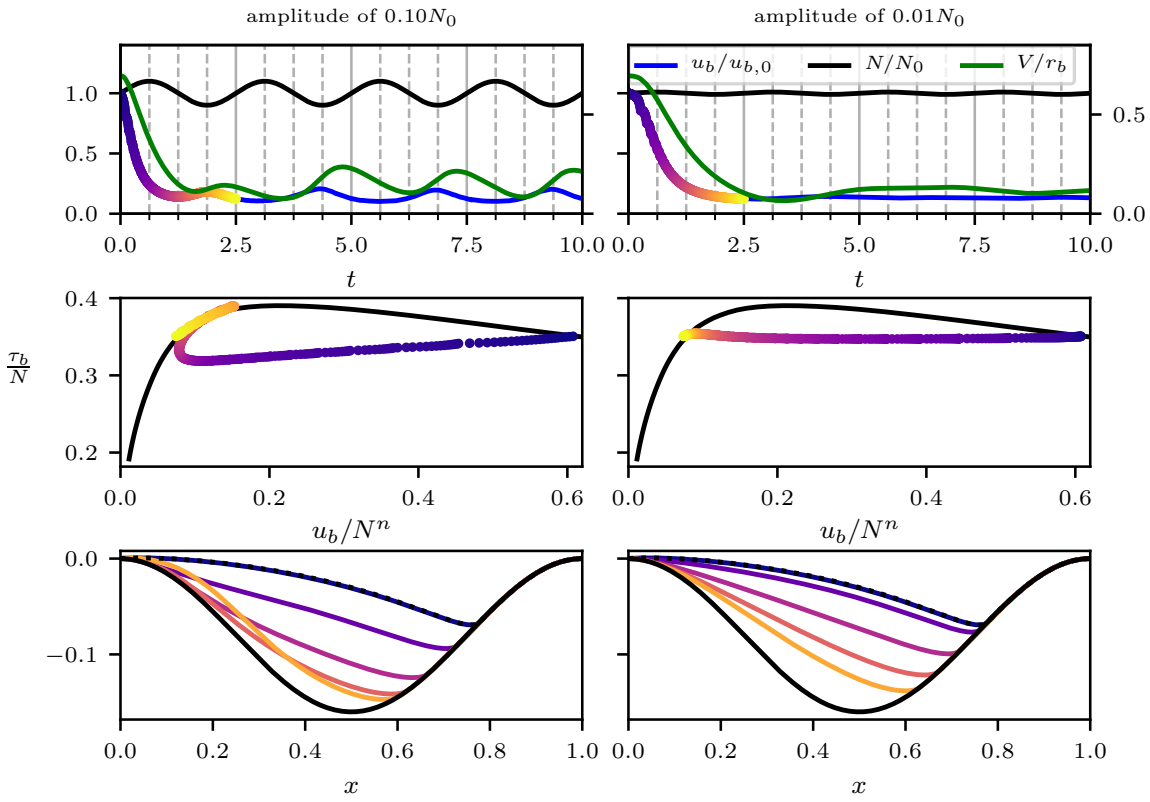

Figure 4.7: Unsteady cavitation around the state with $(u_{b,0}, N_0) = (1, 1.0937)$ for imposed oscillating effective pressures N, with amplitudes of $0.1N_0$ (left) and $0.01N_0$ (right), and fixed basal shear stress τ_b . (top) Evolution of the cavity volume V (right axis) and basal sliding speed u_b (left axis, also for N). (middle) One period of each solution is superimposed on the steady sliding law, as indicated by the coloured dots. (bottom) Cavity shapes at different time instants with coloured lines; the dotted lines represent the steady cavity shapes for $(u_{b,0}, N_0)$.

law with a rate-weakening regime: since such a regime is unstable in the sense described above, we could expect it to be unachievable under natural conditions.

4.5 Discussion

After a review of the literature dedicated to glacial sliding with cavitation, we formulate the subglacial cavitation problem in a similar manner to [36], following our general formulation of viscous contact problems introduced in Chapter 1. We then derive some properties of the system, such as Iken's bound and the dependence of sliding parameters on the effective pressure $N = p_i - p_w$, rather than the individual values of p_i and p_w. In Section 4.3 we compute steady cavity configurations with the numerical method for viscous contact problems presented in Section 2.3. Here, we validate our computations by comparing our method with the linearised approach in [31, 87] and we reconstruct steady sliding laws for

different values of the rheological exponent n, as in [36]. Finally, in Section 4.4, we explore the temporal evolution of cavities under unsteady effective pressures and its effect on glacial sliding. One of the features of unsteady sliding studied in this work is the phase difference between the sliding speed, the cavity volume, and the effective pressures. Our results show that, with increasing frequencies, the phase difference between the sliding speed and cavity volume increases. They also seem to indicate that the maximum sliding speed occurs at the point of minimum effective pressure, at least for sufficiently cavitated states. Similar phase differences have been found in data obtained from field measurements [60, 98, 4]. Although our results could offer an explanation in terms of an idealised model, it should be noted that changes in measurements of surface elevation of an ice sheet can be the result of many cavities in different states. Another interesting finding is that, when we fix the value of τ_b as a Neumann boundary condition, the downsloping section of the sliding law, also known as the rate-weakening regime, is unstable under finite perturbations. That is, if we perturb a steady state along the downsloping section, the cavity quickly evolves towards the corresponding point with a similar value of τ_b/N along the upsloping part.

We remark that we have compared our numerical method and its application to subglacial cavitation with that of [36]. When computing the points along the steady sliding law in Figure 4.4 with our method, the number of time steps required to converge to a steady state can become very large (of order 1000) in the highly cavitated stages along the downsloping region of the curve. This is due to very small scale oscillations that travel across the cavity but have a significant effect on the calculated values of τ_b due to the stress singularity at the reattachment point, as explained in Section 4.3.1. Contrastingly, when using the method from [36], these oscillations seem to dampen and the method can converge in about 100 iterations for highly cavitated states. We speculate that this is due to the use of a numerical stabilisation in Elmer when solving the advection equation, see (11) in [37]. Despite this difference in computational times, we find that the basal stress computations carried out with our method appear to be more accurate due to the exact enforcement of discrete contact conditions (see Figure 4.2 and compare with [36, Figure 1]).

We expect that the long computational times required to find steady cavity states can be drastically reduced by directly solving for the steady solution. That is, instead of advancing towards a steady state from a given initial condition, we could formulate and implement a method that applies a nonlinear solver (ideally the semi-smooth Newton method) to a system that couples the Stokes equations with the free boundary equations. Such a method is also proposed at the end of Chapter 2 for building implicit solvers for viscous contact problems. Accuracy could also be improved substantially without a disproportionate increase in computational cost by using adaptive refinement around the contact points. The

main obstacles to developing both a steady state solver and an adaptive refinement scheme are the computational implementation in Firedrake.

Chapter 5

Marine ice sheets

Marine ice sheets are ice sheets which slide from the continent into the ocean, where they go afloat at the so-called grounding line, the interface where ice, bedrock, and ocean meet. This configuration is found in much of the West Antarctic ice sheet, where a large portion of its bedrock lies beneath sea level [75], and in some of Greenland's glaciers, such as Petermann Glacier [53]. Marine ice sheets contribute to sea level rise by discharging grounded ice into the ocean. The rate of discharge is determined by the dynamics of the grounding line, and much research has been undertaken to understand the possibility of a marine ice sheet instability that could trigger an acceleration in the rate of discharge [89, 88, 24, 46, 28].

This chapter investigates steady marine ice sheet configurations. We do this by computing numerical solutions to a model problem, the parallel slab marine ice sheet problem presented in Section 5.2. It consists of a slab of ice of uniform thickness flowing down an inclined bedrock into the ocean, where it detaches from the bedrock at the grounding line. The main focus of this chapter is the relationship between the ice flux and the thickness at the grounding line, which is crucial for constructing simple but accurate models of marine ice sheets and understanding their dynamics.

The original contribution of this chapter lies in the computation of steady flux-thickness relationships at the grounding line by solving the viscous contact problem based on the Stokes equations. To do so, we use our solver for viscous contact problems presented in Chapter 2. We first explore the form taken by this relationship under different flow regimes. In Section 5.3, we present a first set of results which suggest that, in the limits of pure sliding and pure shearing, this relationship tends towards power laws of exponents $n+1$ and $n+2$, respectively. Then, in Section 5.4, we explore each of these limits more rigorously and analytically derive approximations to these laws by means of simple models as in [89, 67, 86, 80]. These comparisons allow us to rigorously establish the range of validity of these models.

5.1 Existing studies on grounding line dynamics

The possibility of an eventual disintegration of the West Antarctic ice sheet has motivated many studies on the dynamics of grounding lines in the past decades. Of this extensive literature, here we focus on a small subset which has attempted to understand the mechanisms regulating the ice flux q and thickness h at the grounding line. In particular, unless the contrary is stated, all the studies we cite in this review concentrate on two-dimensional (i.e. one horizontal dimension) marine ice sheets. In this setting, the grounding line is a point, which we denote by x_g.

Almost five decades ago, Weertman [105] studied the transition region between grounded and floating ice using rough estimates of the viscous stresses and flow velocity of the ice, and established that stable grounding line positions may exist whenever the bed slopes upwards towards the floating ice shelf from the centre of the ice sheet. Underlying this stability analysis was the hypothesis that the ice flux at the grounding line must be a single-valued function of the ice thickness. With this study, Weertman pointed out the importance of this transition region in marine ice sheet dynamics.

Weertman's use of ad-hoc arguments made the extent to which his conclusions were valid unclear. Three decades later, a first rigorous attempt to understand the junction from grounded to floating ice was provided by Wilchinsky and Chugonov [106]. Here, the authors focused on a stationary Stokes flow with no slip boundary conditions along the base of the grounded region. By arguing that shear stresses should be of the same order as the extensional stresses at the junction, they found a flux-thickness relationship of the form

$$q = \frac{2}{\beta_0^n} \mathcal{A} \left(\rho g \delta\right)^n h^{n+2} \quad \text{at } x = x_g, \tag{5.1}$$

where the non-negative parameters n and $\mathcal{A}$ are those found in Glen's law, see Section 1.3, ρ and g are the ice density and the gravitational acceleration, respectively, and δ is given by

$$\delta = 1 - \frac{\rho}{\rho_w}, \tag{5.2}$$

with ρ_w denoting the density of the ocean water. The constant β_0 is to be computed by solving the Stokes flow along the junction numerically. For the case where $n = 1$, they find that $\beta_0 = 3/2$. The main limitation of this work is that the contact boundary conditions that determine where the ice detaches from the bedrock are not acknowledged. Instead, when solving the junction problem, the authors set the first and second derivatives of the ice thickness at the grounding line to zero.

A breakthrough in our understanding of grounding line dynamics was made when Schoof [89] used matched asymptotic expansions to show that, under certain (different) assumptions, the flux-thickness relationship takes the form of the power law

$$q = \left(\frac{\mathcal{A}(\rho g)^{n+1}(1-\rho/\rho_w)^n}{4^n C} \right)^{1/(m+1)} h^{(m+n+3)/(m+1)} \quad \text{at } x = x_g. \tag{5.3}$$

Here, $C > 0$ is the sliding coefficient and $m > 0$ is an exponent appearing in the friction law, which we set to $m = 1/n$, see the friction boundary condition (5.15) below. Unlike (5.1), Schoof's power law does not contain any constants that must be calculated with numerical methods. Moreover, (5.3) is argued to be valid under unsteady conditions, and this point is exploited by Schoof in [88, 92] to prove that steady marine ice sheet configurations must have their grounding lines on downwards sloping bedrocks. In particular, Schoof identified a flux-thickness relationship as the missing condition required to close a depth-integrated approximation for a marine ice sheet. In this sense, (5.3) acts like a Stefan condition for a free boundary problem where x_g is an additional unknown.

Equation (5.3) was derived from the shallow stream approximation of the Stokes equations, which is valid for thin flows whose velocity field hardly varies along the vertical direction (that is, a so-called plug flow). Two additional assumptions required for (5.3) to hold are that the extensional stresses be negligible on most of the grounded flow and that the ice be thin at the grounding line. Further investigations have explored the flux-thickness relationship under different flow regimes. For example, Nowicki and Wingham [76] studied the transition problem by solving the Stokes equations on a flat bedrock with a fixed grounding line. They claimed that a single valued flux-thickness relationship may not hold when no sliding occurs (as opposed to (5.3), which is strictly monotonically increasing). A remarkable aspect of this study is that it solved the Stokes equations instead of a depth-integrated model. However, unlike our study in this chapter, contact boundary conditions were not enforced. Instead, the authors find steady states ignoring the contact inequalities, and then investigate whether these contact conditions hold or not.

Sergienko and Wingham [95] challenged Schoof's assumptions and derived an implicit flux-thickness relationship for a plug flow regime where the extensional stresses are no longer negligible. One of the main reasons for considering this flow regime is that, according to the authors, the large ice surface gradients near the grounding line required for Schoof's law (5.3) to be valid are not observed in many West Antarctic ice streams. The implicit relationship derived by Sergienko and Wingham includes a more prominent role for the bedrock. As a result, the authors find that for certain bedrock profiles, marine ice sheets can be stable on upwards sloping bedrocks, contrary to the claims Weertman and Schoof had made previously.

Viscous grounding lines have also been studied experimentally. In [86], Robison, Huppert, and Worster proposed a depth-integrated approximation of a marine ice sheet under the assumptions of a linear rheology and no-slip boundary conditions along the grounded region. For unsteady regimes, a Stefan-like condition was derived analytically which involved time derivatives; however, under the assumption of a steady flow, this condition took the form of a simple power law which relates the flux to the cube of the thickness (as in (5.1) when $n = 1$). Experimental results indicated a slight discrepancy with this power law. The authors suggested this discrepancy could be due to a rise in the water line, caused by the introduction of the viscous fluid acting as the ice sheet, and to the viscous shear stress exerted by the sidewalls of the tank. In order to avoid sidewall effects, Pegler and Worster [80] derived a similar model for a three-dimensional axisymmetric flow, radially flowing from a point source. A similar Stefan condition to the one derived in [86], but including three-dimensional effects, was derived and used by Katz and Worster [67] to study the stability of grounding lines.

An understanding of the transition region around the grounding line is thus fundamental for making any predictions about the behaviour of marine ice sheets. In particular, as we have seen, grounding line dynamics are commonly parametrised with a flux-thickness relationship. With a grounding line parametrisation and depth-integrated approximations of the Stokes equations, one can build simplified models for marine ice sheets. Since solving a Stokes problem over long timescales and large spatial scales is currently impractical, these simplified models are used for simulating the evolution of Earth's ice sheets. Schoof's law (5.3), for example, has been used in large-scale numerical solvers which investigate the dynamics of the Antarctic continent [81, 82], although comparisons with other models for three-dimensional problems have suggested that using Schoof's law as a parametrisation of the grounding line position is not valid for short transients [78].

Although a numerical verification of the marine ice sheet instability was simulated with Elmer/Ice [24, 28], to date there exist no detailed studies on the transition region around the grounding line which solve the complete Stokes viscous contact problem. The main contribution of this chapter is a rigorous investigation of the steady flux-thickness relationship at the grounding line in the context of the parallel slab marine ice sheet problem. We consider a wide range of flow configurations with different amounts of slip, ranging from pure sliding to pure shear flow, and include comparisons to analytically derived flux-thickness relationships. With this study, we seek to disclose the structure of the steady flux-thickness relationship for the parallel slab problem. This will allow us to explore many aspects of these relationships, such as the range of validity of methods commonly used to approximate

them, the effects of the bedrock profile on them, and whether they are single-valued or not under different conditions.

5.2 The parallel slab marine ice sheet problem

For our model setup, we suppose a slab of uniform thickness ice flows down an inclined bedrock which slopes downwards into the sea, where the ice goes afloat at the grounding line, see Figure 5.1. In this section, we present two different models for the parallel slab marine ice sheet problem: the Stokes equations and the shallow stream/shelf approximation (SSA). We focus solely on two-dimensional marine ice sheets, where the grounding line x_g is a point. For simplicity, we will assume that the ice detaches from the bedrock at a single point, without considering cases where the ice reattaches at a further point $x > x_g$.

In this problem, the inflow boundary conditions we enforce are based on the parallel slab solution to the Stokes equations or the SSA, depending on the model we are solving. Then, if the portion of ice located above sea level is sufficiently long, we can expect the ice to transition smoothly from a slab of constant thickness to a floating ice shelf. These boundary conditions are presented below for the Stokes equations and the SSA. We choose this setup for our model problem because it facilitates numerical computations of the transition region around the grounding line, since we have a well-defined boundary condition for the ice surfaces s and θ at the left-hand side of the domain. In this way, we can discretise the free boundary equations with an upwinding scheme, as explained in Section 2.3. Moreover, with the parallel slab inflow boundary conditions we can fix the incoming flux of ice and, in the case of the Stokes equations, control the ratio of incoming flux due to sliding and shearing. This allows us to model the dynamics of a marine ice sheet around the grounding line under different flow regimes. In this setup, since we assume that no ice is gained or lost through the upper and lower surfaces, the flux through any vertical line is the same as the influx whenever the ice sheet is in a steady state. In particular, the flux at the grounding line is equal to the influx.

For the remainder of this chapter, we fix a Cartesian coordinate system (x, z) with origin at the point where the sea level intersects the bedrock. We denote the angle at which the bedrock slopes by β and write

$$b(x) = -x \tan \beta \tag{5.4}$$

for the bedrock deviation, relative to the sea level. The domains under consideration are of length L and occupy a region which extends horizontally from a point $-x_0 < 0$ to a calving front at $L - x_0$. Towards $x = -x_0$, the flow approaches that of a parallel slab whose thickness is set equal to H.

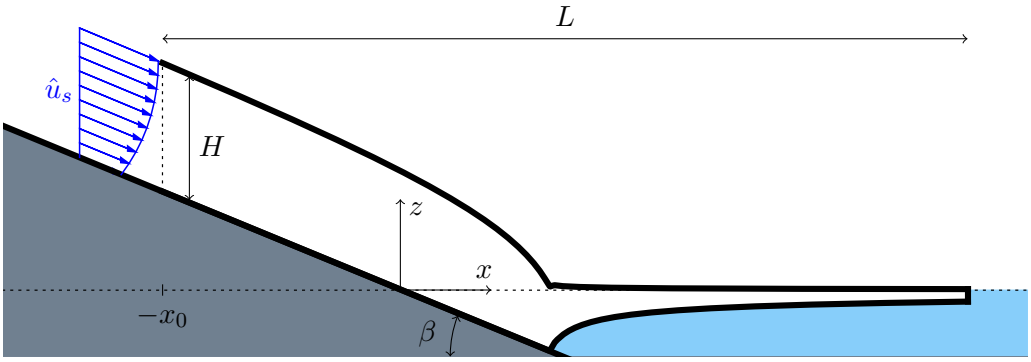

Figure 5.1: The parallel slab marine ice sheet problem. Far upstream of the grounding line, the grounded ice sheet approaches a parallel slab of ice of thickness H on an inclined slope of angle β. The dotted line represents the sea level.

5.2.1 Modelling the marine ice sheet problem with the Stokes equations

The marine ice sheet problem proposed in this section is a viscous contact problem and can therefore be modelled with the Stokes equations, as in Chapter 1. Following the notation introduced in Section 1.7, the ice sheet occupies the domain $\Omega(t)$, enclosed between an upper surface $s(x,t)$ and a lower surface $\theta(x,t)$:

$$\Omega(t) = \left\{(x,z) \in \mathbb{R}^2 : -x_0 < x < L - x_0, \quad \text{and} \quad \theta(x,t) < z < s(x,t)\right\}. \tag{5.5}$$

The flow in $\Omega(t)$ is described according to the Stokes equations with a nonlinear rheology:

$$-\nabla \cdot \left(\alpha |\mathbf{D}\boldsymbol{u}|^{\frac{1-n}{n}} \mathbf{D}\boldsymbol{u}\right) + \nabla p = \boldsymbol{f} \quad \text{in } \Omega, \tag{5.6a}$$

$$\nabla \cdot \boldsymbol{u} = 0 \quad \text{in } \Omega. \tag{5.6b}$$

Here $\alpha = 2^{(n-1)/(2n)} \mathcal{A}^{-1/n}$ is factor which we take to be constant and $\boldsymbol{f} = (0, -\rho g)$ is the gravitational force density. On the top domain Γ_t, defined by

$$\Gamma_t(t) = \left\{(x,z) \in \mathbb{R}^2 : -x_0 < x < L - x_0, \quad \text{and} \quad z = s(x,t)\right\}, \tag{5.7}$$

the ice is in contact with the atmosphere and we set

$$\boldsymbol{\sigma}\boldsymbol{n} = 0 \quad \text{on } \Gamma_t. \tag{5.8}$$

On the detached region,

$$\Gamma_d(t) = \left\{(x,z) \in \mathbb{R}^2 : -x_0 < x < L - x_0, \quad z = \theta(x,t), \quad \text{and} \quad b < \theta(x,t)\right\}, \tag{5.9}$$

and at the calving front,

$$\Gamma_c(t) = \left\{(x,z) \in \mathbb{R}^2 : x = L - x_0 \quad \text{and} \quad \theta(x,t) \leq z \leq s(x,t)\right\}, \tag{5.10}$$

the ice is in contact with the water and therefore we enforce

$$\boldsymbol{\sigma n} = -p_w \boldsymbol{n} \quad \text{on } \Gamma_d \cup \Gamma_c. \tag{5.11}$$

Since we assume the water to be in hydrostatic equilibrium, we write

$$p_w(z) = \rho_w g \max\{0, -z\}. \tag{5.12}$$

The attached region Γ_a is the region along the lower boundary where the ice is contact with the bedrock, that is,

$$\Gamma_a(t) = \left\{(x,z) \in \mathbb{R}^2 : -x_0 < x < L - x_0, \quad z = \theta(x,t), \quad \text{and} \quad b = \theta(x,t)\right\}. \tag{5.13}$$

As explained in Section 1.4, on Γ_a we allow the ice to detach from the bedrock by enforcing the following contact boundary conditions:

$$\boldsymbol{u} \cdot \boldsymbol{n} \leq 0, \quad \sigma_{nn} \leq -p_w \quad \text{and} \quad (\boldsymbol{u} \cdot \boldsymbol{n})(\sigma_{nn} + p_w) = 0 \quad \text{on } \Gamma_a. \tag{5.14}$$

In the tangential direction, we enforce a Weertman-style friction law [104]:

$$\boldsymbol{\sigma}_{nt} = -C|\mathbf{T}\boldsymbol{u}|^{1/n-1}\mathbf{T}\boldsymbol{u} \quad \text{on } \Gamma_a. \tag{5.15}$$

On the left boundary of the domain, which we assume to remain unchanged with time and we define as

$$\Gamma_i = \left\{(-x_0, z) \in \mathbb{R}^2 : b(-x_0) \leq z \leq s(-x_0, t)\right\}, \tag{5.16}$$

we enforce inflow boundary conditions given by the parallel slab solution. This solution is best described in a frame of reference aligned with the bed. Therefore, we introduce an additional coordinate system $(\hat{x}, \hat{z})$ with origin at the point $(-x_0, b(-x_0))$, rotated such that $\hat{x}$ aligns with the bed. We denote by $\hat{H}$ the thickness of the ice sheet in the $\hat{z}$ direction (so that $\hat{H} = H\cos\beta$). Then, in this frame, the velocity field of the slab solution is given by $\hat{\boldsymbol{u}} = (\hat{u}_s, 0)$, where

$$\hat{u}_s(\hat{z}) = \left(\rho g \hat{H} \sin\beta\right)^n \left[\frac{1}{C^n} + \frac{2\mathcal{A}\hat{H}}{n+1}\left(1 - \left(1 - \frac{\hat{z}}{\hat{H}}\right)^{n+1}\right)\right], \tag{5.17}$$

and the pressure field by

$$p_s(\hat{z}) = \rho g \cos(\beta)(\hat{H} - \hat{z}), \tag{5.18}$$

see the derivation in [44, Section 7.2]. Therefore, in our standard coordinate system (x, z), we enforce

$$u = \hat{u}_s \cos\beta \quad \text{on } \Gamma_i \tag{5.19}$$

and

$$\boldsymbol{\sigma}_{nt} = -\rho g(\hat{H} - \hat{z}) \cos(\beta) \sin(\beta) \left(\cos^2\beta - \sin^2\beta\right) \begin{pmatrix} 0 \\ 1 \end{pmatrix} \quad \text{on } \Gamma_i. \tag{5.20}$$

The total incoming flux into the domain Ω is then given by

$$q_s = \left(\rho g \hat{H} \sin\beta\right)^n \left(\frac{\hat{H}}{C^n} + \frac{2\mathcal{A}\hat{H}^2}{n+2}\right). \tag{5.21}$$

One can observe that the parallel slab flow is the sum of a sliding and a shearing contribution, given by $(\rho g \sin\beta/C)^n \hat{H}^{n+1}$ and $2\mathcal{A}/(n+2)(\rho g \sin\beta)^n \hat{H}^{n+2}$, respectively. The ratio between shearing and sliding is then controlled by the nondimensional parameter

$$\Delta_s = C^n \mathcal{A} H. \tag{5.22}$$

Whenever $\Delta_s \to 0$, the flow around $x = -x_0$ will approach that of a plug flow, where the velocity field does not change through the depth of the ice sheet. On the other hand, when $\Delta_s \to \infty$, the ice will flow due to shearing at $x = -x_0$, with no sliding along the bedrock.

Finally, we complete the model with the evolution equations for the upper and lower surfaces of the ice sheet. The surfaces $\theta(x,t)$ and $s(x,t)$ evolve from $t = 0$ to $t = T$ according to the free boundary equations

$$\frac{\partial s}{\partial t} + u\frac{\partial s}{\partial x} - w = 0 \quad \text{on } (-x_0, L - x_0) \times (0, T], \tag{5.23a}$$

$$\frac{\partial \theta}{\partial t} + u\frac{\partial \theta}{\partial x} - w = 0 \quad \text{on } (-x_0, L - x_0) \times (0, T], \tag{5.23b}$$

together with the boundary conditions

$$\theta(-x_0, t) = b(-x_0) \quad \text{and} \quad s(-x_0, t) = b(-x_0) + H \quad \text{for } 0 < t \leq T, \tag{5.24}$$

and initial conditions for s and θ at $t = 0$. As explained in Section 1.4, we do not add any source terms to (5.23) because in the problems under consideration here we assume all of the ice flux to be delivered into the domain through the left hand inflow boundary Γ_i.

5.2.2 The shallow stream/shelf approximation (SSA)

Marine ice sheets are commonly modelled with a depth-integrated approximation of the Stokes equations. This approximation is often referred to as the shallow stream approximation when the ice is grounded and as the shallow shelf approximation when it is floating. In either case, throughout this chapter we will refer to it as the SSA.

The SSA is based on three fundamental assumptions: first, that the ice sheet is shallow and smooth, such that the unit vectors normal to its surface are approximately vertical;

second, that the vertical component of the Cauchy stress tensor is in hydrostatic balance; and third, that the ice flows like a plug flow with no vertical variations in its velocity field. Early derivations of the the SSA can be found in [74] for ice shelves and in [71] for ice streams. A more recent exposition is contained in [44, Chapter 6].

In this chapter, we will write the components of the Cauchy stress tensor $\boldsymbol{\sigma}$ and its deviatoric component τ as

$$\boldsymbol{\sigma} = \begin{bmatrix} \sigma_{xx} & \sigma_{xz} \\ \sigma_{xz} & \sigma_{zz} \end{bmatrix} \quad \text{and} \quad \tau = \begin{bmatrix} \tau_{xx} & \tau_{xz} \\ \tau_{xz} & \tau_{zz} \end{bmatrix}. \tag{5.25}$$

The vertical component of the momentum balance equation (5.6a) can be written as

$$\frac{\partial \sigma_{xz}}{\partial x} + \frac{\partial \sigma_{zz}}{\partial z} = \rho g. \tag{5.26}$$

As explained in [44, Section 5.2], the shear stress σ_{xz} is generally small compared to the vertical stress σ_{zz}. If we neglect the shear term in (5.26), we deduce that the vertical stress is in hydrostatic balance; that is,

$$\sigma_{zz} = -\rho g(s - z) \tag{5.27}$$

after integrating and using the fact that $\sigma_{zz} = 0$ at $z = s$ due to the boundary condition (5.8). As a consequence, the momentum balance equation in the horizontal direction takes the following form:

$$2\frac{\partial \tau_{xx}}{\partial x} + \frac{\partial \tau_{xz}}{\partial z} = \rho g \frac{\partial s}{\partial x}. \tag{5.28}$$

We now proceed to reduce the problem to one dimension by integrating along the depth of the ice sheet. To this end, we introduce the ice thickness variable

$$h(x,t) = s(x,t) - \theta(x,t) \tag{5.29}$$

and the depth-integrated extensional stress and velocity

$$\overline{\tau}_{xx} = \frac{1}{h}\int_\theta^s \tau_{xx}\,\mathrm{d}z \quad \text{and} \quad \overline{u} = \frac{1}{h}\int_\theta^s u\,\mathrm{d}z. \tag{5.30}$$

Then, by integrating (5.28) from $z = \theta$ to $z = s$ and applying Lebniz's rule of integration, we arrive at the following equality:

$$2\frac{\partial}{\partial x}\left(h\overline{\tau}_{xx}\right) - \left[\tau_{xz} - 2\frac{\partial \theta}{\partial x}\tau_{xx}\right]_{z=\theta} = \rho g h \frac{\partial s}{\partial x}. \tag{5.31}$$

The boundary term in (5.31) is handled differently depending on whether the ice sheet is grounded or floating. Below, we consider both cases and derive the corresponding SSA equations. Finally, we show how these two derivations can be used to formulate a free boundary problem for the complete marine ice sheet problem.

Grounded ice

For grounded ice, located in the interval $(-x_0, x_g)$, we enforce the friction law (5.15) along the base $z = \theta$. At this point, we must assume that variations in the bedrock slope are small. This allows us to rewrite (5.15) as

$$2\frac{\partial\theta}{\partial x}\tau_{xx} - \tau_{xz} = -C|u|^{1/n-1}u \quad \text{on } \Gamma_a. \tag{5.32}$$

As a result, for grounded ice, the momentum balance equation for the SSA is

$$2\frac{\partial}{\partial x}\left(h\overline{\tau}_{xx}\right) - C|u|^{1/n-1}u = \rho g h\frac{\partial s}{\partial x} \quad \text{on } (-x_0, x_g). \tag{5.33}$$

Finally, by appealing to our assumption of a plug flow, we find that

$$2\mathcal{A}^{-1/n}\frac{\partial}{\partial x}\left(h\left|\frac{\partial\overline{u}}{\partial x}\right|^{1/n-1}\frac{\partial\overline{u}}{\partial x}\right) - C|\overline{u}|^{1/n-1}\overline{u} = \rho g h\frac{\partial s}{\partial x} \quad \text{on } (-x_0, x_g). \tag{5.34}$$

Floating ice

In the interval $(x_g, L-x_0)$, where ice is floating, we enforce the boundary condition (5.11) at the base of the shelf. By neglecting the shear stress and applying the hydrostatic expression for the vertical stress term (5.27), we deduce the flotation condition,

$$-\rho h = \rho_w\theta, \tag{5.35}$$

which corresponds with Archimedes' principle. Then, by taking the horizontal component of (5.11) and, once again, using (5.27), we see that

$$(2\tau_{xx} - \rho g h)\frac{\partial\theta}{\partial x} - \tau_{xz} = \rho_w g\theta\frac{\partial\theta}{\partial x}. \tag{5.36}$$

As a result of the flotation condition (5.35), we find that $2\tau_{xx} - \tau_{xz} = 0$ at $z = \theta$ and that $s = \delta h$. Hence, we may write

$$2\frac{\partial}{\partial x}\left(h\overline{\tau}_{xx}\right) = \rho g\delta h\frac{\partial h}{\partial x} \quad \text{on } (x_g, L - x_0). \tag{5.37}$$

for the SSA on a floating ice shelf. At the calving front, (5.11) implies that

$$2h\overline{\tau}_{xx} = \frac{1}{2}\rho g\delta h^2 \quad \text{at } x = L - x_0. \tag{5.38}$$

Therefore, by integrating (5.37) from a point $x_g < x < L - x_0$ to the calving front, and using (5.38), we find that the depth-integrated stress $\overline{\tau}_{xx}$ along the shelf can be expressed as

$$\overline{\tau}_{xx} = \frac{1}{4}\rho g\delta h \quad \text{on } (x_g, L - x_0). \tag{5.39}$$

The SSA formulation of the parallel slab marine ice sheet problem

The SSA formulation of the parallel slab marine ice sheet problem is written in terms of three unknowns: the depth-averaged velocity $\overline{u}$, the ice thickness h, and the grounding line position x_g. The momentum equation for the SSA, which we have derived above in (5.34) for grounded ice and in (5.39) for floating ice, must be complemented with the thickness equation, which is a reformulation of conservation of mass in terms of the ice thickness. A derivation can be found in [44, Section 5.1.3]. By vertically integrating (5.6b) along the depth of the ice sheet and using the free boundary equations (5.23), we obtain

$$\frac{\partial h}{\partial t} + \frac{\partial}{\partial x}\left(h\overline{u}\right) = 0 \quad \text{on } (-x_0, L - x_0). \tag{5.40}$$

We note that, unlike the momentum equations (5.34) and (5.39), no simplifying assumptions on the ice flow are required for the derivation of (5.40).

Finally, in order to close the SSA formulation of the parallel slab problem, we need a boundary condition at $x = -x_0$. Towards $x = -x_0$, we want the flow of ice to approach the parallel slab solution with thickness H, as in Figure 5.1. When assuming the SSA to hold, the parallel slab differs from (5.17) because we assume the ice to behave like a plug flow. We can obtain the parallel slab velocity for the SSA by setting the derivatives for $\overline{u}$ and h to zero in (5.34); this yields

$$\overline{u}_{s,SSA} = \left(\frac{\rho g H \tan\beta}{C}\right)^n. \tag{5.41}$$

because $\partial b/\partial x = -\tan\beta$. In this case, the incoming flux for the SSA is given by

$$\overline{q}_{s,SSA} = \left(\frac{\rho g \tan\beta}{C}\right)^n H^{n+1}. \tag{5.42}$$

Several combinations of boundary conditions for h and $\overline{u}$ are available. For example, one can set the velocity to (5.41) and the thickness to H as Dirichlet boundary conditions. From a numerical point of view, we obtained the most accurate solutions by setting a Neumann condition of zero extensional stresses together with a Dirichlet condition for the ice thickness:

$$2\mathcal{A}^{-\frac{1}{n}} h \left|\frac{\partial \overline{u}}{\partial x}\right|^{\frac{1}{n}-1} \frac{\partial \overline{u}}{\partial x} = 0 \quad \text{and} \quad h = H \quad \text{at } x = -x_0. \tag{5.43}$$

When we impose (5.43), the difference between $\overline{u}(-x_0)$ and $\overline{u}_{s,SSA}$ is an indicator for how close our solution is to that of a slab flow at $x = -x_0$.

When solving the SSA of a two-dimensional marine ice sheet (which results in a one-dimensional problem), the ice shelf does not need to be considered. As explained in [89], thanks to the possibility of integrating the SSA momentum equation along the ice shelf, it is sufficient to solve (5.34) and (5.40) along $(-x_0, x_g)$, together with boundary conditions (5.43) at $x = -x_0$ and (5.35) and (5.39) at $x = x_g$.

5.3 Steady grounding line configurations

We compute steady grounding line positions on a bedrock of angle $\beta = 1°$ for different combinations of material parameters. We examine the resulting flux-thickness relationships in Section 5.3.2 and compare some of these results with depth-integrated models for grounded and floating ice in Section 5.3.3. These computations reveal a structure in the flux-thickness relationships at the grounding line that motivate the investigations of Section 5.4. The two models for a marine ice sheet presented in the previous section, based on the Stokes equations and the SSA, are used to compute these steady configurations. Although this chapter focuses primarily on understanding the transition region resulting from the Stokes equations, we also include the SSA of the parallel slab marine ice sheet in order to understand its accuracy and how it compares with Schoof's law (5.3).

5.3.1 Computational considerations

For the Stokes equations, we advance the marine ice sheet in time from an initial position that is either given by the SSA, whenever the flow is dominated by sliding, or by a constant thickness slab of ice that goes afloat as soon as the flotation condition (5.35) holds. We solve the viscous contact problem using the solver presented in Section 2.3 with a mesh constructed with Gmsh [39] which is refined around the initial position of the grounding line to a mesh size of around $H/10$. Whenever the final position of the grounding line differs greatly from its initial position, we remesh and continue the computations in order to have a high degree of mesh refinement near the grounding line's final position. In general, the meshes we consider have around 10^4 cells. Ideally, we would prefer finer cells around the grounding line, but this requires smaller time steps for the scheme to be stable. The combination of longer computational times to solve the nonlinear Stokes system together with more steps in time to reach a steady state makes finer computations infeasible.

As in the subglacial cavity problem, see Section 4.3.1, we consider a steady state has been reached when the discrete derivative in time of the free surfaces is below a given tolerance which we set to 10^{-2}. In this chapter, we work with the following non-dimensional discrete derivative:

$$D_t^k = \frac{1}{q_s \Delta t} \left(\sum_{i=1}^{M^\theta} \left(x_i^\theta - x_{i-1}^\theta \right) \left| \theta_i^k - \theta_{i-1}^k \right| + \sum_{j=1}^{M^s} \left(x_j^s - x_{j-1}^s \right) \left| s_j^k - s_{j-1}^k \right| \right). \tag{5.44}$$

In (5.44), the notation for the mesh nodes (x_i^θ, θ_i^k) and (x_j^s, s_j^k) follows that of Section 2.1. We choose this discrete derivative because, for the parallel slab marine ice sheet problem, it guarantees that the difference between the incoming flux q_s and the flux through any vertical face Γ that traverses the ice sheet is bounded from above by D_t^k. Indeed, if at

$t = t^k$ we denote by Ω_Γ the portion of the domain Ω^k enclosed between Γ_i and Γ, then by the divergence theorem we find that

$$q_s - \int_\Gamma \boldsymbol{u}_h^k \cdot \boldsymbol{n} \, \mathrm{d}s = \int_{\overline{\Omega}_\Gamma \cap \Gamma_b^k} \boldsymbol{u}_h^k \cdot \boldsymbol{n} \, \mathrm{d}s + \int_{\overline{\Omega}_\Gamma \cap \Gamma_t^k} \boldsymbol{u}_h^k \cdot \boldsymbol{n} \, \mathrm{d}s.$$

Now, since we advance the free boundary by using the average-wise values of $\boldsymbol{u}_h^k \cdot \boldsymbol{n}$ along the mesh edges, see (2.17), we have that

$$\begin{aligned} &\left| \int_{\overline{\Omega}_\Gamma \cup \Gamma_b^k} \boldsymbol{u}_h^k \cdot \boldsymbol{n} \, \mathrm{d}s + \int_{\overline{\Omega}_\Gamma \cup \Gamma_t^k} \boldsymbol{u}_h^k \cdot \boldsymbol{n} \, \mathrm{d}s \right| \leq \\ &\frac{1}{\Delta t} \left(\sum_{i=1}^{M^\theta} \left(x_i^\theta - x_{i-1}^\theta \right) \left| \theta_i^k - \theta_{i+1}^k \right| + \sum_{j=1}^{M^s} \left(x_j^s - x_{j-1}^s \right) \left| s_j^k - s_{j+1}^k \right| \right) \end{aligned} \tag{5.45}$$

As a result,

$$\left| q_s - \int_\Gamma \boldsymbol{u}_h^k \cdot \boldsymbol{n} \, \mathrm{d}s \right| \leq q_s D_t^k.$$

For the parallel slab marine ice sheet problem, L and x_0 should be large enough for the solution around the grounding line to lose its dependence on the length of the grounded ice sheet and shelf. For most of the computations, we find that $x_0 = 2H/\tan\beta$ and $L = x_0 + 2H/\tan\beta$ works well except for very rigid and fast sliding ice sheets, as in the left panels of Figure 5.7, where we set $x_0 = 5H/\tan\beta$ to guarantee that a constant ice thickness is maintained around $x = -x_0$. Regarding the time step, we set $\Delta t = 0.01 t_c$, where t_c is a characteristic time given by $t_c = H^2/q_s$. With this time step, we generally need around 10^4 steps to reach a steady state.

As explained in Section 5.2.2, in the case of the SSA of the parallel slab marine ice sheet, we only need to solve the grounded ice sheet. This is because the effect of the ice shelf comes in only as a Neumann boundary condition which enforces (5.39). Since x_g is also an unknown, we effectively have a free boundary problem. Following [88, Appendix A], we solve it numerically by rewriting it in terms of the spatial coordinate $\hat{x} = x/x_g$. As a result, the grounding line position x_g emerges explicitly as a new unknown. We implement a finite element solver in Firedrake [83] and seek the depth-averaged velocity $\overline{u}$ and the ice thickness h in a space of continuous piecewise-linear functions. When seeking steady marine ice sheet configurations with the SSA, we are able to solve the steady problem directly with Newton's method instead of advancing the ice sheet in time from an initial condition. This accelerates the computation of steady states significantly. We work with non-uniform meshes on the unit interval, such that the mesh nodes become increasingly refined towards the rightmost node $\hat{x} = 1$.

5.3.2 The steady flux-thickness relationship at the grounding line

In Figure 5.2, we plot the ice flux q against the ice thickness at the grounding line h for different steady grounding line positions. For each panel, we fix the material parameters n, $\mathcal{A}$, and C and compute steady configurations for different values of the initial slab thickness H with both the Stokes equations and the SSA. For the top panels in Figure 5.2, we consider a linear rheology and set $n = 1$ in Glen's law (1.3). On the other hand, for the lower panels, we set $n = 3$ as is commonly done in glaciology. The material parameters $\mathcal{A}$ and C are set such that the steady solutions to the Stokes equations plotted in the leftmost panels are in a sliding-dominated regime ($\Delta_s < 1$), while in the rightmost panels we have a shear-dominated regime ($\Delta_s > 1$), where we recall that $\Delta_s = C^n \mathcal{A} H$.

Since the SSA assumes a plug flow regime, a large value for Δ_s has a different implication. Numerically, we find that an increase in Δ_s is followed by a thinning of the ice thickness at the grounding line, together with an increase in the magnitude of the surface gradient $|\partial s/\partial x|$ immediately upstream. We provide numerical evidence for this in the upper panels of Figure 5.3, where we plot the SSA solutions around the steady grounding lines. As we explain further below, a consequence of this is that, as Δ_s increases, the SSA approaches the flow regime considered in [89] for deriving the flux-thickness law (5.3). The top panels of Figure 5.3 also include the Stokes solution; we see that, in this case, an increase in Δ_s is also accompanied by an increased surface gradient upstream of the grounding line.

In the sliding-dominated regime (the leftmost panels in Figure 5.2), we find that the SSA yields a very accurate approximation of the Stokes equations. This is natural, because whenever Δ_s is much smaller than one, the influx velocity profile $\hat{u}_s$ for the Stokes equations and, as a result, the flow along the whole ice sheet, closely resembles a plug flow. This is also apparent from the top left panel of Figure 5.3. In this case, we have that $n = 1$, $\mathcal{A} = 10^{-15}\,\mathrm{Pa}^{-1}\,\mathrm{s}^{-1}$, and $C = 10^{10}\,\mathrm{Pa\,m}^{-1}\,\mathrm{s}$; this results in a factor $\Delta_s \approx 5 \times 10^{-3}$, such that the Stokes solution is very close to a plug flow. The grounding line locations differ by about 1 km, an approximation which we consider accurate given that the characteristic lengths involved in this problem are at least of the order of $H/\tan\beta \approx 34\,\mathrm{km}$.

In Figure 5.2, we have also included a least-squares power law fit to the flux-thickness relationships obtained from the Stokes equations and the SSA. Additionally, we display the power law exponent for each of these functions to see how this exponent varies with Δ_s. What Figure 5.2 suggests is that, as Δ_s increases, the slope of the flux-thickness relationship resulting from the Stokes equations increases from $n + 1$ to $n + 2$; this is confirmed in Section 5.4 below, where we present flux-thickness relationships in the limits $\Delta_s \to 0$ and $\Delta_s \to \infty$. We remark that this is in accordance with the prediction made by Chugonov and Wilchinsky [106], who proposed a power law with an exponent of $n+2$ for the flux-thickness

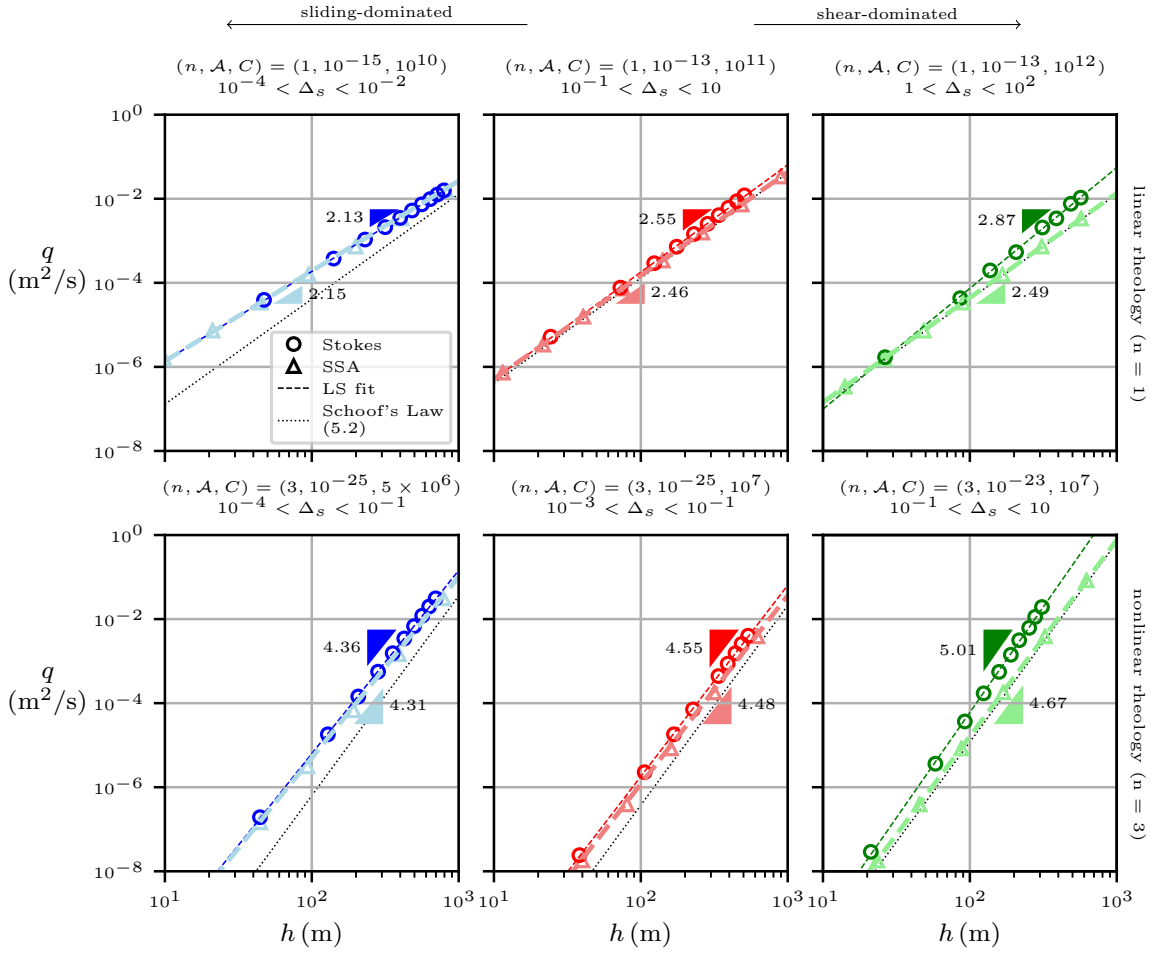

Figure 5.2: The ice flux q plotted against the ice thickness at the grounding line h for different steady grounding line positions. In all cases, the bedrock is inclined with an angle $\beta = 1°$. For each panel, the material parameters n, $\mathcal{A}\,(\mathrm{Pa}^{-n}\mathrm{s}^{-1})$, and $C\,(\mathrm{Pa\,m}^{-n}\mathrm{s}^{n})$ are fixed and steady states are computed for different initial slab thicknesses H with the Stokes equations and the SSA. We include least-squares power law fits for these curves together with the exponent of these laws. We also plot Schoof's law, equation (5.3), as a reference.

relationship at the grounding line for a marine ice sheet with no slip boundary conditions along its grounded region. No slip boundary conditions effectively correspond with the limit $\Delta_s \to \infty$.

For the SSA solutions, we find that the flux-thickness function coincides with Schoof's law (5.3) as Δ_s increases. In this case, the slope of the flux-thickness function computed with the SSA approaches $n+1+n/(n+1)$, which is what one obtains in (5.3) when $m = 1/n$ (this is 2.5 for $n = 1$ and 4.75 when $n = 3$). This approach to (5.3) is expected since, as Δ_s increases, the ice thickness at the grounding line for the SSA decreases, as shown in Figure 5.3. Moreover, due to the parallel slab setup, the divergence of the extensional stresses is eventually zero when the ice is sufficiently upstream of the grounding line, and remains

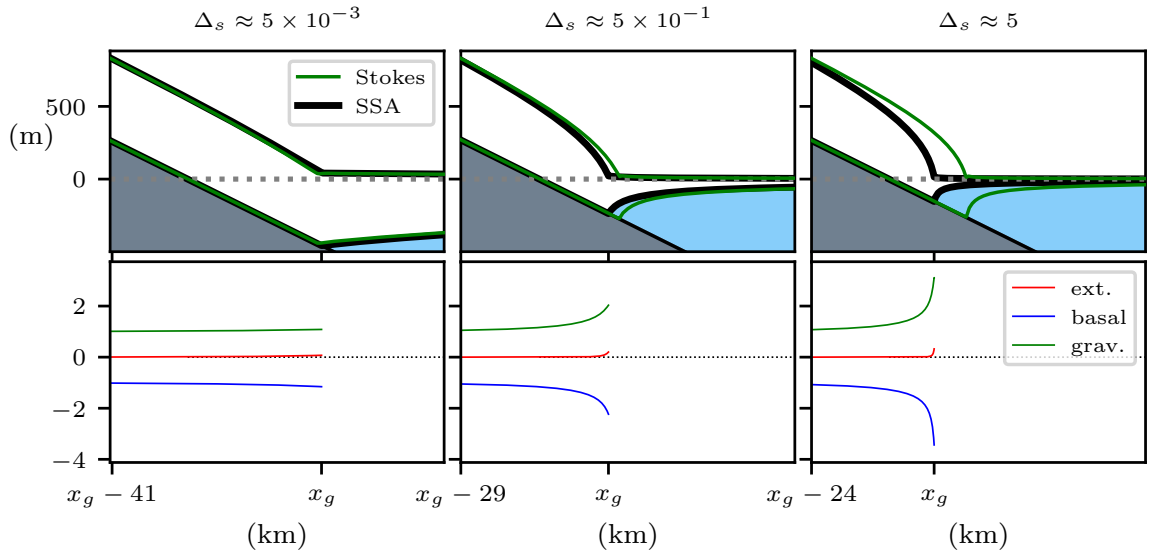

Figure 5.3: Computations of steady marine ice sheets with $H = 577\,\mathrm{m}$, $n = 1$, and $\beta = 1°$ with SSA and Stokes. The parameter Δ_s increases from left to right: we have $\mathcal{A} = 10^{-15}\,\mathrm{Pa}^{-1}\,\mathrm{s}^{-1}$ and $C = 10^{10}\,\mathrm{Pa\,m^{-1}\,s}$ (left), $\mathcal{A} = 10^{-13}\,\mathrm{Pa}^{-1}\,\mathrm{s}^{-1}$ and $C = 10^{10}\,\mathrm{Pa\,m^{-1}\,s}$ (middle), and $\mathcal{A} = 10^{-13}\,\mathrm{Pa}^{-1}\,\mathrm{s}^{-1}$ and $C = 10^{11}\,\mathrm{Pa\,m^{-1}\,s}$ (right). In the upper panels we present the geometry around the grounding line, including a comparison with the Stokes solution. In the lower panels, we show the three terms in the momentum equation for the SSA along the grounded region. Here, "ext." refers to the divergence of the extensional stresses (first term from the left in (5.34)), "basal" to the basal stress term (second term in (5.34)), and "grav." to the gravitational forces (third term in (5.34)).

small for the remainder of the sheet. This becomes apparent by looking at the lower panels of Figure 5.3, where we plot the components of the SSA momentum balance equation (5.34) along the grounded region.

5.3.3 A comparison with depth-integrated models for grounded and floating ice

We now examine in more detail two of the steady states computed with the Stokes equations with $n = 1$ and $H = 577\,\mathrm{m}$. These two states correspond with points in the top left and right panels of Figure 5.2 and are therefore in a sliding and a shear-dominated regime, respectively. We compare the ice sheet geometry and its velocity field with two depth-integrated models, one for the grounded ice and another for the floating ice. The reasons for this comparison are twofold. On the one hand, the accuracy of these models are an additional validation of our Stokes solver for viscous contact problems, since we expect a good agreement. On the other hand, they motivate our investigation in the next section, where we explore analytical derivations of flux-thickness functions. As we explain below, once we have a flux-thickness relationship, we can then calculate the grounding line position and apply these two very

simple depth-integrated models to reconstruct the marine ice sheet.

For the grounded ice on $(-x_0, x_g)$, we consider the shallow ice approximation (SIA) [35]. The SIA can be derived by assuming, on the one hand, that the extensional stress τ_{xx} is negligible against the pressure p and the shear stress τ_{xz}, and, on the other hand, that the ice sheet geometry is shallow and the outwards-pointing normal vectors are therefore vertical. Under these conditions, we find the pressure to be in hydrostatic equilibrium,

$$p = \rho g(s - z), \tag{5.46}$$

and the shear stress to balance gravitational forces in the horizontal momentum balance, such that

$$\tau_{xz} = -\rho g(s - z)\frac{\partial s}{\partial z}. \tag{5.47}$$

By integrating once more, we find the following expression for the horizontal velocity

$$u = -(\rho g h)^n \left|\frac{\partial s}{\partial x}\right|^{n-1} \frac{\partial s}{\partial x}\left(\frac{1}{C^n} + \frac{2\mathcal{A}h}{n+1}\left(1 - \left(\frac{s-z}{h}\right)^{n+1}\right)\right). \tag{5.48}$$

Thus, the ice flux q is given by

$$q = -(\rho g h)^n \left|\frac{\partial s}{\partial x}\right|^{n-1} \frac{\partial s}{\partial x}\left(\frac{h}{C^n} + \frac{2\mathcal{A}h^2}{n+2}\right). \tag{5.49}$$

For the parallel slab marine ice sheet in a steady state, the flux is constant throughout its horizontal extent and equal to q_s. Therefore, by rearranging (5.49) and noting that $s = h + b$, we find the SIA of the steady slab problem, which corresponds with the following ordinary differential equation in h:

$$\frac{\partial h}{\partial x} = -\frac{db}{dx} - \frac{1}{\rho g h}\left[\frac{q_s}{h/C^n + (2\mathcal{A}h^2)/(n+1)}\right]^{1/n} \quad \text{on } (-x_0, x_g). \tag{5.50}$$

The flotation criterion (5.35) for the ice thickness can then be used as a boundary condition at $x = x_g$. Once we calculate the ice thickness, we find the horizontal velocity with (5.48) and then integrated the conservation of mass equation (5.6b) to obtain the vertical component of the velocity field.

Two-dimensional ice shelves are generally modelled with the SSA, as in (5.39) [74]. For the steady slab problem, where $q_s = h\overline{u}$ is constant, we may find an analytical solution to (5.39). To do so, we integrate from the grounding line, where the flotation condition (5.35) applies once more. This yields the following expression for the ice velocity:

$$\overline{u} = \left[\left(\frac{q_s}{h(x_g)}\right)^{n+1} + (n+1)\mathcal{A}\left(\frac{q_s \rho g \delta}{4}\right)^n (x - x_g)\right]^{1/(n+1)} \quad \text{on } (x_g, L - x_0), \tag{5.51}$$

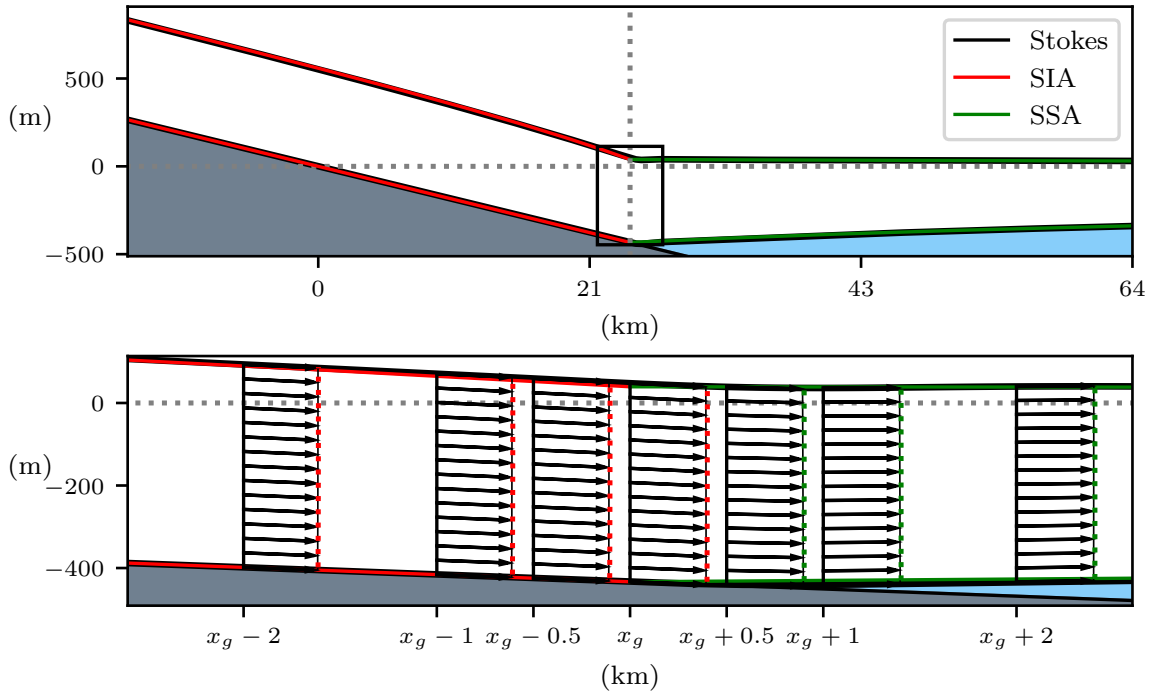

Figure 5.4: (top) Steady marine ice sheet computed with the Stokes equations for a sliding-dominated flow with material parameters $n = 1$, $\mathcal{A} = 10^{-15}\,\mathrm{Pa}^{-1}\,\mathrm{s}^{-1}$, and $C = 10^{10}\,\mathrm{Pa\,m}^{-1}\,\mathrm{s}$. The bedrock is inclined with an angle $\beta = 1°$. In red, the SIA for the grounded sheet, in green the SSA for the floating shelf. (bottom) Close-up around the grounding line including velocity field of the Stokes solution and of the SIA (red) and SSA (green). Both the SIA and SSA profiles for the geometry and the velocity are calculated using the grounding line location x_g from the Stokes solutions.

from which we may calculate the ice geometry with $q_s = h\overline{u}$ and (5.35).

In Figures 5.4 and 5.5, we present the ice sheet geometry and its velocity field around the grounding line for the two steady states we focus on. For the marine ice sheet in Figure 5.4, we set $\mathcal{A} = 10^{-15}\,\mathrm{Pa}^{-1}\,\mathrm{s}^{-1}$ and $C = 10^{10}\,\mathrm{Pa\,m}^{-1}\,\mathrm{s}$, and therefore we have that $\Delta_s \approx 5 \times 10^{-3}$. Hence, in this case, the flow regime is dominated by sliding. On the other hand, the computations for Figure 5.5 are carried out with $\mathcal{A} = 10^{-13}\,\mathrm{Pa}^{-1}\,\mathrm{s}^{-1}$ and $C = 10^{12}\,\mathrm{Pa\,m}^{-1}\,\mathrm{s}$. In this case, we have that $\Delta_s \approx 50$, so that shear dominates the ice flow. The prevalence of these flow regimes is visible when observing the lower panels of Figures 5.4 and 5.5: in Figure 5.4, the velocity shows no visible vertical variations, whilst in Figure 5.5 no sliding appears to occur at the base of the grounded ice sheet. As occurs with the SSA, see Figure 5.3, we observe a much larger surface slope upstream of the grounding line for the higher value of Δ_s, which in the case of the Stokes equations corresponds with a shear-dominated flow.

The ice sheet geometries and the velocity profiles calculated with the SIA over the

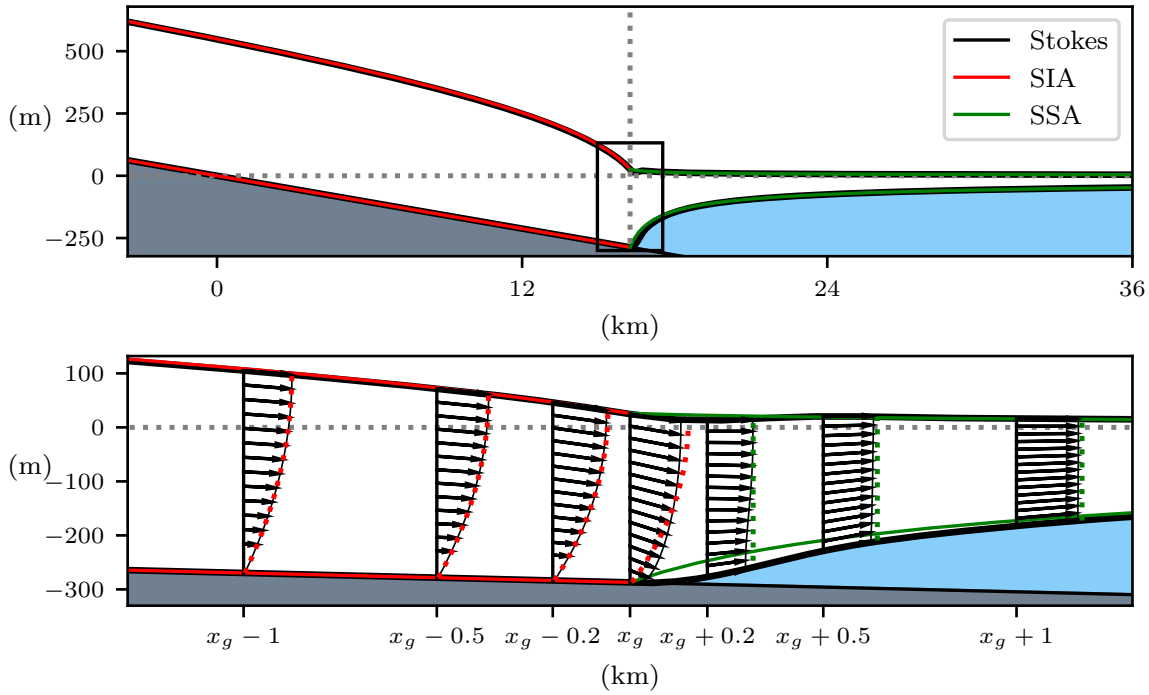

Figure 5.5: (top) Steady marine ice sheet computed with the Stokes equations for a shear-dominated flow with material parameters $n = 1$, $\mathcal{A} = 10^{-13}\,\mathrm{Pa}^{-1}\,\mathrm{s}^{-1}$, and $C = 10^{12}\,\mathrm{Pa\,m}^{-1}\,\mathrm{s}$. The bedrock is inclined with an angle $\beta = 1°$. In red, the SIA for the grounded sheet, in green the SSA for the floating shelf. (bottom) Close-up around the grounding line including velocity field of the Stokes solution and of the SIA (red) and SSA (green). Both the SIA and SSA profiles for the geometry and the velocity are calculated using the grounding line location x_g from the Stokes solutions.

grounded region and with the SSA at the ice shelf accurately approximate the Stokes solution over most of the ice sheet. In both cases, we find that the flotation criterion (5.35), which sets the ice thickness at the grounding line for the SIA and the SSA, is extremely precise in approximating the ice thickness at x_g resulting from the Stokes equations. When sliding dominates, we have that $h(x_g) + b(x_g)\rho_w/\rho_i \approx 8\,\mathrm{m}$, and in the case of a shear-dominated flow, $h(x_g) + b(x_g)\rho_w/\rho_i \approx -1\,\mathrm{m}$.

For the sliding-dominated case, in Figure 5.4, the differences between the Stokes solution and its approximations are hardly visible, in both the ice geometry and the velocity field. However, for the shear-dominated flow in Figure 5.5, we find that the ice shelf geometry is not well approximated immediately downstream of the grounding line, as revealed in the lower panel. In this case, we see that the flow is driven mostly by shearing up to the grounding line, although it quickly evolves into a plug flow. This transition into a plug flow, which does not need to occur in the sliding-dominated case, is seen in the lower panel of Figure 5.5.

The comparisons in the top panels of Figures 5.4 and 5.5 indicate that we can expect a very accurate reconstruction of the ice sheet using very simple models, provided we know the grounding line position x_g. We remark that the SSA system for the complete marine ice sheet, presented in Section 5.2.2, is capable only of approximating the Stokes solutions in a sliding-dominated regime, as seen in Figures 5.2 and 5.3. However, what Figures 5.4 and 5.5 reveal is that the overall accuracy of this joint SIA-SSA approximation remains high for all flow regimes, as long as we have an accurate approximation of the grounding line position.

The comparisons in Figures 5.4 and 5.5 also indicate that, with our parallel slab problem, we are essentially modelling the transition between a grounded SIA flow and a floating SSA flow. In this sense, our problem closely resembles the one considered by Nowicki and Wingham [76] and mentioned in Section 5.1, with the important difference that we enforce the contact boundary conditions.

5.4 Parametrising the steady grounding line position

The computations presented in Section 5.3 reveal, on the one hand, that the steady flux-thickness relationships at the grounding line for the parallel slab problem appear to have a very specific structure: in the limits of sliding and shear-dominated flows, this relationship tends towards power laws of exponents $n+1$ and $n+2$, respectively, see Figure 5.2. On the other hand, the grounded and floating regions of a steady marine ice sheet, computed with the Stokes equations, are approximated excellently by the SIA and the SSA, respectively, as seen in Figures 5.4 and 5.5.

These two findings motivate an investigation of the flux-thickness relationship at the grounding line. If we are able to understand this relationship and construct a good approximation of it, we then have an accurate and simple model for steady marine ice sheets, since a flux-thickness function, in conjunction with the flotation condition (5.35), allows us to find the grounding line position. For this reason, an approximation of the flux-thickness function at the grounding line essentially amounts to a parametrisation of the steady grounding line position. We remark that, for unsteady problems, parametrisations of the grounding line usually require additional equations which are no longer algebraic relationships between flux and thickness, see for example [86].

In this section we explore two approximations of the steady flux-thickness relationship at the grounding line, one valid in the sliding-dominated limit ($\Delta_s \to 0$) and the other in the limit of pure shear ($\Delta_s \to \infty$). Following existing approaches in the literature [89, 86, 80, 95], we construct grounding line parametrisations by equating an approximation of the depth-averaged extensional stress upstream of the grounding line with its downstream

counterpart. We recall that the extensional stress τ_{xx} is determined with the power-law rheology (i.e. Glen's law in glaciology),

$$\tau_{xx} = \mathcal{A}^{-1/n} \left(\frac{1}{2} |\mathbf{D}\boldsymbol{u}|^2 \right)^{\frac{1-n}{2n}} \frac{\partial u}{\partial x}, \tag{5.52}$$

as explained in Section 1.3.

5.4.1 The sliding-dominated case

For a steady marine ice sheet whose flow is mostly driven by sliding, we may assume that velocity variations in the horizontal directions are larger than those along the vertical, such that

$$\frac{1}{2} |\mathbf{D}\boldsymbol{u}|^2 \approx \left| \frac{\partial u}{\partial x} \right|^2. \tag{5.53}$$

As a result, we may approximate τ_{xx} as

$$\tau_{xx} \approx \left(\frac{1}{\mathcal{A}} \frac{\partial u}{\partial x} \right)^{1/n}, \tag{5.54}$$

where we set $\partial u/\partial x > 0$, as expected near the grounding line for the slab problem. Now, by assuming that vertical variations in $\partial u/\partial x$ are negligible, we have that

$$\overline{\tau}_{xx} \approx \left(\frac{1}{\mathcal{A}} \frac{\partial \overline{u}}{\partial x} \right)^{1/n}. \tag{5.55}$$

We can rewrite (5.55) in terms of the ice thickness by noting that $q = \overline{u}h$, and therefore

$$\frac{\partial \overline{u}}{\partial x} = -\frac{q}{h^2} \frac{\partial h}{\partial x}. \tag{5.56}$$

For the grounded flow, the SIA provides an accurate approximation of the ice sheet solution. In the limit of pure sliding, equation (5.49) becomes

$$q = -\left(\frac{\rho g}{C} \right)^n \left| \frac{\partial s}{\partial x} \right|^{n-1} \frac{\partial s}{\partial x} h^{n+1}. \tag{5.57}$$

We then obtain an approximation of $\overline{\tau}_{xx}$ upstream of the grounding line by substituting (5.56) and (5.57) into (5.55), and using the fact that $h = s + b$. This leads to the following approximation for the depth-averaged extensional stress $\overline{\tau}_{xx}$ upstream of x_g:

$$\overline{\tau}_{xx}^{\mathrm{SIA}} = \left(\frac{q}{\mathcal{A}h^2} \left(\frac{Cq^{1/n}}{\rho g h^{(n+1)/n}} + \frac{db}{dx} \right) \right)^{1/n} \quad \text{on } (-x_0, x_g). \tag{5.58}$$

Downstream of the grounding line, we use the SSA to approximate the flow along the ice shelf. In this case, (5.39) implies that

$$\overline{\tau}_{xx}^{\mathrm{SSA}} = \frac{1}{4} \delta \rho g h \quad \text{on } (-x_g, L - x_0). \tag{5.59}$$

Now, equating (5.58) with (5.59) leads to the following implicit flux-thickness relationship at the grounding line after reordering the terms:

$$\left(\frac{C}{\rho g h^{(n+1)/n}}\right) q^{\frac{n+1}{n}} + \frac{db}{dx} q = \mathcal{A}\left(\frac{\delta \rho g}{4}\right)^n h^{n+2} \quad \text{at } x = x_g. \tag{5.60}$$

Whenever the surface gradient $\partial s/\partial x$ is approximately equal to the thickness gradient $\partial h/\partial x$, we can neglect the bedrock slope in (5.58) and we recover Schoof's law (5.3) for the case where $m = 1/n$. For our bedrock, we have that $db/dx = -\tan\beta$. By defining

$$q_* = h^{n+1}\left(\frac{\rho g \tan\beta}{C}\right)^n \quad \text{and} \quad h_* = \frac{\tan\beta}{\mathcal{A}}\left(\frac{4\tan\beta}{\delta C}\right)^n, \tag{5.61}$$

we may introduce the non-dimensional variables

$$\hat{q} = \frac{q}{q_*} \quad \text{and} \quad \hat{h} = \frac{h}{h_*} \tag{5.62}$$

into (5.60) and obtain the following equation:

$$\hat{q}^{\frac{n+1}{n}} - \hat{q} = \hat{h}. \tag{5.63}$$

By examining (5.63), we can show that (5.60) implicitly defines a monotonically increasing function $q = q(h)$ for all $h > 0$.

Lemma 5.1. *Let $db/dx = -\tan\beta < 0$, as in the parallel slab problem. Then, there exists a well defined function $q = q(h)$ for all $h > 0$ such that (5.60) holds for each pair (h, q), with the additional property that $q(h) > 0$ for all $h > 0$. Moreover, this function $q = q(h)$ is strictly monotonically increasing for all $h > 0$.*

Proof. Equation (5.63) defines a function $\hat{q} \mapsto \hat{h}$ from $(1, \infty)$ to $(0, \infty)$ which is strictly monotonically increasing. Therefore, we can define the function $\hat{q} = F(\hat{h})$ for all $\hat{h} > 0$, which is also strictly monotonically increasing. As a result, the relationship $q = q(h)$ is given by

$$q = h^{n+1}\left(\frac{\rho g \tan\beta}{C}\right)^n F(h/h_*), \tag{5.64}$$

and the statement of the lemma follows. □

In order to test the accuracy of (5.60), we first plot the non-dimensional values $(\hat{q}, \hat{h})$ for several sliding dominated regimes with $\Delta_s < 1$ and compare these with (5.63) in Figure 5.6. These results indicate, on the one hand, that with the non-dimensionalisation (5.62) the different points $(\hat{q}, \hat{h})$ collapse onto a single curve for different values of n. On the other hand, Figure 5.6 also indicates that (5.63) is not fully capable of predicting the results

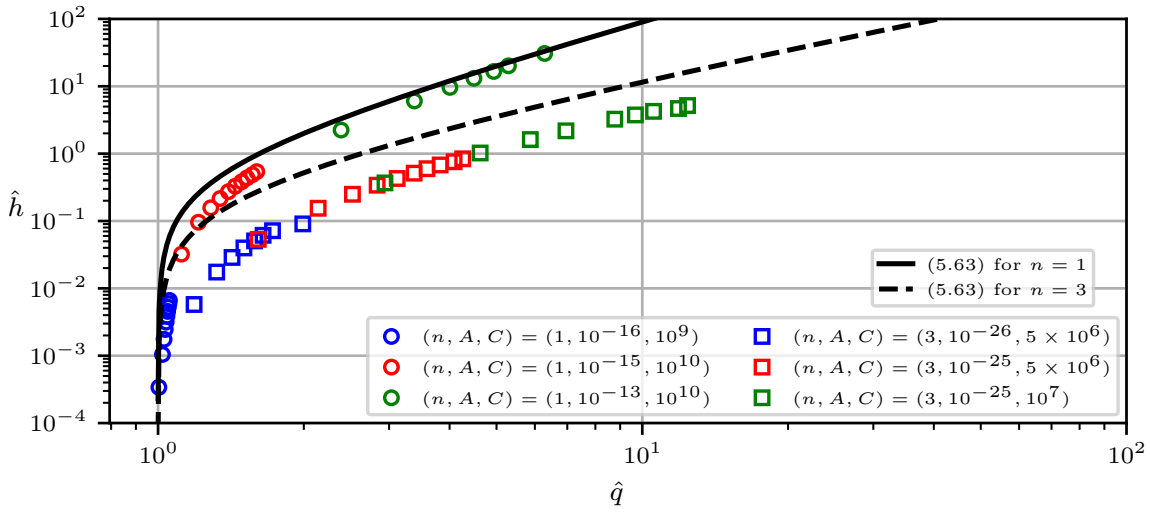

Figure 5.6: Non-dimensional ice flux $\hat{q}$ and ice thickness $\hat{h}$ at the grounding line for different steady grounding line configurations. In all cases, the bedrock is inclined with an angle $\beta = 1°$. For each panel, the material parameters n, $\mathcal{A}\,(\mathrm{Pa}^{-n}\mathrm{s}^{-1})$, and $C\,(\mathrm{Pa\,m}^{-n}\mathrm{s}^{n})$ are fixed and steady states are computed for different initial slab thicknesses H with the Stokes equations. We compare the results with (5.63).

computed with the Stokes equations. We see that, overall, the slope of these curves is captured accurately and that it performs better for $n = 1$ than for $n = 3$.

We can obtain further insight into the accuracy of (5.60) by comparing the dimensional values of (h, q) at the grounding line with (5.60). We plot the resulting flux-thickness relationships in Figure 5.7, together with (5.60). We also plot Schoof's law (5.3) as a reference. The top panels in Figure 5.7 correspond with calculations with a linear rheology $n = 1$, while the lower panels are computed for a nonlinear rheology $n = 3$. These panels are ordered such that Δ_s increases from left to right. From Figure 5.7, we deduce that (5.60) provides an excellent approximation of the flux-thickness relationship when $n = 1$. On the other hand, for $n = 3$, the accuracy of this approximation appears to deteriorate. Moreover, as expected, the flux-thickness relationship (5.60) approaches Schoof's law as Δ_s increases. However, for the flow regimes we consider here, Schoof's law is not a good approximation of the Stokes solution, indicating that the shape of the bedrock is in fact important in most cases. More specifically, from the derivation of (5.60), we see that this is the case because in general the surface slope $\partial s/\partial x$ is of the same order as the bedrock slope $\partial b/\partial x$. As already indicated in Section 5.1, we note that this situation is observed in many West Antarctic ice streams. Below, we look closely into three steady configurations and explore the validity of the assumptions made above in the derivation of (5.60).

We first examine a steady state corresponding to a point in the upper right panel of Figure 5.7; that is, a steady grounding line configuration for a linear rheology in a moderately

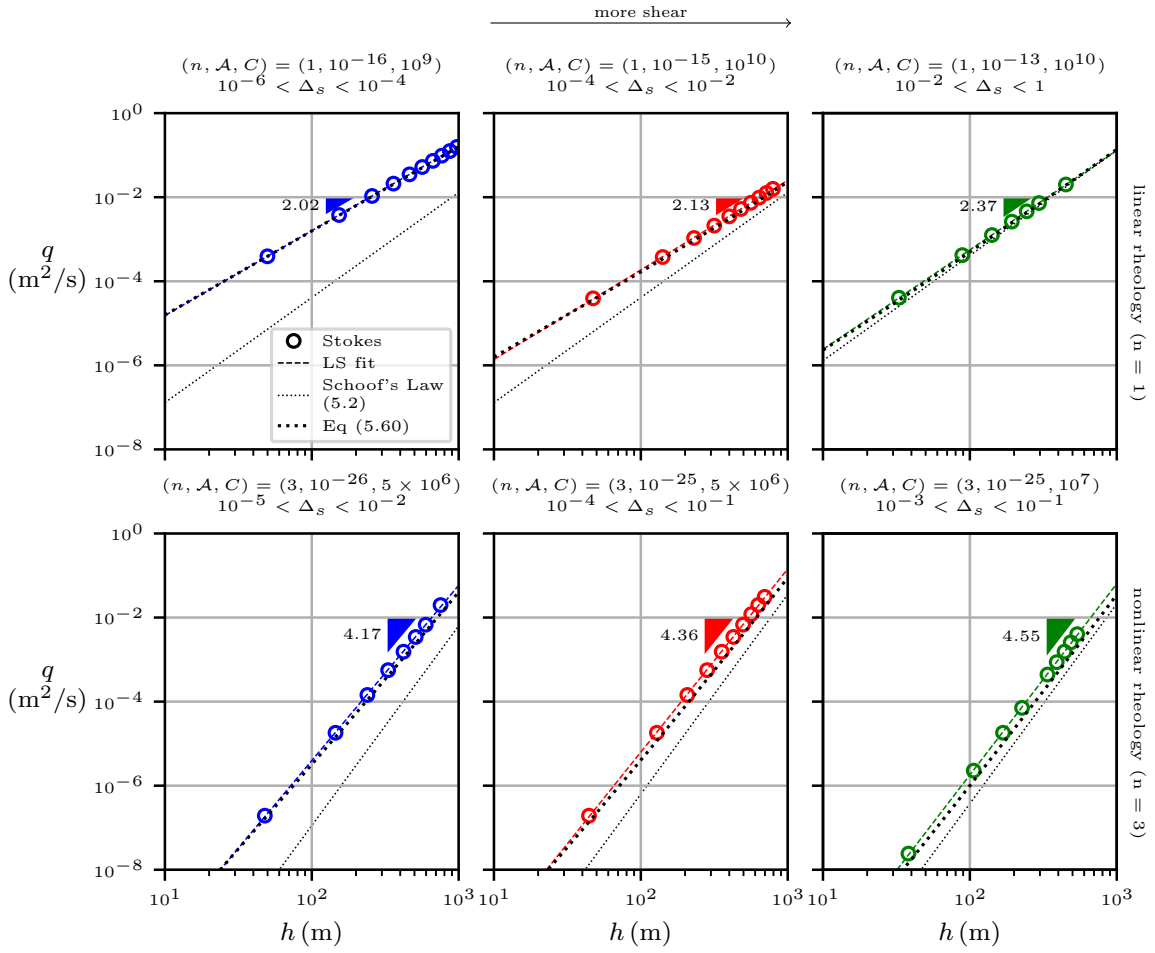

Figure 5.7: The ice flux q plotted against the ice thickness at the grounding line h for different steady grounding line positions. In all cases, the bedrock is inclined with an angle $\beta = 1°$. For each panel, the material parameters n, $\mathcal{A}\,(\mathrm{Pa}^{-n}\mathrm{s}^{-1})$, and $C\,(\mathrm{Pa\,m}^{-n}\mathrm{s}^{n})$ are fixed and steady states are computed for different initial slab thicknesses H with the Stokes equations. We include least-squares power law fits for these curves together with the exponent of these laws. We also plot the implicit flux-thickness relationship (5.60).

fast sliding regime with $\Delta_s \approx 0.5$. In Figure 5.8, we plot the depth-averaged extensional stresses $\overline{\tau}_{xx}$ in the lower panel resulting from the Stokes equations in the vicinity of the grounding line. For this computation, we set the initial slab thickness to $H = 577\,\mathrm{m}$ and the material parameters to $n = 1$, $\mathcal{A} = 10^{-13}\,\mathrm{Pa}^{-1}\,\mathrm{s}^{-1}$, and $C = 10^{10}\,\mathrm{Pa\,m}^{-1}\,\mathrm{s}$. Additionally, we plot expression (5.55), which results from the assumption that the velocity field is close to a plug flow, and the approximations for $\overline{\tau}_{xx}$ resulting from the SIA and SSA and given by (5.58) and (5.59), respectively. From Figure 5.8 we can see that these approximations are accurate along most of the ice sheet, although they do not capture certain variations very close to the grounding line. Importantly, even though $\overline{\tau}_{xx}^{\mathrm{SIA}}$ and $\overline{\tau}_{xx}^{\mathrm{SSA}}$ do not approximate $\overline{\tau}_{xx}$ too well at the grounding line, we do see that $\overline{\tau}_{xx}^{\mathrm{SIA}} \approx \overline{\tau}_{xx}^{\mathrm{SSA}}$ there. This might explain

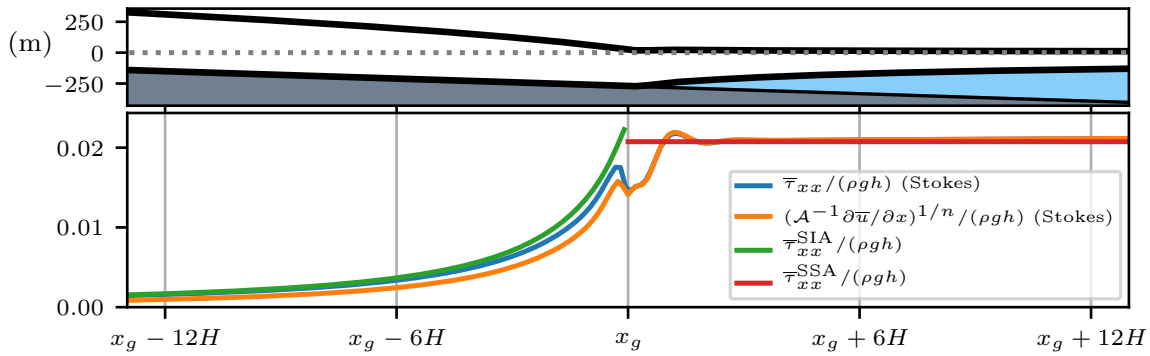

Figure 5.8: Steady marine ice sheet geometry (top) and depth-averaged extensional stresses $\overline{\tau}_{xx}$ (bottom) computed with the Stokes equations with $H = 577\,\mathrm{m}$ and $n = 1$, $\mathcal{A} = 10^{-13}\,\mathrm{Pa}^{-1}\,\mathrm{s}^{-1}$, and $C = 10^{10}\,\mathrm{Pa}\,\mathrm{m}^{-1}\,\mathrm{s}$ (as in the top right panel of Figure 5.2). In the lower panel, we also present three approximations of $\overline{\tau}_{xx}$ based on (5.55), the SIA, and the SSA. We compute these approximations of $\overline{\tau}_{xx}$ by inserting the functions $\overline{u}$ and h computed from the Stokes equations into (5.55), (5.58), and (5.59), respectively.

the relative success of (5.60) in approximating the Stokes solutions in the top right panel of Figure 5.7.

For a very fast sliding ice sheet with $n = 1$, as in the top left panel of Figure 5.7, the situation is very different to the moderately fast sliding one from Figure 5.8. The middle panel of Figure 5.9 presents the depth-averaged extensional stress $\overline{\tau}_{xx}$ and its approximations, as before. In this case, where we have set $H = 577\,\mathrm{m}$ and $n = 1$, $\mathcal{A} = 10^{-16}\,\mathrm{Pa}^{-1}\,\mathrm{s}^{-1}$, and $C = 9^{10}\,\mathrm{Pa}\,\mathrm{m}^{-1}\,\mathrm{s}$, the approximation $\overline{\tau}_{xx}^{\mathrm{SIA}}$ is an order of magnitude larger than $\overline{\tau}_{xx}$ for $x < x_g$. However, (5.55) provides an excellent approximation of $\overline{\tau}_{xx}$ along the grounded region. Therefore, in order to understand what goes wrong here, we plot the surface slope $\partial s/\partial x$, together with its approximation by SIA, computed from (5.57), and the bedrock slope $\partial b/\partial x$ in the lower panel of Figure 5.9. We see that the surface slope is well approximated by the SIA. The issue is that, since the ice hardly thins in this regime, the derivative of the thickness provided by the SIA, which is given by

$$\left[\frac{\partial h}{\partial x}\right]^{\mathrm{SIA}} = -\frac{C}{\rho g}\left(\frac{q}{h^{n+2}}\right)^{1/n} - \frac{db}{dx}, \tag{5.65}$$

is not an accurate approximation of $\partial h/\partial x$, as we can deduce from Figure 5.9. We can see this by noting that the difference between the first and second terms in the right hand side of (5.65), which in the lower panel of Figure 5.9 is the difference between the yellow and green curves, is much larger than $\partial h/\partial x$, which is given by the difference between the blue and green curves. Now, since we derive (5.58) by introducing (5.65) into (5.60), this causes the inaccuracy of $\overline{\tau}_{xx}^{\mathrm{SIA}}$.

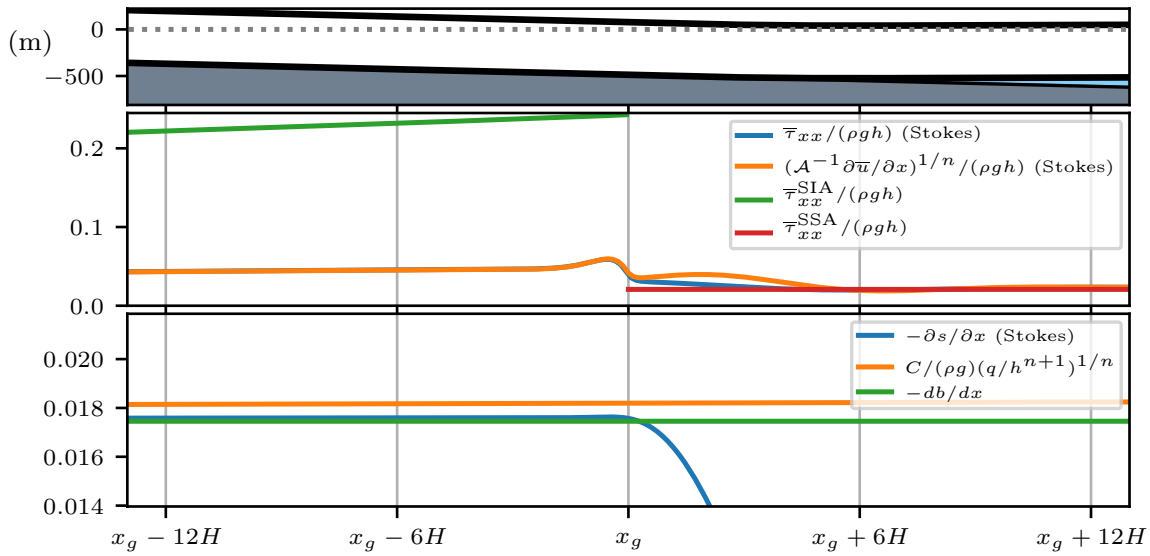

Figure 5.9: Steady marine ice sheet geometry (top), depth-averaged extensional stresses $\overline{\tau}_{xx}$ (middle), and surface slope $\partial s/\partial x$ (bottom) computed with the Stokes equations with $H = 577\,\mathrm{m}$ and $n = 1$, $\mathcal{A} = 10^{-16}\,\mathrm{Pa}^{-1}\,\mathrm{s}^{-1}$, and $C = 10^{9}\,\mathrm{Pa}\,\mathrm{m}^{-1}\,\mathrm{s}$ (as in the top left panel of Figure 5.2). In the middle and lower panels we present approximations of $\overline{\tau}_{xx}$ and $\partial s/\partial x$ based on the SIA (5.57) (middle and lower) and on (5.55) and the SSA (middle). We compute these approximations of $\overline{\tau}_{xx}$ by inserting the functions $\overline{u}$ and h computed from the Stokes equations into (5.55), (5.58), and (5.59), respectively.

Interestingly, although $\overline{\tau}^{\mathrm{SIA}}_{xx}$ fails to approximate $\overline{\tau}_{xx}$, and it is nowhere near $\overline{\tau}^{\mathrm{SSA}}_{xx}$ at $x = x_g$, our estimate (5.60) anyway approximates the flux-thickness relationship excellently in the top-left panel of Figure 5.7. This occurs because, for very low values of Δ_s, the right-hand side of (5.60) becomes approximately zero when compared to the left-hand side. Note that, in the parallel slab problem, whenever the marine ice sheet is in a steady state, the ice flux through any cross section of the ice sheet is given by (5.21). If the flow is dominated by sliding, we may write $q \approx (\rho g \tan\beta/C)^n H^{n+1}$. Then,if we multiply (5.60) by $(C/(\rho g))^n (H\tan\beta)^{-(n+1)}$, which is approximately equal to $1/(q\tan beta)$, we find that

$$(C/(\rho g))^n (H\tan\beta)^{-(n+1)} \left[\left(\frac{C}{\rho g h^{(n+1)/n}}\right) q^{\frac{n+1}{n}} + \frac{db}{dx} q - \mathcal{A}\left(\frac{\delta\rho g}{4}\right)^n h^{n+2}\right] \approx \left(\frac{H}{h}\right)^{\frac{n+1}{n}} - 1 - \Delta_s \left(\frac{h}{H}\right)^{n+1}. \tag{5.66}$$

Since the ice thickness hardly changes in this regime, we have that $h \approx H$, and the last term to the right in (5.66) can be neglected, because $\Delta_s \approx 5 \times 10^{-5}$ in this case. The fact that we can neglect this term in (5.60) means that, in this regime of very fast sliding, we can simplify (5.60) to

$$\frac{C}{\rho g}\left(\frac{q}{h^{n+1}}\right)^{1/n} = -\frac{db}{dx}. \tag{5.67}$$

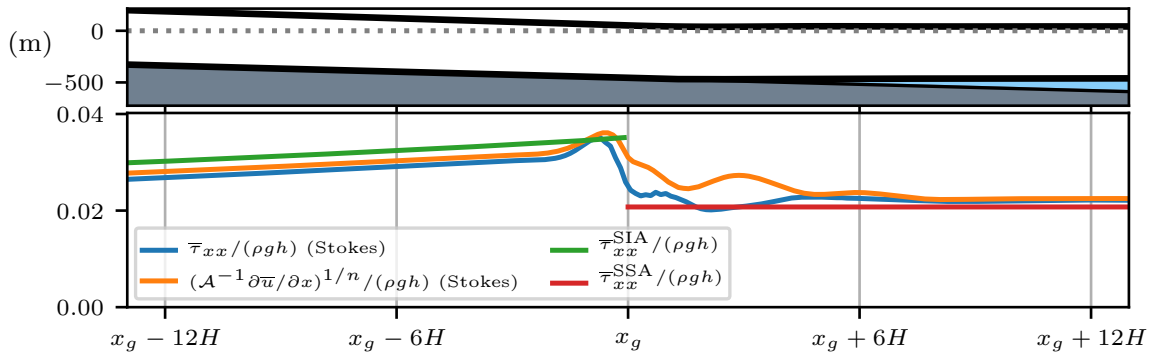

Figure 5.10: Steady marine ice sheet geometry (top) and depth-averaged extensional stresses $\overline{\tau}_{xx}$ (bottom) computed with the Stokes equations with $H = 577\,\mathrm{m}$ and $n = 3$, $\mathcal{A} = 10^{-26}\,\mathrm{Pa}^{-3}\mathrm{s}^{-1}$, and $C = 5 \times 10^6\,\mathrm{Pa\,m}^{-3}\mathrm{s}^3$ (as in the lower left panel of Figure 5.2). In the lower panel, we also present three approximations of the $\overline{\tau}_{xx}$ based on (5.55), the SIA, and the SSA. We compute these approximations of $\overline{\tau}_{xx}$ by inserting the functions $\overline{u}$ and h computed from the Stokes equations into (5.55), (5.58), and (5.59), respectively.

We see from the lower panel of Figure 5.9 that this is indeed the case up to a small error. Equation (5.67) establishes the flux-thickness power law with exponent $n + 1$ that our numerical results suggested.

For all of the steady cases computed with a nonlinear rheology, we find that $\overline{\tau}_{xx}^{\mathrm{SIA}}$ approximates $\overline{\tau}_{xx}$ relatively well. This is unlike the case when $n = 1$, where $\overline{\tau}_{xx}^{\mathrm{SIA}}$ fails to approximate $\overline{\tau}_{xx}$ for very small values of Δ_s. In order to illustrate this, we plot the depth-averaged extensional stresses $\overline{\tau}_{xx}$ and its approximations in Figure 5.10. This steady state corresponds to a point in the lower left panel of Figure 5.7, with a parameter $\Delta_s \approx 7 \times 10^{-4}$. Unlike the linear case with similar values of Δ_s, as in Figure 5.9, we find that our SIA approximation of the extensional stresses is much better. However, in this case we have a relatively large discrepancy between $\overline{\tau}_{xx}^{\mathrm{SIA}}$ and $\overline{\tau}_{xx}^{\mathrm{SSA}}$ at the grounding line. This discrepancy is found in all of the computations with $n = 3$ found in the lower panels of Figure 5.7 and is therefore the reason for the slight deviation between the Stokes solutions and (5.60).

5.4.2 The shear-dominated case

We now investigate the flux-thickness relationship at the grounding line for a steady flow driven purely by shear deformation along its grounded region. To do so, we first derive a simple flux-thickness function for a linear rheology with $n = 1$. As we explain below, when $n > 1$ it is unclear whether a simple algebraic relationship between the ice flux and thickness at the grounding line can be derived. However, in this section we also compute steady grounding line configurations for the nonlinear rheology to give numerical evidence that this relationship takes the form of a power law.

In this derivation, we assume no-slip boundary conditions are enforced for the velocity field along the attached region Γ_a. No-slip boundary conditions hold in the limit where $C \to \infty$; therefore, this flow regime corresponds to the limit $\Delta_s \to \infty$. For $n = 1$, the depth-averaged extensional stress is given by

$$\overline{\tau}_{xx} = \mathcal{A}^{-1} \frac{1}{h} \int_\theta^s \frac{\partial u}{\partial x} \, \mathrm{d}z. \tag{5.68}$$

It is desirable to rewrite (5.68) in terms of the horizontal velocity on the ice sheet's upper surface $u|_{z=s}$ and the gradient of the upper surface $\partial s/\partial x$. This will allow us to introduce the flux q into the expression by introducing the SIA approximation. To do so, we use Leibniz's integration rule to write

$$\frac{1}{h} \frac{\partial}{\partial x} \left(\int_\theta^s u \, \mathrm{d}z \right) = \frac{u|_{z=s}}{h} \frac{\partial s}{\partial x} + \frac{1}{h} \int_\theta^s \frac{\partial u}{\partial x} \, \mathrm{d}z. \tag{5.69}$$

Since we are assuming the ice sheet to be in a steady state, the left-hand side of (5.69) is zero. As a result, we may write that

$$\frac{1}{h} \int_\theta^s \frac{\partial u}{\partial x} \, \mathrm{d}z = -\frac{u|_{z=s}}{h} \frac{\partial s}{\partial x}. \tag{5.70}$$

We now make two additional assumptions in order to find a simple expression for the extensional stresses upstream of the grounding line. As before, we assume the velocity field is closely approximated by the SIA. For pure shear and a linear rheology, the velocity and flux expressions for the SIA, given by (5.49) and (5.48), respectively, yield the following equality:

$$u|_{z=s} \approx \frac{3}{2} \frac{q}{h}. \tag{5.71}$$

On the other hand, we may assume that the surface gradient is approximately equal to the thickness gradient. As we saw in Section 5.3, this is a reasonable assumption for shear-driven flows, where we observe that the ice surface has a large slope immediately upstream of the grounding line. Under this assumption, and using (5.49), we have that

$$\frac{\partial s}{\partial x} \approx \frac{\partial h}{\partial x} \approx -\frac{3q}{2\mathcal{A}} \frac{1}{\rho g h^3}. \tag{5.72}$$

By inserting (5.71) and (5.72) into (5.70), we find the SIA approximation for the extensional stresses along the grounded region of the ice sheet:

$$\overline{\tau}_{xx}^{\mathrm{SIA}} = \frac{9}{4} \frac{q^2}{\mathcal{A}^2 \rho g h^5} \quad \text{on } (-x_0, x_g). \tag{5.73}$$

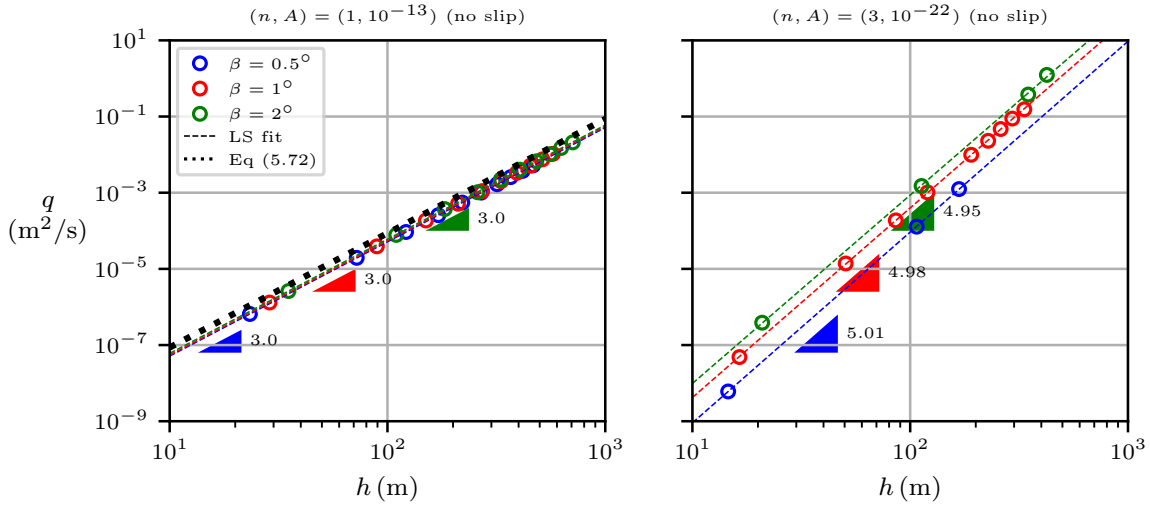

Figure 5.11: The ice flux q plotted against the ice thickness at the grounding line h for different steady grounding line positions. For each panel, the material parameters n and $\mathcal{A}\,(\mathrm{Pa}^{-n}\mathrm{s}^{-1})$ are fixed and steady states are computed for different initial slab thicknesses H and bedrock slopes β with the Stokes equations with no-slip boundary conditions along Γ_a. We include least-squares power law fits for these curves together with the exponent of these laws. We also plot the power law (5.74), for the left panel, where $n = 1$.

For the floating shelf, we use the SSA as in Section 5.4.1 and use expression (5.59) for $\overline{\tau}_{xx}^{\mathrm{SSA}}$. Then by setting it equal to $\overline{\tau}_{xx}^{\mathrm{SIA}}$ at the grounding line, we derive the following flux-thickness power law:

$$q = \frac{2}{3}\sqrt{\frac{\delta}{4}}\mathcal{A}\rho g h^3. \tag{5.74}$$

Expression (5.74) was derived previously in [86]; similarly, the power law (5.1) with exponent $n + 2$ and prefactor to be determined numerically, was proposed in [106] for a flow regime with no-slip conditions. For a nonlinear rheology, additional terms are contained inside the integral in (5.68), and one can no longer find a simple expression as in (5.69) by means of Leibniz's integration rule. We note that, unlike the implicit function (5.60) we find for the sliding-dominated case, there is no dependence on the bedrock shape in (5.74). Below we explore whether this is true for solutions to the Stokes equations with $n = 1$ and 3.

The results in Section 5.3.2, and also (5.74) when $n = 1$, suggest that the flux-thickness relationship at the grounding line takes the form of a power law with exponent $n + 2$ in the limit of pure shear, as $\Delta_s \to \infty$. We provide a numerical confirmation in Figure 5.11, which presents the flux-thickness relationship computed from the steady Stokes system with no slip boundary conditions for $n = 1$ (left panel) and $n = 3$ (right panel). Moreover, we consider three different bedrock angles β in order to test the dependence of the flux-thickness relationship on the bedrock's shape. As expected, the numerical solutions for

$n = 1$ show almost no variations with a change in β. The explanation for this, deduced from our derivation of (5.74), is that the dependence on the bedrock is lost whenever $|\partial b/\partial x|$ is much smaller than $|\partial s/\partial x|$ immediately upstream of the grounding line, which we see happens whenever Δ_s is large (compare Figure 5.5 with Figure 5.4).

For the nonlinear rheology, our numerically-computed flux-thickness relationships are clearly affected by the bedrock slope. A numerical issue arose in these computations that made it impossible to achieve the unsteady tolerance $D_t^k \leq 0.01$. As we approached a steady state, we found that a regime was reached in which the grounding line oscillated between two or three adjacent nodes from one time step to another. For this reason, the discrete time derivative stalled around a value of 0.1. It remains to investigate whether the mismatch between the flux-thickness relationships for $n = 3$ is a consequence of numerical errors or whether the effects of the bedrock slope are no longer negligible when $n = 3$.

For the linear rheology, we also compare (5.74) against the flux-thickness relationships resulting from the Stokes equations in the left panel of Figure 5.11. We find that, although (5.74) perfectly captures the rate of change of q with h, a visible difference can be observed. Our Stokes solutions indicate that, by multiplying the right hand side (5.74) with a prefactor of about 0.65, the resulting power law coincides neatly with the Stokes flux-thickness relationships. In order to understand why this difference might exist, we take one of these steady points and explore the validity of the assumptions underlying the derivation (5.74).

Figure 5.12 contains a detailed examination of a steady Stokes solution around the vicinity of the grounding line. This steady state is computed with a linear rheology and corresponds with a point in the left panel of Figure 5.11. In the middle panel of Figure 5.12, we can see that $\overline{\tau}_{xx}^{\mathrm{SIA}}$, given by expression (5.73), approximates $\overline{\tau}_{xx}$ with a high precision over the grounded region. Two thicknesses downstream of the grounding line, we find that $\overline{\tau}_{xx}$ becomes almost indistinguishable from $\overline{\tau}_{xx}^{\mathrm{SSA}}$. However, there is a transition region in the ice shelf where $\overline{\tau}_{xx}$ departs from its SSA counterpart. This region causes the mismatch between (5.74) and the steady Stokes solutions. As we also saw in Figure 5.5 of Section 5.3.3, the evolution from pure shear to a plug flow in the ice shelf occurs here. We remark that the expression for $\overline{\tau}_{xx}^{\mathrm{SSA}}$, given by (5.59), is derived by assuming the flotation condition (5.35) and the hydrostatic balance (5.27) for the vertical Cauchy stress component. We test these assumptions in the lower panel of Figure 5.12 and find that the flotation condition holds quite closely, but the normal basal stresses visibly depart in this transition region. Therefore, from the lower panel of Figure 5.12 we deduce that an accurate model of the flow along this thin region downstream of the grounding line must dismiss the assumption that the vertical stress is in hydrostatic balance.

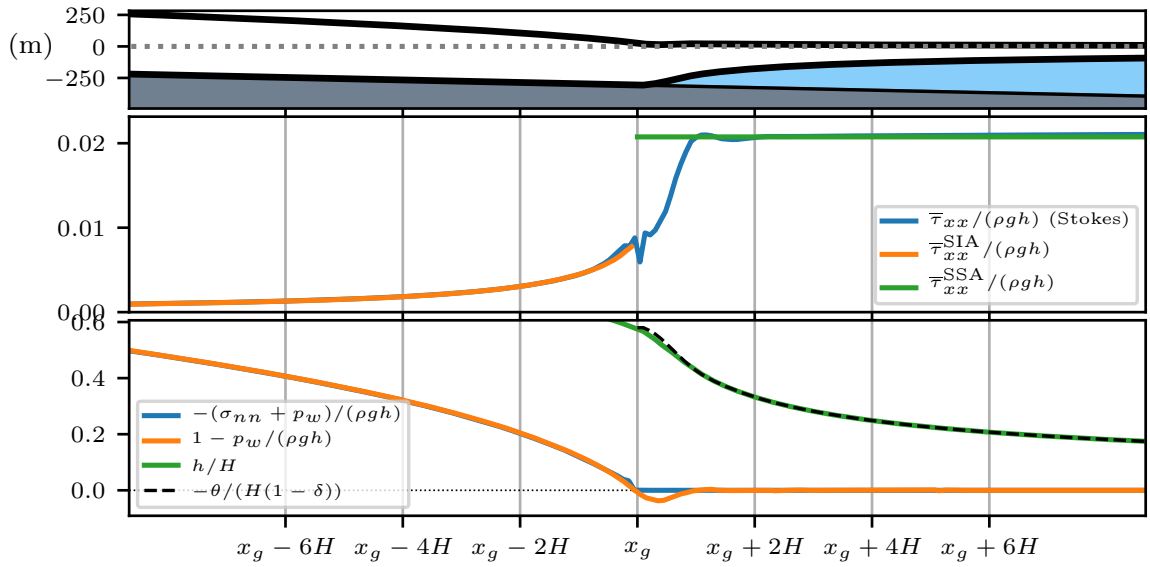

Figure 5.12: Steady marine ice sheet computed with the Stokes equations with $H = 577\,\mathrm{m}$ and $n = 1$, $\mathcal{A} = 10^{-13}\,\mathrm{Pa}^{-3}\mathrm{s}^{-1}$ and $\beta = 1°$ (as in the left panel of Figure 5.11). (top) Marine ice sheet geometry. (middle) Depth-averaged extensional stresses $\overline{\tau}_{xx}$ and approximations with SIA and SSA (using h computed with Stokes). (bottom) Basal normal stresses, together with its hydrostatic approximation, and the ice thickness, also with its hydrostatic approximation.

5.5 Discussion

This chapter contains a numerical exploration of steady flux-thickness relationships at the grounding line for the parallel slab marine ice sheet problem, which we summarised in Section 5.2. The setup of this problem allows us to consider a spectrum of flow regimes, from sliding to shear-dominated flow. Using our solver for viscous contact problems presented in Section 2.3, which solves the Stokes equations with contact boundary conditions, we compute steady grounding line configurations for different flow regimes. The resulting flux-thickness relationships suggest the existence of power laws for pure sliding and pure shear flow. Motivated by this finding, we derive approximations to these flux-thickness relationships in these two flow regimes using two depth-integrated models for marine ice sheets, the SIA and the SSA. In particular, at the grounding line, we find that

$$q \approx \left(\frac{\rho g}{C}\tan(\beta)\right)^n h^{n+1} \quad \text{as } \Delta_s \to 0, \tag{5.75}$$

and

$$q \approx \kappa \frac{2}{3}\sqrt{\frac{\delta}{4}}\mathcal{A}\rho g h^3 \quad \text{for } n = 1 \text{ and as } \Delta_s \to \infty, \tag{5.76}$$

where $\kappa \approx 0.65$ is a prefactor we find numerically. Moreover, Schoof's law (5.3) appears to hold with some accuracy when $\Delta_s \sim 1$; that is,

$$q = \left(\frac{\mathcal{A}(\rho g)^{n+1}(1-\rho/\rho_w)^n}{4^n C} \right)^{n/(n+1)} h^{n+1+n/(n+1)} \quad \text{for } \Delta_s \sim 1. \tag{5.77}$$

Our analytically derived flux-thickness relationships generally exhibit a good, but not perfect, agreement with our Stokes computations. These analytical expressions are found by equating approximations of the extensional stress upstream and downstream of the grounding line, as in [89, 67, 86, 80]. In most cases, we find that these approximations of the stresses do well up to a few ice thicknesses away from the grounding line; however, at the grounding line itself, these approximations can differ, giving rise to the discrepancy we see between the Stokes and the analytically derived flux-thickness relationships. Nevertheless, it is important to note that the analytically derived relationships capture the essential qualities we observe in the Stokes solutions, such as the power laws arising in the limit cases of pure sliding and pure shear, and, when the flow is dominated by sliding, the increasing influence of the bedrock slope as Δ_s (the ratio of shear to sliding in the incoming ice flux) decreases.

Given the scarcity of marine ice sheet computations that solve the full viscous contact problem with the Stokes equations, our results can offer insight into some of the previous findings in the literature, which we summarised in Section 5.1. Regarding Schoof's law (5.3), whose use is widespread, it is interesting to note that most of the steady states we compute in this section depart from this law, see Figures 5.2 and 5.7. In Section 5.4.1, we show that this mismatch is due to the fact that the surface gradient near the grounding line is of the same order as the bedrock gradient. Sergienko and Wingham [95] also explored a situation where these two gradients are of the same order, but in their case they considered flow regimes with very low basal stresses. This is very much unlike our setup, where the parallel slab upstream of the grounding line requires the basal stresses to balance the gravitational forces. However, it is interesting to note that in both cases we arrive at a configuration found in nature, since, as explained in [95], many Antarctic ice streams do not exhibit surface slopes much larger than the bedrock's.

Although the work by Nowicki and Wingham [76] also solved the Stokes equations, in this case contact conditions were not enforced. The authors sought steady states for a flow transitioning from a grounded SIA solution into a floating SSA flow through a fixed grounding line. Then, they checked whether these steady states satisfied the contact conditions or not, although the basal stresses were not inspected close to the grounding line due to the presence of singularities. They claimed that, under certain cases, the flux-thickness relationship arising from Stokes solutions may not be multi-valued, such as in the case of no-sliding. Our results demonstrate the contrary, since both our numerical results and

our analytically derived flux-thickness laws are strictly increasing functions and therefore single-valued.

Another insightful result we obtain that should be compared with previous work is the slight mismatch between the analytically derived power law (5.74) and the Stokes solutions for a pure shear flow when $n = 1$. This case was studied in [86] with an experimental setup that is very similar to our slab problem. Moreover, in [86], the authors also derive (5.74). When comparing their experimental results against (5.74), the mismatch they also find is attributed to experimental conditions that differ from the idealised setup, such as the shear stress exerted by the sidewalls of the tank. However, thanks to our numerical results we can see that the assumptions underlying the derivation of (5.74) are not fully satisfied in the limit of pure shear. In particular, as we show in Section 5.4.2, there is a considerable discrepancy between $\overline{\tau}_{xx}$ and its approximation $\overline{\tau}_{xx}^{\mathrm{SSA}}$ immediately downstream of the grounding line.

One outstanding issue that should be investigated in the future is the dependence of the flux-thickness relationship on the bedrock slope when $n = 3$ and no-slip boundary conditions are enforced. In this case, we had issues converging to a steady state and therefore a different numerical approach for computing steady marine ice sheets should be explored. One possibility would be to implement a solver that, instead of finding a steady state by evolving the system in time, directly solves for the ice surfaces and the Stokes solutions with a nonlinear solver like the semi-smooth Newton method [54]. We expect this approach to also reduce computational times since, at the moment, we usually need to advance in the order of 10^4 time steps before a steady state is reached.

All of our conclusions are deduced in the context of the parallel slab marine ice sheet problem. Therefore, it is natural to ask how our findings extend to different configurations. A proper answer to this question requires a numerical investigation of marine ice sheet problems different to the parallel slab problem, and this is left as future work. However, we can speculate that, in the cases where the bedrock shape becomes unimportant, such as in the limit of pure shear or, in the case of a sliding-dominated flow, for values of Δ_s of unit order, we can expect similar flux-thickness relationships to arise. Another important point to consider in future work is the extension of these results to unsteady problems. It would therefore be interesting to explore how flux-thickness relationships deviate from their steady counterparts under unsteady conditions and investigate the analytical derivation of laws under these conditions. We recall that an unsteady flux-thickness law is required for studying marine ice sheet instabilities, since these are fundamentally unsteady problems.

Chapter 6

Conclusions and further work

This thesis is an investigation into the numerical resolution of viscous contact problems with a focus on applications arising in glaciology. Two problems of fundamental importance in glaciology can be interpreted as viscous contact problems: that of subglacial cavitation and of a marine ice sheet. Below, we gather the conclusions and ideas for future work presented at the end of Chapters 2 to 5. For a more detailed presentation of these points, we refer the reader to Sections 2.5, 3.4, 4.5, and 5.5.

Construction and analysis of numerical schemes for viscous contact problems

Chapters 2 and 3 are concerned with the construction and analysis of numerical schemes for solving two-dimensional viscous contact problems. As we explain in Chapter 1, viscous contact problems can be formulated in terms of the Stokes equations with contact boundary conditions, coupled with two free boundary equations that evolve the fluid domain in time. Very few numerical methods have been proposed for solving these problems, and in most cases the rich mathematical structures underlying these models have been left unexplored. In particular, the Stokes equations with contact boundary conditions can be reformulated as a variational inequality. By noting this property of the Stokes problem, in Chapters 2 and 3 we draw inspiration from the vast literature in computational mathematics focused on variational inequalities (with a particular emphasis on the literature dedicated to elastic contact problems, which can also be reformulated as a variational inequality similar to our Stokes problem).

In Chapter 2, we propose a class of numerical methods for solving viscous contact problems. These methods solve the free boundary equations with an explicit Euler scheme. As a result, the Stokes and free boundary equations are decoupled. At the discrete level, the Stokes variational inequality and the free boundary equations are formulated in terms of abstract normal trace operators, to be chosen when designing a concrete numerical scheme. These trace operators are discrete versions of the operation that maps a vector field to

its normal component along the boundary. We propose two properties that these discrete normal trace operators should satisfy to achieve robust schemes: (1) the operators used for the variational inequality and the free boundary equations should be chosen in a "contact consistent" way to avoid introducing excessive numerical errors into the evolution of the domain, and (2) the discrete free boundary equations should be stabilised due to their advective nature.

We introduce several schemes that fit into this framework, and evaluate their performance by solving two numerical tests. With these tests, we also show the importance of the two properties mentioned above; whenever one of these two properties does not hold, a substantial loss in accuracy can be observed. One of these schemes works particularly well, and we select it to be the main numerical scheme of this thesis with which we carry out the glaciological investigations of the subsequent chapters. This scheme enforces an edge-wise averaged version of the contact boundary conditions with a Lagrange multiplier.

An in-depth analysis of the Stokes variational inequality is provided in Chapter 3. We first give rigorous statements on the conditions under which this variational inequality is well-posed. Then, with the goal of justifying the use of the main scheme of the thesis, we analyse the convergence of solutions to the discrete variational inequality which enforces the contact boundary conditions in an edge-wise averaged manner with a Lagrange multiplier. Two substantial differences arise in this analysis that make it different from its counterparts in elastic contact problems: the nonlinear rheology used in glaciology and the nonlinear friction boundary condition that we enforce for the marine ice sheet problem. An additional difficulty is the presence of rigid body modes in the space of admissible velocities, which render the problem semicoercive. The main contribution of this chapter is the development of analytical tools for dealing with these difficulties. Moreover, our analysis shows that, if the variational inequality is well-posed at the continuous level, we can expect its discrete solution to converge to its continuous counterpart as the mesh is refined.

Several questions are left open in Chapters 2 and 3. Both the design of numerical schemes for the viscous contact problem in Chapter 2 and the analysis of the finite element approximation of the variational inequality in Chapter 3 exploit the two-dimensionality of the problems under consideration. Since three-dimensional problems are very important in glaciology, the extension to three dimensions should be considered carefully in the future. Another question that should be addressed eventually is the construction of implicit schemes that couple the Stokes and free boundary equations. In particular, implicit solvers would pave the way for solving steady viscous contact problems directly with a nonlinear solver, instead of advancing towards the steady solution in time, as we do in Chapters 4 and 5. Finally, a limitation of the finite element analysis of Chapter 3 is that, in order to avoid

certain technical difficulties, we assume the pressure to be approximated with piecewise constant functions, instead of continuous piecewise linear functions, which we use in practice. Therefore, an analysis that dismisses this assumption should be explored.

Glaciological applications of viscous contact problems

This thesis then turns to the two viscous contact problems previously mentioned. The first problem, which is studied in Chapter 4, is that of subglacial cavitation, which takes place in the ice-bedrock interface and is a fundamental mechanism in glacier sliding. Water-filled subglacial cavities form along the downstream side of obstacles when the ice detaches from the bedrock due to high water pressures. In Chapter 5, we study marine ice sheets, which flow from the continent into the ocean, detaching from the bedrock and going afloat at the so-called grounding line. This configuration is found in much of the West Antarctic ice sheet and a vast amount of research has studied the response of these systems to changing climatic conditions.

Our numerical investigation of subglacial cavitation in Chapter 4 formulates the viscous contact problem as a boundary layer between ice and bedrock, as in [36]. For simplicity, we restrict our attention to sinusoidal beds. We first compute steady friction laws as in [36] for different bed amplitudes and parameters n in Glen's law. Then, motivated by a body of research that finds correlations between variations in basal water pressure and surface speeds and uplift, we study glacier sliding under unsteady water pressures. We find that a phase difference emerges between the sliding speed and the cavity volume that increases as the frequency of the water pressure variations also increase. Our results also indicate that, for sufficiently cavitated states, the maximum sliding speed occurs at the instant in time when the minimum water pressure is reached, in line with field measurements from [60, 98, 4]. We also find that, when we enforce the basal shear stress as a Neumann boundary condition, the steady states along the rate-weakening section of the friction law are unstable. When these steady states are perturbed, the cavity quickly evolves towards the rate-strengthening region.

Chapter 5 explores steady grounding line configurations for the parallel slab marine ice sheet problem. In this problem, which we introduce in Chapter 5, a constant thickness slab of ice flows down an inclined bedrock into the ocean. We enforce influx conditions based on the parallel slab solution of the Stokes equations. One advantage of this setup is that we can set the amount of incoming ice flux due to shear and sliding, and in this way we can study a spectrum of flow regimes that range from sliding to shear-dominated flows. We then reconstruct steady ice flux-thickness relationships at the grounding line. This relationship is fundamental for understanding marine ice sheet instabilities and is used

for closing simplified models based on thin film approximations of the grounded and floating regions of the ice sheet. Our main contribution in this chapter is an investigation of what we believe are the first computations of these flux-thickness relationships with the Stokes equations with contact boundary conditions. Our results show that these relationships clearly tend towards power laws in the limits of pure sliding and pure shear. Then, we derive analytical approximations of these flux-thickness relationships in these two limits. Our approximations show a close match to the Stokes solutions, with visible differences in some cases. Our numerical computations and our analytically-derived approximations indicate that the bed slope becomes important in very fast sliding regimes. As the ratio of incoming flux due to sliding and shearing approaches one, the influence of the bed slope decreases and the flux-thickness relationship approaches the power law proposed by Schoof in [89]. Finally, we find a complete independence with the bed slope in the shear-dominated regime for a linear rheology with $n = 1$.

We compute steady states for the viscous contact problems in Chapters 4 and 5 by advancing the model in time from a given initial state. A limitation of this approach is that it is very time consuming. On the one hand, we are forced to use small time steps due to explicit Euler scheme with which we solve the free boundary equations. On the other hand, under certain circumstances, these computations are prolonged or at times even incapable of converging to steady states due to the emergence of oscillating regimes. For example, for the subglacial cavity problem, waves of decreasing amplitude travel along the cavity roof when converging towards a steady state. In the case of the marine ice sheet problem, in some very specific cases, the system does not converge towards a steady state because the grounding line oscillates from one time step to another between two adjacent nodes. This happens for shear-dominated flows with a nonlinear rheology. A possible remedy for these computational challenges is to avoid advancing the system in time but directly solve the complete steady viscous contact problem with a nonlinear Newton-type solver.

Chapter 5 leaves several open questions regarding the validity of our conclusions beyond the steady parallel slab problem that should be addressed in future work. One should examine the steady flux-thickness laws that emerge for different marine ice sheet configurations and bedrock profiles. We speculate that, for those cases where the dependence on the bedrock slope is lost in the parallel slab problem, we can expect this independence to persist under different bedrock shapes. It would also be of interest to compute and examine flux-thickness relationships under unsteady conditions, and see how they compare to their steady counterparts.

Appendix A

Existence and uniqueness of solutions to an abstract semicoercive variational inequality

Our objective here is to define an abstract minimisation problem analogous to Variational inequalities A-C. We keep the notation consistent with that of Chapter 3, and introduce an operator Φ which generalises operators A and $A+G$ found in Variational inequalities A-C.

Consider a closed subspace $V \subset \boldsymbol{W}^{1,r}(\Omega)$, with $1 < r < \infty$ and Ω a bounded domain in $\mathbb{R}^2$, equipped with the $\boldsymbol{W}^{1,r}(\Omega)$ norm. We also define a closed convex cone $\mathring{K} \subset V$ such that $0 \in \mathring{K}$. Then, the abstract minimisation problem which we study in this appendix consists in finding an element $\boldsymbol{u} \in \mathring{K}$ which minimises

$$\mathcal{J}(\boldsymbol{v}) = \langle \frac{1}{r}\Phi\boldsymbol{v} - f, \boldsymbol{v}\rangle_V \tag{A.1}$$

over $\mathring{K}$. Here, $f \in V'$ and $\Phi : V \to V'$ is an operator which we assume has the following properties: due to Φ, the functional $\mathcal{J} : V \to \mathbb{R}$ is convex and Gâteaux differentiable, with a derivative $D\mathcal{J} : V \to V'$, evaluated at $u \in V$ in the direction of $v \in V$, given by

$$\langle D\mathcal{J}(u), v\rangle_V = \langle \Phi u - f, v\rangle_V. \tag{A.2}$$

As a result, it follows that $\boldsymbol{u} \in \mathring{K}$ minimises $\mathcal{J}$ over $\mathring{K}$ if and only if

$$\langle \Phi\boldsymbol{u} - f, \boldsymbol{v} - \boldsymbol{u}\rangle_V \geq 0 \quad \forall \boldsymbol{v} \in \mathring{K}. \tag{A.3}$$

Moreover, we also assume that $\langle \Phi\boldsymbol{u}, \boldsymbol{u}\rangle_V \geq 0$ for all $\boldsymbol{u} \in V$. By [27, Theorem 1, Section 8.2] it follows that $\mathcal{J}$ is weakly lower semicontinuous in V. A further assumption is that

$$R_V = \{\boldsymbol{v}_R \in V : \langle \Phi\boldsymbol{v}_R, \boldsymbol{v}_R\rangle_V = 0\}$$

is a finite dimensional subspace for which we also have that $\Phi(\boldsymbol{v}+\boldsymbol{v}_R) = \Phi\boldsymbol{v}$ and $\langle \Phi\boldsymbol{v}, \boldsymbol{v}_R\rangle_V = 0$ for all $(\boldsymbol{v}, \boldsymbol{v}_R) \in V \times R_V$. We also define the subspace

$$R_V^* = \left\{ \boldsymbol{v}_R \in R_V \cap \mathring{K} : -\boldsymbol{v}_R \in R_V \cap \mathring{K} \right\},$$

and we consider the decomposition

$$R_V = R_V^* \oplus (R_V^*)^\perp.$$

Let $\mathbb{P} : V \to R_V$ be a continuous projection onto R_V and $\mathbb{Q} = \mathbb{I} - \mathbb{P}$. We assume the following abstract Korn inequality to hold:

$$\|\mathbb{Q}\boldsymbol{v}\|_V^r \lesssim \langle \Phi\boldsymbol{v}, \boldsymbol{v}\rangle_V \quad \forall \boldsymbol{v} \in V. \tag{A.4}$$

Finally, we denote by $\mathbb{P}^* : V \to R_V^*$ and $\mathbb{P}^\perp : V \to R_V^\perp$ two continuous projections onto R_V^* and $(R_V^*)^\perp$, respectively, for which we have $\mathbb{P} = \mathbb{P}^* + \mathbb{P}^\perp$. We also define $\mathbb{Q}^* = \mathbb{I} - \mathbb{P}^*$ and $\mathbb{Q}^\perp = \mathbb{I} - \mathbb{P}^\perp$.

Below, we include a theorem on the conditions under which the functional $\mathcal{J}$ has a minimiser in $\mathring{K}$, and when this minimiser is unique. This proof is a straightforward extension from a setup in Hilbert spaces to one in reflexive Banach spaces of [29, Theorem 1.II].

Theorem A.1. *If the following inequalities hold,*

$$\langle f, \boldsymbol{v}_R\rangle_V \leq 0 \qquad \forall \boldsymbol{v}_R \in \mathring{K} \cap R_V, \tag{A.5a}$$

$$\langle f, \boldsymbol{v}_R\rangle_V < 0 \qquad \forall \boldsymbol{v}_R \in (\mathring{K} \cap R_V) \setminus R_V^*, \tag{A.5b}$$

then $\mathcal{J}$ has a minimser in $\mathring{K}$. For any minimiser $\boldsymbol{u} \in \mathring{K}$, we have that $\boldsymbol{u} + \boldsymbol{v}_R$ also minimises $\mathcal{J}$ for all $\boldsymbol{v}_R \in R_V$ such that $\boldsymbol{u} + \boldsymbol{v}_R \in \mathring{K}$ and $\langle f, \boldsymbol{v}_R\rangle_V = 0$. Conversely, if $\mathcal{J}$ has a minimiser in $\mathring{K}$, then it holds that

$$\langle f, \boldsymbol{v}_R\rangle_V \leq 0 \quad \forall \boldsymbol{v}_R \in \mathring{K} \cap R_V. \tag{A.6}$$

Proof. For the first part of the proof, we begin by assuming inequalities (A.5) and noting that a consequence of these is that

$$R_V^* = \left(\mathring{K} \cap R_V\right) \cap \operatorname{Ker} f. \tag{A.7}$$

It is also possible to show that $\mathbb{Q}^*(K) = \operatorname{Ran}\mathbb{Q}^* \cap \mathring{K}$ and therefore $\mathbb{Q}^*(K)$ is closed. We now take a minimising sequence $(\boldsymbol{u}_n) \subset \mathring{K}$ of $\mathcal{J}$. Suppose $(Q^*\boldsymbol{u}_n) \subset \mathring{K}$ had a bounded subsequence; if this were the case, we could extract a further subsequence, also denoted $(Q^*\boldsymbol{u}_n)$, such that $(Q^*\boldsymbol{u}_n) \rightharpoonup \boldsymbol{u}$ for some $\boldsymbol{u} \in V$. Moreover, we would have that $\boldsymbol{u} \in \mathring{K}$

because $\mathbb{Q}^*(K) = \operatorname{Ran}\mathbb{Q}^* \cap \mathring{K}$ and $\operatorname{Ran}\mathbb{Q}^* \cap \mathring{K}$ is closed and convex, hence weakly closed, see for example [12, Theorem 3.7]. In fact, we could show that $\boldsymbol{u} \in \mathring{K}$ is a minimiser, since

$$\lim_{n\to\infty} \mathcal{J}(\boldsymbol{u}_n) = \lim_{n\to\infty} \mathcal{J}(\mathbb{Q}^*\boldsymbol{u}_n) \geq \mathcal{J}(\mathbb{Q}^*\boldsymbol{u}_n) = \mathcal{J}(\boldsymbol{u}_n).$$

Here, we have just used (A.7) for the first and last equalities, and the weakly lower semi-continuity of $\langle \Phi\boldsymbol{v}, \boldsymbol{v}\rangle_V$ to establish the upper bound.

Therefore, it remains to show that $(\mathbb{Q}^*\boldsymbol{u}_n)$ has a bounded subsequence. We proceed by contradiction: Assume that $\|\mathbb{Q}^*\boldsymbol{u}_n\|_V \to \infty$ as $n \to \infty$. By (A.4), we have that

$$\|\mathbb{Q}\boldsymbol{u}_n\|_V^r \lesssim \mathcal{J}(\boldsymbol{u}_n) + \langle f, \boldsymbol{u}_n\rangle_V. \tag{A.8}$$

We introduce the sequence $\boldsymbol{w}_n = \boldsymbol{u}_n / \|\mathbb{Q}^*\boldsymbol{u}_n\|_V$ in $\mathring{K}$. By (A.8),

$$\|\mathbb{Q}\boldsymbol{w}_n\|_V^r \lesssim \mathcal{J}(\boldsymbol{u}_n) / \|\mathbb{Q}^*\boldsymbol{u}_n\|_V^r + \|f\|_{V^*} / \|\mathbb{Q}^*\boldsymbol{u}_n\|_V^{r-1}, \tag{A.9}$$

so we clearly have that $\|\mathbb{Q}\boldsymbol{w}_n\|_V \to 0$. Note that $\|\mathbb{Q}^*\boldsymbol{w}_n\|_V = 1$ and, by assumption, $\mathbb{P} = \mathbb{P}^* + \mathbb{P}^\perp$, which implies $\mathbb{P}^\perp = \mathbb{Q}^* - \mathbb{Q}$; hence,

$$\left\|\mathbb{P}^\perp\boldsymbol{w}_n\right\|_V \leq \|\mathbb{Q}^*\boldsymbol{w}_n\|_V + \|\mathbb{Q}\boldsymbol{w}_n\|_V, \tag{A.10}$$

implying that $(\mathbb{P}^\perp\boldsymbol{w}_n)$ is a bounded sequence from which we may extract a subsequence, which we also denote by $(\mathbb{Q}^*\boldsymbol{w}_n)$, such that $\mathbb{P}^\perp\boldsymbol{w}_n \to \boldsymbol{\rho} \in (R_V^*)^\perp$ as $n \to \infty$ and $\|\boldsymbol{\rho}\|_V = 1$. However, since $\mathbb{P}^\perp = \mathbb{Q}^* - \mathbb{Q}$, and $\|\mathbb{Q}\boldsymbol{w}\|_V \to 0$ as $n \to \infty$, we have that

$$\mathbb{Q}^*\boldsymbol{w}_n \to \boldsymbol{\rho} \in (\mathring{K} \cap R_V) \setminus R_V^* \quad \text{as } n \to \infty. \tag{A.11}$$

By our initial assumption, that inequality (A.5b) holds, we then have that

$$\langle f, \boldsymbol{\rho}\rangle_V < 0. \tag{A.12}$$

We reach a contradiction when we write (A.9) as

$$\|\boldsymbol{u}_n\|_V^{r-1} \|\mathbb{Q}\boldsymbol{w}_n\|_V^r \lesssim \frac{1}{\|\boldsymbol{u}_n\|_V} (\mathcal{J}(\boldsymbol{u}_n) - \mathcal{J}(0)) + \langle f, \mathbb{Q}^*\boldsymbol{w}_n\rangle_V.$$

and observe that the lim sup of the left-hand side is strictly positive, while the lim inf of the right-hand side is strictly negative due to inequality (A.12).

For the second part of the theorem, if $\boldsymbol{u} \in \mathring{K}$ minimises $\mathcal{J}$ and if $\boldsymbol{v}_R \in R_V$ satisfies both $\boldsymbol{u} + \boldsymbol{v}_R \in \mathring{K}$ and $\langle f, \boldsymbol{v}_R\rangle_V = 0$, then we clearly have that

$$\mathcal{J}(\boldsymbol{u}) = \mathcal{J}(\boldsymbol{u} + \boldsymbol{v}_R)$$

and therefore $\boldsymbol{u} + \boldsymbol{v}_R$ is also a minimiser of $\mathcal{J}$ in $\mathring{K}$.

Finally, the last part of the theorem is a simple consequence of the equivalence between the minimisation of $\mathcal{J}$ over $\mathring{K}$ and variational inequality (A.3). We assume that $\boldsymbol{u} \in \mathring{K}$ solves (A.3). Since $\mathring{K}$ is a cone, we have that both 0 and $2\boldsymbol{u}$ are in $\mathring{K}$, so we may test both of them in (A.3) and show that

$$\langle \Phi \boldsymbol{u} - f, \boldsymbol{u} \rangle_V = 0.$$

Then, by testing with $\boldsymbol{v} = \boldsymbol{v}_R$, we obtain (A.6). □

Appendix B

Some technical results on finite element spaces

This appendix contains technical results that are required for establishing the convergence of the finite element approximations in Section 3.3.1. First, we consider the canonical projection $\pi_\Sigma : L^2(\Gamma_a) \to \Sigma_h^a$ onto piecewise constant functions and prove approximation properties in terms of fractional order Sobolev space norms and their dual. We require these properties to prove the convergence of the approximate Lagrange multiplier in Σ'. Then, we build an interpolation operator $\pi_V : V \to V_h$ for the velocity using a construction from [41] and examine some of its properties. Finally, we present an extension operator Φ from Σ into V_h that allows us to show that the pair $V_h \times \Sigma_h^a$ is stable in the sense of (3.37).

B.1 Approximation properties in a fractional order Sobolev space and its dual

Several technicalities arise from the need to handle the dual space of the fractional Sobolev space $W^{1-1/r,r}(\Gamma_a)$ and its finite element approximation Σ_h^a. The norm of the fractional Sobolev space $W^{s,m}(\Gamma_a)$ with $s \in (0,1)$ and $m \in [1,\infty]$ can be defined by

$$\|\phi\|^m_{W^{s,m}(\Gamma_a)} = \|\phi\|^m_{L^m(\Gamma_a)} + [\phi]^m_{W^{s,m}(\Gamma_a)}, \tag{B.1}$$

where

$$[\phi]^m_{W^{s,m}(\Gamma_a)} = \int_{\Gamma_a}\int_{\Gamma_a} \frac{|\phi(x)-\phi(y)|^m}{|x-y|^{1+sm}}\,\mathrm{d}x\mathrm{d}y,$$

see [21]. In order to prove certain approximation properties on Σ_h^a we need to introduce some theoretical results. We start by defining the following pair of spaces

$$L^m_0(e) = \left\{\phi \in L^m(e) : \int_e \phi\,\mathrm{d}x = 0\right\}, \quad W^{s,m}_0(e) = W^{s,m}(e) \cap L^r_0(e)$$

for an edge $e \in \mathcal{E}(\mathcal{T}_h, \Gamma_a)$. We can use the fractional normed Poincaré inequality proved in [26, Lemma 7.1] to show that

$$\|\phi\|_{L^m(e)} \leq |e|^s [\phi]_{W^{s,m}(e)} \quad \forall \phi \in W_0^{s,m}(e). \tag{B.2}$$

Inequality (B.2) can be extended to negative norms by writing the $L^m(e)$ norm for any $\phi \in L^m(\Gamma_a)$ as

$$\|\phi\|_{L^m(e)} = \sup_{\psi \in L^{m'}(e)} \frac{\int_e \phi\psi \, \mathrm{d}s}{\|\psi\|_{L^{m'}(e)}},$$

which is a consequence of the Riesz representation theorem. Then, we deduce that, if $\phi \in L_0^m(e)$, we have

$$\begin{aligned} \|\phi\|_{(W^{s,m}(e))'} &= \sup_{\psi \in W_0^{s,m}(e)} \frac{\int_e \phi\psi \, \mathrm{d}s}{\|\psi\|_{W^{s,m}(e)}} \\ &\leq |e|^s \sup_{\psi \in L^{m'}(e)} \frac{\int_e \phi\psi \, \mathrm{d}s}{\|\psi\|_{L^{m'}(e)}} = |e|^s \, \|\phi\|_{L^{m'}(e)} . \end{aligned} \tag{B.3}$$

For the finite element space Σ_h^a defined in (3.53c), let $\pi_\Sigma : L^m(\Gamma_a) \to \Sigma_h^a$ be the standard interpolation operator onto piecewise constant polynomials which takes the average of functions over each $e \in \mathcal{E}(\mathcal{T}_h, \Gamma_a)$. Then, from inequality (B.2) we can prove error estimates in fractional norms. Moreover, since $\phi - \pi_\Sigma \phi \in L_0^m(e)$ for all edges e in Γ_a for sufficiently smooth ϕ, then (B.3) leads to

$$\|\phi - \pi_\Sigma \phi\|_{(W^{s,m}(\Gamma_a))'} \lesssim h^{2s} \, \|\phi\|_{W^{s,m'}(\Gamma_a)} , \tag{B.4}$$

where $h = \max\{|e| : e \in \mathcal{E}(\mathcal{T}_h, \Gamma_a)\}$.

B.2 An interpolation operator for the velocity

Here, we compile a variety of results from different sources and prove an additional one regarding an interpolation operator for the velocity that preserves the discrete divergence and maps elements of K into K_h. We denote by π_V the interpolation operator introduced in [41, Section 3.1] that is defined as follows for each component of a vector-valued function: for a non-degenerate simplex $c \in \mathcal{T}_h$ with edges $\{e_i\}_{i=1}^3$ and vertices $\{\boldsymbol{a}_i\}_{i=1}^3$, we define the nodal basis functions ϕ_x with $x \in \{e_i\}_{i=1}^3 \cup \{\boldsymbol{a}_i\}_{i=1}^3$ by

$$\phi_{\boldsymbol{a}_i}(\boldsymbol{a}_j) = \delta_{ij}, \quad \int_{e_j} \phi_{\boldsymbol{a}_i} \, \mathrm{d}s = 0, \quad \int_{e_j} \phi_{e_i} \, \mathrm{d}s = \delta_{ij}, \quad \phi_{e_i}(\boldsymbol{a}_j) = 0,$$

for all $i, j \in \{1, 2, 3\}$. For each vertex $\boldsymbol{a}_i$ we choose a an edge $e_{\boldsymbol{a}_i} \in \{e_i\}_{i=1}^3$ such that $\boldsymbol{a}_i \in \overline{e_{\boldsymbol{a}_i}}$. We then define the dual basis functions $\{\psi_{\boldsymbol{a}_i}\}_{i=1}^3$ by

$$\int_{e_{\boldsymbol{a}_i}} \psi_{\boldsymbol{a}_i} \phi_x \, \mathrm{d}s = \delta_{\boldsymbol{a}_i x}, \quad \psi_{\boldsymbol{a}_i} \in \mathbb{P}_2(e_{\boldsymbol{a}_i}),$$

where x denotes the edge $e_{\boldsymbol{a}_i}$ or its two end-points. Then, (the scalar version of) the operator π_V can be defined as

$$(\pi_V u)(\boldsymbol{x}) = \sum_{i=1}^{3} \left(\left[\int_{e_{\boldsymbol{a}_i}} u\psi_{\boldsymbol{a}_i} \, \mathrm{d}s \right] \phi_{\boldsymbol{a}_i}(\boldsymbol{x}) + \left[\int_{e_i} u \, \mathrm{d}s \right] \phi_{e_i}(\boldsymbol{x}) \right).$$

When considering the definition of π_V in terms of a triangulation $\mathcal{T}_h$ of Ω, for vertices $\boldsymbol{a} \in \partial\Omega$, we set the associated edge $e_{\boldsymbol{a}}$ to also be contained in $\partial\Omega$. Then, we have that $\pi_V(V) \subset V_h$ and we can prove (B.9).

If the spaces V_h, Q_h and Σ_h^a are defined as in (3.53), a straightforward consequence of the definition of π_V is that

$$\langle Bq_h, \boldsymbol{v} \rangle_V = \langle Bq_h, \pi_V \boldsymbol{v} \rangle_V \qquad \forall (\boldsymbol{v}, q_h) \in V \times Q_h, \tag{B.5}$$

$$\langle \mu_h, \gamma_n \boldsymbol{v} \rangle_\Sigma = \langle \mu_h, \gamma_n \pi_V \boldsymbol{v} \rangle_\Sigma \qquad \forall (\boldsymbol{v}, \mu_h) \in V \times \Sigma_h^a. \tag{B.6}$$

Additionally, the interpolation operator π_V has two key approximation properties. First, the optimal approximation property

$$\|\boldsymbol{v} - \pi_V \boldsymbol{v}\|_{\boldsymbol{W}^{s,m}(\Omega)} \lesssim h^k \, |\boldsymbol{v}|_{\boldsymbol{W}^{s+k,m}(\Omega)} \tag{B.7}$$

holds for all $m \geq 0$ and $s, k \in \mathbb{N}$ such that $0 \leq s \leq 3$ and $0 \leq k \leq 3 - s$. Finally, given the operator $\mathbf{F}$ defined in (3.38), the additional approximation property holds:

$$\|\mathbf{F}(\mathbf{D}\boldsymbol{v}) - \mathbf{F}(\mathbf{D}\pi_V \boldsymbol{v})\|_{L^2(\Omega)} \lesssim h \, |\nabla \mathbf{F}(\mathbf{D}\boldsymbol{v})|_{L^2(\Omega)}. \tag{B.8}$$

Property (B.7) is shown to hold in [41]. On the other hand, (B.8) follows from [7, Theorem 3.4] by applying Poincaré's inequality once points (a) and (b) from Assumption 2.9 in that reference are shown to hold. These two points result from (B.5) and (B.7).

Finally, we may also prove that

$$\|\mathbf{F}(\mathbf{T}\boldsymbol{v}) - \mathbf{F}(\mathbf{T}\pi_V \boldsymbol{v})\|_{L^2(\Gamma_a)} \lesssim h \sum_{\substack{e \in \mathcal{E}(\mathcal{T}_h, \partial\Omega) \\ \overline{e} \cap \overline{\Gamma}_b \neq \emptyset}} |\nabla \mathbf{F}(\mathbf{T}\boldsymbol{v})|_{L^2(e)} \tag{B.9}$$

by imitating the proof for [7, Theorem 3.4] and applying Poincaré's inequality. Most of the steps in this proof draw from algebraic relations for the function $\mathbf{F}$ and the N-functions considered therein that continue to be valid in our context. Additionally, we need the following Orlicz-continuity result analogous to that of [7, Theorem 3.2]: for an N-function ψ with $\Delta_2(\psi) < \infty$ and an edge $e \in \mathcal{E}(\mathcal{T}_h, \Gamma_a)$,

$$\int_e \psi(|\mathbf{T}\pi_V \boldsymbol{v}|) \, \mathrm{d}s \lesssim \sum_{\substack{e' \in \mathcal{E}(\mathcal{T}_h, \partial\Omega) \\ \overline{e} \cap \overline{e'} \neq \emptyset}} \int_{e'} \psi(|\mathbf{T}\boldsymbol{v}|) \, \mathrm{d}s.$$

We may show the above inequality to hold by following the proof of [22, Theorem 4.5] and using the local L^1-estimate for $e \in \mathcal{E}(\mathcal{T}_h, \Gamma_a)$:

$$\int_e |\mathbf{T}\pi_V \boldsymbol{v}| \, \mathrm{d}s \lesssim \sum_{\substack{e' \in \mathcal{E}(\mathcal{T}_h, \partial\Omega) \\ \overline{e} \cap \overline{e'} \neq \emptyset}} \int_{e'} |\mathbf{T}\boldsymbol{v}| \, \mathrm{d}s.$$

To prove this inequality, we turn to the definition of π_V and use the bounds

$$\|\psi_{\boldsymbol{a}}\|_{L^\infty(e_{\boldsymbol{a}})} \lesssim |e|^{-1}, \quad \|\phi_{\boldsymbol{a}}\|_{L^1(e_{\boldsymbol{a}})} \lesssim |e| \quad \text{and} \quad \|\phi_e\|_{L^1(e)} \lesssim 1,$$

which result from inverse estimates as introduced in [11, Section 4.5].

B.3 An extension operator

In this section we prove an auxiliary result required for showing that the pair $V_h \times \Sigma_h^a$, defined in (3.53), is "inf-sup" stable in the sense of (3.37). We build an extension operator $\Phi : \Sigma \to V_h$ which is uniformly bounded and satisfies

$$\langle \mu_h, \gamma_n(\Phi\phi) \rangle_\Sigma = \langle \mu_h, \phi \rangle_\Sigma \quad \forall \mu_h \in \Sigma_h^a. \tag{B.10}$$

Step 1. We first find a uniformly bounded linear operator $\Pi : \Sigma \to \gamma_n(V_h)$ with the property that

$$\int_e (\phi - \Pi\phi) \, \mathrm{d}s = 0 \quad \text{for any } e \in \mathcal{E}(\mathcal{T}_h, \Gamma_a) \text{ and } \phi \in \Sigma. \tag{B.11}$$

Let

$$Z_h = \{\phi_h \in \mathcal{C}(\Gamma_a) : \phi_h|_e \in \mathcal{P}_2(e) \quad \forall e \in \mathcal{E}(\mathcal{T}_h, \Gamma_a)\}$$

and note that $Z_h \subset \gamma_n(V_h)$. For $\phi \in \Sigma$ and $e \in \mathcal{E}(\mathcal{T}_h, \Gamma_a)$, we define $\Pi_2 : \Sigma \to Z_h$ by setting

$$\begin{aligned} &(\Pi_2\phi)(a) = 0 \quad \text{for the endpoints } a \text{ in } e, \\ &\int_e \Pi_2\phi \, \mathrm{d}s = \int_e \phi \, \mathrm{d}s. \end{aligned}$$

We clearly have that $\Pi_2\phi = 0$ if and only if $\sum_{e \in \mathcal{E}(\mathcal{T}_h, \Gamma_a)} \int_e |\phi| \, \mathrm{d}s = 0$, so the latter defines a norm on $\Pi_2(\Sigma)$. By exploiting this fact and the norm equivalence on finite dimensional spaces, one can see that

$$\|\Pi_2\phi\|_{W^{1-1/r,r}(e)} \lesssim |e|^{-1/r'} \|\phi\|_{L^r(e)} \quad \forall e \in \mathcal{E}(\mathcal{T}_h, \Gamma_a)$$

for all $\phi \in \Sigma$. Now, let $\pi_Z : \Sigma \to Z_h$ be the quasi-interpolation operator defined in [26]. This operator is uniformly bounded in the $W^{1-1/r,r}(\Gamma_a)$ norm and satisfies

$$\|\phi - \pi_Z\phi\|_{L^r(e)} \lesssim |e|^{1-1/r} \|\phi\|_{W^{1-1/r,r}(e)}$$

for any edge $e \in \mathcal{E}(\mathcal{T}_h, \Gamma_a)$ and function $\phi \in \Sigma$. As a result, the operator $\Pi = \pi_Z + \Pi_2(I - \pi_Z)$ is uniformly bounded and possesses the required property (B.11).

Step 2. For the final step, we define a uniformly bounded operator $\gamma_{n,h}^{-1} : \gamma_n(V_h) \to V_h$ for which $\gamma_{n,h}^{-1}\phi_h \cdot \boldsymbol{n} = \phi_h$ on Γ_a. This operator can be defined as the solution of the problem:

$$\begin{aligned} \int_\Omega \nabla(\gamma_{n,h}^{-1}\phi_h) : \nabla \boldsymbol{v}_h \, \mathrm{d}x = 0 \qquad & \forall \boldsymbol{v}_h \in V_h, \\ \gamma_{n,h}^{-1}\phi_h \cdot \boldsymbol{n} = \phi_h \qquad & \text{on } \Gamma_a, \\ \gamma_{n,h}^{-1}\phi_h \cdot \boldsymbol{n} = 0 \qquad & \text{on } \Gamma_i. \end{aligned}$$

Then, the operator $\Phi = \gamma_{n,h}^{-1} \circ \Pi$ is uniformly bounded and property (B.10) holds.

Remark B.1. The construction of the uniformly bounded operator $\Pi : \Sigma \to \gamma_n(V_h)$ in step 1 above closely resembles that of the Fortin operator in [10, Proposition 8.4.3]. In fact, the operator $\Phi \circ \gamma_n : V \to V_h$ acts as a Fortin operator in the proof of Lemma 3.8.

Appendix C

Linearised solution of the steady subglacial cavity problem

For a Newtonian flow ($n = 1$) and a bedrock with small amplitude topography, the theory of [31] and [87] can be used to find steady solutions to the subglacial cavity problem presented in Sections 1.6 and 4.2 with which the numerical calculations can be compared. The method involves a linearisation of the boundary conditions and the use of complex variables to solve a Riemann-Hilbert problem for the velocities and stresses. We summarise the result for the particular case when $b = rL\cos(2\pi x/L)$.

It is convenient to parameterise the solution in terms of the scaled cavity end points c and d, such that the cavity occupies the region $d < \hat{x} < c+1$, where $\hat{x} = x/L$. The velocity is $\mathbf{u} = (u, w)$ with $u \approx u_b$, and on the cavitated region the vertical velocity w satisfies

$$\begin{aligned}\frac{\partial w}{\partial x} = &-\frac{4\pi^2 r u_b}{L}\cos\left(\frac{2\pi x}{L}\right)\\ &+\frac{4\pi^2 r u_b}{L}\left|\frac{\sin\pi(d-\hat{x})}{\sin\pi(\hat{x}-c)}\right|^{1/2}\left[\cos\pi\left(2\hat{x}+\tfrac{1}{2}(d-c)\right)-\sin\pi(c+d)\sin\frac{\pi}{2}(d-c)\right].\end{aligned} \tag{C.1}$$

The linearised steady kinematic condition for the cavity roof is $u_b\frac{\partial\theta}{\partial x} = w$, and integrating this subject to the conditions that $\theta = b$ at the cavity end points provides a constraint between c and d. In addition, c and d are related to the effective pressure by

$$N = \frac{8\pi^2 r\eta u_b}{L}\cos\frac{\pi}{2}(3d+c)\sin\frac{\pi}{2}(d-c). \tag{C.2}$$

Thus, for given values of N and u_b, these two constraints determine the end points c and d. Further, the normal stress on the contact region $c < \hat{x} < d$ is given by

$$\begin{aligned}&\sigma_{nn} + p_w =\\ &-\frac{8\pi^2 r\eta u_b}{L}\left|\frac{\sin\pi(d-\hat{x})}{\sin\pi(\hat{x}-c)}\right|^{1/2}\left[\cos\pi\left(2\hat{x}+\tfrac{1}{2}(d-c)\right)-\sin\pi(c+d)\sin\frac{\pi}{2}(d-c)\right],\end{aligned} \tag{C.3}$$

and the integral in (4.13) then gives the basal shear stress as

$$\tau_b = \frac{\pi^3 r^2 \eta u_b}{L} \left[5 - \sin 2\pi(c+d) \sin 2\pi(d-c) - \cos 2\pi(d-c) - 4\cos \pi(d-c) \right. \\ \left. - \cos \pi(3c+d) + \cos \pi(c+3d)\right]. \tag{C.4}$$

This cavitated solution requires $N < 8\pi^2 r\eta u_b/L$. Otherwise, there is no cavity and we have $\tau_b = 8\pi^3 r^2 \eta u_b/L$.

Bibliography

[1] *Sobolev Spaces*, Pure and Applied Mathematics 140, Academic Press, Elsevier, 2003.

[2] S. Adly and D. Goeleven, *A discretization theory for a class of semi-coercive unilateral problems*, Numerische Mathematik, 87 (2000), pp. 1–34.

[3] C. Amrouche and V. Girault, *Decomposition of vector spaces and application to the Stokes problem in arbitrary dimension*, Czechoslovak Mathematical Journal, 44 (1994), pp. 109–140.

[4] L. C. Andrews, G. A. Catania, M. J. Hoffman, J. D. Gulley, M. P. Lüthi, C. Ryser, R. L. Hawley, and T. A. Neumann, *Direct observations of evolving subglacial drainage beneath the Greenland Ice Sheet*, Nature, 514 (2014), pp. 80–83.

[5] J. W. Barrett and W. B. Liu, *Finite element approximation of the p-Laplacian*, Mathematics of Computation, 61 (1993), pp. 523–537.

[6] ——, *Quasi-norm error bounds for the finite element approximation of a non-Newtonian flow*, Numerische Mathematik, 68 (1994), pp. 437–456.

[7] L. Belenki, L. C. Berselli, L. Diening, and M. Růžička, *On the finite element approximation of p-Stokes systems*, SIAM Journal on Numerical Analysis, 50 (2012), pp. 373–397.

[8] F. B. Belgacem and Y. Renard, *Hybrid finite element methods for the Signorini problem*, Mathematics of Computation, 72 (2003), pp. 1117–1145.

[9] R. Bindschadler, H. Choi, A. Wichlacz, R. Bingham, J. Bohlander, K. Brunt, H. Corr, R. Drews, H. Fricker, M. Hall, et al., *Getting around Antarctica: new high-resolution mappings of the grounded and freely-floating boundaries of the Antarctic ice sheet created for the International Polar Year*, The Cryosphere, 5 (2011), pp. 569–588.

[10] D. Boffi, F. Brezzi, and M. Fortin, *Mixed Finite Element Methods and Applications*, Springer Series in Computational Mathematics, Springer, 2013.

[11] S. Brenner and R. Scott, *The Mathematical Theory of Finite Element Methods*, Texts in Applied Mathematics, Springer New York, 2007.

[12] H. Brezis, *Functional Analysis, Sobolev Spaces and Partial Differential Equations*, Universitext, Springer New York, 2010.

[13] F. Brezzi, W. W. Hager, and P. A. Raviart, *Error estimates for the finite element solution of variational inequalities. Part I. Primal theory*, Numerische Mathematik, 28 (1977), pp. 431–444.

[14] F. Brezzi, W. W. Hager, and P. A. Raviart, *Error estimates for the finite element solution of variational inequalities. Part II. Mixed methods*, Numerische Mathematik, 31 (1978), pp. 1–16.

[15] J. Brondex, O. Gagliardini, F. Gillet-Chaulet, and G. Durand, *Sensitivity of grounding line dynamics to the choice of the friction law*, Journal of Glaciology, 63 (2017), pp. 854–866.

[16] O. Chadli, J. Gwinner, and N. Ocharova, *On semicoercive variational-hemivariational inequalities—existence, approximation, and regularization*, Vietnam Journal of Mathematics, 46 (2018), pp. 329–342.

[17] Q. Chen, M. Gunzburger, and M. Perego, *Well-posedness results for a nonlinear Stokes problem arising in glaciology*, SIAM Journal on Mathematical Analysis, 45 (2013), pp. 2710–2733.

[18] P. Coorevits, P. Hild, K. Lhalouani, and T. Sassi, *Mixed finite element methods for unilateral problems: convergence analysis and numerical studies*, Mathematics of Computation, 71 (2002), pp. 1–25.

[19] G. G. de Diego, P. E. Farrell, and I. J. Hewitt, *Numerical approximation of viscous contact problems applied to glacial sliding*, Journal of Fluid Mechanics, 938 (2022), p. A21.

[20] G. G. de Diego, P. E. Farrell, and I. J. Hewitt, *On the finite element approximation of a semicoercive Stokes variational inequality arising in glaciology*, SIAM Journal on Numerical Analysis, 61 (2023), pp. 1–25.

[21] E. Di Nezza, G. Palatucci, and E. Valdinoci, *Hitchhiker's guide to the fractional Sobolev spaces*, Bulletin des Sciences Mathématiques, 136 (2012), pp. 521–573.

[22] L. Diening and M. Ruzicka, *Interpolation operators in Orlicz-Sobolev spaces*, Numerische Mathematik, 107 (2007), pp. 107–129.

[23] G. Drouet and P. Hild, *Optimal convergence for discrete variational inequalities modelling Signorini contact in 2D and 3D without additional assumptions on the unknown contact set*, SIAM Journal on Numerical Analysis, 53 (2015), pp. 1488–1507.

[24] G. Durand, O. Gagliardini, B. de Fleurian, T. Zwinger, and E. Le Meur, *Marine ice sheet dynamics: Hysteresis and neutral equilibrium*, Journal of Geophysical Research: Earth Surface, 114 (2009).

[25] T. L. Edwards, S. Nowicki, B. Marzeion, R. Hock, H. Goelzer, H. Seroussi, N. C. Jourdain, D. A. Slater, F. E. Turner, C. J. Smith, et al., *Projected land ice contributions to twenty-first-century sea level rise*, Nature, 593 (2021), pp. 74–82.

[26] A. Ern and J. L. Guermond, *Finite element quasi-interpolation and best approximation*, ESAIM: M2AN, 51 (2017), pp. 1367–1385.

[27] L. Evans, *Partial Differential Equations*, Graduate studies in mathematics, American Mathematical Society, 1998.

[28] L. Favier, O. Gagliardini, G. Durand, and T. Zwinger, *A three-dimensional full Stokes model of the grounding line dynamics: effect of a pinning point beneath the ice shelf*, Cryosphere, 6 (2012), pp. 101–112.

[29] G. Fichera, *Boundary Value Problems of Elasticity with Unilateral Constraints*, Springer Berlin Heidelberg, 1973, pp. 391–424.

[30] G. E. Flowers, *Modelling water flow under glaciers and ice sheets*, Proceedings of the Royal Society A: Mathematical, Physical and Engineering Sciences, 471 (2015), p. 20140907.

[31] A. C. Fowler, *A sliding law for glaciers of constant viscosity in the presence of subglacial cavitation*, Proceedings of the Royal Society of London. A. Mathematical and Physical Sciences, 407 (1986), pp. 147–170.

[32] ——, *Sliding with cavity formation*, Journal of Glaciology, 33 (1987), pp. 255–267.

[33] ——, *Mathematical Geoscience*, Interdisciplinary Applied Mathematics, Springer London, 2011.

[34] A. C. Fowler and F. C. Frank, *A theoretical treatment of the sliding of glaciers in the absense of cavitation*, Philosophical Transactions of the Royal Society of London. Series A, Mathematical and Physical Sciences, 298 (1981), pp. 637–681.

[35] A. C. Fowler, D. A. Larson, and F. C. Frank, *On the flow of polythermal glaciers - I. Model and preliminary analysis*, Proceedings of the Royal Society of London. A. Mathematical and Physical Sciences, 363 (1978), pp. 217–242.

[36] O. Gagliardini, D. Cohen, P. Råback, and T. Zwinger, *Finite-element modeling of subglacial cavities and related friction law*, Journal of Geophysical Research: Earth Surface, 112 (2007).

[37] O. Gagliardini and T. Zwinger, *The ISMIP-HOM benchmark experiments performed using the finite-element code Elmer*, The Cryosphere, 2 (2008), pp. 67–76.

[38] O. Gagliardini, T. Zwinger, F. Gillet-Chaulet, G. Durand, L. Favier, B. De Fleurian, R. Greve, M. Malinen, C. Martín, P. Råback, et al., *Capabilities and performance of Elmer/Ice, a new-generation ice sheet model*, Geoscientific Model Development, 6 (2013), pp. 1299–1318.

[39] C. Geuzaine and J.-F. Remacle, *Gmsh: A 3-D finite element mesh generator with built-in pre- and post-processing facilities*, International Journal for Numerical Methods in Engineering, 79 (2009), pp. 1309–1331.

[40] A. Gilbert, F. Gimbert, K. Thøgersen, T. V. Schuler, and A. Kääb, *A consistent framework for coupling basal friction with subglacial hydrology on hard-bedded glaciers*, Geophysical Research Letters, 49 (2022), p. e2021GL097507.

[41] V. Girault and L. R. Scott, *A quasi-local interpolation operator preserving the discrete divergence*, Calcolo, 40 (2003), pp. 1–19.

[42] J. Glen, *The flow law of ice: a discussion of the assumptions made in glacier theory, their experimental foundation and consequences*, in Physics of the Movement of Ice: Symposium at Chamonix 1958, Int. Assoc. Hydrol. Sci., Wallingford, UK, 1958, pp. 171–183.

[43] R. Glowinski, J. L. Lions, and R. Trémoliéres, *Numerical Analysis of Variational Inequalities*, North Holland, 1981.

[44] R. Greve and H. Blatter, *Dynamics of ice sheets and glaciers*, Springer Science & Business Media, 2009.

[45] G. H. Gudmundsson, *Basal-flow characteristics of a non-linear flow sliding frictionless over strongly undulating bedrock*, Journal of Glaciology, 43 (1997), pp. 80–89.

[46] G. H. Gudmundsson, J. Krug, G. Durand, L. Favier, and O. Gagliardini, *The stability of grounding lines on retrograde slopes*, The Cryosphere, 6 (2012), pp. 1497–1505.

[47] J. Gwinner, *Discretization of semicoercive variational inequalities*, Aequationes Math., 42 (1991), pp. 72–79.

[48] J. Haslinger, I. Hlaváček, and J. Nečas, *Numerical methods for unilateral problems in solid mechanics*, in Finite Element Methods (Part 2), Numerical Methods for Solids (Part 2), vol. 4 of Handbook of Numerical Analysis, Elsevier, 1996, pp. 313–485.

[49] C. Helanow, N. R. Iverson, J. B. Woodard, and L. K. Zoet, *A slip law for hard-bedded glaciers derived from observed bed topography*, Science Advances, 7 (2021), p. eabe7798.

[50] C. Helanow, N. R. Iverson, L. K. Zoet, and O. Gagliardini, *Sliding relations for glacier slip with cavities over three-dimensional beds*, Geophysical Research Letters, 47 (2020).

[51] I. J. Hewitt, *Modelling distributed and channelized subglacial drainage: the spacing of channels*, Journal of Glaciology, 57 (2011), pp. 302–314.

[52] P. Hild and P. Laborde, *Quadratic finite element methods for unilateral contact problems*, Applied Numerical Mathematics, 41 (2002), pp. 401–421.

[53] E. A. Hill, J. R. Carr, and C. R. Stokes, *A review of recent changes in major marine-terminating outlet glaciers in Northern Greenland*, Frontiers in Earth Science, 4 (2017), p. 111.

[54] M. Hintermüller, K. Ito, and K. Kunisch, *The primal-dual active set strategy as a semismooth Newton method*, SIAM Journal on Optimization, 13 (2002), pp. 865–888.

[55] A. Hirn, *Approximation of the p-Stokes equations with equal-order finite elements*, Journal of Mathematical Fluid Mechanics, 15 (2013), pp. 65–88.

[56] I. Hlaváček, *Dual finite element analysis for semi-coercive unilateral boundary value problems*, Aplikace Matematiky, 23 (1978), pp. 52–71.

[57] M. J. Hoffman, L. C. Andrews, S. F. Price, G. A. Catania, T. A. Neumann, M. P. Lüthi, J. Gulley, C. Ryser, R. L. Hawley, and B. Morriss, *Greenland subglacial drainage evolution regulated by weakly connected regions of the bed*, Nature Communications, 7 (2016), p. 13903.

[58] K. Hutter, *Theoretical glaciology: material science of ice and the mechanics of glaciers and ice sheets*, Springer, 1983.

[59] A. Iken, *The effect of the subglacial water pressure on the sliding velocity of a glacier in an idealized numerical model*, Journal of Glaciology, 27 (1981), pp. 407–421.

[60] A. Iken and R. A. Bindschadler, *Combined measurements of subglacial water pressure and surface velocity of Findelengletscher, Switzerland: Conclusions about drainage system and sliding mechanism*, Journal of Glaciology, 32 (1986), pp. 101–119.

[61] V. John, A. Linke, C. Merdon, M. Neilan, and L. G. Rebholz, *On the divergence constraint in mixed finite element methods for incompressible flows*, SIAM Review, 59 (2017), pp. 492–544.

[62] J. Jost and X. Li-Jost, *Calculus of variations*, vol. 64, Cambridge University Press, 1998.

[63] I. Joughin, B. E. Smith, and C. Schoof, *Regularized Coulomb friction laws for ice sheet sliding: application to Pine Island Glacier, Antarctica*, Geophysical Research Letters, 46 (2019), pp. 4764–4771.

[64] G. Jouvet, *Modélisation, analyse mathématique et simulation numérique de la dynamique des glaciers*, PhD thesis, École Polytechnique Fédérale de Lausanne, Lausanne, Switzerland, 2010.

[65] B. Kamb, *Sliding motion of glaciers: Theory and observation*, Reviews of Geophysics, 8 (1970), pp. 673–728.

[66] ——, *Glacier surge mechanism based on linked cavity configuration of the basal water conduit system*, Journal of Geophysical Research: Solid Earth, 92 (1987), pp. 9083–9100.

[67] R. F. Katz and M. G. Worster, *Stability of ice-sheet grounding lines*, Proceedings of the Royal Society A: Mathematical, Physical and Engineering Sciences, 466 (2010), pp. 1597–1620.

[68] N. Kikuchi and J. T. Oden, *Contact Problems in Elasticity*, Society for Industrial and Applied Mathematics, 1988.

[69] R. J. LeVeque, *Finite difference methods for ordinary and partial differential equations: Steady-state and time-dependent problems*, SIAM, 2007.

[70] L. Lliboutry, *General theory of subglacial cavitation and sliding of temperate glaciers*, Journal of Glaciology, 7 (1968), pp. 21–58.

[71] D. R. MacAyeal, *Large-scale ice flow over a viscous basal sediment: Theory and application to ice stream B, Antarctica*, Journal of Geophysical Research: Solid Earth, 94 (1989), pp. 4071–4087.

[72] D. W. F. Mair, M. J. Sharp, and I. C. Willis, *Evidence for basal cavity opening from analysis of surface uplift during a high-velocity event: Haut Glacier d'Arolla, Switzerland*, Journal of Glaciology, 48 (2002), pp. 208–216.

[73] B. Minchew and I. Joughin, *Toward a universal glacier slip law*, Science, 368 (2020), pp. 29–30.

[74] L. W. Morland, *Unconfined ice-shelf flow*, in Dynamics of the West Antarctic Ice Sheet, C. J. Van der Veen and J. Oerlemans, eds., Springer Netherlands, 1987, pp. 99–116.

[75] M. Morlighem, E. Rignot, T. Binder, D. Blankenship, R. Drews, G. Eagles, O. Eisen, F. Ferraccioli, R. Forsberg, P. Fretwell, et al., *Deep glacial troughs and stabilizing ridges unveiled beneath the margins of the Antarctic ice sheet*, Nature Geoscience, 13 (2020), pp. 132–137.

[76] S. M. J. Nowicki and D. J. Wingham, *Conditions for a steady ice sheet-ice shelf junction*, Earth and Planetary Science Letters, 265 (2008), pp. 246–255.

[77] J. Nye, *A calculation on the sliding of ice over a wavy surface using a Newtonian viscous approximation*, Proceedings of the Royal Society, 311 (1969).

[78] F. Pattyn, L. Perichon, G. Durand, L. Favier, O. Gagliardini, R. C. Hindmarsh, T. Zwinger, T. Albrecht, S. Cornford, D. Docquier, and et al., *Grounding-line migration in plan-view marine ice-sheet models: results of the ice2sea MISMIP3d intercomparison*, Journal of Glaciology, 59 (2013), pp. 410–422.

[79] F. Pattyn, C. Schoof, L. Perichon, R. C. A. Hindmarsh, E. Bueler, B. de Fleurian, G. Durand, O. Gagliardini, R. Gladstone, D. Goldberg, G. H. Gudmundsson, P. Huybrechts, V. Lee, F. M. Nick, A. J. Payne, D. Pollard, O. Rybak, F. Saito, and A. Vieli, *Results of the marine ice sheet model intercomparison project, MISMIP*, The Cryosphere, 6 (2012), pp. 573–588.

[80] S. S. Pegler and M. G. Worster, *An experimental and theoretical study of the dynamics of grounding lines*, Journal of Fluid Mechanics, 728 (2013), pp. 5–28.

[81] D. Pollard and R. M. DeConto, *Description of a hybrid ice sheet-shelf model, and application to Antarctica*, Geoscientific Model Development, 5 (2012), pp. 1273–1295.

[82] ——, *Improvements in one-dimensional grounding-line parameterizations in an ice-sheet model with lateral variations (PSUICE3D v2.1)*, Geoscientific Model Development, 13 (2020), pp. 6481–6500.

[83] F. Rathgeber, D. A. Ham, L. Mitchell, M. Lange, F. Luporini, A. T. McRae, G.-T. Bercea, G. R. Markall, and P. H. Kelly, *Firedrake: automating the finite element method by composing abstractions*, ACM Transactions on Mathematical Software (TOMS), 43 (2016), pp. 1–27.

[84] J. N. Reddy, *Energy principles and variational methods in applied mechanics*, John Wiley & Sons, 2017.

[85] C. Ritz, T. L. Edwards, G. Durand, A. J. Payne, V. Peyaud, and R. C. A. Hindmarsh, *Potential sea-level rise from Antarctic ice-sheet instability constrained by observations*, Nature, 528 (2015), pp. 115–118.

[86] R. A. V. Robison, H. E. Huppert, and M. G. Worster, *Dynamics of viscous grounding lines*, Journal of Fluid Mechanics, 648 (2010), pp. 363–380.

[87] C. Schoof, *The effect of cavitation on glacier sliding*, Proceedings of the Royal Society A: Mathematical, Physical and Engineering Sciences, 461 (2005), pp. 609–627.

[88] ——, *Ice sheet grounding line dynamics: steady states, stability, and hysteresis*, Journal of Geophysical Research: Earth Surface, 112 (2007).

[89] ——, *Marine ice-sheet dynamics. Part 1. The case of rapid sliding*, Journal of Fluid Mechanics, 573 (2007), pp. 27–55.

[90] ——, *Coulomb friction and other sliding laws in a higher order glacier flow model*, Mathematical Methods in the Applied Sciences, 20 (2010), pp. 157–189.

[91] ——, *Marine ice sheet dynamics. Part 2. A Stokes flow contact problem*, Journal of Fluid Mechanics, 679 (2011), pp. 122–155.

[92] ——, *Marine ice sheet stability*, Journal of Fluid Mechanics, 698 (2012), pp. 62–72.

[93] C. Schoof and I. J. Hewitt, *Ice-sheet dynamics*, Annual Review of Fluid Mechanics, 45 (2013), pp. 217–239.

[94] C. Schoof, I. J. Hewitt, and M. A. Werder, *Flotation and free surface flow in a model for subglacial drainage. Part 1. Distributed drainage*, Journal of Fluid Mechanics, 702 (2012), pp. 126–156.

[95] O. V. Sergienko and D. J. Wingham, *Grounding line stability in a regime of low driving and basal stresses*, Journal of Glaciology, 65 (2019), pp. 833–849.

[96] W. Spann, *Error estimates for the approximation of semicoercive variational inequalities*, Numerische Mathematik, 69 (1994), pp. 103–116.

[97] A. G. Stubblefield, M. Spiegelman, and T. T. Creyts, *Variational formulation of marine ice-sheet and subglacial-lake grounding-line dynamics*, Journal of Fluid Mechanics, 919 (2021), p. A23.

[98] S. Sugiyama and G. H. Gudmundsson, *Short-term variations in glacier flow controlled by subglacial water pressure at Lauteraargletscher, Bernese Alps, Switzerland*, Journal of Glaciology, 50 (2004), pp. 353–362.

[99] C. Taylor and P. Hood, *A numerical solution of the Navier-Stokes equations using the finite element technique*, Computers & Fluids, 1 (1973), pp. 73–100.

[100] R. Trémolières, J. Lions, and R. Glowinski, *Numerical Analysis of Variational Inequalities*, Elsevier Science, 2011.

[101] V. C. Tsai, A. L. Stewart, and A. F. Thompson, *Marine ice-sheet profiles and stability under Coulomb basal conditions*, Journal of Glaciology, 61 (2015), pp. 205–215.

[102] S. Tulaczyk, W. B. Kamb, and H. F. Engelhardt, *Basal mechanics of Ice Stream B, West Antarctica: 1. Till mechanics*, Journal of Geophysical Research: Solid Earth, 105 (2000), pp. 463–481.

[103] T. Van Bon, *Finite element analysis of primal and dual variational formulations of semicoercive elliptic problems with nonhomogeneous obstacles on the boundary*, Aplikace Matematiky, 33 (1988), pp. 1–21.

[104] J. Weertman, *On the sliding of glaciers*, Journal of Glaciology, 3 (1957), pp. 33–38.

[105] ——, *Stability of the junction of an ice sheet and an ice shelf*, Journal of Glaciology, 13 (1974), pp. 3–11.

[106] A. Wilchinsky and V. Chugunov, *Modelling ice flow in various glacier zones*, Journal of Applied Mathematics and Mechanics, 65 (2001), pp. 479–493.

[107] L. K. Zoet and N. R. Iverson, *Experimental determination of a double-valued drag relationship for glacier sliding*, Journal of Glaciology, 61 (2015), pp. 1–7.

[108] L. K. Zoet and N. R. Iverson, *Rate-weakening drag during glacier sliding*, Journal of Geophysical Research: Earth Surface, 121 (2016), pp. 1206–1217.